Numerical and Experimental Study of Methane and Propane Flames in Relation to Gas Flaring

Alechenu Audu Aboje (MSc)

Submitted in accordance with the requirements for the degree of

Doctor of Philosophy

The University of Leeds

School of Chemical and Process Engineering

Department of Energy Technology and Innovation Initiative (ETII)

January 2015

The candidate confirms that the work submitted is his own, except where work which has formed part of jointly authored publications has been included. The contribution of the candidate and the other authors to this work has been explicitly indicated below. The candidate confirms that appropriate credit has been given within the thesis where reference has been made to the work of others.

The work which appears in the jointly authored publication appears in chapters 5 and 6 of this thesis and the details of the works are as follows:
A. Aboje, J. Erete, K.J. Hughes, L. Ma, M. Pourkashanian and A. Williams. An investigation of methane and propane flares. Submitted to *The Journal of the Energy Institute,* January 2015.
A. Aboje, K.J. Hughes, D.B. Ingham, L. Ma, M. Pourkashanian and A. Williams. Prediction of a wake-stabilized propane flame in a cross-flow of air. Submitted to *The Journal of the Energy Institute,* January 2015.

All the work within the publication is directly attributable to the lead author, and the contributions of the other authors was aiding in the interpretation of the results and the actual writing of the paper.

Acknowledgements

I would like to express my deep gratitude to my research supervisors – Professor Alan Williams, Professor Mohamed Pourkashanian, Professor Derek Ingham, Dr Kevin Hughes and Dr Lin Ma for their patient guidance and invaluable encouragement throughout the course of this project. The contribution of Professor Michael Fairweather is also greatly appreciated.

Special thanks to Dr Sandy Black and James Erete for their selfless and patient assistance during the course of this project. My sincere gratitude also goes to Dr Alessandro Prazantelli, Dr Richard Porter, Dr Irina Flyagina, Detlev Mielczarek, Armin Arfaie, Paul Crosby, Alastair Clements, Wenlei Luo, Davide Poggio, Lisa Flaherty and Charlotte Kelsall. Immense gratitude also goes to my financial sponsors - The Petroleum Technology Development Fund (PTDF). Finally, I would like to acknowledge my family for their support throughout the course of this project.

Conferences and Publications

Conference:

A. Aboje, J. Erete, K.J. Hughes, L. Ma, M. Pourkashanian and A. Williams

An Investigation of methane and propane flares.

Joint Meeting of the British and Scandanavian-Nordic Sections of the Combustion Institute, Cambridge, 27-28 March 2014.

Journal Papers:

A. Aboje, J. Erete, K.J. Hughes, L. Ma, M. Pourkashanian and A. Williams. An investigation of methane and propane flares. Submitted to *The Journal of the Energy Institute,* January 2015.

A. Aboje, K.J. Hughes, D.B. Ingham, L. Ma, M. Pourkashanian and A. Williams. Prediction of a wake-stabilized propane flame in a cross-flow of air. Submitted to *The Journal of the Energy Institute,* January 2015.

Abstract

This research is concerned with the application of experimental and numerical methods to the investigation of gas flares. Gas flares are ubiquitous in the oil and gas industry and knowledge of the emissions from flares are of vital importance. Also, flares subjected to a cross-wind behave differently from flares in quiescent atmosphere and the stability of flares are important due to the possibility of blow offs in strong cross-winds. Natural gas flares are common on oil and gas production fields and given that natural gas is predominantly methane, many researchers have carried out numerical studies on methane cross-flow flames. In the present study, a propane cross-flow flame has been numerically investigated in addition to the investigations on methane and the predicted results have been compared against experimental data. The first chapter presents an introduction to the topic of gas flares and also outlines the objectives of the project. The second chapter presents a review of the literature on related topics. The third chapter presents the methods of investigation employed in this thesis. The fourth, fifth and sixth chapters present the results of the investigations carried out while the final chapter gives the general conclusions and suggestions for future investigations. The numerical aspect of the work investigates the capability of the existing codes in the ANSYS Fluent software to predict propane flares both with and without cross-flows. Comparisons have been made between the non-premixed and the partially premixed combustion models in their capability to predict wake-stabilized cross-flow flames. Also, the results obtained using the Reynolds stress turbulence model was compared against the Large Eddy Simulation technique with the latter showing better predictions for the temperature and species. The reaction mechanism of Ranzi et al. (2012) was used to model the kinetics of the propane reactions while the GRI 3.0 was used to model the kinetics of the methane reactions. Soot in the propane flame was modelled with the Moss-Brooke-Hall model. The experimental aspect of the work involved comparing the lift-off behaviour of the methane and the propane flames given the effect of lift-off on the emission from the flames.

Table of Content

List of Figures

List of Tables

Nomenclature

Latin Alphabets

a	Absorbtion coefficient
c_p	Specific heat at constant pressure
d	Pipe diameter
Da	Damkohler number
D_i	Diffusion coefficient of species
F_j	Body force source term
Fr	Froude number
g	Acceleration due to gravity
G	Filter function
h	Mixture enthalpy
I	Radiation intensity
k	Turbulent kinetic energy
lm	Turbulent mixing length
Le	Lewis number
p	Pressure
P	Production of turbulence kinetic energy
Pr	Prandtl number
$P(Z)$	Probability density function of the mixture fraction
q	Radiative heat flux vector
R_{rad}	Radiation heat source term
r	Position of radiation intensity
R	Jet-to-cross-flow momentum flux ratio
Re	Reynolds number
R_0	Universal gas constant
s	Stoichiometric air-fuel mass ratio
Sc	Schmidt number

S_L	Laminar flame speed
S_{ij}	Mean stress tensor
t	Time
T	Temperature
u_f	Fuel jet nozzle exit velocity
u_k	Cartesian velocity components
v	Number of moles
$\dot{w}_i$	Reaction rate source term
W_i	Molecular mass of species
Y_i	Mass fraction of species
Z	Mixture fraction

Greek Alphabets

α	Parameter in the beta PDF
α_i	Coefficient of thermal diffusivity
β	Parameter in the beta PDF
$\bar{\Delta}$	Width of filtering function
Γ	Gamma function
δ	Delta function
δ_L	Laminar flame thickness
δ_{ij}	Kronecker delta
ε	Rate of scalar dissipation of turbulent kinetic energy
η	Combustion efficiency
θ	Angular velocity
μ	Dynamic viscosity
μ_t	Turbulent eddy viscosity
ν	Kinematic viscosity
μ_t	Turbulent eddy viscosity

ρ	Density
σ_S	Scattering coefficient
τ_{ij}	Stress tensor
ϕ	Scalar variable
φ	Fuel-air mass ratio ratio
χ	Scalar (mixture fraction) dissipation rate
ω	Turbulence frequency of energy containing eddies
Ω	Mean rate of rotation tensor

Abbreviations

CFD	Computational Fluid Dynamic
DECC	Department of Energy and Climate Change
DNS	Direct Numerical Simulation
EPA	Environmental Protection Agency
EPFM	Eulerian Particle Flamelet Model
GGFR	Global Gas Flaring Reduction
IPCC	Intergovernmental Panel on Climate Change
JFICF	Jet Flame In a Cross-Flow
LES	Large Eddy Simulation
NOAA	National Oceanic and Atmospheric Administration
PAH	Poly-Aromatic Hydrocarbons
PDF	Probability Density Function
RANS	Reynolds average Navier-Stokes
RSM	Reynolds Stress Model
SGS	SubGrid-Scale model
SLFM	Stationary Laminar Flamelet Model
VOC	Volatile Organic Compounds
WSGGM	Weighted-Sum-of-Gray-Gas-Models

Chapter 1

Introduction

1.1 Background of the research

The study of gas flares has traditionally revolved around three key problems: economics, safety and the environment. Of these three issues, environmental issues now receives the most attention. According to the NOAA satellite data reports, global gas flaring volumes were estimated at about 140 bcm in 2011 and this is equivalent to about 25 percent of the United States' gas consumption or about 32 percent of the European Union's gas consumption (Elvidge et al., 2009). Table 1.1 shows the NOAA flaring estimates for 2007-2011 for the top ten flaring countries. In 2011, Russia had the largest flaring volume, with 37 bcm, followed by Nigeria at 15 bcm with both countries accounting for an estimated 42% of global gas flaring.

Table 1-1 Estimated flared volumes for the top 10 Countries (2007-2011) Source: GGFR website.

Volumes in bcm	2007	2008	2009	2010	2011	Changes from 2010 to 2011
Russia	52.3	42.0	46.6	35.6	37.4	1.8
Nigeria	16.3	15.5	14.9	15.0	14.6	-0.3
Iran	10.7	10.8	10.9	11.3	11.4	0.0
Iraq	6.7	7.1	8.1	9.0	9.4	0.3
USA	2.2	2.4	3.3	4.6	7.1	2.5
Algeria	5.6	6.2	4.9	5.3	5.0	-0.3
Kazakhstan	5.5	5.4	5.0	3.8	4.7	0.9
Angola	3.5	3.5	3.4	4.1	4.1	0.0
Saudi Arabia	3.9	3.9	3.6	3.6	3.7	0.1
Venezuela	2.2	2.7	2.8	2.8	3.5	0.7

Gas flaring is the process of disposing unwanted flammable gases and vapours by combustion into the open atmosphere. Flaring is less damaging to the environment than gas venting because, according to the (IPCC), methane, which is a major constituent of natural gas, has been found to be about 25 times more effective at trapping heat in the atmosphere than carbon dioxide over a 100-year period. This means that the global warming potential of methane is 25 times that of carbon dioxide. Oxidation of the waste gases may therefore preclude emissions of methane and other greenhouse gases, although situations may arise when the toxicity of the waste gases relative to that of the products of combustion need to be taken into consideration. On the other hand, inefficient or poorly operated flares lead to the release of pollutants, such as CO, NOx, VOCs and particulate matter (soot) into the atmosphere with an adverse effect on life and on the environment. A study by the Alberta Research Council (M. Strosher, 1996) found more than 150 volatile organic compounds (VOCs) and polyaromatic hydrocarbons (PAH) species in the plumes of flare products in the oilfields of Alberta. The most abundant compound found in flare emissions were ethyl benzene, toluene, benzene, xylenes, styrene, acenapthalene and biphenyl with some of these compounds having been established as carcinogens or mutagens.

The relationship between the emission from gas flares and their combustion efficiencies has been the subject of numerous research papers. In the context of flare performance, combustion efficiency represents the degree to which the carbon containing species in the hydrocarbons is converted to carbon dioxide based on the assumption of complete combustion. The combustion performance of a flare system is largely impacted by the design of the flare system, energy density of the flare gas stream, composition of the flare gas stream, and environmental conditions, such as ambient temperature, wind speed, and wind direction (Kostiuk et al., 2004). The improvement of flare systems design and the optimization of flare operating parameters are fundamental to the enhancement of flare performance and is an issue of high priority for the industries concerned, as well as governments around the world. The Kyoto Protocol - an international treaty negotiated in

December 1997 in the city of Kyoto, as an improvement on the United Nations Framework Convention on Climate Change which came into force in February, 1992. It is a legally binding treaty under which industrialized nations will decrease their total emissions of greenhouse gases by 5.2% compared to the year 1990. The aim is to lower the overall emissions for six greenhouse gases - nitrous oxide, carbon dioxide, sulphur, methane, hexafluoride, HFCs, and PFCs - calculated as a mean over the five-year period of 2008-12. To this end, various countries have enacted legislations specifying national targets for emission control. For instance, in the UK, the government is committed to reducing green house gas (GHG) emissions by 36% below the 1990 level by the year 2020, and by 80% by the year 2050 (DECC, 2009). Industries have therefore been mandated by governments to achieve this stated goal with emission taxes in place to enforce compliance. Much research effort has gone into the investigation of the various problems associated with flares, such as pollutant emissions, heat radiation and even noise generation. Most of these investigations have been either theoretical or experimental in nature. However in the light of the rapid progress in computational technology, numerical analysis has emerged as an effective tool for complementing and validating experimental efforts as well as investigating areas where traditional methods have proved expensive or impossible.

1.2 Motivation for this study

According to a recent study, 5% of the world's natural gas production is wasted by burning or 'flaring' unused gas (Farina, 2011). However, this economic wastage is a secondary issue compared to the environmental and health impact of gas flaring activities. The process of gas flaring releases tonnes of toxic compounds into the atmosphere among which includes the oxides of nitrogen, sulphur, VOCs, etc. Nowhere is this tragedy more pronounced than in the Niger Delta region of Nigeria. Solution gas flaring in the upstream sector of the oil and gas industry has been the major cause of the environmental concerns in the region, but with the present government

policies for natural gas utilization, there has been a steady decline in the volume of flared gas in the region. However, in the light of current developments in the downstream sector of the oil and gas industry, increased local refinery output is being envisaged with even new refineries possibly coming on stream. Therefore, the need to investigate more environmentally friendly ways of refining crude oil and gas is crucial. Furthermore, in the upstream sector, even though the volume of solution gas flaring is steadily on the decline, it is however unrealistic to conclude that solution gas flares can be completely eradicated in the near future. This is because situations may still arise where it is uneconomical to invest in gas recovery infrastructure due to the gas volume available and furthermore, the geological formation may not support reinjection of the gas leaving only the option of flaring the gas. Therefore, there is also a need to keep investigating ways of improving the environmental quality of both solution gas flaring as well as refinery gas flaring processes. The application of mathematical models to the study of gas flaring has been increasing over the years. A model is an abstract or physical representation of reality. Computational Fluid Dynamic (CFD) is a technique of investigation that uses numerical methods to solve the governing nonlinear differential equations that describes the fluid flow for predefined boundary conditions. This results in a vast amount of predicted data for the temperature, density, flow velocity and species concentrations for any region where combustion is present. This technique, although fairly recent, has proved to have certain advantages over the more traditional methods of investigation, i.e., analytical and experimental methods. CFD data can thus be utilized to validate or optimize various parameters obtained experimentally and as such can be a powerful complementary tool to experiments. Thus a key advantage of CFD is that once a CFD model is experimentally validated, it can then be used to predict system performance before construction, installation or modification. This leads to great savings in costs when compared to the experimental method as physical modifications are not necessary. CFD has seen immense growth over the last several decades and the technology has been widely applied to various engineering feats, such as automobile and aircraft design.

1.3 Objectives of the study

The objective of this is study is to investigate the combustion and emission characteristics of methane and propane both experimentally and numerically. Both straight jet and cross-flow flames are investigated in this project. A previous work has been made by Lawal (2011) where he predicted the flow structure of a methane flame burning in a cross-flow. However the models employed were unable to capture the partially premixed region occurring at the shear layer of the fuel-air interaction. Castiñeira and Edgar (2008) have also employed the numerical method to investigate the flow structure of a natural gas flame in a cross-flow. This work will employ propane burning in a cross-flow to investigate the physical and chemical structures of the flame. Furthermore, changes in the geometry of the burner tip has been shown to improve flame stability and hence contribute to a reduction in the emissions (Pardiwalla, 1996). This present study aims at building on these findings by:

(i) Experimental investigation of the effect of the burner nozzle thickness on the flame lift off heights for methane and propane flames.

(ii) Numerical prediction of flame lengths for propane and methane flames and the comparison of inflame and post flame emissions.

(iii) Investigation of the capability of the existing CFD models implemented in the Fluent solver to predict cross-flow flames for propane combustion.

1.4 Scope of the thesis

The laboratory aspect of the work will be limited to the investigation of straight-jet diffusion flames operating in the transitional to near turbulent regime, due to the absence of a wind-tunnel and also, due to the limitations on the diffusion burner available for the project. The numerical aspect will be limited to the investigation of cross-flow diffusion flames using wind-tunnel experimental data obtained from the literature.

1.5 Flares

A gas flare, alternatively known as a flare stack, is a device primarily designed to eliminate by oxidation in the open atmosphere, waste gases which is otherwise not feasible to use or transport, in a safe, reliable and efficient manner such that it produces a more desirable emission to the atmosphere than simply venting the gases. Industries require different flare designs for flares operating under different conditions and various strategies have been designed over the last fifty years or so to meet these varying needs. For instance, gases can be flared under emergency situations to deal with plant upsets or flares may be used intermittently for scheduled maintenance. Emergency flares tend to be larger in size and are often intended to handle very high flow rates of flare gas at near sonic exit velocities. Also, flares can be used to handle continuous combustible gas flows that arise within the facility and are not economical to recover. These types of flares constitute over 90 % of flaring activities. Typically, continuous flares involve lower gas flow rates and subsequently low exit velocities compared to an emergency type flare (Kostiuk et al., 2004).

1.5.1 Flare types

Flares are broadly categorized in two ways: (i) elevated flares, and (ii) enclosed ground flares. Elevated flares can be further subdivided according to the type of flare tip gas mixing employed (air-, steam-, pressure- and non-assisted). Elevated flares can have single-point, or multiple-point point burners for improved burning. However, the most commonly used utility flares are the single-point, elevated, circular nozzle flares without assist media, such as air or steam. Potentially dangerous conditions that exist at ground level can be prevented by elevating the flare far above sources of ignitions (flammable gases, etc.). Also, the effects of heat, smoke, noise and objectionable odours can be reduced and the products of combustion can be well dispersed above working areas (Stone et al., 1995). Elevated flares find the most application in practice and are preferred primarily on economic grounds, having a large capacity for a relatively small capital outlay. Waste gases that are composed of heavier compounds have a greater tendency to

smoke and hence steam assisted flares have been designed to dispose of these gases. Steam is injected into the waste gases using induction tubes or steam rings. The injection of steam induces turbulence in the waste gases which enhances mixing and therefore improves combustion efficiency. Furthermore, the process causes additional air to be induced into the waste stream supplying the oxygen needed for augmented smokeless capacity. Forced air is employed in some of the flares to generate the combustion air as well as the mixing needed for smokeless operation. These types of flares have burners with spider-shaped designs which are situated close to the top of a cylindrical steel three feet or more in diameter. The major advantage of the air-assisted flares is that they can be employed where steam is not accessible. Although air-assist is not often employed in large flares (due to economic reasons) the number of air assisted flares being built is still on the increase (Stone et al., 1995). On the other hand, many facilities routinely flare smaller quantities of hydrocarbon gases that are exhausted at pressures too low to allow them to be routed to the facility fuel gas system or high elevation. Thus, smaller ground flares are sometimes used to handle the smaller, more routine flows. As the name implies, ground flares basically locate the flare tip and combustion zone at ground level, however these types of flare may still require an elevated stack for the discharge of the effluent gases.

1.5.2 Flares in the oil and gas industry

Flares are used in a wide range of industries including nuclear plants, chemical plants, and steel mills. They are however extensively employed in the oil and gas industries to dispose waste gases that are uneconomical to process. Flares in the oil and gas industry can be classified in two ways:

(i) Production flares are flares associated with oil and gas production fields. When oil is recovered and brought to the earth's surface, the hydrocarbon gases that are dissolved in the oil come out of solution due to a reduction in the pressure. These gases vary widely in composition and energy content depending on the reservoir. If it is uneconomical to recover the gases for sale as natural gas, then they are usually flared at or near the

oil-well site. Thus solution gas flaring, sometimes called associated gas flaring is used to dispose of the unwanted combustible gases that are associated with the oil during conventional oil recovery. The term “solution gas” is applied to the total sum of gases that come out-of-solution when heavy or conventional oil is extracted from high pressure reservoir conditions and lowered to near atmospheric pressure.

(ii) Process flares are flares that occur due to the activities of oil and gas processing industries, such as oil refineries and petrochemical plants. In process flares, the gases that leak past the safety valves protecting the various process units is brought together via a network of collecting pipes and burnt at the flare tip. This gas feeds the flame which continuously burns on oil refinery stacks. To reduce smoke formation in process flares, it is necessary to inject steam into the flared gas. The amount of steam per unit mass of hydrocarbon depends on both the type of hydrocarbon (least for light saturated hydrocarbons, increasing with molecular weight and extent of unsaturation, most for aromatics) and on the design of the flare tips. In practice, these ratios range from about 0.2 kg steam per kg hydrocarbon to over 1 kg steam per kg of hydrocarbon (Brzustowski, 1976). However, this process of steam addition is a principal source of noise in process flaring. Further, depending on the situation, flares can be designed for continuous or intermittent operation. Continuous flares usually involve relatively low gas flow rates and consequently low exit velocities. Solution gas and acid gas flares constitute important examples of low momentum gas flares used in the upstream sector of the oil and gas industry. Refinery gas flares on the other hand are typically operated in the high momentum regime. Under emergency conditions, for example the flaring rates of a single refinery flare can be of the order 10^5 kg/h, with a single release rate of the order of 1000 MW for a few minutes. The largest flare installations can reach rates which are even higher, perhaps by an order of magnitude (Brzustowski, 1976). They are characterized by high waste gas velocities in the range of Mach number 0.2 to 1 with values of $R \gg 1$ and often employ facilities to inject air, water or steam into the base of the flame to decrease the formation and emission of soot (Kostiuk et al., 2004).

1.5.3 Operating regimes of flares

Flares can operate in quiescent atmospheres, where the velocity of the cross-wind is negligible compared to the velocity of the flare gas (Figure 1-1) or flares may also operate in a cross-wind, where the velocity of the cross-wind is comparable to or higher than the velocity of the flare gas (Figure 1-2). The structure and emission characteristics of the flare will be different for these two broad categories of flare regimes and these are reviewed in more detail below.

1.5.3.1. Flares in a quiescent atmosphere

Flares in quiescent wind conditions may be classified depending on whether the flame behaviour is controlled by the buoyancy of the hot gases or the momentum of the fuel jet. Studies of turbulent diffusion flames make use of a fuel derived Froude number (defined as the ratio of fuel momentum to buoyancy of hot gases) to achieve this. Using this approach, Becker et al. (1978) have defined the flame regime of flares in quiescent wind conditions as either buoyancy or momentum driven. Delichatsios (1993) has expounded on this idea to define a regime map for straight-jet turbulent diffusion flames where the different regimes of the flames are defined based on whether the turbulence is generated by the large buoyancy forces present in the flame or by instabilities present in the cold flow. Thus, the fuel derived Froude number is an important dimensionless number that has been found to significantly influence the flow regime of flares in quiescent wind conditions and it is given by:

$$Fr = \frac{\rho_f u_f^2}{(\rho_f - \rho_p) g d_f} \tag{1.1}$$

where u_f is the fuel jet nozzle exit velocity, ρ_f and ρ_p are the densities of the fuel jet and the burnt gas plume respectively, d_f is the diameter of the flare pipe nozzle and g is the magnitude of the earth's gravitational acceleration.

Figure 1-1 Photograph of a flare in a quiescent atmosphere (adapted from Dreamstime Images, 2011)**.**

When buoyance effects become insignificant, such as in a situation of high nozzle exit velocity combined with a small nozzle exit diameter, the Froude number reduces to the more familiar form:

$$Fr = \frac{u_f^2}{g d_f} \tag{1.2}$$

Flares operating under quiescent conditions are often encountered in the oil and gas refining industry where a strong cross-wind may not be present due to the shielding effects of other refinery structures. On the other hand, flares in a cross-wind are prevalent in production fields and are discussed next.

1.5.3.2. Flares in a cross-wind

Investigations of flares in a cross-winds have shown that the cross-wind interacts intricately with the jet to produce a unique set of flow and combustion characteristics. Therefore, the cross-wind velocity has been correlated with the nozzle exit velocity of the flare gas to give a dimensionless number – the jet-to-cross-flow momentum flux ratio, the value of which is used to determine the regime of cross-wind flares.

Figure 1-2 Photograph of a flare in a cross-wind (adapted from cyberhawk innovations, 2014)**.**

The jet-to-cross-flow momentum flux ratio is defined as:

$$R = \frac{\rho_f u_f^2}{\rho_{cf} u_{cf}^2} \tag{1.3}$$

where ρ_f, ρ_{cf} and u_f, u_{cf} are the densities and velocities of the fuel jet and the cross-flow respectively. Based on the value of R, two very different flow regimes for cross-wind flares have been identified – the high momentum regime corresponding to high values of R and the low momentum regime

corresponding to low values of R. At high momentum flux ratios, the flame normally exists as a lifted diffusion flame slightly bent over by the cross-wind, while at low values of the momentum flux ratio the flame is "wake-stabilized" by a standing vortex that exists on the wake of the burner pipe as shown in Figure 1.3. The high momentum regime (also called the jetting regime) is characterized by values of $R > 10$, where the flame may be lifted or seated on the flare release pipe depending on the magnitude of u_f and the burner diameter (Huang & Wang, 1999). At high momentum flux ratios, the strength of the jet dominates, and the cross-wind effects are relatively unimportant. Refinery and emergency flares are typically operated in this regime. The low momentum regime on the other hand is characterized by values of $R \leq 10$, where the flame bends over significantly in the wind and is usually attached to the burner tip, i.e. rim-stabilized. However, at very low momentum flux ratios $R \ll 10$, the flame stabilizes in the wake of the burner (Periasamy & Gollahalli, 2011). The structure of wake-stabilized flares was first thoroughly investigated by Gollahalli & Nanjundappa (1995) where they described a three-zone flame structure with a recirculating eddy attached to the lee-side of the pipe, a mixing layer of non-reacting fuel from the pipe carried over the eddy, and an axisymmetric main tail of the flame. In this flow regime, the momentum of the cross-wind dominates the entrainment and mixing because of the low values ofu_f. Huang & Wang (1999) further categorised low-momentum flames as being down-washed ($R < 0.1$), cross-flow-dominated ($0.1 \leq R < 1$), transitional ($1 \leq R < 3$) and jet dominated ($3 \leq R < 10$). These flow conditions are common in normal operating condition of production flares where values of $R < 0.1$ are typical (Gogolek et al., 2010). A general regime map covering both cross-wind conditions and flares in quiescent atmospheres has been provided by Gogolek. The regime map identifies: (i) the jetting or momentum regime, where fuel inertia dominates both buoyancy and cross-wind, (ii) buoyant flames, where there is little initial fuel momentum and little or no cross-wind, and (iii) wake-stabilized where the cross-wind momentum dominates both fuel momentum and buoyancy, with each of these regimes having its own distinct mechanism.

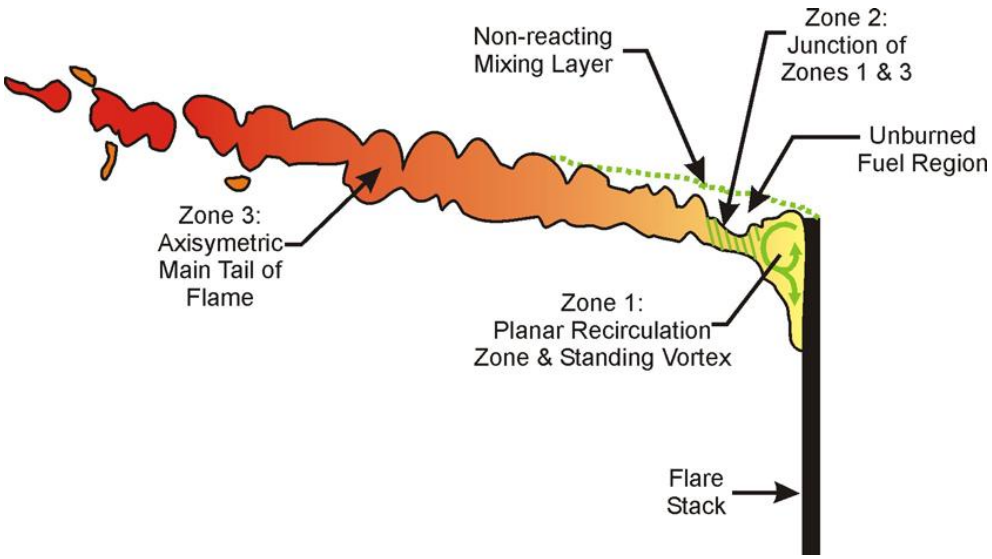

Figure 1-3 Schematic of a wake-stabilized flare showing the three-zone structure (adapted from Johnson et al., 2001).

1.5.4 Flare system

The typical flare system consists of (i) a single- or multiple-burner unit, (ii) the flare riser, (iii) the pipings for gas collection and a gas collection header, (iv) the knockout drum to remove entrained liquids in the waste gases (v) a purge gas supply or water seal to avoid flashbacks (vi) the igniter and gas pilots to ignite the waste gases in cases of blow outs, and (vii) a provision for external sources of momentum if required (forced air or steam injection). Nitrogen, inert gases or natural gas can be used as a purge gas. In principle, nitrogen is often preferred as a purge gas given that the use of fuel gas in purge systems can also contribute to environmental pollution. These can be in the form of carbon dioxide or the oxides of sulphur when fuel gas used in the high pressure and low pressure flare headers are burnt off. The purge gas is used to keep a positive pressure in the flare header when the flare gas flow rate is quite low (near zero), and thus prevent the risk of atmospheric air ingression into the header through the flare tip or even through the valves. Such an occurrence would be very dangerous since it could lead to an explosion if the flashback system is to fail. Figure 1-4 is a schematic diagram of a typical steam-assisted elevated smokeless flare system.

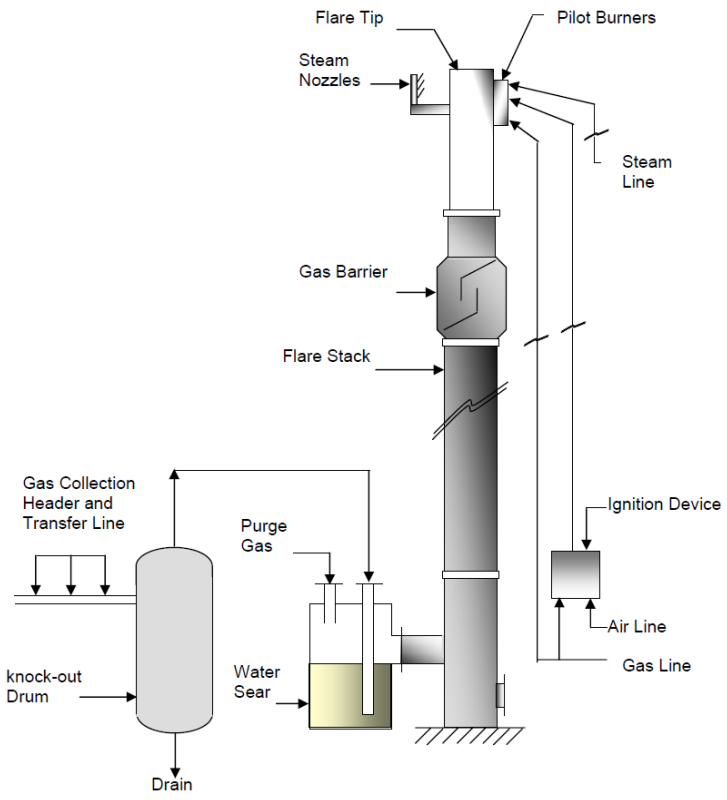

Figure 1-4 Diagram of a steam-assisted elevated flare system (KLM, 2012)**.**

1.5.4.1. Flare gas burner

At the top of a flare stack is the flare tip which is comprised of the burners and a system to mix the air and the fuel. The dimensionless parameter R, which governs the behaviour of the flare gas jet in cross-winds in the region near the tip is also useful in the design of the flare gas burner. The flare gas burner is designed to deliver environmentally acceptable combustion of the waste gases over the flare system's capacity range. They are normally proprietary in design and thus the minimum or the maximum capacity of a flare system to burn waste gases with a stable flame is a function of the flare tip design. Flame stability may be improved by utilizing flame holder retention devices built into the flare tip inner circumference. Burners incorporating more recent flame holder designs can sustain a stable flame over a flare gas exit velocity range of about 1 to 180 m/sec (Kalcevic, 1980). The practical maximum capacity of a flare tip is often limited by the vent stream pressure available to overcome the pressure drop in the system (API, 1982).

Figure 1-5 Photograph of a typical flare gas burner with pilot gas burners and a steam nozzle (adapted from Thermal Solutions Asia).

1.5.4.2. Pilot gas burner

The flare burner tip is usually equipped with pilots manufactured from heat - resistant steel material incorporating a nozzle that is designed for maximum pilot flame stability, an igniter which is designed to fit directly into the nozzle and an inspirator assembly for controlling the gas and air mixture to the pilot. Figure 1-5 shows a photograph of a flare head featuring pilot gas burners and a steam nozzle (to the right). The purpose of the gas pilot is to provide the flame required to ignite the waste gas stream coming out of the main burner. Although several flares are being operated without any pilot gas burners, it should be understood that the flare reliability is compromised where pilot burners are not used. Facilities that have vital flaring requirements (such as sour gas flares) must operate pilots, monitor them continuously and have a reliable ignition system – usually with a suitable backup system. Pilot burners have to be designed to withstand strong winds, heavy rains and high temperatures along with direct flame impingement from the flare tip.

Chapter 2

Literature Review

The performance of a gas flare is evaluated in terms of its radiation output, pollutant emissions, stability limits, combustion efficiency and noise level. These performance parameters are affected by several operating factors, such as the flare size, shape and trajectory, the flare gas heating value and exit velocity, the burner geometry, cross-wind effects, etc. The radiation from a flare flame can significantly affect the environment and also pose a health hazard to personnel and hence a flare site needs to be appropriately selected. The pollutant emissions are also of environmental and health concerns while the stability of a flare flame is believed to impact the emissions from the flare as well as being important to avoiding flame blowout or blowdown. Several authors have investigated these parameters and have come up with various theoretical, empirical and numerical based correlations for predicting their effects. A gas flare is a typical example of a diffusion flame and the study of diffusion flames can be widely categorized into the study of vertical jet diffusion flames and the study of jet diffusion flames in a cross-flow of air and these are reviewed in the next section.

2.1 Vertical jet diffusion flames

Vertical jet diffusion flames have several applications, such as in industrial furnaces, environmental waste incinerators as well as in gas flaring that occur in quiescent atmosphere among others. This has led to a large body of literature on the experimental and numerical investigations into jet diffusion flames. Jet diffusion flames are usually classified as either being laminar, transitional or turbulent depending on the fuel Reynolds number. It is more difficult to give a general discourse on diffusion flames in comparison to premixed flames because no simple, measurable parameter similar to the burning velocity or the flame thickness in premixed flames can be defined. However, for a simple laminar diffusion flame on a circular nozzle, the flame

height is mostly used to characterize the flame. In the mathematical analysis of diffusion flames, diffusion of species is only considered in the radial direction, while diffusion in the axial direction is usually neglected as shown by the flame schematic in Figure 2.1. As the fuel flows along the flame axis, it diffuses outwards in the radial direction while the oxidizer diffuses radially inwards. A diffusion flame is rate determining and the rate of reaction is directly related to the amounts of fuel and oxidant diffusing into the reaction zone. Combustion depends more on the rate of diffusion of the reactant than on the rate of the chemical processed involved. This is to say that the average reaction rate depends on the average mixing rate. In a diffusion flame, combustion takes place at the interface of the fuel and oxidant gas and the products of combustion begin to form at this interface and diffuse outwards as shown schematically by Figure 2.2. The flame length is independent of pressure at a given mass flow rate, but will increase with an increase in the fuel volumetric flow rate. In addition to the study of flame lengths, the study of flame temperatures and the species distribution in the flames form the central theme in the flame investigation. The seminal study by Hottel and Hawthorne (1949) of a methane jet diffusion flame has shed ample light into the structure of jet diffusion flames. In this work, they came up with empirical correlations for predicting the visible flame length as well as the concentration patterns for turbulent jet diffusion flames formed by combustible gases issuing from circular jets into the stagnant air. They concluded that the agreement between the theoretical analysis and the data obtained on the flame lengths and axial concentration patterns indicated clearly that the mixing process and buoyancy were the controlling factor in determining the progress of the combustion process in jet diffusion flames. They determined that for free flames in which the effect of buoyancy is negligible (high nozzle velocity, small nozzle diameter), the following relationship may hold for the length of free turbulent flame jets:

$$L/d = \frac{5.3}{C_T}\sqrt{\frac{T_F}{\alpha_T T_N}\left[C_T + (1 - C_T)\frac{M_S}{M_N}\right]} \qquad (2.1)$$

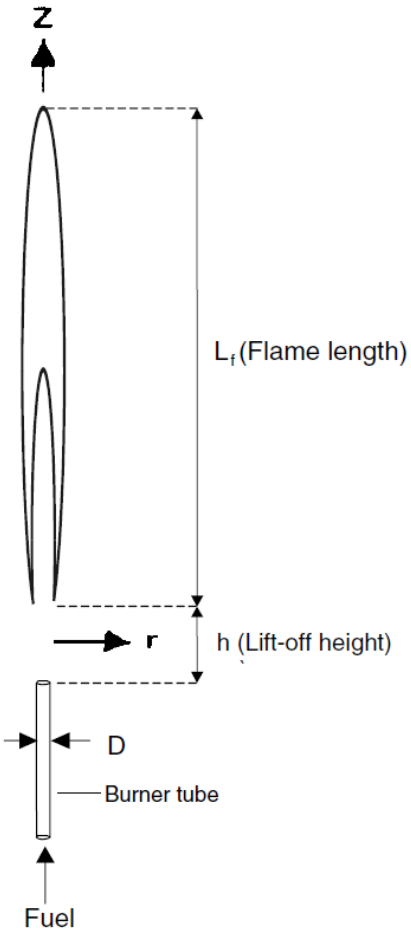

Figure 2-1 Schematic of a vertical jet diffusion flame (Mahmud et al., 2007).

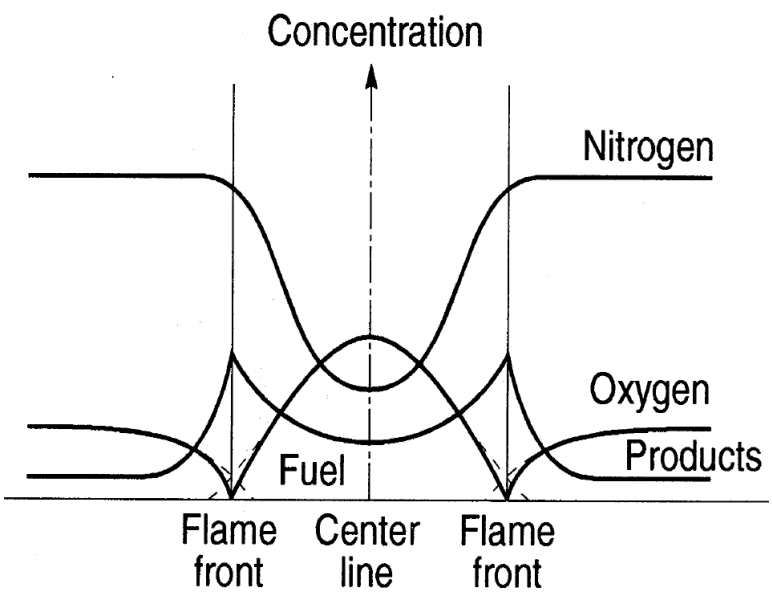

Figure 2-2 Diffusion flame structure (Hottel and Hawthorne, 1949)**.**

where d is the nozzle diameter, T_F is the absolute adiabatic flame temperatue, T_N is the absolute temperature of the nozzle fluid, M_S and $M_N$are the molecular mass of the surrounding and nozzle fluid, respectively, C_T is the mole fraction of the nozzle fluid in the unreacted stoichiometric mixture, and α_T is the moles of reactants/mole of products for the stoichiometric mixture.

Gollahalli & Zadeh (1985) performed extensive experimental work on propane jet diffusion flames where they investigated the effect of the gas heating value on the flame-length, the flame lift-off, radiation, temperature and the species distribution in the flame. They observed that the combined effect of the low flame velocity of propagation and higher gas velocities needed for the required energy release rates in low calorific value gases was found to pose a challenge in terms of flame stability. It is an established fact that above a certain critical gas exit velocity, the diffusion flame gets detached from the burner and stabilizes downstream in a lifted off configuration (Kalghatgi (1981a). This behaviour is more likely to occur when a low calorific gas is burned. With further increase in the gas flow exit velocity, the flame stabilization region will move further downstream of the burner and above a second critical value of the gas flow exit velocity, the flame will blow out. Hence a flame lift-off may occur due to the aerodynamic effect of increasing the fuel jet exit velocity or due to the decrease in the volumetric energy content of the fuel. Flame lift-off and blowout can therefore occur at much lower exit velocities when the energy content of the gas jet is lowered. However, the work did not take into consideration the effect of the burner nozzle thickness on the flame stability. The stability of jet diffusion flames is very important due to its contribution to the phenomena of blowout and blowdown in flares. Flame stability has been defined as the condition where a decrease in flare gas heating value or an increase in flare gas exit velocity results in flame blowout (Pohl et al., 1986). This is known as the blowout stability limit of the flame. A jet diffusion flame in still air will detach itself from the burner tip if the flow rate through the burner is increased above a certain limiting value and this is known as the lift-off stability limit. A flame is stabilized when the turbulent burning velocity, S_t of

the burnt gases becomes equal to the local flow velocity, U of the jet. "The flame will blowout when the change in S_t cannot keep up with the changes in U anywhere in the jet". Hence a flame can be stabilized in a rim-attached of lifted configuration. Both have their advantages and disadvantages. The rim-attached flames are less prone to blowouts, operate at lower temperatures and hence generate less NO_x emissions. However lifted flames prolong the life of flare burner tips and also allow gases to be burnt at a faster rate. Kalghatgi (1981a) carried out an important study on the stability of jet diffusion flames in still air and established a correlation between the blowout stability limits and the burner internal diameter for different hydrocarbon flames. Furthermore, he established a relationship between the burner exit velocity at blowout $\bar{U}_e$ and the fuel Reynolds number R_H as follows:

$$\bar{U}_e = 0.017 R_H (1 - 3.5 \times 10^{-6} R_H) \tag{2.2}$$

where

$$\bar{U}_e = \frac{U_e}{S_u}\left(\frac{\rho_e}{\rho_\infty}\right)^{1.5} \tag{2.3}$$

and R_H is given by

$$R_H = (H \cdot S_u / \nu_e) \tag{2.4}$$

where S_u is the laminar velocity, ν_e is the kinematic viscosity and H is the distance along the burner axis where the average fuel concentration drops to the stoichiometric level and is given by

$$H = 4\left[\frac{\theta_e}{\theta_\delta}\left(\frac{\rho_g}{\rho_\infty}\right)^{1/2} - 5.8\right] d_e \tag{2.5}$$

where is θ_δ is the fuel mass fraction in the stoichiometric mixture of the fuel and ambient gas, θ_e is the fuel mass fraction at the burner exit, d_e is the effective burner diameter, ρ_g is the density of the burner gas at the burner exit, and ρ_∞ is the ambient density. The relationship (2.2) was initially developed for pure hydrocarbon fuels, however further tests have revealed that this so called "universal formula for describing the blowout limit of jet

diffusion flames" was also applicable to hydrocarbon mixtures. The mixtures investigated by the author included methane/air, methane/CO_2, propane/air and propane/CO_2 mixtures. He observed that for a fixed burner internal diameter, the blow out stability limit decreased as the concentration of diluents in the gas increased. Furthermore, extrapolation of equation (2.2) by the author to cases where the burner exit flow is choked revealed that for a given gas, there exists a critical burner internal diameter d_{cr}, beyond which a stable flame cannot exist at any flow rate. However, it must be noted that the investigation did not consider the effects of the burner thickness on the flame stability.

In addition to the flame stability discussed above, the emission of pollutants from flames is also of major concern in industries involved in gas flaring (Strosher, 2011; Pohl, 1986). Of note are the emissions of nitrogen oxides and carbon particulates (soot). Many authors have also looked into the relationship between the emission of these pollutants from flames and the fluid mechanical properties of the flames as well as the geometrical properties of the gas burners (Meunier et al., 1998; Gollahalli et al., 1992). Primary variables such as the jet velocity, jet exit Reynolds or Froude numbers and nozzle internal diameter have been investigated and have been found to have substantial influence on flame emissions (Meunier et al., 1998). Meunier et al. (1998) showed that the Fenimore (or the so called prompt mechanism) mechanism is the major route for the formation of NO in turbulent jet diffusion flames, confirming similar observations in laminar diffusion flames (Drake and Blint, 1991). The Zeldovich (or thermal) mechanism and the Fenimore mechanism are the two known kinetic routes involved in the formation of NO_x in the combustion of fuels that containing no bound nitrogen. It is known that in the combustion of hydrocarbon fuels, both mechanisms may dominate the process of NO formation, whereas for non-hydrocarbon fuels, only the thermal mechanism is often active. The dependence of NO_x (defined as the combined concentration of NO and NO_2) emissions on the fluid mechanical and geometrical properties was investigated by the authors in a later work (Munier et al., 1998). In this work, they studied the variation of the emission index of NO_x ($EINO_x$), defined as

the grams of NO_x produced for every kilogram of fuel burnt (assuming all the carbon in fuel is converted to CO_2) with the fluid mechanical properties i.e. the fuel jet velocity, Reynolds number and Froude number. $EINO_x$ can be expressed mathematically as (Meunier et al., 1998):

$$EINO_x(g/kg) = \frac{3[NO_x]MW_{NO2}1000}{[CO_2]MW_{C3H8}} \tag{2.6}$$

where MW is the molecular weight of the compounds, the brackets refer to the mole fractions of the compounds and the factor 3 accounts for the formation of 3 moles CO_2 from one mole of C_3H_8. Also, the authors studied the variation of $EINO_x$ with burner diameter by investigating burners of three different internal diameters for the same fluid mechanical properties. With respect to the emissions, the results from the experiments showed a decreasing trend of $EINO_x$ with increasing fuel jet exit velocity. However, the study did not take the external diameter of the pipes (i.e. the pipe thickness) into consideration, which could impact the blowout stability limit due to the the recirculation effects caused by increasing the pipe thickness.

With respect to the numerical aspect of flame investigations, methane/air jet diffusion flames are relatively easier to simulate because of the non-sooty nature of the flames. The GRI reaction mechanism has been widely used for the simulation of this fuel, as well as for the simulation of natural gas, which is predominantly methane. Norton et al. (1992) compared measurements of temperature and concentration for major fuel and hydrocarbon radicals with the results of the numerical simulation of the chemical structure of an axis-symmetric laminar methane/air diffusion flame burning at atmospheric pressure. Particular attention was given to the prediction of radical species because their concentrations generally provides a more critical and demanding test of reaction mechanisms and model predictions compared to the major species (Westoreland et al., 1986). It has been the goal of immense research effort to discover universal state relationships for temperature and species concentrations as a function of a single variable in order to create libraries of flamelets for the modelling of turbulent diffusion flames. The mixture fraction, Z which has served this purpose well, may be

defined as a form of equivalence ratio normalised such that it varies from zero in the oxidizer stream to one in the fuel stream. It represents the mass fraction originating from the fuel stream and it is a conserved quantity hence very useful in the modelling of flames since it does not generate a source term. Despite the success recorded with the use of the mixture fraction, it was discovered in general that another variable was required because the so called “universal relationships” were not applicable to chemical intermediates. Also, the concentration of the species change with the local stretch or strain rate in a flame (Smyth et al., 1993). Therefore in addition to the mixture fraction, at least one additional variable, such as the strain rate needs to be matched in order for the computed results to agree with experimental observations more closely. It has been found that the strain rate can be characterized conveniently by the scalar dissipation rate, which is a function of the mixture fraction gradient. The scalar dissipation rate captures the departure of the flame from equilibrium conditions, hence helps in the prediction of slow reacting species such as flame radical species. Mahmud et al. (2007) performed a numerical investigation of a turbulent methane/air diffusion flame at atmospheric pressure and reported good agreement between numerical and experimental data for temperature and major species at different axial stations downstream of the burner nozzle. In this work, the author compared two radiation models frequently employed for the calculation of radiation heat losses in diffusion flames, namely the optically thin flame approximation model and the Discrete transfer model of Lockwood & Shah (1981). Previous work (Giordano & Lentini, 2001) showed that the optically thin flame approximation model (OTFAM) tends to over-predict the heat losses causing an under-prediction of the in-flame temperature because this approach does not account for the absorption of radiation. Therefore a thermal radiation model that can account for both emitting and absorbing medium is required in order to accurately account for the heat losses. The author showed that the discrete transfer model (DTM) was a much more comprehensive model, capable of resolving the above mentioned limitation of the OTFAM.

The simulation of propane flames are more challenging due to its relatively complex reaction mechanism as well as the substantial amount of soot produced in such flames. With the development of simplified soot mechanisms, some authors have simulated propane diffusion flames with relatively good agreement between experimental and numerical results. Fairweather et al. (1992) applied the soot model of Leung and Lindstedt (1991) to the prediction of soot in a turbulent propane jet diffusion flame in atmospheric pressure conditions and obtained good agreement with experimental data from Nishida and Mukohara (1982). The Leung and Lindstedt model is a two-step model which solves a transport equation for the mean soot mass fraction and another for the soot particle number density. Soot models developed and implemented in an earlier work (Syed et al., 1990) suffered from the simple assumption that the soot formation process is related to the local fuel concentration, despite the fact that the reactions leading to initial formation of the soot nucleus and the further growth of the soot particles are known to proceed from pyrolysis products arising from the breakdown of the fuel rather than from the parent fuel itself. The authors used a global approach in their work where they linked the important reactions of soot formation to the gas phase via a pyrolysis product, taken to be acetylene.

2.2 Cross-flow diffusion flames

A turbulent jet diffusion flame in a cross-flow is the closest representation of a gas flare burning in a cross-wind and it is characterized by it's jet-to-cross-flow momentum ratio as well as its shape, size and centreline trajectory. Thermochemical properties, such as the radiation from the flares and pollutant emissions are of paramount importance in flare design. Figure 2-3 is a schematic of a turbulent diffusion flame in a cross-flow and showing the flame shape. The trajectory is defined as the curvilinear length of the flame centreline. The vertical height of the flame is defined as the vertical projection of the flame from the burner tip to the end of the contagious flame, while the projection of the flame as measured from the burner tip to the end of the contagious flame in the direction of the cross-flow is its horizontal

length. Collecting samples from flares burning in the open atmosphere is very difficult due to the size and turbulence of the flames, which are often located at the tip of the stack anywhere from 10 to over a 100 m in height. For these reasons, experimental studies of cross-flow flames are typically carried out in open-loop wind tunnels to simulate the field conditions. Such wind tunnels are meant to create a uniform cross-flow pattern with relatively

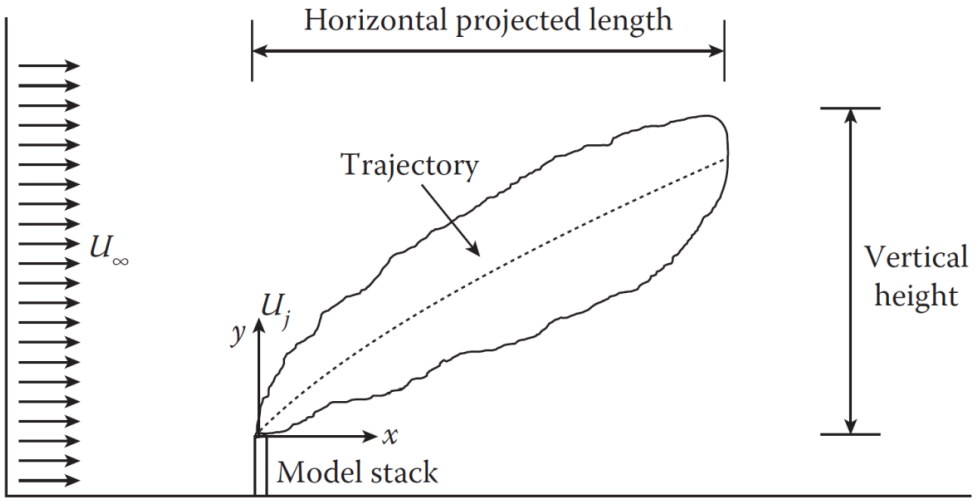

Figure 2-3 Schematic of a turbulent diffusion flame in a cross-flow.

low turbulence intensity of about 0.1 – 0.5% (Huang & Yang, 1996). This provides the opportunity to vary the wind speed inside the test section. Kostiuk and co-workers (2004) carried out a wind tunnel study of a flare in a cross-flow to determine the effect of the cross-wind on the combustion efficiency of a flare as well as the emissions from the flare. The work helped in correlating the combustion efficiency with the cross-flow velocity as well as the pipe geometry for solution gas flares operating in the wake-stabilized regime. The combustion efficiency of the flare, sometimes called the carbon conversion efficiency is defined as the ratio between the mass of carbon in the form of carbon dioxide which is produced by the flame and the mass of carbon in the form of hydrocarbon fuel exiting the flare (Kostiuk et al., 2004):

$$\eta = \frac{mass\ rate\ of\ carbon\ in\ the\ form\ of\ CO_2\ produced\ by\ the\ flame}{mass\ rate\ of\ carbon\ in\ the\ form\ of\ HC\ fuel\ exiting\ the\ flare} \quad (2.7)$$

The hydrocarbon destruction efficiency is the fraction of hydrocarbons consumed by the flare. If the post combustion gas contains methane, then this represents an increase in greenhouse gas emissions. Results from the Kostiuk et al. (2004) experiments indicated that the dependence of the combustion efficiency, η on the cross-flow velocity, u_{cf} is a function of the ratio $u_{cf}/{u_j}^{1/3}$, i.e., the efficiency reduces by about the cube of the wind speed, thus showing that the wind speed can have a strong effect on flare efficiency. However, the results also showed that higher velocity fuel jets are less susceptible to the effects of the cross-wind. The effect of the flare pipe diameter on the combustion efficiency was also investigated by Kostiuk and his co-workers and the results indicated that the efficiency characteristics are roughly the same for the different pipe diameters tested. However the larger diameter flare stacks showed more resistance to the effects of increased cross-wind speed. Kostiuk and his co-workers developed a model for the combustion efficiency for flares in the wake-stabilized regime and also showed that the dominant fluid mechanical forces associated with wake-stabilized flares are the momentum flux of the cross-wind and the buoyancy flux of the combustion products. By taking into consideration the ratio of the buoyancy flux of the plume to the momentum flux of the cross-wind as the major factors defining the flow, a simple model was developed to correlate the effects of wind speed (u_{cf}), exit velocity (u_f), and outside stack diameter (d_o). This model resulted in the application of the buoyant plume dimensionless parameter $u_{cf}/\left(gu_f d_o\right)^{1/3}$, which was successful in collapsing data for any particular flare stream composition. By factoring in the fuel energy density, an empirical model was developed for the combustion efficiency of low-momentum flares (Kostiuk et al., 2004):

$$(1-\eta)\cdot(LHV_{mass})^3 = A\cdot\exp\left(B\frac{u_{cf}}{\left(gu_f d_o\right)^{1/3}}\right) \tag{2.8}$$

where η is the combustion efficiency, LHV_{mass}, is the lower heating value of the flare stream on a mass basis and g is the gravitational acceleration. The

coefficients A and B take the following values: A = 133.3-(MJ/kg)^3 and B = 0.317 for methane based flares; and A = 32.06-(MJ/kg)^3 and B = 0.272 for propane and ethane based flares.

Furthermore, Huang & Chang (1994) categorized cross-flow flames in the low-momentum regime into the liftable and never-lift flames. They observed that if the flame was lit at a cross-wind velocity above a critical value, then the base of the flame could never leave the burner before blow-off, i.e., the flame always attached to the wake of the burner, even at high jet exit velocities. Huang & Wang (1999) further categorized wake-stabilized flames as down-washed flames ($R < 0.1$) and cross-flow-dominated flames ($0.1 < R < 1$) with the down-wash and reverse flow regions being recognized as the primary regions related to flame stability. Huang & Yang (1996) investigated the thermal and concentration field of burner-attached propane flames in a cross-flow with the conclusion that the resulting complex characteristics of the concentration and temperature fields implied that the diffusion flame model used for liftable jet flames was not suitable for the burner attached jet flames in a cross-flow. Gollahalli & Nanjundappa (1995) also investigated burner wake-stabilized propane flames where they described a three-zone flame structure with a recirculating eddy attached to the wake of the pipe, a mixing layer of non-reacting fuel from the pipe carried over the eddy, and an axisymmetric main tail of flame. They observed that at very low momentum flux ratio ($R \approx 0.02$), the axisymmetric main tail of the flame disappeared and the planar flame zone became more yellow and luminous. In the high momentum regime however, they had observed that the planar flame zone or recirculation zone, disappeared and only the tail part remained attached to the burner. For cross-wind flames in the high momentum regime, Pohl (1986) had shown that the combustion efficiency was independent of the pipe diameter while Mcdaniel (1983) has shown that the combustion efficiency of low-heat content gases tend to degrade at the high exit velocities. Kalghatgi (1981b) had demonstrated that a stable flame was impossible to achieve for cross-wind speeds greater than a limiting value in the high momentum regime. Bandaru & Turns (2000) performed a well-defined laboratory scale study of high momentum turbulent diffusion jet

flames in a cross-flow for methane, propane, ethylene and H_2/CO flames. They calculated the emission indices of the pollutants from these flames as a function of the jet- to-cross-flow momentum ratio as well as the effect of hydrogen pilot flames on the emissions. They reported relatively higher unburned hydrocarbon and CO emission indices, together with higher NO_2-to-NO_x ratios in the cross-flow flames in comparison with their straight, vertical, jet flame counterparts. They observed that cross-flow flames produced two to three times more NO_x emissions than similar jet flames. They also measured the radiant fraction from the flames and found that the NO_x emission index magnitudes tends to show a strong inverse correlation with the respective radiant fractions associated with the flames. They speculated that higher cross-flow velocity lead to substantially less soot being formed within the flame thus making the flame less radiative and thus hotter, which in turn leads to higher NOx emissions.

An early attempt at the numerical modelling of cross-flow flames was made by Botros & Brzustowski (1979), where they used the flame-sheet combustion model of Burke and Schumann (1928) and the standard $k-\varepsilon$ eddy viscosity turbulence closure model to calculate the flow structure of a propane jet in a cross-flow. The flame sheet model is simplistic in its approach given that it assumes fast chemistry (i.e. chemical reactions proceed via a fast single irreversible step). They employed a simple radiation model in predicting the flame radiation and reported good agreement with the experimental data. Subsequent attempts at modelling turbulent diffusion flames employed modifications of the eddy break-up combustion model (Spalding, 1971) in conjunction with improved versions of the $k-\varepsilon$ eddy viscosity turbulence closure model. Galant et al. (1985) employed the eddy dissipation concept (EDC) combustion model of Magnussen (1981) and the standard $k-\varepsilon$ turbulence model in their work which resulted in an improved radiation model for flares based on a pseudo stream function formulation for the fluid flow equations. The EDC model represented a significant improvement over the flame-sheet model given its ability to account for finite rate chemistry effects (i.e. it accounts for slow forming species that exhibit reversible non-equilibrium reactions) and also its wider application to include

both premixed and diffusion flames. Morvan et al. (1998) used the EDC combustion model, and an improved version of the standard $k-\varepsilon$ turbulence closure model namely, the RNG $k-\varepsilon$ turbulence model to simulate a turbulent methane/air diffusion flame in a cross-flow. One advantage of the RNG model over the standard $k-\varepsilon$ model is that it has been found to be effective in both low and high Reynolds number flows. They included a radiation and soot model which enabled them to study the effects of soot on the radiation from the cross-flow flame. Other researchers have employed the laminar flamelet concept combustion model in an attempt to model finite rate chemistry effects. Fairweather et al. (1992) used this approach in conjunction with the probability density function (PDF) of the mean mixture fraction and its variance to predict the radiation and soot emissions from a turbulent reacting jet in a cross-wind. By using the PDF approach, the calculation of the chemistry of the flame is decoupled from the turbulent flow field calculations leading to significant computational saving. The mathematical model was based on the solutions of the three-dimensional form of the partial differential conservation equations for mass, momentum and conserved scalar transport. Favre averages of the steady state equations were used for the variable density flows of interest. The Reynolds stresses and scalar fluxes appearing in these equations were calculated using the standard two-equation $k-\varepsilon$ turbulence model. Predictions were compared against experimental data obtained from laboratory and field-scale studies of natural gas flares and the predictions were in satisfactory agreement with the data collected. Results indicated that the predicted soot and radiation level of the flame was within 20% of measured values and that a single flamelet with a 60-s^{-1} strain rate sufficed for the calculation. The flamelet concept was again used by Fairweather et al. (1991) to simulate the structure of a high momentum methane/air flame in cross-flow. The study showed that the temperature measurements obtained from the predictions were in good agreement with the experimental data of Birch et al. (1989). However the counter-rotating vortex pair flow pattern observed by Birch et al. was over-predicted by the model. This was attributed to the shortcoming of the standard two-equation $k-\varepsilon$ eddy-

viscosity turbulence model employed. In the low momentum regime, Majeski et al. (2003) also used the flamelet concept and the standard two-equation $k-\varepsilon$ turbulence model in predicting the flow pattern of flares, however they observed that the model failed to resolve the secondary flame region attached to the flare release pipe. Again, this was attributed to the drawbacks associated with the standard two-equation $k-\varepsilon$ eddy-viscosity turbulence model employed. More recently, Lawal et al. (2010) successfully employed the flamelet concept in predicting the flow structure of high-momentum flares by employing an improved version of the standard $k-\varepsilon$ turbulence model, namely the realizable $k-\varepsilon$ model and was able to resolve the counter-rotating vortex pair that has been observed in the work of Birch et al. (1989). In the low momentum flare regime, Lawal (2011) also resolved the characteristic three zone flame structure of wake-stabilized flames reported in the works of Gollahalli & Nanjundappa (1995) and Kostiuk et al. (2004), namely the planar flame zone attached to the flare pipe, the symmetric tail flame, and a transition zone connecting the first two zones. However, the shear layer (region of the fuel-air mixture that becomes partially premixed by the turbulence) was not resolved and the simulation results were not validated against temperature and species concentration measurements in the flame. Castiñeira and Edgar (2008) also performed a computational fluid dynamics simulation of a wind tunnel experiment on natural gas flares using the k-ε realizable turbulence closure model. However the results obtained were also not validated against experimental measurements for the inflame species concentration and temperature profile of the flame. In the present study, inflame predictions of the temperature and the species distribution in a cross flow propane diffusion flame will be performed using the advanced flow modelling techniques of Reynolds stress modelling and Large Eddy Simulation in conjunction with the combustion modelling techniques of non-premixed and partially premixed combustion. However, the fundamentals of flow and combustion modelling will be discussed first and this is presented in the next chapter.

Chapter 3

Methodology

3.1 Numerical methods

Computational fluid dynamics (CFD) is the mathematical modelling and the numerical solution of the non-linear partial differential equations that govern the transport of such phenomena as fluid flow, heat transfer, species transport and chemical reactions with the aim of predicting such. The governing equations of fluid flow represent mathematical statements of the fundamental conservation laws of physics, namely the conservation of mass, momentum and energy. Simplifying assumptions are usually made where possible with the objective of making the problem more tractable (e.g. steady-state, incompressible, inviscid, two-dimensional, etc.). For the analysis of the flow, the fluid is regarded as a continuum, i.e. the molecular structure of matter and molecular motion is considered negligible. The fluid behaviour is thus described in terms of the space and time derivatives of the macroscopic properties such as velocity, pressure, density and temperature. The first step in every CFD simulation process essentially involves building the geometry and then applying a suitable computational mesh. The mesh (or grid) is the collection of all cells (or elements) that make up the domain of flow. A cell or element is a discrete representation of the geometry of the problem, and several different methods are used by the solver for the spatial discretization and interpolation of scalar variables from the cell centre. Meshes are commonly grouped as structured, unstructured or hybrid meshes depending on the connectivity in the mesh. The quality of the mesh is fundamental to the accuracy of a CFD simulation and several methods are available to test the mesh quality among which include the aspect ratio and the skewness of the cells. The solution procedure involves setting the appropriate chemical and physical models that govern the problem of interest, such as radiation, diffusion and combustion.

3.1.1 Fluid flow modelling

3.1.1.1. Background

- *Conservation equations for fluid flow*

The conservation equations represent balance equations for mass, momentum and energy and show how these quantities change in space and with time. Before proceeding to discuss the conservation equations, it is worth introducing the use of the index notations, which helps to keep the equations in a more compact and clear form. In the Cartesian system, the spatial coordinates are assigned the alphabets x, y and z and the velocities in these directions are u, v and w respectively. In this thesis, the Cartesian tensor notation is adopted, where the subscripts i and j represents quantities associated with the coordinate directions. The continuity equation is an expression of the law of conservation of mass and can be expressed in the differential form as:

$$\frac{\partial \rho}{\partial t} + \frac{\partial}{\partial x_i}(\rho u_i) = 0 \tag{3.5}$$

The balance of momentum unlike the balance of mass involves a vector, hence the mass balance must be performed for all its three components. In the tensor notation, The three components of the momentum are designated as u_x, u_y and u_z. In index notation, these three components will be represented by u_i or u_j, where i is associated with the velocity vector in the mass formula ($m = \rho \vec{u} A$), and j is associated with the velocity vector in the momentum formula ($\vec{P} = m\vec{u}$), where m is the mass, A is the surface area of a fluid element, and $\vec{P}$ is the momentum. Accounting for the stress terms and the flux terms, the Cauchy momentum equation is given as:

$$\frac{\partial \rho u_i}{\partial t} + \frac{\partial}{\partial x_j}\left(\rho u_i u_j\right) = \frac{\partial \tau_{ij}}{\partial x_j} + \rho g_i \tag{3.6}$$

where the two terms on the left hand side of equation (3.6) represent the accumulation and the convective terms (flow terms) respectively, while the two terms on the right hand side represents the shear forces and the body forces (gravitational forces) respectively.

Conduction is the energy flux due to the diffusive transport of energy, and according to Fourier's law of conduction:

$$q_i = -k\frac{\partial T}{\partial x_i} \tag{3.7}$$

where q is energy flux due to the diffusive transport and k is the thermal conductivity. Applying the general balance equation to energy, we obtain:

$$\frac{\partial \rho e}{\partial t} + \frac{\partial}{\partial x_i}(\rho e u_i) = \frac{\partial q_i}{\partial x_i} + \frac{\partial}{\partial x_i}\left(\tau_{ij} u_j\right) - \frac{\partial}{\partial x_i}(p u_i) \tag{3.8}$$

This is the energy balance equation, where the two terms on the left hand side of equation (3.8) represents the rate of accumulation of energy and the convective transport of energy, respectively. The first term on the right hand side is the diffusive transport of energy and the last two terms are the viscous and pressure work respectively. The enthalpy form of the energy equation can be derived and it is expressed as:

$$\frac{\partial}{\partial t}(\rho h) + \frac{\partial}{\partial x_j}\left(\rho u_j h\right) = \frac{\partial}{\partial x_j}\left(\frac{\mu}{Pr}\frac{\partial h}{\partial x_j}\right) + q_{rad} \tag{3.9}$$

where h and Pr are the specific enthalpy and Prandtl number of the mixture, respectively, and q_{rad} is the source term due to radiation heat loss. The conservation equations (3.5) – (3.9) have to be completed with the caloric equation of state:

$$\sum_{i=1}^{N} Y_i\, h_i = 0 \tag{3.10}$$

where

$$h_i = h_i^0 + \int_{T_0}^{T} C_{p,i}(\vartheta)\, d\vartheta \tag{3.11}$$

and h is a function of the temperature T and the species mass fractions Y_i. Further, the thermal equation of state is given by:

$$p = \rho R_0 T \sum_{k=1}^{N} \frac{Y_i}{W_i} \tag{3.12}$$

where R_0 is the universal gas constant and W_i is the molecular weight of species i.

- *The Navier-Stokes equation*

The modelling of the stresses (due to the viscous effects in the fluid) in the momentum equations results in the Navier-Stokes equations. In deriving the Navier-Stokes equations, the major assumption is that the fluid be Newtonian. i.e., the shear stress between layers of fluid is proportional to the velocity gradient in the direction perpendicular to the layers as expressed by Newton's law of viscosity:

$$\tau_{yx} = \mu \frac{\partial u_x}{\partial y} \tag{3.13}$$

For a three-dimensional flow, equation (3.13) generalizes to:

$$\tau_{ij} = \mu \left(\frac{\partial u_i}{\partial x_j} + \frac{\partial u_j}{\partial x_i} - \frac{2}{3} \frac{\partial u_j}{\partial x_j} \delta_{ij} \right) \tag{3.14}$$

where μ is the dynamic viscosity and δ_{ij} is the Kronecker delta. Substituting equation (3.14) for the viscous stress tensor τ_{ij} in the momentum balance equation (3.6) we get:

$$\frac{\partial u_i}{\partial t} + \frac{\partial (u_i u_j)}{\partial x_j} = -\frac{1}{\rho} \frac{\partial p}{\partial x_i} + \frac{\partial}{\partial x_j} \left[\nu \left(\frac{\partial u_i}{\partial x_j} + \frac{\partial u_j}{\partial x_i} \right) \right] \tag{3.15}$$

where ν is the kinematic viscosity, given as $\nu = \mu/\rho$. Equation (3.15) is the Navier-Stokes equation and together with the continuity equation (3.5) and the energy equation (3.9) form the underlying equations for the analysis of the behaviour of incompressible Newtonian fluid flow.

- *Reynolds Averaged Navier-Stokes equations (RANS)*

While simple cases of low Reynolds number flows or laminar flows can be resolved with the Navier-Stokes equation, a turbulent flow cannot easily be resolved. A turbulent flow is characterized by a high level of local fluctuations of the transport quantities in various directions and in time and has an infinite number of scales which makes a deterministic treatment of turbulent flow very difficult. Solving the Navier-Stokes equation for a turbulent flow is thus extremely difficult because the equations are elliptical, non-linear and coupled (pressure-velocity, temperature-velocity). The flow is chaotic, intermittent, diffusive, dissipative and three-dimensional. The main difficulty

in solving the basic governing equations under turbulent conditions is the inability to resolve the wide range of spatial and temporal scales simultaneously. The most vital characteristic of a turbulent flow is thus the infinite number of scales which makes a full numerical resolution of the flow difficult, requiring the construction of a grid with a number of nodes that is proportional to $Re^{9/4}$ (Wilcox, 1993). There have been many attempts to simplify the analysis of turbulent flows and the statistical approach of Reynolds averaging has been used widely. In this approach, Instead of solving for the instantaneous flow-field, the statistical evolution of the flow is sought with the unsteady processes occurring in turbulent flows being visualized as a combination of some mean process and small-scale fluctuations around it. Hence an instantaneous value of any variable is decomposed into a mean, obtained by averaging over an appropriate time interval, and a fluctuating component:

$$\phi = \bar{\phi} + \phi' \tag{3.16}$$

This is called the Reynolds decomposition, where the overbar denotes time averaging. The time averaged quantity is defined as:

$$\bar{\phi} = \frac{1}{\Delta t}\int_{t}^{t+\Delta t} \phi dt \tag{3.17}$$

A turbulent flow can therefore be characterized in terms of the mean values of flow properties ($\bar{u}$, $\bar{v}$, $\bar{w}$, $\bar{p}$), etc., and some statistical properties of their fluctuations (u', v', w', p'). Since the rationale for Reynolds averaging is that we are not interested in the part of the flow solution that can be described as "turbulent fluctuations" (i.e., ϕ') and instead, it is the mean value (velocity, pressure, lift, drag, etc.) that is of interest, then by the mathematical operation of substituting the Reynolds decomposition into the Navier-Stokes equation (3.15), and setting the fluctuations to zero, we obtain:

$$\frac{\partial \rho \bar{u}_i}{\partial t} + \frac{\partial (\rho \bar{u}_i \bar{u}_j)}{\partial x_j} = -\frac{\partial \bar{p}}{\partial x_i} + \frac{\partial}{\partial x_j}\left[\mu\left(\frac{\partial \bar{u}_i}{\partial x_j} + \frac{\partial \bar{u}_j}{\partial x_i}\right)\right] - \frac{\partial}{\partial x_j}\left(\rho \overline{u_i' u_j'}\right) \tag{3.18}$$

In a similar manner, the continuity equation (3.5) can be decomposed and time-averaged for an incompressible flow to give:

$$\frac{\partial \bar{\rho}}{\partial t} + \frac{\partial}{\partial x_i}(\rho \bar{u}_i) = 0 \tag{3.19}$$

Equations (3.18) and (3.19) are called the Reynolds-averaged Navier-Stokes (RANS) equations. Hence, in the Reynolds averaging approach, it is not required to resolve all the small scale (spatial and temporal) phenomena given that the changes in the time-averaged quantities occurs at a much larger scale. This process thus requires far less computing resources than the LES or DNS approach. Nevertheless, time averaging of the Navier-Stokes equations comes with this inherent problem, the so called 'closure' problem. Close examination of equation (3.18) shows that it has the same form as equation (3.15) except that the process of time-averaging leads to the appearance of the new term $-\rho\overline{u_i' u_j'}$ in the governing equations, the so called Reynolds or turbulent stresses. These Reynolds or turbulent stresses can be interpreted as 'apparent' stress gradients and heat and mass fluxes connected with the turbulent motion. In general, governing equations for this new term can be derived; however such equations will contain further new unknown terms. Therefore, these terms cannot be obtained directly from the Navier-Stokes equations and require modelling, i.e. It becomes necessary to introduce a 'turbulence model', which relates the new unknown terms to known terms in order to 'close' equation (3.18). The process of closing the set of equations through a 'turbulence model' introduces some approximations and assumptions which form the basis of turbulence modelling. A turbulence model is a set of equations which expresses the relations between the unknown terms appearing in the Reynolds-averaged (RANS) governing equations, i.e., the Reynolds stress tensors $-\rho\overline{u_i' u_j'}$ with known quantities. Examination of the Reynolds-averaged equations (3.18) and (3.19) reveals that there are only four equations (one continuity and three momentum conservation equations) but ten unknowns (three mean velocities, mean pressure and six Reynolds stresses). As the number of unknowns is greater than the number of equations, the problem is indeterminate and needs to be 'closed' in order to obtain a solution. Thus, the desired turbulence model needs to develop a relationship between these extra unknown fluxes and known mean variables. These models are then

solved alongside the RANS equation to obtain a solution. In principle, for many engineering applications, averaged equations are 'closed' by using first-order or second-order closures. The cost-to-benefit ratio for using higher than second-order closures are generally not favourable (Ranade, 1988). The common turbulence models are sometimes grouped on the basis of the number of additional transport equations that needs to be solved alongside the RANS equation. However, RANS-based turbulence models can also be grouped into two classes: one which uses the concept of turbulent or eddy viscosity and another which does not and models pertaining to these two classes are discussed in the next section.

3.1.1.2. Eddy viscosity based models

The eddy viscosity models, also known as first-order closure models, use an eddy viscosity hypothesis based on the analogy that exists between molecular and turbulent motions. Though fluids are treated as homogenous, it is actually the interaction of the individual molecules that produce the viscous effect. For example, according the kinetic theory of gases, the dynamic viscosity of a gas is proportional to the molecular spacing and the molecular velocity i.e., $\mu \sim \rho l_m v_m$. This analogy can be extended to fluid turbulence, but on a molar rather than a molecular scale. Thus we can say that the turbulent or eddy viscosity is proportional to a measure of the eddy size and the eddy velocity i.e., $\mu_T \sim \rho l_e u_e$. Hence, turbulent eddies are visualized as molecules, colliding and exchanging momentum and obeying laws similar to the kinetic theory of gases. This is classical gradient transport theory introduced by Boussinesq, cited in Hinze (1975) and allows the description of the turbulent or Reynolds stresses in terms of the turbulence or eddy viscosity and the mean velocity gradients:

$$-\rho\overline{u_i' u_j'} = \mu_T \left(\frac{\partial \bar{u}_i}{\partial x_j} + \frac{\partial \bar{u}_j}{\partial x_i} \right) - \frac{2}{3} \rho k \delta_{ij} \tag{3.20}$$

This equation is known as the Boussinesq eddy-viscosity approximation and it forms the basis for the one and the two-equation eddy viscosity turbulence models. In turbulence models that use the Boussinesq approach, the main

issue is how the eddy viscosity is calculated. The Reynolds stresses are considered to be linearly related to the rate of strain and the kinetic energy k of the turbulent fluctuation (normal turbulent stresses) and can be expressed as:

$$k = \frac{1}{2}\overline{u_i' u_i'} = \left(\overline{u_1'^2} + \overline{u_2'^2} + \overline{u_3'^2}\right) \tag{3.21}$$

It must be noted that just like the Reynolds stresses, the eddy viscosity is not a fluid property but depends on the local state of flow or turbulence. Substitution of equation (3.20) into the Reynolds averaged momentum conservation equation (3.18) leads to a closed set, provided that the eddy or turbulent viscosity μ_T is known. Turbulence models that are based on the Boussinesq's approximation are called eddy viscosity models, also known as first-order closure models and their cornerstone is the determination of the turbulent or eddy viscosity, which dimensional considerations indicates to be a function of a velocity scale (or its turbulent kinetic energy) and a length scale. The two-equation models based on the turbulence kinetic energy and their corollaries are discussed next.

- $k - \varepsilon$ models

Two-equation turbulence models are the simplest ones that promise success for flows in which length scales cannot be prescribed empirically and are therefore the recommended first choice for simulating internal turbulent flows. Several different two-equation models have been proposed in the literature (Launder, B.E. & Spalding, 1972; Rodi, 1984; Wilcox, 1993). All these models employ a modelled form of the turbulent kinetic energy, k (modelling of the gradient diffusion term may however be different). The main differentiating factor among these models is the choice of the second model transport equation from which the length scale is determined. Instead of a length scale alone, a general combination of the turbulent kinetic energy, k and the length scale, l_e, having the form:

$$z = k^m l_T^n \tag{3.22}$$

is chosen as dependent variable, z. Some popular form of z include the turbulence frequency of the large eddies ω (i.e., dissipation per unit kinetic energy ε/k), the time averaged square of the vorticity fluctuations W_v, and the turbulent energy dissipation rate ε. Three turbulence models based on the modelling of k and ε have been widely accepted. These are the standard $k-\varepsilon$, the RNG $k-\varepsilon$, and the realizable $k-\varepsilon$ models. The major difference in these models are the method of calculating the turbulent viscosity, the turbulent Prandtl numbers governing the turbulent diffusion of k and ε and the production and destruction terms in the ε equation (Ranade, 1988).

Standard $k-\varepsilon$ model

The modelled transport equations for z differ mainly in the diffusion and the secondary source term. The variable $z=\varepsilon$ is more often used since it does not require an additional source, and simple gradient diffusion hypothesis is often enough for the diffusion (Launder & Spalding, 1974). Also, the turbulence Prandtl number for ε has a reasonable value of 1.3, which fits the experimental data for the spread of various quantities at positions far from the walls, without modifications of any constants . Because of these factors, the standard $k-\varepsilon$ model of turbulence has been the most extensively studied and used and it is recommended as a baseline model for typical internal flows encountered in engineering (Ranade, 1988). In the standard $k-\varepsilon$ model of turbulence, two transport equations are solved, one for the velocity scale (expressed in terms of the turbulent kinetic energy k) and another for the length scale (expressed in terms of the dissipation rate of the turbulent kinetic energy ε). Dimensional analysis shows that these two quantities are related to the turbulent viscosity:

$$\mu_T = \frac{C_\mu \rho k^2}{\varepsilon} \tag{3.23}$$

where C_μ is an empirical coefficient. Therefore, in order to close the set of equations, it is required to obtain values for k and ε. Transport equations for k and ε can be obtained from the Navier-Stokes equation (Jones & Launder, 1972; Launder & Sharma, 1974). The operation yields the following model equations for k and ε, respectively:

$$\frac{\partial(\rho k)}{\partial t}+\frac{\partial(\rho \bar{u}_i k)}{\partial x_i}=\frac{\partial}{\partial x_i}\left(\frac{\mu_T}{\sigma_k}\frac{\partial k}{\partial x_i}\right)+P-\rho\varepsilon \tag{3.24}$$

$$\frac{\partial(\rho \varepsilon)}{\partial t}+\frac{\partial(\rho \bar{u}_i \varepsilon)}{\partial x_i}=\frac{\partial}{\partial x_i}\left(\frac{\mu_T}{\sigma_\varepsilon}\frac{\partial \varepsilon}{\partial x_i}\right)+\frac{\varepsilon}{k}(C_1 P-C_2\rho\varepsilon) \tag{3.25}$$

where P is a term due to the production of turbulent kinetic energy and originates from the energy transfer from the mean flow to the turbulence:

$$P=\mu_T\left(\frac{\partial \bar{u}_i}{\partial x_j}+\frac{\partial \bar{u}_j}{\partial x_i}\right)\frac{\partial \bar{u}_i}{\partial x_j} \tag{3.26}$$

The first term on the left hand side of equation (3.24) represents the rate of change of k, while the second term represents the convective transport of k. On the right hand side, we have the diffusive transport of k as the first term, while the last two terms represent the source and sink terms for k respectively. It is worth noting that the diffusive transport of k has three contributions: transport of k by Reynolds stresses, transport of k by pressure and transport of k by viscous stresses. These are however modelled into the form of the first right hand term of equation (3.24). The model equation for the dissipation of turbulent kinetic energy, equation (3.25), can be analysed in a similar manner. Hence we see that the diffusive transport comprises a molecular as well as turbulent component. Therefore, velocity and pressure fluctuations contribute to the diffusive transport of turbulent kinetic energy as well as the energy dissipation rates and are modelled using a gradient diffusion approximation. The turbulent diffusivity of k and ε are related to the turbulent viscosity with additional empirical constants, which are known as turbulent Prandtl numbers for k and ε. The production term in the transport equation for ε represents vortex stretching by the mean and the fluctuating flow. The dissipation term in the transport equation for k is simply equal to ε. The viscous dissipation term appearing in the equation for ε cannot be modelled separately, however the difference between the generation and dissipation terms can be modelled with the help of two additional constants C_1 and C_2.

Table 3-1 Model constants for the standard $k-\varepsilon$ model.

σ_k	σ_ε	C_μ	C_1	C_2
1.0	1.3	0.09	1.44	1.92

The transport equations for k and ε thus contain four empirical constants (Launder & Sharma, 1974), listed in Table 3.1. These model constants have been obtained from comprehensive data fittings for benchmark experiments of non-reacting flows and are optimised to handle a variety of flows. With the above information, the Reynolds stresses can be approximated using equation (3.20). Arguably, the standard $k-\varepsilon$ turbulence model is the most complete, simple and widely used turbulence model with a broad range of applicability, which include turbulent reactive flows (Pope, 2000). Despite its versatility, the standard $k-\varepsilon$ turbulence model has its drawbacks. In the derivation of the standard $k-\varepsilon$ model, the assumption is that the flow is fully turbulent and the effects of molecular viscosity are negligible. The standard $k-\varepsilon$ model is hence only valid for fully turbulent flows. Also, the model is only valid for fully developed circular pipe flows. It gives poor predictions for fully developed turbulent flow in non-circular ducts. It also gives poor predictions for flows with strong separations as well as swirling and rotating flows and also yields a too high turbulent viscosity in near wall regions (Shih et al., 1995). The model has also been reported to suffer from stability issues due to numerical stiffness. Numerical stiffness problems can arise from the need to peform matrix inversion at each successive iteration. Numerical stiffness is also associated with the fact that the balance of terms at the wall in transport equations modelling dissipation rate depends on higher order correlations (Speziale et a., 1992). Furthermore, the assumption of turbulence isotropy implies a linear relationship between the Reynolds stress and the rate of strain and this contributes to the deficiencies in the standard $k-\varepsilon$ model. These drawbacks have led to some modification to the standard $k-\varepsilon$ model such as the development of a non-linear version of the standard $k-\varepsilon$ model known as the realizable $k-\varepsilon$ model.

Realizable $k-\varepsilon$ model

The realizable $k-\varepsilon$ model (Shih et al., 1995) introduces a new formula for the turbulent viscosity and a new transport equation for the dissipation rate ε derived from an exact equation for the transport of the mean-square vorticity fluctuation. The word "realizable" means that the model satisfies certain mathematical constraints on the Reynolds stresses that are consistent with the physics of turbulent flows The equation for the dissipation rate in the realizable $k-\varepsilon$ model is given by (Shih et al., 1995):

$$\frac{\partial(\rho\varepsilon)}{\partial t}+\frac{\partial(\rho\bar{u}_i\varepsilon)}{\partial x_i}=\frac{\partial}{\partial x_i}\left(\frac{\mu_{ef}}{\sigma_\varepsilon}\frac{\partial\varepsilon}{\partial x_i}\right)+\rho C_1 S\varepsilon-\rho C_2\frac{\varepsilon^2}{k+\sqrt{\nu\varepsilon}}+C_{1\varepsilon}\frac{\varepsilon}{k}C_{3\varepsilon}G \tag{3.27}$$

where $C_1=\max[0.43,\eta/\eta+5]$, $\eta=Sk/\varepsilon$ and $S=\left(2S_{ij}S_{ij}\right)^{1/2}$. In this case, the eddy viscosity empirical constant C_μ is modified to a variable, which is given as (Shih et al., 1995):

$$C_\mu=\left(A_o+A_s kU^*/\varepsilon\right)^{-1} \tag{3.28}$$

where,

$$U^*=\sqrt{S_{ij}S_{ij}+\widetilde{\Omega}_{ij}\widetilde{\Omega}_{ij}} \tag{3.29}$$

and

$$\widetilde{\Omega}_{ij}=\Omega_{ij}-2\varepsilon_{ijk}\omega_k;\ \ \Omega_{ij}=\bar{\Omega}_{ij}-\varepsilon_{ijk}\omega_k \tag{3.30}$$

In equations (3.28) to (3.30) above, $\bar{\Omega}_{ij}$ is the mean rate of rotation tensor with angular velocity ω_k in a rotating reference frame, and A_o and A_s are constants defined for a given angular velocity of the system rotation θ and S_{ij} is the mean stress tensor. The model constants for the realizable $k-\varepsilon$ model are (Shih et al., 1995):

Table 3-2 Model constants for the realizable $k-\varepsilon$ model.

σ_k	σ_ε	C_2	A_o
1.0	1.2	1.9	4.0

Among the reported benefit of the realizable $k-\varepsilon$ model over its standard version is that it more accurately predicts the spreading rate of both planar and round jets as well as providing improved predictions of the flow where boundary layers are affected by strong pressure gradients, rotation, recirculation and separation (Shih et al., 1995).

- *$k-\omega$ models*

The $k-\omega$ models, first introduced by Wilcox (1988) are the second most widely used turbulence models after the $k-\varepsilon$ models. The standard $k-\omega$ model solves a modified version of the k equation used in the standard $k-\varepsilon$ model and a transport equation for ω, which is the dissipation per unit kinetic energy ($\omega = k/\varepsilon$). Therefore ω is chosen as the length scale of the turbulence for this model and the turbulent viscosity becomes ($\mu_T = \rho k/\omega$). Compared to the standard $k-\varepsilon$ model, the standard $k-\omega$ model solves a slightly modified length scale equation. This provides superior treatment in the viscous near-wall region and in flow applications with a low Reynolds number and adverse pressure gradients. The standard $k-\omega$ model is applicable to wall-bounded flows and free shear flows and includes modifications for the effects of low-Reynolds-number flows, compressibility, and shear flow spreading. A modified version of the standard $k-\omega$, known as the shear-stress transport (SST) $k-\omega$ model was developed by Menter (1994) to combine the reliable formulation of the $k-\omega$ model in the near-wall region with the free-stream independence of the $k-\varepsilon$ model in the far field. This model has been further modified to give the transitional SST model.

Transitional SST model

The transitional SST model is a four equation model based on the coupling of the (SST) $k-\omega$ equation, which is a two equation model developed by Menter (1994) with two other transport equations, one for the transition onset criteria, defined by the momentum-thickness Reynolds number and one for the intermittency. The intermittency is the fraction of time that the flow is turbulent during the transition phase. This concept is used to blend the flow from laminar to turbulent regions. The intermittency is assigned a

value of zero in the laminar flow and becomes unity in the fully developed flow. The transition model works with the SST turbulence model by modification of the $k-\varepsilon$ equation and the model is appropriate for the prediction of laminar-turbulent transition of wall boundary layers. However additional effort is needed during the mesh generation phase because a low-Re mesh with sufficient streamwise resolution is required to accurately resolve the region where transition occurs. In order to capture the laminar-transitional boundary layers correctly, a y^+ of about one is required for the mesh. If the y^+ is too large (>5), then the transition onset location will move upstream with increasing y^+ (Menter et al, 2005).

3.1.1.3. Reynolds stress model

The eddy viscosity models have been the workhorse of industrial and engineering simulation over the years; however they do have their limitations. One of the most significant drawbacks to these models is the inability to predict flows with strong anistotropy, such as flows in rotating fluids (Launder et al., 1975). In order to rectify this and some other limitations, a second order closure model is required. The Reynolds stress transport model (Launder et al., 1975) solves the transport equation for the turbulent or Reynolds stresses directly and this eliminate the need for the turbulent viscosity and the gradient transport theory. The exact transport equation for the Reynolds stresses can be derived from the Navier-Stokes equation, following similar procedures to those employed to derive the transport equation for turbulent kinetic energy. the Reynolds stress transport model can be can be written in symbolic form as:

$$\frac{\partial}{\partial t}\left(\rho\overline{u_i'u_j'}\right)+\frac{\partial}{\partial x_k}\left(\rho u_k\overline{u_i'u_j'}\right)=D_{ij}+P_{ij}+G_{ij}+\phi_{ij}-\varepsilon_{ij}-F_{ij} \qquad (3.31)$$

where the first and second left hand terms are the transience and convection terms, respectively. The six right hand terms give the diffusion, shear production, buoyancy production, redistribution, dissipation and production by system rotation terms, respectively. The redistribution term, commonly known as the pressure-strain term is the most important term requiring closure. The pressure strain correlation term ϕ_{ij} accounts for the effects of

pressure fluctuations, which redistributes the turbulence among the other components, thus making it more isotropic. The pressure rate of strain takes the form (Launder et al., 1978):

$$\phi_{ij} = \phi_{ij,1} + \phi_{ij,2} + \phi_{ij,w} \tag{3.32}$$

where the slow part of the pressure rate of strain $\phi_{ij,1}$ is modelled as:

$$\phi_{ij,1} \equiv -C_1 \rho \frac{\varepsilon}{k}\left[\overline{u_i' u_j'} - \frac{2}{3}\delta_{ij} k\right] \tag{3.33}$$

and the rapid part $\phi_{ij,2}$ is modelled as:

$$\phi_{ij,2} = -C_2\left[\left(P_{ij} + F_{ij} + 5/6G_{ij} - C_{ij}\right) - \frac{2}{3}\delta_{ij}(P + 5/6G - C)\right] \tag{3.34}$$

where ε is the rate of dissipation of turbulent kinetic energy, k is the turbulent kinetic energy, G_{ij} is the buoyancy term, and $P = \frac{1}{2} P_{kk}$, $C = \frac{1}{2} C_{kk}$, and $G = \frac{1}{2} G_{kk}$. The model constants C_1 and C_2 are given as 1.8 and 0.6 respectively. The last term in equation (3.32) is known as the wall reflection term and is responsible for the redistribution of normal stresses near the wall. These transport equations are complex and contain several unknown correlations including triple correlations of fluctuating velocities. Hence second order closures i.e., closing the transport equation for the turbulent stresses in order to avoid modelling the triple and higher correlation is necessary and usually sufficient since the effects of higher correlations are usually small in practical flows and need not be simulated. The RSM thus closes the Reynolds-averaged Navier-Stokes equations by solving transport equations for the Reynolds stresses, together with an equation for the dissipation rate. This means that in addition to the Navier-Stokes equations, five additional transport equations must be solved for two-dimensional flows while seven additional transport equations must be solved in three-dimensional flows. In an attempt to avoid the numerical difficulties associated with the differential Reynolds stress model, Rodi (1984) introduced approximations into the convective and diffusive transport terms, while still accounting for the Reynolds stress anisotropy. The approximations reduce the RSM to a set of algebraic equations, known as the algebraic stress model (ASM). However, whenever the convective and diffusive

transport of Reynolds stresses become important, for example in flows that are far from equilibrium, then the algebraic stress model may prove to be inadequate and solutions of the full transport equations of the Reynolds stresses may become necessary. The advantages of the Reynolds stress models over the eddy viscosity models include their ability to account for the effects of rapid changes in strain rate, swirl, streamline curvature and rotation in a more rigorous manner hence they have greater capabilities of giving accurate predictions for complex flows. These include rotating flows in passages, cyclone flows and highly swirling flows in combustors (Launder et al., 1975). However, the two equation $k-\varepsilon$ models are still recommended as a baseline model since the RSM may not yield results that are obviously better than the simpler models at all times to warrant the extra computational expenses.

3.1.1.4. Large Eddy Simulation

One of the underlying deficiencies of the RANS models is that they are based on equilibrium turbulence dynamics, which means they assume turbulence has responded completely to the imposed shear on the flow (Pope, 2000). This assumption can lead to loss of information on the physics of the flow, especially when the fluctuation magnitude is substantial relative to the mean. The concept of Large Eddy Simulation (LES) is based on the observation that the large scale in turbulence are not chaotic but deterministic and the large scale motions being much more energetic than the small scale motions are the main contributors to the transport of conserved quantities while the sensitivity, randomness, and chaotic dynamics associated with the turbulence is restricted to the small scales. Hence LES attempts to resolve rigorously these large scale motions, while the small scales are modelled with a subgrid scale model (in lieu of being resolved), with the maximum wave number resolved with the LES approach chosen to lie in the inertial sub-range of the turbulence energy spectrum. This approach is much less costly and flexible than the DNS approach, although LES models are three dimensional and also time dependent making them more costly than RANS (Boudier et al., 2007). In order to

distinguish between the larger, resolved and smaller, unresolved turbulent motions, any flow variable, ϕ, in the fluid domain can be decomposed into a large scale part, $\langle\phi\rangle$ and small scale part ϕ'' as (Mahesh et al., 2006):

$$\phi = \langle\phi\rangle + \phi'' \tag{3.35}$$

The technique employed in LES is to filter the Navier-Stokes equation to some appropriate scale using a mathematical tool such as a Gaussian filter or piecewise continuous function. The spatial filtering operation is defined based on a convolution integral (Leonard 1974) such that :

$$\langle\phi\rangle = \int G(x - x^*; \bar{\Delta}(x))\phi(x^*)dx^* \tag{3.36}$$

where G denotes the filtering function of width $\bar{\Delta}$, with the width determining the size of the smallest resolved scales and the integration extending over the entire domain. Among the several filters suggested for LES applications, the ones that find the most common applications are the box filter, the Gaussian filter and the spectral cut off filter. Ideally, the filter width should be greater than the numerical grid size h (i.e. $\bar{\Delta} > h$). When the box filter is employed, the filter width is taken as a simple average of the order of the grid size h, given as (Hartel, 2004):

$$\bar{\Delta} \equiv h \equiv (\Delta x \Delta y \Delta z)^{1/3} \tag{3.37}$$

where Δx, Δy, and Δz represent the grid or the cell width in the three coordinate directions. The box filter is defined such that (Hartel, 2004):

$$\begin{aligned} \bar{\Delta}G(x - x^*) &= 1 \qquad |x - x^*| < \bar{\Delta} \\ &= 0 \qquad |x - x^*| > \bar{\Delta} \end{aligned} \tag{3.38}$$

Applying this mathematical tool to the instantaneous governing equations of fluid flow produces the filtered form of the the Navier-Stokes equations as follows (Hartel, 2004):

$$\frac{\partial \rho \bar{u}_i}{\partial x_i} = 0 \tag{3.39}$$

$$\frac{\partial \bar{u}_i}{\partial t} + \frac{\partial}{\partial x_j}(\bar{u}_i \bar{u}_j) = -\frac{1}{\rho}\frac{\partial \bar{p}}{\partial x_i} - \frac{\partial \tau_{ij}}{\partial x_j} + \frac{\partial}{\partial x_j}\left[\nu\left(\frac{\partial \bar{u}_i}{\partial x_j} + \frac{\partial \bar{u}_j}{\partial x_i}\right)\right] \tag{3.40}$$

where the overbars denote spatial filtering and τ_{ij} is the subgrid scale stress originating from non-linear inertial terms. Since LES is based on the spatial averaging of the instantaneous parameters, the space averages of the fluctuating components around filtered or surface-averaged quantities are not zero. Fluctuations around the surface or volume-averaged quantities generate additional terms in the governing transport equations which require further modelling so as to close the set of equations. These models represent the effects of scales, smaller than the characteristic filter scale and are called 'subgrid scale' stress models (SGS). Smagorinsky (1963) was the first to propose a sub-grid scale stress model with several other models having been proposed since then (Ferziger, 1976; Rogallo & Moin, 1984). The subgrid scale stress is given as (Smagorinsky, 1963):

$$\tau_{ij} = \frac{1}{3}\tau_{kk}\delta_{ij} - 2\mu_t\bar{S}_{ij} \tag{3.41}$$

and

$$\bar{S}_{ij} = \frac{1}{2}\left(\frac{\partial\bar{u}_i}{\partial x_j} + \frac{\partial\bar{u}_j}{\partial x_i}\right) \tag{3.42}$$

where μ_t is the subgrid scale turbulent viscosity, τ_{kk} is the isotropic part of the subgrid scale stresses (which is not modelled, but added to the filtered static pressure term), $\bar{S}_{ij}$ the rate-of-strain tensor for the resolved scale and δ_{ij} is the Kronecker delta. The main objective of the SGS model is to resolve the energy cascade from large to small scales, and in flows such as transitional flows, from small to large scales, also known as backscatter (Piomelli et al., 1996). Furthermore, since it is the resolved scales that provide information required for the flow statistics of interest, the SGS model must ensure that the accuracy of the resolved statistics is not significantly influenced by the absence of the effect of the small scale motion (Hartel, 2004). LES is well suited to handle transient flows of large scales and has also been used to simulate flows with moderately high Reynolds numbers. However, LES is still computationally intensive and suffers some of the disadvantages of DNS such as the difficulties associated with specifying boundary conditions (Ranade, 1988).

3.1.1.5. Direct Numerical Simulation

Direct Numerical simulation (DNS) as the name implies, attempts to resolve all the dynamically important scales of turbulence by directly solving the Navier-stokes equations without resorting to any form of modelling. This is probably the most direct approach to turbulence modelling and requires sufficient spatial and temporal resolution in order to solve for the instantaneous properties of the flow for all turbulent time and length scales. Consequently, DNS is the most accurate turbulence simulation technique available but requires enormous computing resources even for the simplest cases. For example, in the DNS study of a three dimensional, non-reacting turbulent flow, the number of grid points required increases as $Re^{9/4}$, while the CPU time is proportional to Re^3 (Hartel, 2004). This makes DNS unrealistically expensive for flows of engineering interest, however it still has a role for example in gathering data for model evaluation and validation and in investigations into the fundamental understanding of turbulence (Rogallo & Moin, 1984). Figure 3-1 is a schematic representation of the scale of eddies resolved by the LES and DNS with the DNS approach resolving the smallest scale eddies. Current DNS simulations involve simple geometries but still generates a huge amount of data containing time histories at each point which requires much averaging.

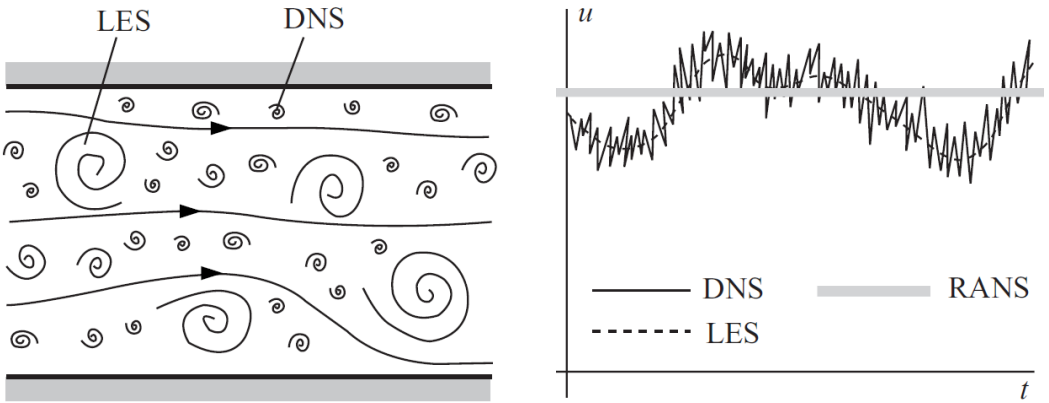

Figure 3-1 Schematic representation of scales in turbulent flows and their relationship with modelling approaches (adapted from Ferziger and Peric, 1995).

3.1.2 Combustion modelling

3.1.2.1. Background

- *Conservation equations for combustion*

In addition to the fluid flow equations discussed in section 3.1.1, species concentrations must be calculated in order to describe a reacting flow. The species conservation (or transport) equation for combustion is given as (Versteeg & Malalasekera, 2007):

$$\frac{\partial}{\partial t}(\rho Y_i) + \frac{\partial}{\partial x_k}(\rho u_k Y_i) = \frac{\partial}{\partial x_k}\left[\rho D_i \frac{\partial Y_i}{\partial x_k}\right] + \dot{w}_i \qquad (3.49)$$

where the first and second terms on the left hand side represent the accumulation term and the convective term (transport due to bulk motion), respectively. While the first and second terms on the right hand represent the diffusive term (transport due to molecular motion) and the source or sink term (due to chemical reactions), respectively for the ith specie. Further, D_i is the species diffusion coefficient and it is a great simplification albeit not always accurate, to assign a single diffusion coefficient D for all the species. This approach simplifies equation (3.49) to (Versteeg & Malalasekera, 2007):

$$\frac{\partial}{\partial t}(\rho Y_i) + \frac{\partial}{\partial x_k}(\rho u_k Y_i) = \frac{\partial}{\partial x_k}\left[\rho D \frac{\partial Y_i}{\partial x_k}\right] + \dot{w}_i \qquad (3.50)$$

The internal structure of diffusion flames is more conveniently discussed and analysed using the extent of mixing between the fuel and oxidizer. It is first assumed that the fuel and the oxidizer molecular diffusivities are equal (i.e. $D_F = D_O = D$). By combining the transport equation for the fuel mass fraction, Y_F and the oxidizer mass fraction Y_O, a conserved scalar quantity that is independent of the chemical reaction, (a Schwab-Zeldovitch variable) $\varphi(Y_F, Y_O) = Y_F - Y_O/s$ is introduced, where s is the the mass stoichiometric coefficient given as s=$(v_O W_O / v_F W_F)$. The difficulties associated with the evaluation of the average species reaction rate $\dot{w}_i$ and the nonlinear Arrhenius term associated with this term can thus be overcome. Hence the mixture fraction Z, can be mathematically defined as a variable whose

transport equation does not contain a source term. The transport equation for the mixture fraction is given by (Versteeg & Malalasekera, 2007):

$$\frac{\partial}{\partial t}(\rho Z) + \frac{\partial}{\partial x_k}(\rho u_k Z) = \frac{\partial}{\partial x_k}\left[\rho D \frac{\partial Z}{\partial x_k}\right] \tag{3.51}$$

The energy conservation equation has several forms and the enthalpy form of this equation has been presented in section 3.1.1. The temperature form of the energy conservation equation takes the form (Mahesh et al., 2006).

$$\frac{\partial}{\partial t}(\rho T) + \frac{\partial}{\partial x_k}(\rho u_k T) = \frac{\partial}{\partial x_k}\left[\rho \alpha_i \frac{\partial T}{\partial x_k}\right] + \rho S_T \tag{3.52}$$

where the first and second terms on the left hand side represent the local rate of change of temperature and the decrease of temperature due to convection respectively, while the first and second terms on the right hand side represent the increase of temperature due to diffusion and the source or sink term (due to a chemical reaction, radiation, etc.) respectively, and α_i is the thermal diffusivity of species i.

- *Favre averaged equations*

For flows with considerable density variation (such as compressible and reacting flows), the density weighted Favre-averaging technique (Favre, 1969; Jones & Whitelaw, 1982) is more appropriate than the unweighted Reynolds-averaging technique which has been developed for non-reacting fluid mechanics. Thus Favre averaging represents a statistical approach that accommodates variable-density flow. Due to this approach, additional terms ($\overline{\rho' u_\iota'}$) arise, representing the coupling of the density-velocity fluctuations and must be modelled. Favre-averaged equations offer considerable advantage given that they simplify the formulation of the averaged Navier-Stokes equations in variable density flow. The Favre-averaged equation leads to a more compact equation with simpler physical interpretations that is more appropriate for combustion. The Favre decomposition for a velocity variable can be written as:

$$u_i = \widetilde{u_\iota} + u_i'', \qquad \widetilde{\rho u_i''} = 0 \tag{3.53}$$

where double primes represent the fluctuating components or the deviation from the mean or average value, and the tildes the density weighted ensemble average or the Favre average component which is calculated as:

$$\widetilde{u_\iota} = \frac{\overline{\rho u_\iota}}{\bar{\rho}} = \frac{1}{\bar{\rho}} \lim_{N\to\infty} \frac{1}{N} \sum_{p=1}^{N} (\rho u_i)^{(p)} \tag{3.54}$$

In contrast to the Reynolds decomposition, where u_i' represents a turbulent velocity fluctuation, the quantity u_i'' includes the effect of density fluctuations. Applying the Favre averaging to equations (3.5), (3.6), (3.9), (3.50) and (3.51) yields the Favre averaged form of the governing equations as follows:

Continuity:

$$\frac{\partial \bar{\rho}}{\partial t} + \frac{\partial}{\partial x_k}(\bar{\rho}\tilde{u}_k) = 0 \tag{3.55}$$

Momentum:

$$\frac{\partial(\bar{\rho}\tilde{u}_i)}{\partial t} + \frac{\partial}{\partial x_k}(\bar{\rho}\tilde{u}_k\tilde{u}_i) = \frac{\partial \bar{P}}{\partial x_i} + \frac{\partial \tau_{ik}}{\partial x_k} + \tilde{F}_k - \frac{\partial}{\partial x_k}\left(\widetilde{\rho u_k'' u_i''}\right) \tag{3.56}$$

Enthalpy:

$$\frac{\partial(\bar{\rho}\tilde{h})}{\partial t} + \frac{\partial}{\partial x_k}(\bar{\rho}\tilde{u}_k\tilde{h}) = \frac{\partial}{\partial x_k}\left(\widetilde{\frac{\mu}{Pr}\frac{\partial h}{\partial x_k}}\right) + q_{rad} - \frac{\partial}{\partial x_k}\left(\widetilde{\rho u_k'' h''}\right) \tag{3.57}$$

Species:

$$\frac{\partial(\bar{\rho}\tilde{Y}_i)}{\partial t} + \frac{\partial}{\partial x_k}(\bar{\rho}\tilde{u}_k\tilde{Y}_i) = \frac{\partial}{\partial x_k}\left(\widetilde{\rho D_\iota \frac{\partial Y_\iota}{\partial x_k}}\right) + \widetilde{\dot{w}_\iota} - \frac{\partial}{\partial x_k}\left(\widetilde{\rho u_k'' Y_\iota''}\right) \tag{3.58}$$

Mixture fractions:

$$\frac{\partial}{\partial t}(\bar{\rho}Z) + \frac{\partial}{\partial x_k}(\bar{\rho}\tilde{u}_k\tilde{Z}) = \frac{\partial}{\partial x_k}\left(\widetilde{\rho D \frac{\partial Z}{\partial x_k}}\right) - \frac{\partial}{\partial x_k}\left(\widetilde{\rho u_k'' Z''}\right) \tag{3.59}$$

These equations govern the mean quantities of the flow variables for all turbulent time and length scales. The Reynolds stresses $\left(\widetilde{\rho u_k'' Y_\iota''}\right)$, fluxes $\left(\widetilde{\rho u_k'' Z''}\right)$ and the chemical source term $\widetilde{\dot{w}_\iota}$ all need to be modelled with the modelling of the chemical source term forming the central theme in turbulent combustion modelling.

3.1.2.2. Non-premixed combustion models

The mixture fraction Z, forms the backbone of most of the non-premixed combustion models, where Z is normalised to zero in the pure oxidizer stream and to one in the fuel stream. As shown in equation (3.59), it is assumed that the mixture fraction is given in the flow field as a function of space and time $Z(x_k, t)$. In simple hydrocarbon oxidation reactions, such as the combustion of methane, an extensive and complex array of chemical reactions involves a large number of species. Attempts to solve the transport equations for this detailed reaction chemistry and closing the mean reaction rate source term is an enormous undertaking that is computationally intractable. However, if the hypothesis that the elemental mass fractions are conserved in a chemical system is employed, then the need to model the chemical source terms is avoided. The use of this conserved scalar, the mixture fraction Z, removes the need to solve transport equation for each reacting scalar. This greatly simplifies the calculations of the reacting flows i.e, the temperature and species concentration can be determined from the mixture fraction field, which is in turn explained in terms of the statistics of the turbulent flow. If a reactive system is considered to be in a state of chemical equilibrium, that is the chemical reaction rate is much faster than mixing by molecular diffusion, then the instantaneous values of temperature, density and mass fractions depend solely on the instantaneous mixture fraction, Z:

$$\phi_i = \phi_i(Z), \qquad \phi = T, \rho, Y_i \tag{3.60}$$

This equation shows that the mixture fraction assumes the vital role of tracking the mixing and the transport of other conserved scalars in a reactive system. In equations (3.60), ϕ_i represents the instantaneous species mass, temperature, density or mass fraction. In the case of non-adiabatic systems, the effect of heat loss/gain is parameterized as:

$$\phi_i = \phi_i(Z, h), \phi = T, \rho, Y_i \tag{3.61}$$

for a single mixture fraction system, where h is the instantaneous enthalpy. Models based on the conserved scalar approach will be described next.

- *Equilibrium model*

This model assumes complete reaction and uses equilibrium calculations as an alternative to the fast chemistry approach. The model predicts equilibrium species concentration, including minor species as a function of the mixture fraction and approaches the problem from two angles: firstly, a mixing problem which is concerned with locating the flame surface, i.e. a non-reactive problem concerning the propagation of a passive scalar, the mixture fraction; and second, the flame structure problem, which is concerned with the distribution of the reactive species inside a flamelet. To obtain the distribution of reactive species inside the flame front, the assumption is that it is locally one-dimensional and depends only on time and the scalar coordinates (mixture fraction space). It is worth noting that both the temperature T and the species mass fraction Y_i can both be expressed as a function of the mixture fraction Z. By definition, the new coordinate Z is locally normal to the surface of the stoichiometric mixture and by applying the transformation rules and substituting into the specie transport equation, the flamelet equation is obtained as (Peters, 1984):

$$\rho \frac{\partial Y_i}{\partial t} = \rho \frac{\chi}{2} \frac{\partial^2 Y_i}{\partial Z^2} + \dot{w}_i \tag{3.62}$$

where

$$\chi = 2D \left(\frac{\partial Z}{\partial x_j} \right)^2 \tag{3.63}$$

is the scalar dissipation rate which controls the mixing and provides the interaction between the flow and the chemistry, and D is the diffusion coefficient of the scalar. The strength of the combustion in a diffusion flame is determined by the gradient of the fuel on one side of the flame and the oxidizer on the other side, thus dictating the feeding rate of the flame via diffusion. Also the position of the stoichiometric line dictates where the flame sheet lies. The rate at which the reaction zone is fed is characterized using the inverse of the time. Since this is achieved through diffusion, it must then make use of a combination of the mixture fraction gradient and diffusion coefficient as evident in the equation for the scalar dissipation rate. The

scalar dissipation rate is a fundamental parameter in all combustion models that are derived from the mixing controlled paradigm and must therefore be modelled. High values of the scalar dissipation rate in the flow can lead to the local or global extinction of the flame. Studies have shown that the rate of the reaction is proportional to the rate of the scalar dissipation, i.e. the rate of molecular mixing of the mixture fraction (Bilger, 1976). This idea produces the viewpoint that the reactive species and temperature should depend on both the mixture fraction and its rate of scalar dissipation. Subsequent studies on laminar counter-flow diffusion flames also show a strong dependence of the species composition and temperature on the strain rate in the flow (Tsuji & Yamaoka, 1969), which relates linearly to the scalar dissipation of the mixture fraction. If the flame is considered steady, i.e. time independent, then equation (3.62) reduces to:

$$\dot{w}_i = -\frac{\chi}{2}\frac{\partial^2 Y_i}{\partial Z^2} \tag{3.64}$$

Under the assumption that the flame is infinitely fast (i.e., one step, global reaction where reactants are instantly converted to products), then the resultant flame distribution is in equilibrium, $\dot{w}_i$ = 0 and the flame configuration $Y_i(Z)$ is independent of the strain. The CHEMKIN program is widely used to predict the equilibrium species concentration, including the minor species. Models in non-premixed turbulent combustion are often based on the presumed shape probability density function approach. The PDF is a statistical approach and is useful because of the presence of the turbulence in the flow field that introduces fluctuations in the mixture fraction and the scalar variables. Therefore, the relation between the mixture fraction with the reacting species composition and the temperature become nonlinear and can no longer be obtained using equation (3.61). Therefore the PDF is used to obtain the mean values of the species composition and temperature by weighing their instantaneous relationship with the mixture fraction. Therefore, to calculate the mean value of the fluctuating scalars $\widetilde{Y_i}$ and $\tilde{T}$, we need to know the statistics of the instantaneous variables ρ, T, Y_i as a function of the mixture fraction Z. Thus, the use of the PDF requires the

knowledge of the Favre mean mixture fraction $\tilde{Z}$ and its intensity $\tilde{Z}^{"2}$ also known as its variance at position *x* and time *t*. A simplified numerical description of a reacting flow would consist of solving the transport equations for the mean mixture fraction and its variance at each point of the turbulent flow field, provided that the density field is known. In addition, of course, equations for the turbulent flow field, the Reynolds stress equations (or the equation for the turbulent kinetic energy) and the equation for the dissipation must be solved. Hence, a conserved, Favre averaged transport equation is derived and solved for the mean mixture fraction, $\widetilde{Z}$ and its intensity $\widetilde{Z_k}^{"2}$ (Libby & Williams, 1994):

$$\frac{\partial}{\partial x_k}\left(\bar{\rho}\tilde{u}_k\tilde{Z}\right) = \frac{\partial}{\partial x_k}\left(\frac{\mu_t}{\sigma_z}\frac{\partial \tilde{Z}}{\partial x_k}\right) \tag{3.65}$$

$$\frac{\partial}{\partial x_k}\left(\bar{\rho}\tilde{u}_j\widetilde{Z_k}^{"2}\right) = \frac{\partial}{\partial x_k}\left(\frac{\mu_t}{\sigma_z}\frac{\partial \tilde{Z}^{"2}}{\partial x_k}\right) + C_1\mu_t\left(\frac{\partial \tilde{Z}^{"2}}{\partial x_j}\right)^2 - C_2\frac{\tilde{\varepsilon}}{\tilde{k}}\bar{\rho}\tilde{Z}^{"2} \tag{3.66}$$

where C_1 and C_2 are dimensionless model constants with values 2.0 and 2.8, respectively (Lockwood, 1977). The averaged values of the variables that depend on Z are computed from the probability density function $P(Z)$, which describes the temporal fluctuations of Z in the turbulent flow field. For a non-adiabatic combusting system with heat loss/gain and/or heat transfer to the wall, the local thermochemical state is no longer related only to Z, but also to the enthalpy h. Given that the enthalpy of the system affects the chemical equilibrium calculation as well as the calculation of species concentration and temperature in the reacting flow, the variations in enthalpy due to heat loss must be taken in account when calculating scalars from the mixture fraction, as in equation (3.60). The Favre average of the fluctuating scalar variables is then defined by (Bray & Peters, 1994):

$$\tilde{\phi}_i = \int_0^1 P\left(Z.\tilde{h}\right)\phi_i(Z)dZ \tag{3.67}$$

where $P\left(Z.\tilde{h}\right)$ is the joint PDF of the mixture fraction and the mean enthalpy for a system with a single mixture fraction. Therefore, knowing the PDF of the mixture fraction $P(Z)$ for a sufficiently large number of realisations, the

Favre averages of the fluctuating scalars $\tilde{\phi}$ that depend on Z can be determined through the PDF integration of equation (3.67). Also, the PDF shape $P(Z)$ is a function of only its first two moments, namely the mean mixture fraction $\tilde{Z}$, and the mixture fraction variance $\widetilde{Z_k^{"2}}$. In order to apply the PDF method, a suitable two-parameter probability density function is "presumed" beforehand, hence fixing the functional form of the PDF by linking the two parameters in terms of the known values of the mean mixture fraction and its variance at each point of the flow. The shape of the assumed PDF is described by several mathematical functions, however the β-function shape of the PDF (single- and two-mixture-fraction cases) most closely represents experimentally observed PDFs and is given by (Bray & Peters, 1994):

$$\tilde{P}(Z) = Z^{\alpha-1}(1-Z)^{\beta-1}\frac{\Gamma(\alpha+\beta)}{\Gamma(\alpha).\Gamma(\beta)} \tag{3.68}$$

where Γ is the gamma function, and α and β are parameters that can be determined from the mean variance of Z as follows:

$$\alpha = \tilde{Z}\left[\frac{\tilde{Z}(1-\tilde{Z})}{\widetilde{Z^{"2}}} - 1\right] \tag{3.69}$$

$$\beta = \left(1-\tilde{Z}\right)\frac{\alpha}{\tilde{Z}} \tag{3.70}$$

By using the PDF approach, the calculation of the chemistry of the flame is decoupled from the turbulent flow field calculations. This procedure produces significant computational savings compared to solving the transport equations for the individual species PDFs and closing the mean reaction rate, as obtained in the PDF transport equation model (Dapazo & O'brien, 1974; Pope, 1985).

- *Laminar Flamelet model*

The laminar flamelet model is an extension of the equilibrium model to account for non-equilibrium effects. The model assumes the chemistry to be fast but not infinitely fast and hence the model is a conserved scalar model that can account for finite rate kinetic-effects. This is important for a slow

reaction where the formation of intermediate species need to be accounted for and thus the kinetics of the reaction becomes important. Another key assumption of the laminar flamelet model is that of unity Lewis number since this significantly simplifies the equation. The Lewis number is a dimensionless number and it gives the ratio of the thermal diffusivity to the mass diffusivity for a given species. The view of a turbulent diffusion flame as an ensemble of stretched laminar flamelets is due to Williams (1985) and approximates a turbulent flame as a combination of thin, locally one-dimensional flamelet structures that are embedded within, and strained by the turbulent flow field. The laminar flamelets are embedded into the turbulent flame by using the statistical PDF method. The strain parameter that couples the flamelet equations to the turbulent flow field is the stoichiometric scalar dissipation rate χ_{st}. The scalar dissipation rate is a non-equilibrium parameter that accounts for the departure of the flame from the equilibrium mixture and it is modelled according to equation (3.63) while small values of χ signify reactions tending towards equilibrium, larger values represent a significant departure from chemical equilibrium. Peters (1984) defined flamelets as "thin diffusion layers embedded in a turbulent non-reactive flow field". The flamelet model is essentially a topological model. In topological models, the flame is assumed to be a surface that can be tracked by the solver. The flame surface location is often linked to the resolution of a specific field (for example, an iso-surface of the mixture fraction field in a non-premixed equation or an iso-surface of a reaction progress variable in premixed combustion), Peters (1984). The flame surface can be approximated as the surface to which the fuel and oxygen rates of delivery are in stoichiometric proportions $Z(x,t) = Z_{st}$. Therefore, the fundamental assumption of the flamelet model is that the chemistry is active only within the flame surface. The flame surface is considered to be very thin, and assumed to be smaller than the Kolmogorov length scale and therefore the region is locally laminar (Bray & Peters, 1994). Within this thickness, fluctuations in the scalar variables ϕ_i and the flame reaction rate ω_i due to the turbulence are considered negligible. The flamelet regime is often considered as one that preserves the integrity of the flame structure during

turbulent combustion modelling. Turbulent eddies do not penetrate the structure and only contort the flame at a large scale. Hence, it is often normal to describe the flamelet equation as the equation that represents the diffusion flame structure when not perturbed by turbulence. The laminar flamelet equation is similar to that of the equilibrium chemistry except that the chemical source term $\dot{w}_i$ is not zero, namely:

$$\frac{\chi}{2}\frac{\partial^2 Y_i}{\partial Z^2} + \dot{w}_i = 0 \tag{3.71}$$

Equation (3.71) is known as the stationary laminar flamelet model (SLFM) because the time dependent term is ignored. This is usually acceptable, except in certain situations such as ignition or extinction of the flame. The scalar dissipation rate χ, acts as an external parameter that is imposed on the flamelet structure by the mixture fraction field. Using χ, the influence of convection and diffusion is implicitly incorporated into the surface normal to the stoichiometric mixture fraction. This makes the flamelet equation a function of both Z and χ,

$$\phi_i = \phi_i(Z, \chi), \phi = \rho, T, Y_i \tag{3.72}$$

This approach has the advantage that flamelet profiles $Y_k = \phi\,(Z, \chi)$ can be pre-computed and stored in a dataset or file which is called a "flamelet library" with all the required complex chemistry. The library consists of a set of relationships $\phi\,(Z)$ between the scalar flow properties ϕ and the mixture fraction Z. Overall, the laminar flamelet model predictions are very good, given that they incorporate complex and detailed chemistry at an acceptable cost. The flow field is reasonably well reproduced and the temperature and concentration of minor species are also well reproduced by the flamelet. The model has been proved to be valid in flows with room temperature reactants and low gas velocities as well as in combustion chemistry that is mixing limited (Bilger et al., 2005). However the model has its drawbacks and limitations. For example the prediction of NO is not as good as that of other minor species, and it is suggested that the inclusion of other NO formation mechanisms can improve NO predictions (Dally et al., 1996).

3.1.2.3. Partially premixed combustion model

Partially premixed flames possess the properties of both premixed and non-premixed flames, therefore the partially premixed model (Pierce & Moin, 2004) adopts two scalars: a progress variable, C which tracks the global extent-of-reaction, and a mixture fraction variable, Z which tracks the mixing of fuel and oxidizer. This flamelet/progress variable approach (unlike the flamelet model) is able to account for flame phenomena such as ignition (when reaction rate is higher than mixing rate), extinction (when reaction rate is lower than mixing rate) or the effects of unsteady mixing (when reaction rates lag behind changes in mixing rate). Partially premixed flames can occur when a diffusion flame becomes lifted so that some premixing occurs before the onset of combustion. The premixed reaction-progress variable is used to calculate the position of the flame front. At the back of the flame front ($C = 1$)**,** the mixture is considered to be burnt and the equilibrium or laminar flamelet mixture fraction solution is used. In the front of the flame, $C = 0$)**,** the temperature, density and species concentrations are calculated from the mixed but unburnt mixture fraction. Within the flame (0< $C < 1$)**,** a linear combination of the unburnt and burnt mixtures is utilized. The transport equation for the partially premixed combustion model in the absence of favre averaging or spatial filtering are given as (Mahesh et al., 2006):

$$\frac{\partial}{\partial t}(\rho Z) + \frac{\partial}{\partial x_k}(\rho u_k Z) = \frac{\partial}{\partial x_k}\left[\rho D \frac{\partial Z}{\partial x_k}\right] \tag{3.73}$$

$$\frac{\partial}{\partial t}(\rho C) + \frac{\partial}{\partial x_k}(\rho u_k C) = \frac{\partial}{\partial x_k}\left[\rho D \frac{\partial C}{\partial x_k}\right] + \rho \dot{w}_c \tag{3.74}$$

where Z denotes the mixture fraction which is a conserved scalar, and C is a progress variable that models the “progress”of the reaction. D and $\dot{w}_c$ denote the molecular scalar diffusivity and the chemical source term, respectively. The partially premixed model solves the transport equations for the mean reaction variable $\bar{c}$ to determine the position of the flame front as well as a transport equation for the mean mixture fraction $\bar{Z}$ and the mixture fraction variance $\overline{Z'^2}$.

3.1.3 Radiation modelling

The terms radiative heat transfer or thermal radiation are often used to denote heat transfer due to electromagnetic waves. All materials above absolute zero temperature emit and absorb electromagnetic waves on a continual basis and the strength of the emission will depend on the temperature of the radiating body. Wavelengths in the infrared spectrum are usually of the greatest importance. Furthermore radiative heat transfer, unlike conductive or convective heat transfer, does not require a material medium for propagation and while the strength of the first two is linearly proportional to the temperature difference, the strength of radiation is proportional to the difference in temperature raised to the fourth power. This implies that radiation becomes the dominant heat transfer mechanism in high temperature environments such as what obtains in flames. To determine the fraction of heat lost due to radiation in flames, it is necessary to solve the radiative transfer equation (RTE), which appears a sink in the enthalpy equation (3.9). The governing equation for the radiative heat transfer describes the transport of incoming and outgoing radiation intensity through the computational domain and it can be expressed as (Modest, 2003):

$$\frac{dI(\vec{r},\vec{s})}{ds} + (a+\sigma_s)I(\vec{r},\vec{s}) = an^2\frac{\sigma T^4}{\pi} + \frac{\sigma_s}{4\pi}\int_0^{4\pi} I(\vec{r},\vec{s}')\,\Phi(\vec{s},\vec{s}')d\Omega' \qquad (3.75)$$

where $\vec{r}$, $\vec{s}$ and $\vec{s}'$ are the position, direction and scattering direction vectors respectively. a and σ_s are the absorbtion and the scattering coefficient, s is the path length, n is the refractive index, I is the radiation intensity, T is the local temperature, Φ is the phase function, Ω' is the solid angle and σ is the Stefan-Boltzmann constant given as 5.672×10^{-8} W/m^2-K^4.

The radiative transfer equation is a complex integro-differential equation and the numerical solution of the RTE is computationally intensive given that the solution needs to be determined in advance. Furthermore, the equation needs to be solved as function of three space coordinates, two angular direction and wavelength. The RTE accounts for both the directional and the spectral nature of radiation and various models have been developed to

approximate both of these two aspects of radiation. Several models are available for treating the directional nature of radiation and among the models which have been developed to provide approximations to the RTE in this respect are the Rosseland model (diffusion approximation model), P-1 model (Gibbs model/spherical harmonics model), Monte-Carlo model and the Discrete ordinate model (DOM). Each of these models makes its assumptions and they come with their benefits and limitations. The Monte-Carlo model takes a statistical approach to the approximation of the RTE and is known to yield accurate results even in the most complex geometries (Menguc & Viskanta, 1986). However, the model is computationally intensive and subject to convergence difficulties due to the large number of rays required for the simulation. In the spherical harmonics model, the RTE equation is approximated by transforming the equation into a set of simultaneous partial differential equations, such that the radiation equation is expanded into a set of spherical harmonics. The P-1 approximation is obtained by truncanting the expansion at the first-order term, thus the P-1 method corresponds to the lowest order of the P_N approximation process. The P-1 method can give reasonable accuracy without too much computational effort, however the model is only valid for optical thickness greater than unity as well as requiring boundaries on all external surfaces. The Discrete Ordinate radiation Model (Fiveland, 1984) is similar to the P-1 model where the RTE is transformed into a set of simultaneous partial differential equation with different orders of series expansion. In addition, the DOM solves the RTE for a finite number of discrete 4π solid angles, each associated with a vector direction $\vec{s}$, fixed in the global Cartesian system. The DOM transforms equation (3.75) into a transport equation for radiation intensity in the spatial coordinates such that (Fiveland, 1984):

$$\nabla(I(\vec{r},\vec{s})\vec{s}) + (a+\sigma_s)I(\vec{r},\vec{s}) = an^2\frac{\sigma T^4}{\pi} + \frac{\sigma_s}{4\pi}\int_0^{4\pi} I(\vec{r},\vec{s}')\,\Phi(\vec{s},\vec{s}')d\Omega' \qquad (3.76)$$

The DOM does not perform any ray tracing but instead, it solves equation (3.75) as many times as there are angular directions. This makes the DOM more computationally intensive than the P-1 method, but also more accurate. The major limitation of the DOM is its dependence on the angular

discretization, where each octant of the the angular space 4π at any spatial location is discretized into $N_\theta \times N_\varphi$ solid angles of extent ω_i, where the angles θ and φ are the polar and azimuthal angles respectively, and are measured with respect to the global Cartesian system.

In addition to the directional nature of radiation discussed above, the spectral nature of radiation must be accounted for inorder to fully solve the RTE. The models developed to treat the spectral nature of radiation can be generally classified into three categories namely the spectral line-by-line models, the spectral band models and the global models. The spectral line-by-line models are the most accurate of these categories, however they are computationally intensive. Radiative heat transfer in combustion gases in rendered very complex due to the line structure exhibited by the emission and radiation spectra of most of the combustion gases. Typical absorption spectra of gases such as CO_2, $H_2O_{(v)}$ and CO contain roughly 10^5 to 10^6 lines (Ludwig et al., 1973). At combustion temperature above 2000 K, it is estimated that the number of spectral lines present are well over a million (Rothman et al., 1992). From a modelling perspective, this implies that in order to accurately predict the radiative transport in a flame, one would have to solve the RTE for about a million spectral intervals. Such calculations are known as line-by-line calculations (LBL) and are highly intractable. The band models adopts a spectral averaging technique which results in an expression for the band emissivity/absorptivity. This spectral averaging in necessary in order to reduce the number of spectral intervals for which the RTE has to be solved. For modelling non-gray radiation in molecular gases such as CO_2 and $H_2O_{(v)}$, the global approach is widely used. The WSGGM (Hottel & Sarofim, 1967) replaces the non-gray gas with a number of gray gases (gases, such as N_2 that are transparent to radiation and hence do not absorb/emit radiation and possess an absorption coefficient that is constant throughout the emitting infra-red wavelength region) for which the heat transfer rates are computed from the narrow or the wide band model as functions of the temperature, pressure and concentrations of each gas. The total flux is computed by adding the heat fluxes of the gray gas after multiplication with certain weight factors (Modest, 2003).

3.1.4 Pollutant modelling

The modelling of the pollutants is an essential aspect of the combustion modelling due to the stringent legislative restrictions imposed on industrial combustion devices. The main pollutants of concern are soot and NO_x and both of these species present significant challenges for modellers because of the complexities in the soot chemistry and the slow-rate formation in the NO_x reactions.

3.1.4.1. NO_x models

The production of NO_x in hydrocarbon flames can be attributed to two main chemical routes: (i) the reaction of oxygen with atmospheric nitrogen in the high-temperature region of the flame (thermal NO_x), and (ii) the reaction of hydrocarbon free radicals, such as CH with atmospheric nitrogen under fuel rich conditions in the flame (prompt NO_x). The rate of formation of thermal NO_x is important only at high temperatures (greater than 1800 K) because the fixation of nitrogen requires the breaking of the strong N_2 triple bonds. The term NO_x refers to a group of oxides of nitrogen formed in the flame among which include NO, NO_2, N_2O, etc., with NO (nitrogen oxide) being the dominant nitrogen species that is formed. Hence the term NO_x is sometimes used to refer to the NO produced in the flame. For the thermal and prompt NO_x mechanisms, ANSYS Fluent solves the generic transport equation for mass conservation of nitrogen oxide taking into account the convection, diffusion, production and consumption of nitrogen oxide and related species. The nitrogen oxide transport equation is given by (Mahmud et al., 2007):

$$\frac{\partial}{\partial t}(\rho Y_{NO}) + \frac{\partial}{\partial x_k}(\rho u_k Y_{NO}) = \frac{\partial}{\partial x_k}\left(\rho D \frac{\partial Y_{NO}}{\partial x_k}\right) + S_{NO} \qquad (3.77)$$

where Y_{NO} is the mass fraction of nitrogen oxide and D is the effective diffusion coefficient. The two left hand terms in equation (3.90) represent the transient and convective terms, while the two right hand terms represent the diffusive and reaction source terms, respectively. The nitrogen oxide concentration can also be calculated using the Pollutant Model (Hughes et al., 2001) available in the Fluent code. In this model, the NO is modelled outside the flamelet structure, hence the nitrogen oxide calculations can be

detached from the main combustion calculations. This is justified on the basis that the kinetics of nitrogen oxide formation rate is very slow compared with kinetics of the main hydrocarbon oxidation, hence most of the thermal NO_x is formed after completion of the combustion and hence the NO formation rate is calculated by assuming equilibration of the combustion process. The concentration of oxygen atoms required to calculate the rate of formation of thermal NO_x is determined by assuming partial equilibrium between [O] and [O_2]. The rate constants for the reactions are taken from the works of Baulch et al. (1973). Predictions of the nitrogen oxide formation are obtained using the well-established Zeldovich mechanism (1947) with the inclusion of the reverse reactions. The Zeldovich mechanism is given as:

$$\frac{1}{2}\mathrm{N_2} + \frac{1}{2}\mathrm{O_2} \rightleftarrows \mathrm{NO} \tag{3.78}$$

$$\mathrm{N_2} + \mathrm{O} \rightleftarrows \mathrm{NO} + \mathrm{N} \tag{3.79}$$

$$\mathrm{N} + \mathrm{O_2} \rightarrow \mathrm{NO} + \mathrm{O} \tag{3.80}$$

$$\mathrm{N} + \mathrm{OH} \rightarrow \mathrm{NO} + \mathrm{H} \tag{3.81}$$

Reaction (3.78) represents the global reaction for the formation of NO, while reactions (3.79) to (3.81) represent the known steps for the global reaction. Free oxygen atoms (produced in the flames by the dissociation of $\mathrm{O_2}$ or by the radical attack on $\mathrm{O_2}$) attack the nitrogen molecules and begin the chain reaction as shown in equation (3.79). The concentration of $\mathrm{O_2}$ is low for fuel rich combustion, so reaction (3.78) is less significant than in fuel lean combustion. Reactions with the hydroxyl radical ultimately become the major sink for nitrogen atoms as shown in reaction (3.79). The high activation energy required to rupture the nitrogen triple bonds makes reaction (3.79) the rate limiting step of the Zeldovitch mechanism. The Prompt NO_x formation is modelled via the Fenimore mechanism (1971). Furthermore, the prompt NO_x formation is proportional to the number of carbon atoms present per unit volume and is independent of the parent hydrocarbon identity. A global rate kinetic parameter derived by De Soete (1975) for the combustion of hydrocarbon fuels is used for the calculation of the prompt NO_x formation.

3.1.4.2. Soot models

Soot is predominantly carbon, with a small amount of other elements, such as hydrogen and oxygen, although hydrogen may constitute up to 10% wt of soot. Soot is produced due to the high temperature pyrolysis of the hydrocarbons. The emission of soot from the combustion devices depends on the competition between the soot formation and the soot oxidation rates, therefore all good soot models must account for these two processes. Soot formation is a complex process, consisting of a nucleation and a growth stage. The soot is considered to grow in two ways; (i) the surface growth by the reaction of the neonate soot nucleus with gas phase species, and (ii) the collisional coagulation of the solid soot particles to form larger particles. The first is a chemical process and the second is a physical process and while the second process reduces the number of soot particles, the first process does not. It is worth noting the difference between soot coagulation and soot agglomeration. When larger soot particles collide, experimental results indicate that they will not coalesce (coagulate), but rather form chains and grow into larger soot aggregates. Soot oxidation occurs primarily as a result of the attack by molecular oxygen, O_2 and the OH radical. Due to the above complexities, soot modelling is a difficult mathematical undertaking and the simulations are computational intensive and hence many models are highly simplified. If the soot parameters, *i.e.,* the soot mass density (*M*) and the soot particle number density (*N*) can be expressed by any dependent scalar variable, Φ, its conservation equation can be written as (Wen et al., 2003):

$$\frac{\partial}{\partial t}(\rho\Phi) + \frac{\partial}{\partial x_j}\left(\rho u_j \Phi\right) = \frac{\partial}{\partial x_j}\left(D\,\frac{\partial \Phi}{\partial x_j}\right) + S_\Phi \qquad (3.82)$$

The two left hand terms in equation (3.95) represent the transient and convective terms respectively, while the two right hand terms represent the diffusive and reaction source terms, respectively. The reaction source term, S_Φ is determined by the soot model. A generic expression for the source terms for (*M)* and (*N*) can be written as (Wen et al., 2003):

$$\frac{DM}{Dt} = \left(\frac{DM}{dt}\right)_{Inc.} + \left(\frac{DM}{dt}\right)_{Gro.} + \left(\frac{DM}{dt}\right)_{Oxi.} \qquad (3.83)$$

$$\frac{DN}{Dt} = \left(\frac{DN}{dt}\right)_{Inc.} + \left(\frac{DN}{dt}\right)_{Coa.} \tag{3.84}$$

where the abbreviations *Inc., Gro., Oxi. and Coa.* represent the inception, growth, oxidation and coagulation steps of the soot formation and oxidation, respectively. Different models are available for the inception, coagulation, growth, and oxidation terms in the above equations. The conventional acetylene inception model (Leung & Lindstedt,1991) is based on the simplifying assumption that the soot inception is a first order function of the acetylene concentration, i.e.,:

$$\left(\frac{DN}{dt}\right)_{Inc.} = c_1 N_A \left(\rho \frac{Y_{C_2H_2}}{W_{C_2H_2}}\right) e^{-\frac{21100}{T}} \tag{3.85}$$

where c_1 = 54 s^{-1}, as determined by Brookes & Moss (1999) and the activation temperature was proposed by Lindstedt (1991). For parrafinic fuels, soot particles have been discovered to increase in size primarily by the addition of the gaseous species at their surfaces, particularly acetylene (C_2H_2). For higher hydrocarbons, in addition to acetylene, benzene (C_6H_6) has been found to be an important soot precursor. The Moss-Brookes Hall model (Hall et al., 1997) is a PAH inception model with the soot inception rate being modelled as function of the formation rate of three and two ring aromatics. This model has been validated against aviation grade kerosene combustion experiments with good agreements (Moss et al., 2003). Soot oxidation is based on the model by Lee et. al (1962) and it accounts for the oxidation of soot by both [O_2] and [OH] species given as:

$$\left(\frac{dM}{dt}\right)_{oxid} - C_{oxid} C_{\omega,1} \eta_{coll} \left(\frac{X_{OH} P}{RT}\right) \sqrt{T} (\pi N)^{1/3} \left(\frac{6M}{\rho_{soot}}\right)^{2/3} -$$

$$C_{oxid} C_{\omega,2} \eta_{coll} \left(\frac{X_{O_2} P}{RT}\right) exp\left\{\frac{T_{\omega,2}}{T}\right\} \sqrt{T} (\pi N)^{1/3} \left(\frac{6M}{\rho_{soot}}\right)^{2/3} \tag{3.86}$$

where the collision efficiency η_{coll} is given as 0.13, the oxidation rate scale parameter C_{oxid} is taken to be unity, the constants $C_{\omega,1}$ and $C_{\omega,2}$ are taken to be 105.81 and 8903.51 kg·m·kmol^{-1}·K$^{-1/2}$·s^{-1},respectively, and $T_{\omega,2}$ is given as 19778K.

3.2 Experimental methods

This section discusses the equipment and methods used in the experimental stage of this project as well as the limitations on the equipment. In discussing the experimental set-up, it is necessary to describe the design of the burner, the sampling system and other techniques employed during the investigation.

3.2.1 Burner description

The burner that was used for the experiment was a simple diffusion flame burner whose design was modelled after the burner that was used at the Sandia National Laboratory and at the BOC Group Technical Centre in the USA. The burner is designed to be used for gaseous fuels and firing vertically upwards. It is comprised of a changeable fuel tube centrally mounted in an outer annulus through which an oxidant co-flow air can be passed and an outer shroud of a fixed diameter (102 mm), through which a stabilizing air medium can be passed. The passage for the shroud air contained a layer of honeycomb and three wire meshes, facilitating a smooth outer flow. The burner was later modified for the purpose of the flare experiment by taking out the annulus for the oxidant co-flow air. The central fuel tube used had an inner diameter of 3.25 mm, an outer diameter of 6.2 mm and was 470 mm in length. The fuel flow was controlled with a pressure regulator and a valve, while the flow rate was measured using a rotameter that was calibrated separately for methane and propane using the method described in section 3.2.2. A constant flow of shroud air was maintained at a velocity of 0.3 m/s. Based on the measured fuel flow rate and the nozzle diameter, the fuel nozzle exit velocity was calculated and the fuel Reynolds number was determined. The burner was mounted on a three dimensional (XYZ) transverse system, and the origin was centred at the exit plane of the burner tube. The fuel used was commercial grade propane of about 95 % purity, supplied in standard bottles by BOC. A schematic diagram of the burner is shown in Figure 3-2.

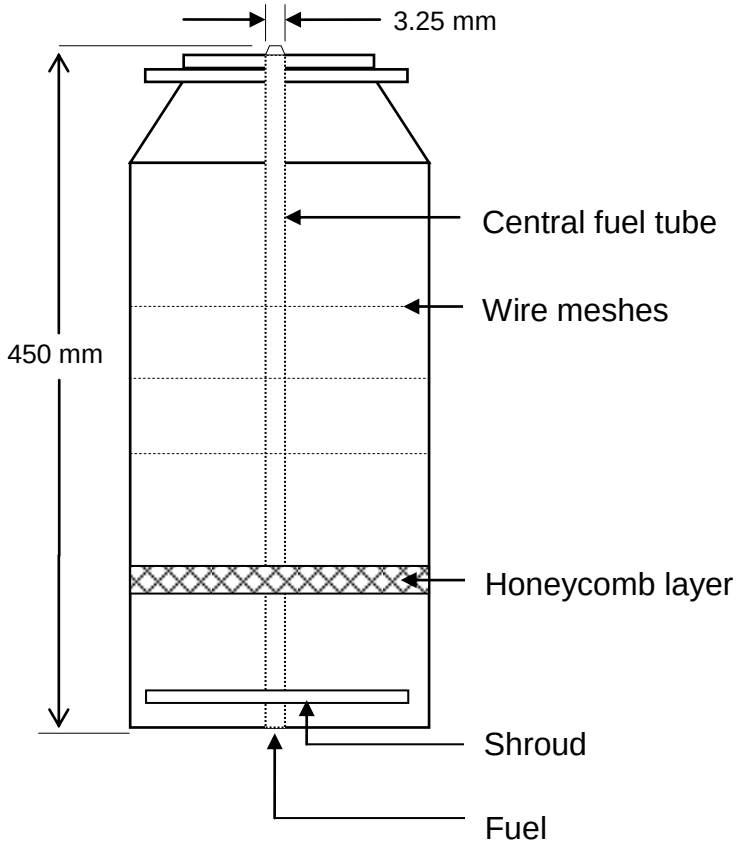

Figure 3-2 Schematic diagram of the diffusion burner (adapted from Lee Howard, 1998)**.**

3.2.2 Rotameter calibration

The gas flow rate was measured using a glass tube rotameter, shown in Figure 3-3. The rotameter consists of a uniformly tapered flow tube, a measurement scale, a needle valve used for flow control, and a float. In these devices, the falling and raising action of the float in the tapered tube provides a measure of the flow rate. The float has a spherical configuration and is often made of plastic. The rotameter is placed in an upright position with the needle valve located on the upstream side of the gas supply. The rotameter is set up for calibration by connecting the outlet to a wet test bubble tube, and used after calibration by connecting the outlet to the gas burner. Calibration was carried out by passing the gas through the rotameter and into the bubble tube. The bubble tube was kept wet on the inside with soapy water, which generated gas bubbles when the gas was introduced into the tube. The gas bubbles then rise up the tube with a speed proportional to the flow rate of the gas. By noting the time it takes for the

bubbles to travel between two selected positions on the tube, it is then possible to determine the flow rate corresponding to each reference point of interest on the measurement scale. By using the dimensions of the bubble tube, one can then calculate the fuel velocity corresponding to each flow rate (see appendix II (a)). The measured flow rates were converted to conditions of standard temperature and pressure based on the ideal gas relationship:

$$Q_i = Q_0 \left(\frac{273.15}{T}\right)\left(\frac{P}{1013.25}\right) \tag{3.87}$$

where Q_i is the corrected flowrate based on the assumption of an ideal gas, Q_0 is the measured flowrate and P and T are the prevailing room temperature and pressure in Kelvin and millibars, respectively. The rotameter calibration exercise was performed separately for the methane and the propane fuels and Figure 3-3 shows the setup for the rotameter calibration exercise.

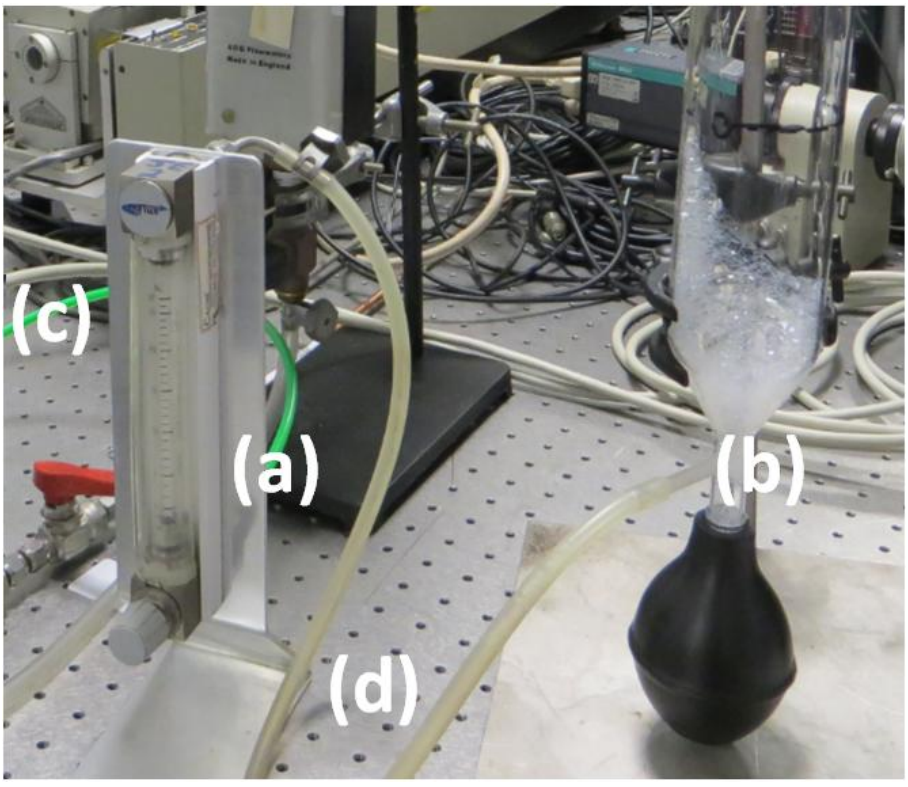

Figure 3-3 Photograph of the rotameter calibration set-up, (a) rotameter, (b) bubble tube, (c) fuel line from the gas cylinder to the rotameter – green line, and (d) fuel line from the rotameter to the bubble tube - white line.

3.2.3 Temperature measurement

A type R thermocouple was used for sampling the inflame and post flame temperature. The thermocouple is made from the finest platinum and platinum-rhodium alloy (Pt/Pt-13%Rh) and covers a temperature range of 0 ^{o}C up to 1450 ^{o}C. The thermocouple used had a wire diameter of 125 µm and a bead diameter of 213 µm and the thermocouple bead was coated with a thin layer of silica to avoid catalytic reaction on the bead surface due to platinum catalysis. The thermal structure of the flame was mapped by traversing the coated thermocouple across the flame in the radial direction at selected heights above the burner nozzle. The thermocouple output was recorded in raw voltage form, by a computer controlled data acquisition system (MultiScan 1200). One hundred and fifty voltage readings were taken over a period of ten seconds, at each sampling location. The voltage readings were converted to temperature readings in degrees Celsius by the DAS software controller (chartview) which uses an in-built linearization formula. The temperature readings were later converted to Kelvin and the mean reading was calculated using Microsoft excel spreadsheet. A schematic diagram of the thermocouple is shown in Figure 3-4.

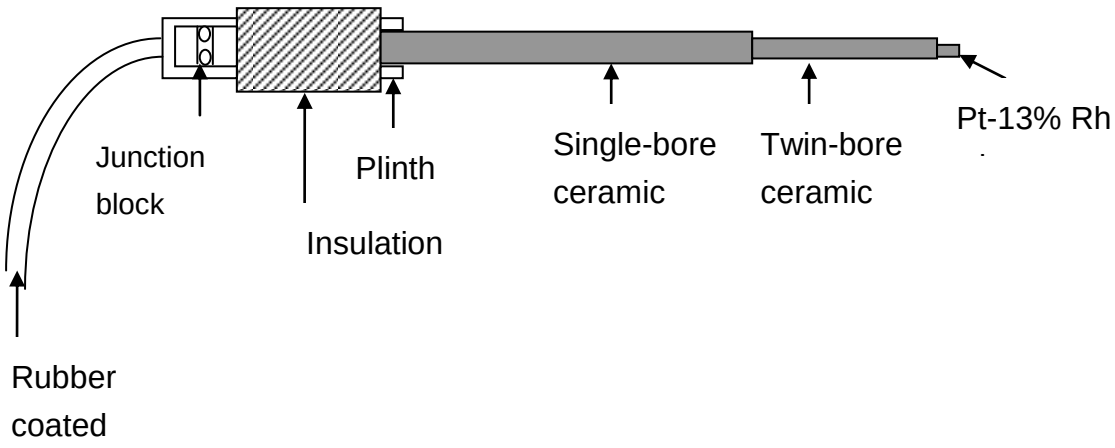

Figure 3-4 Schematic of the Pt-Pt13%Rh fine wire thermocouple employed (adapted from Lee Howards, 1998).

3.2.4 Species measurement

The accessory and instrumentation required for determining the composition of the flame consisted of a quartz in-flame gas sampling probe and a Horiba 3000 gas analysis unit, comprising a chemiluminescent section for NO_x measurements, an infra-red section for CO and CO_2 measurements, paramagnetic section for O_2 measurements and FID section for measuring unburned hydrocarbons in the flame.

- *Gas probe*

The gas probe was made of quartz, with a sampling orifice of 100 µm. The probe is designed to suck the combustion product through a tip with internal diameter of 1 mm, with the end of the tip expanding suddenly in area. This sudden expansion in area leads to a fast quenching of the combustion products and prevents reactions occurring in the probe tip, an occurrence which will lead to an erroneous analysis of the flame species. This design is based on the choked flow principle (Colket, 1982).

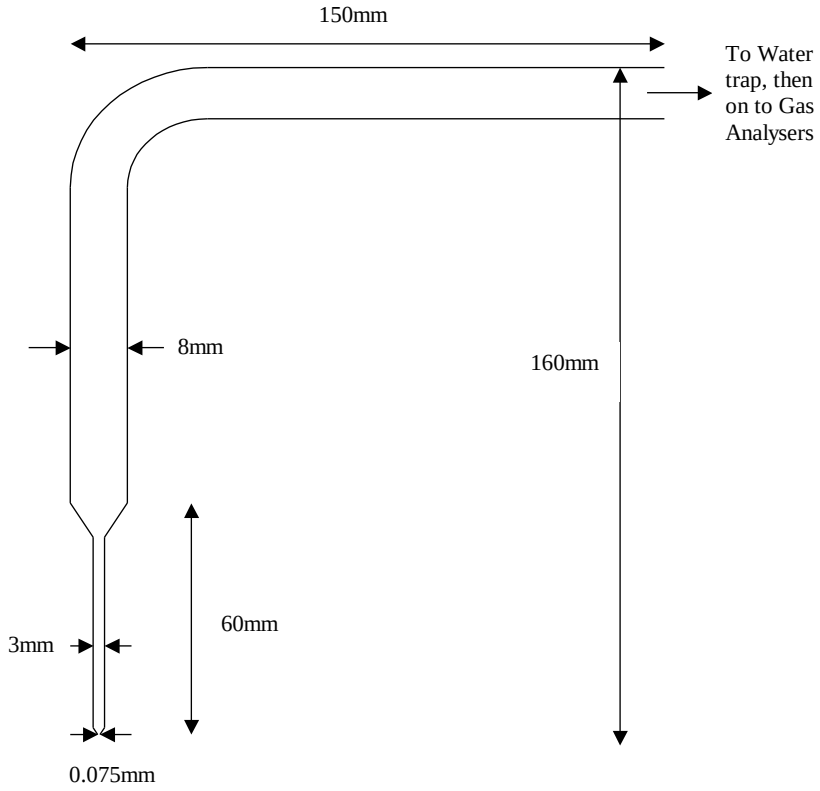

Figure 3-5 Schematic of a quartz sampling probe.

- *Gas analysers*

The Horiba VA-3000 is a multi-module versatile gas analyser capable of measuring a wide selection of gas components by utilizing different types of sensor technologies. The unit comprise of a non-dispersive infra-red (NDIR) module for measuring gases such as CO, CO_2 and SO_2, a chemiluminescent sensor module for measuring NO and NO_x and a paramagnetic oxygen sensor. A hydrogen flame ionization detector is also included for measuring the total hydrocarbons in the flame. The operating principles of the different sensors are discussed below in more detail.

Chemiluminescent NO_x analyzer

Chemiluminescence means the production of light via a chemical reaction. The Chemiluminescent NO_x analyzer works on the principle that nitrogen oxide (NO) is a relatively unstable molecule and will readily oxidize to nitrogen dioxide (NO_2), especially in the presence of ozone. This reaction produces some electronically-exited NO_2 molecule and these molecules will give off energy in the form of light emissions on returning to their ground state. If the volumes of sample gas and the excess ozone are monitored carefully, then the light intensity in the reaction chamber will be proportional to the concentration of NO in the gas sample. This light can be measured using a solid state device, such as a transistor. The light emission occurs within the range of about 600 to 3000 nm with a peak at about 1200 nm. Chemiluminescence NO_x analyzers measure the concentration of NO with the aid of a band pass filter to select light in the region from about 600 to 900 nm. The basic Chemiluminescence chemistry was delineated by Clough and Thrush (1967) as follows:

$$NO + O_3 \rightarrow NO_2^* + O_2 \quad (3.88)$$

$$NO + O_3 \rightarrow NO_2 + O_2 \quad (3.89)$$

$$NO_2^* \rightarrow NO_2 + hv \quad (3.90)$$

$$NO_2^* + M \rightarrow NO_2 + M \quad (3.91)$$

Reactions (3.88) and (3.90) describe the formation of the electronically exited NO_2 molecule and its de-excitation (to emit a photon of light),

respectively hence they are pertinent to the measurement purposes. However the reactions described by equations (3.89) and (3.91) represent a potential limitation to the measurement technique. In reaction (3.89), the NO_2 molecules formed are not excited while in reaction (3.91), the excited NO_2 molecules return to the ground state without radiation emission due to collision with other molecules (M). This means only a fraction of the NO molecules (about 10%) reacts to form the excited NO_2 molecules and emit light. Fortunately, the percentage of the NO molecules in the reaction chamber that follows the pathway described by reactions (3.88) and (3.90) is sufficient to ensure a proportionally linear response in any properly designed instrument. The chemiluminescence process is specific to NO. Hence to determine NO_x ($NO+NO_2$), NO_2 must first be converted to NO prior to entering the reaction chamber. The converted molecules and the original NO molecules in the sample then react with ozone and this results in a signal that equates to the sum of NO and NO_2. To obtain a measure of the NO_2 concentration, the difference between the converted and non-converted modes must then be taken. A basic layout of the NOx analyzer is shown in Figure 3-6.

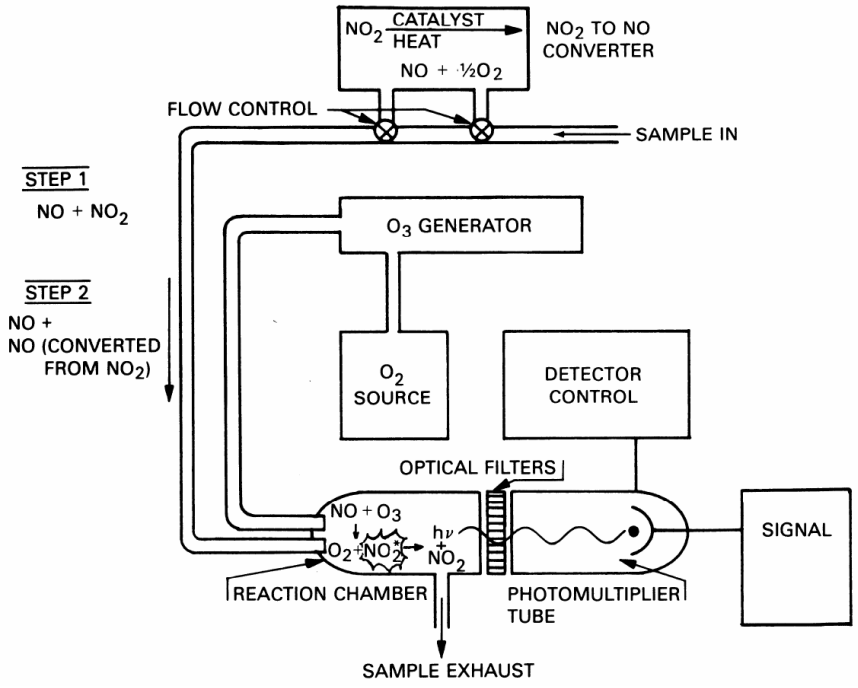

Figure 3-6 Schematic of the NO_2-to-NO converter (EPA 625/6-79-005).

Non dispersive infrared CO/CO_2 analyzer

A light source will emit light over a very wide range of wavelengths and only a very narrow band (400 – 800 nm) will be visible light. Wavelengths shorter than 400 nm are in the ultraviolet region while wavelengths longer than 800 nm are in the infrared region of the spectrum. The infrared region of the spectrum is divided into three wavebands – the very near infrared (800-1100 nm), the near infrared (1100-2500 nm) and the mid-infrared (2500-10000 nm). The non-dispersive infrared analyzer works on the principle that certain heteroatomic gases, such as CO and $CO_{2,}$ absorb radiation in specific wavebands (Mulkey et al., 2008). CO_2 for example, strongly absorbs in the intermediate infra-red waveband. When a gas stream containing carbon dioxide is exposed to a light source, energy from that section of the infrared region of the spectrum is absorbed by the gas. The main components of an infrared analyzer are the radiation source (a lamp), a sample chamber, a wavelength sample chamber, an optical filter and an infrared detector. The infrared gas analyzers work by measuring the reduction in transmission of infrared wavebands caused by the presence of the gas between the radiation source and the detector. When light passes through the gas stream, the components of the gas stream absorb radiation at wavelengths specific to them. The remaining light is passed through the optical filter where it is filtered to a wavelength specific to carbon dioxide for example, before reaching the detector. Hence depending on the concentration of carbon dioxide present in the sample, the gas will absorb some radiation and thus reduce the level of energy reaching the detector. This energy level will then be compared with a pure sample output from the optical filter, the difference in energy is then amplified to give the analyzer output signal.

Magnetodynamic paramagnetic O_2 analyzer

Paramagnetic oxygen analyzers work on the scientific principle that oxygen is a paramagnetic material, meaning that it can be attracted into a magnetic field or it is “magnetically susceptible”. Magnetic susceptibility is defined as a measure of the intensity of the magnetization of the material when it subjected to a magnetic field. The magnetic susceptibility of oxygen is

exceptionally high compared to other gases – actually hundreds of times greater than that of most other gases. The currently available paramagnetic oxygen analyzers use one of several types of oxygen sensors. Three types are widely used and these are the magnetodynamic, thermomagnetic and the magnetopneumatic types (Andrew et al., 2000). The magnetodynamic oxygen analyzer is the most commonly used of the three techniques. The setup consists of small glass dumbbells, two strong magnets and precision optical systems consisting of a light source, photocell, a mirror and a calibrated indicating unit. The dumbbell is filled with an inert gas such as nitrogen or helium and suspended within a strong non-uniform magnetic field by a taut platinum wire. When a test sample containing oxygen is introduced into the analyzer, the oxygen molecules are attracted to the stronger of the two magnetic fields. This causes a push on the dumbbell resulting in a displacement from its zero position. The precision optical system is used to measure the magnitude of the displacement and this is proportional to the concentration of oxygen in the sample.

Flame ionization detector

The flame ionization detector (FID) is the industrial standard for measuring the amount of unburnt hydrocarbons in a flame. The FID typically uses a hydrogen/air mixture to generate a flame within the unit into which the sample is passed (Dewar, 1960). Any unburnt hydrocarbon in the sample will be ionized upon their oxidation and the ions are detected using a metal collector which is biased with a high DC voltage. The ions generate a current across the collector which is proportional to the rate of ionization which in turn depends on the concentration of hydrocarbons in the sample gas. The ionization process is very rapid, thus giving the FID a very quick response time. The sample gases are carried from the probe to the Horiba 3000 multicomponent gas analyzer unit via a heated teflon tube. The heated line is kept a temperature of 160 ^{0}C and left on over a period of 24 hrs to ensure that the samples reaching the gas analysis unit are measured on a dry basis. The gas analyser is inter-faced with the MultiScan 1200 data logger, and the data logger is in turn connected to a computer running a windows

XP operating system. The ChartView software was used to monitor and capture the species concentration in the flame at each measurement location. 100 samples were taken at each measurement location and the readings were averaged using an excel spreadsheet. Further, zeroing and spanning actions were carried out before each measurement session to minimize experimental errors.

3.2.5 Soot measurement

Soot from the flames was collected at the postflame region using a tube connected into the exhaust hood which was used to suck the post flame combustion gases with the aid of a suction pump. The gases were sucked onto a filter paper held in place by a filter holder. The filter papers were dried in an oven to reduce moisture and to eliminate any errors in measurement that may arise due to moisture in the filter papers. The filter papers were weighed both before and after the soot deposition, and the difference in weight was determined. Several runs were performed for each fuel, and average measurements were taken.

3.2.6 Flame photographs, flame Lengths and lift-off heights

A 12.1 MegaPixel CMOS camera (Canon PowerShot SX260HS) was employed to capture the flame images. The visible flame lengths and lift-off heights were obtained by averaging a video record of the flames over 30 frames. The images were then averaged and the mean image selected. All light sources in the laboratory were turned off with the only source of illumination being the flame. Flash options on the camera were disabled and the camera was stabilized on a tripod system to minimize image blur due to camera shaking.

3.2.7 Experimental errors

All experimental processes are bound to be associated with some level of experimental error, either due to limitations on the sensitivity of the equipment used or due to the limitations of the human senses. These issues are discussed below.

- *Errors associated with the temperature measurements*

To minimize errors from the temperature measurements, the thermocouple readings were compensated for room temperature measurements. This was achieved by recording the room temperature before combustion using a digital room thermometer. The room temperature reading from the thermometer was then compared with the room temperature reading from the thermocouple. The error from the thermocouple reading is due to the fact that the thermocouple is designed to take measurements at high temperatures and not room temperatures. The appropriate correction was then applied to the thermocouple readings using the formula:

$$T_{cr}^{tc} = T_{rm}^{tc} + T_{cp} \tag{3.93}$$

where T_{cr}^{tc} is the corrected thermocouple reading, T_{rm}^{tc} is the thermocouple reading at room temperature and T_{cp} is the compensation temperature. The second temperature correction was the correction associated with the thermocouple reading during the combustion. The correction is applied due to the radiation losses from the thermocouple beads, as this has the effect of making the thermocouple under-predict the true flame temperature. Several correction formulas are available in the literature, but in this work, the correction formula proposed by Kaskan (1957) is applied, namely:

$$\Delta T_{rad} = \frac{1.25\varepsilon\sigma T_w^4 D^{0.75}}{\lambda}\left(\frac{\eta}{\rho u}\right)^{0.25} \tag{3.94}$$

where ΔT_{rad} is the temperature correction due to the radiation losses from the thermocouple (K), ε is the emissivity of a coated thermocouple bead (ε=0.22), σ is the Stefan-Boltzmann constant (5.67 X 10^{-8} W/m^2 K^4), T_w is the temperature of the wire, (K), D is the bead diameter (0.3mm), λ and η represent the thermal conductivity and viscosity of the gases at the wire temperature in (J/ m s K) and (kg/m s) respectively, ρ and u are the density and velocity of the fluid passing the thermocouple bead in (kg/m^3) and (m/s) respectively. Values for the velocities were obtained from the computer simulations whereas values for the thermal conductivity, λ and the viscosity, η**,** were obtained from NASA (1962) and is shown in appendix II (b).

- *Errors associated with the species measurements*

Special measures were taken to minimize errors from the gas analysers. Zeroing and spanning operations were conducted after each measurement session. The gas analyser was left to run on idle mode for at least an hour before commencing zeroing operation in order to allow all operating parameters to reach steady state. The spanning range was set within the appropriate range of the span gas cylinders. The specifications of the span gas cylinders, which were certified and supplied by BOC Special Gas is presented in Table 3-3.

Table 3-3 Calibration gases and specifications for the gas analyser.

SPAN GAS	SPECIES	NOMINAL CONC.	CERTIFIED VALUE
Span 1	NO	49.7 ppm in N_2	50 ppm
Span 2	Ambient air	21 %	21%
Span 3	CO_2	6.25 % in N_2	6%
Span 4	CO	8.02 % in N_2	8%

It has been established that the presence of water in a gas sample drawn from a combustion system can result in large errors in the species measurements, especially NO and NO_2 measurements. Water is a third body quenching radial present in combustion gases and will ultimately interfere with the NO results. Furthermore, water condensation in the analysers can result in the removal of NO_2 as a result of its high affinity to dissolve in water (Tidona et al., 1988). The approach used to eliminate the water in the sample gases was to keep the teflon sample-gas line heated at a constant temperature (160 ^{0}C). This approach keeps water in the sample gases substantially above its dew point, and the water in eventually removed via a filter system. Pressure also needs to be maintained constant in the gas analyser to minimize 'drifting'. The pressure must be kept within the range of the manufacturers specifications. The quoted accuracies of the infra-red CO_2 and paramagnetic O_2 analysers are given as $\pm$5% and $\pm$1%, respectively.

Chapter 4

Numerical Study of a Vertical Methane Jet Diffusion Flame: Investigation of the Turbulence and NO_x Models

4.1 Background

This chapter presents the numerical investigations of a vertical methane jet diffusion flame. Methane constitutes more than 90% of natural gas and therefore it has been widely investigated in terms of its combustion characteristics and its emissions. Methane is also a low sooting fuel, hence its modelling in atmospheric conditions usually does not require a soot model. However, due to the high temperature obtained in lifted methane diffusion flames, NO_x emission is of particular concern in flaring conditions. It should be noted that propane is the fuel used in most of the investigations in this thesis, however the initial numerical work was performed on methane during the mesh validation stage and these results are presented in this chapter. This initial work compares three turbulence models namely the $k-\varepsilon$ realizable, the $k-\omega$ SST and transitional SST models, as well as the NO_x models by validating them aganist the experimental data from Lee Howard (1998), which he obtained using the same diffusion burner used for the present investigation. The experimental data was obtained from the investigation of a methane/air jet diffusion flame, with the co-flow oxidant air enriched to 26% oxygen. The flame was rim stabilized at the Reynolds number employed for the investigation (4221), and no pilot flame was required to achieve rim stabilization of the main flame. Measurements of the in-flame temperature, major species (CH_4, O_2, CO_2) and minor species (CO, NO) were made using the methods described in section 3.2. The structure of the flame was reported in terms of the mole fraction profiles of the major species, minor species and the corrected temperature as a function of the radial position across the flame. Three axial locations above the burner have been selected for the validation excercise.

4.2 Experimental details

This section describes the experimental work performed by Lee Howard (1998). The burner used for this work has been described in section 3.2.1. The interchangeable fuel tube used by Lee Howard had an inner diameter (d_i) of 1.75 mm and an outer diameter (d_o) of 3.18 mm, centrally mounted in an outer annulus, through which a stabilizing medium may pass. The fuel jet velocity and Reynolds number were calculated to be about 37 m/s and 4221, respectively. The burner features a fixed concentric outer shroud of diameter 102 mm, through which the oxygen-enriched air was passed with a velocity of 0.43 m/s. The air, in addition to being the oxidizing medium, also helps to shroud the flame from external disturbances. The air was supplied to the burner via a compressed air supply, whereas both the oxygen gas and the methane gas were obtained from gas cylinders supplied by BOC. The flow rotameters in both the oxidant and the fuel lines were manufactured and calibrated by 'KDG' instrumentation, with quoted accuracies of +/-1%. The in-flame temperatures were measured according to the method described in section 3.2.3 while the species concentrations were measured according to the method described in section 3.2.4. The experimental conditions for the Lee Howards case are summarized in Table 4-1.

Table 4-1 Flame parameters and measurement locations (L. Howard, 1998).

Parameter	**Value**
Fuel	Methane
Oxidizer	Oxygen-enriched air
O_2 concentration in oxidant flow, %	26
Fuel average velocity, m/s	37
Oxidant flow average velocity, m/s	0.43
Fuel nozzle Reynolds number	4221
Selected Streamwise sampling locations (x/d_i)	9,60,170

4.3 Computational details

- *Grid independent study*

This section describes the mesh generation procedure for the realizable $k-\varepsilon$ model. A similar technique was used for the $k-\omega$ SST and the transitional SST, with appropriate modifications to the mesh. The computational simulation was achieved on a two-dimensional structured quad mesh generated using the ANSYS-ICEM meshing software. The mesh domain extended 2.3 m (700 d_i) in the axial direction and 0.4 m (123 d_i) in the radial direction with 1190 and 120 mesh nodes in either direction, respectively. A mesh refinement study was conducted to ensure the independence of the solution on the mesh size and density. This entailed comparing the velocity and temperature profiles for mesh sizes of 5 E4, 1 E5 and 1.8 E5 cells, as shown in Figure 4-2 (a-d). Mesh predictions for the axial and radial components of the velocity in the pipe, as well as the velocity at the pipe exit and the axial trend of the temperature were compared for the three mesh resolutions. All the mesh predictions were shown to be in good agreement. The mesh distribution option was selected so as to place finer node distribution in the pipe outlet region and coarser nodes further away from the pipe. The quality of the mesh was checked for the aspect ratio, a_r (ratio of longest to shortest edge of a cell) and the skewness, Sk (a measure of how close the cell is to its ideal shape) of the elements using the ANSYS-ICEM software (See Appendix I). The analysis of the mesh quality revealed that 60 % of the mesh elements had an aspect ratio of $0.5 \leq a_r \leq 1$, where cells with a_r = 1 are considered ideal. Also, the skewness of the cells were between $0.95 \leq Sk \leq 1$ where for a quad. element, the skewness is normalized so that 1 is ideal and 0 is the worst possible (ANSYS, 2014). Furthermore, the y^+ (a non-dimensional distance from the wall to the first mesh node) was ensured to lie in the range of $30 < y^+ < 60$ in order to capture the transition layer in the case of the realizable $k-\varepsilon$ model (Wilcox, 1993). In the case of the $k-\omega$ SST, a $y^+ < 5$ was ensured, which is required in order to capture the viscous sublayer (Menter 1994). The y^+ plots are shown in Figure 4-3.

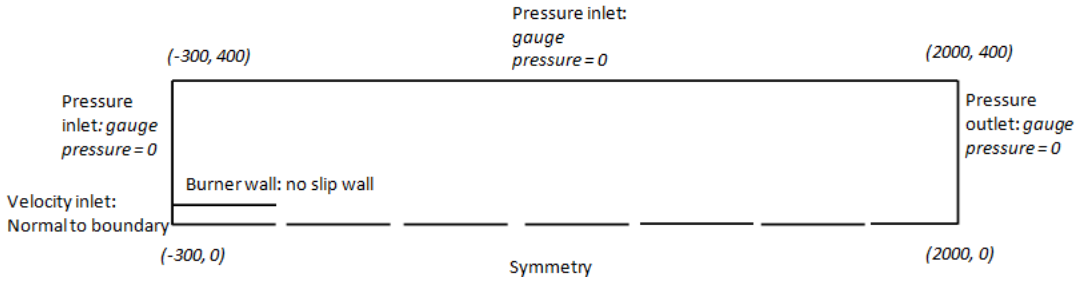

Figure 4-1 Computational flow domain and boundary conditions.

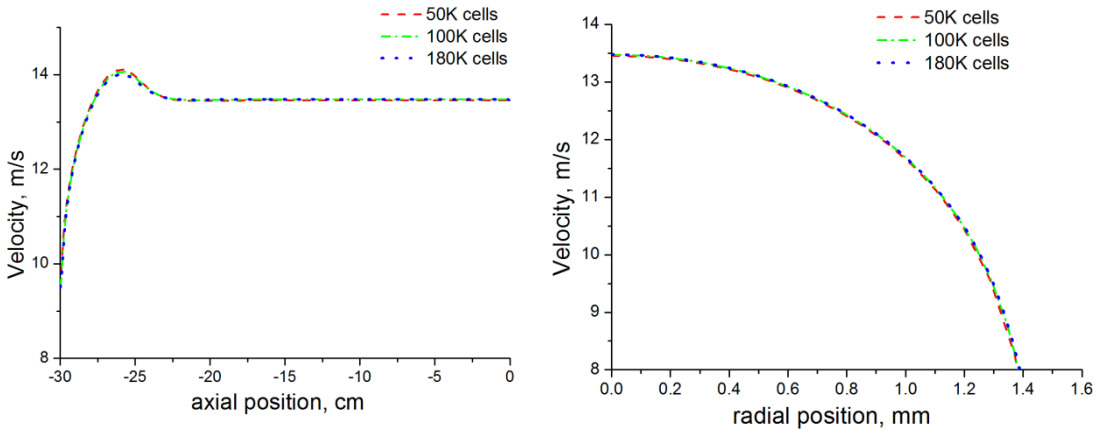

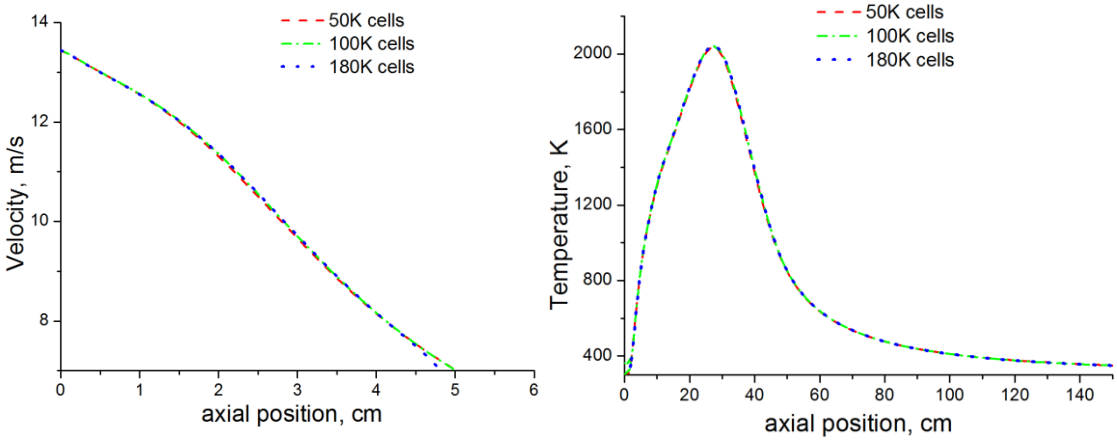

Figure 4-2 predictions of (a) axial velocity (b) radial velocity (c) velocity at pipe exit (d) axial temperature, for 50, 100 and 180K mesh sizes at Re=4221.

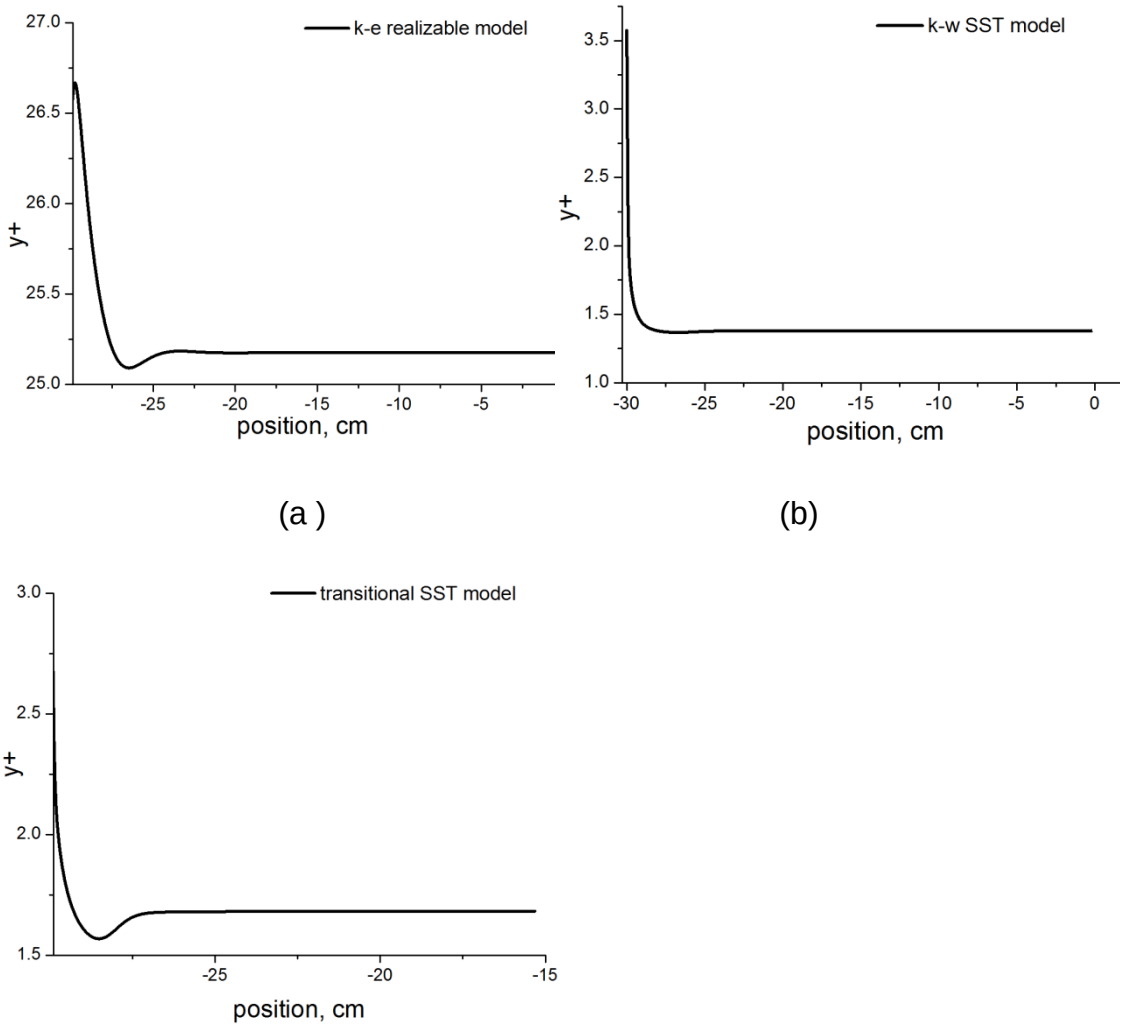

Figure 4-3 Pipe wall y^+ values for (a) $k-\varepsilon$ realizable, (b) $k-\omega$ SST (c) Transitional SST at Re = 4221

- *Boundary conditions*

Axisymmetric condition was implemented in the ANSYS-Fluent solver in view of the symmetry in the geometry. A no slip-wall boundary condtion was implemented at the pipe walls. Pressure inlet boundary conditions were employed at the entrainment boundaries, located 0.3 m (92 d_i) and 0.4 m (123 d_i) from the burner outlet in the axial and radial directions respectively. A pressure outlet boundary condition was employed at the outflow boundary, located 2 m (615 d_i) from the burner outlet (Figure 4-1). Extension of the entrainment boundaries by 20 and 35% in the axial and radial directions,

respectively did not produce any improvement in the predicted results. Similarly, a reduction in the size of the entrainment boundaries by 15 and 25 % in the axial and radial directions, respectively produced a deterioration of the predicted results. 5% turbulence intensity was specified at the velocity inlet while a 0.2% backflow turbulence intensity was prescribed at the pressure outlet and the entrainment boundaries were defined by 1% turbulence intensity. Investigation of the effect of the turbulence intensities on the predicted results showed that the predicted results were insensitive to the changes made to the values of the turbulence intensities. Buoyancy production was activated for all the calculations and the numerical solution was accomplished using a finite-volume discretization technique. No adjustments were made to the model constants and all the terms in the flow and combustion equations were discretized using a second-order upwind scheme, while the coupling between the pressure and velocity fields were handled via the SIMPLE (Pantakar, 1980) algorithm implemented in the Fluent code. Radiation, which appears as a sink in the energy equation was accounted for using the Discrete Ordinate Model (Fiveland, 1986). The gaseous products of the combustion process such as CO_2, H_2O and CO (non-gray gases) have a significant effect on the absorption and emission of radiant energy, hence their participation needs to be accounted for. This is achieved using the Weighted-Sum-of-Gray-Gas-Models (Hottel & Sarofim, 1967), where the absorbtion coefficient is obtained by curve fitting of the total gas emissivity of the medium as determined from experimental data (Smith et al., 1982). Since the radiant emission from non-luminous (non-sooty) hydrocarbon flames comes mostly from the gaseous products of the combustion process, only the absorption coefficients of these species are taken into account. The gas phase combustion reaction was simulated via the stationary laminar flamelet model (SLFM) described in section 3.1.2 and the kinetics of the methane reactions were simulated using the GRI mechanism, version 3.0. (Frenklach et al., 2012) which contained 325 reactions and 53 species. The calculation was intialized using the standard initialization technique implemented in the Fluent solver and interation was continued until convergence was achieved.

4.4 Results and discussion

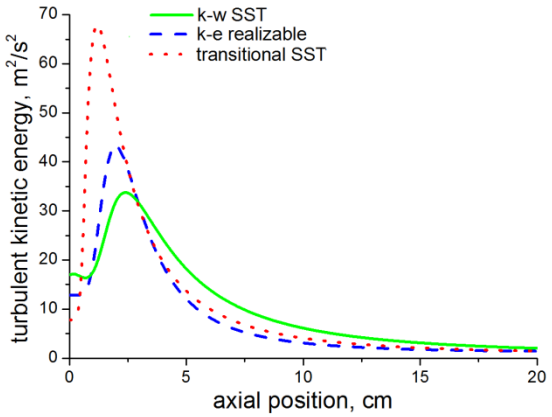

(a)

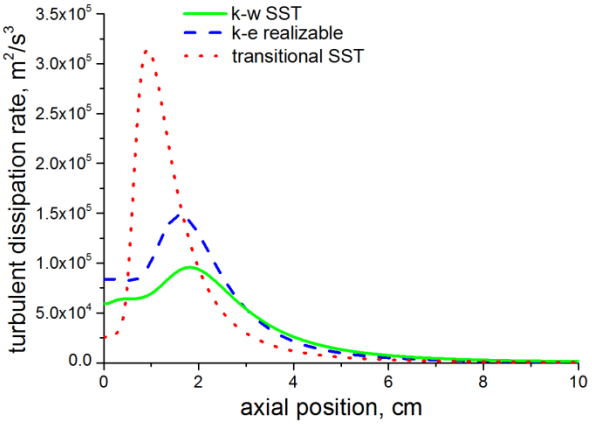

(b)

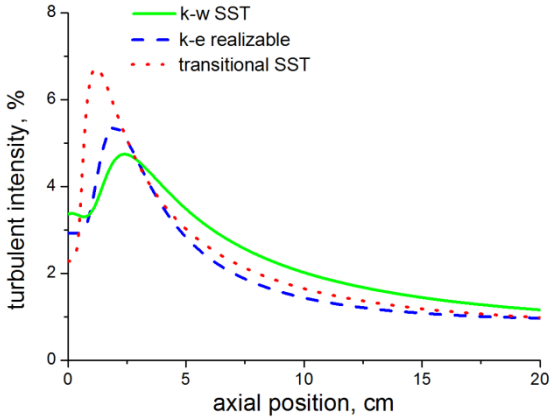

(c)

Figure 4-4 Axial predictions of (a) turbulent kinetic energy (b) turbulent dissipation rate and (c) turbulent intensity for a methane jet diffusion flame at Re = 4221.

This section presents the results obtained from the simulation of Lee Howard's (1998) experiments. Three turbulence models have been investigated and compared, namely the realizable $k-\varepsilon$, the $k-\omega$ SST and the transitional SST models. Figure 4-4 (a), (b) and (c) show the predictions of the turbulent kinetic energy and the turbulent dissipation rate and the turbulent intensity, respectively along the axis of the jet for the three turbulence models investigated. The transisitional SST model is observed to produce a very high turbulence kinetic energy and turbulence dissipation rate in comparison with the realizable $k-\varepsilon$ and the $k-\omega$ SST models. The prediction of the turbulent intensity is also observed to be slightly higher for the transisitional SST model in comparison with the realizable $k-\varepsilon$ and the $k-\omega$ SST models. The chemistry of the flame is strongly coupled with the turbulence and therefore a higher turbulent kinetic energy or turbulence intensity will increase mixing in the flame, thus leading to a faster consumption of the fuel. This can be observed in Figure 4-8 (c) where the transitional SST severly under-predicted the concentration of methane in the mid-flame region. Furthermore, it can be observed that the realizable $k-\varepsilon$ model displayed higher values of all the predicted parameters compared to the $k-\omega$ SST model. The $k-\omega$ SST model (Menter, 1994) has been developed to handle low Reynolds number flow where viscous effects are important, especially close to the walls. The $k-\varepsilon$ models (Launder & Spalding, 1974; Shih et al., 1995) on the other hand were developed to handle high Reynolds number flow where inertial effects dominate. However, the SST version of the $k-\omega$ model is adapted to employ the functionalite of the $k-\varepsilon$ models in the free stream, farther away from the walls. The next section presents the predictions of the temperature and species using the three turbulence models. Three axial locations at x/d_i = 9, 60 and 170 have been investigated, which correspond to the near burner, the mid-flame and the downstream region of the flame respectively. The simulation has been performed without including a soot model since the soot production in laboratory-scale methane/air jet diffusion flames has been shown to be negligible at atmospheric pressure (Brookes & Moss, 1999).

4.4.1 Temperature prediction for oxygen-enriched methane flame

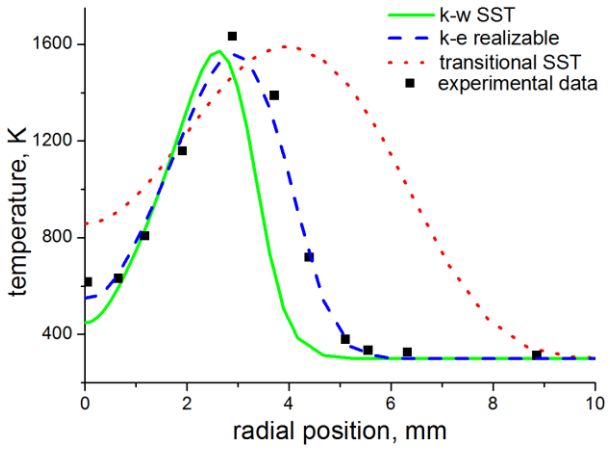

(a)

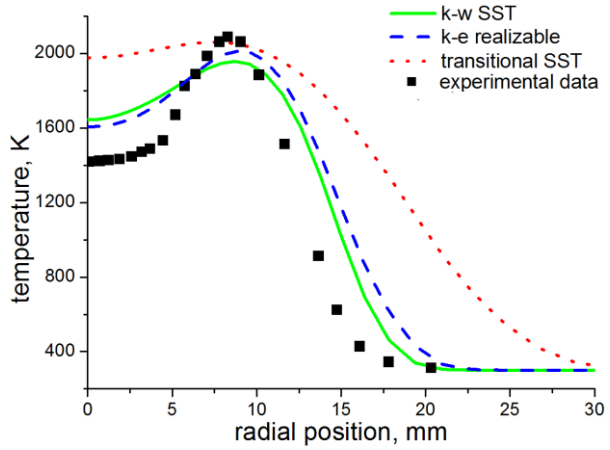

(b)

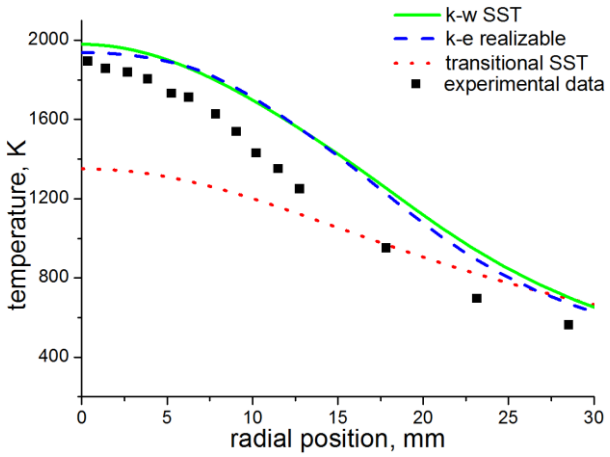

(c)

Figure 4-5 Radial predictions of the temperature at (a) $x/d_i = 9$, (b) $x/ d_i = 60$, and (c) $x\ d_i = 170$ for a methane-air jet diffusion flame at Re = 4221.

The predictions of the temperature as a function of the radial position are shown in Figures 4-5 (a) – (c) for the three selected axial locations (near nozzle, mid-flame and near tip). The predictions from the three turbulence closure models namely the $k-\varepsilon$ realizable, $k-\omega$ SST and the transitional SST have been compared with the experimental data. Lawal (2011) demonstrated the superiority of the $k-\varepsilon$ realizable version over the standard and RNG versions of the $k-\varepsilon$ models in the prediction of the turbulent flames in an earlier work. This model has therefore been selected for comparison with the SST turbulence models. The results presented in Figure 4-5 shows that both the $k-\omega$ SST and the $k-\varepsilon$ realizable turbulence closure models performed well in predicting the radial trend of the temperature at the selected axial locations. The off-axis peak temperatures observed at r = 3 mm and 10 mm in Figure 4-5 (a) and (c) have been matched by the predictions from both models. The prediction from the $k-\varepsilon$ realizable model was particularly very good at the near nozzle location of $x/d_i = 9$, where the model produced an almost perfect fit to the experimental data. The prediction from the $k-\omega$ SST model was also good at this location, except at the flame centreline where the temperature was under-predicted by about 20 %. The spreading rate of the flame was also less accurate between 3 mm < r < 6 mm for the $k-\omega$ SST model. The transitional SST on the other hand has performed poorly at this location and also displays an unsatisfactory trend in terms of the prediction of the spreading rates. Further downstream of the flame at 105 mm ($x/d_i = 60$) above the burner nozzle, the $k-\varepsilon$ realizable version predicts the peak temperature at the off-axis position of *r* = 7.5 mm well. However, the centreline temperature at this location, as well as the spreading rate is not well predicted. A similar behaviour is observed with the $k-\omega$ SST model. Near the flame tip in Figure 4-5 (c), both the $k-\varepsilon$ realizable and $k-\omega$ SST models give near-accurate prediction of the centreline flame temperature, although the spreading rate was poorly predicted. The worsening trend in the prediction of the temperature as one moves downstream of the flame can be attributed to the increase in the turbulence which leads to higher fluctuations in the temperature as one moves downstream of the flame.

4.4.2 Species prediction for oxygen-enriched methane flame

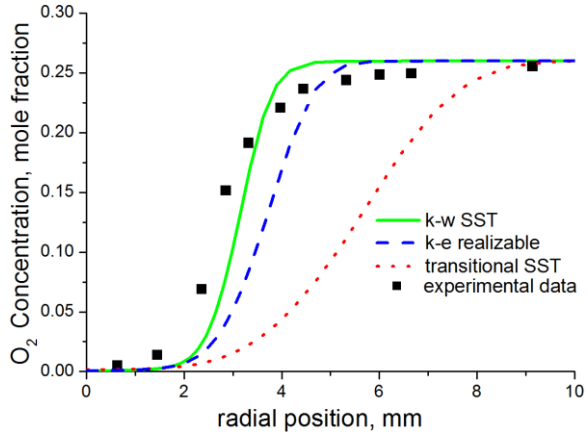

(a)

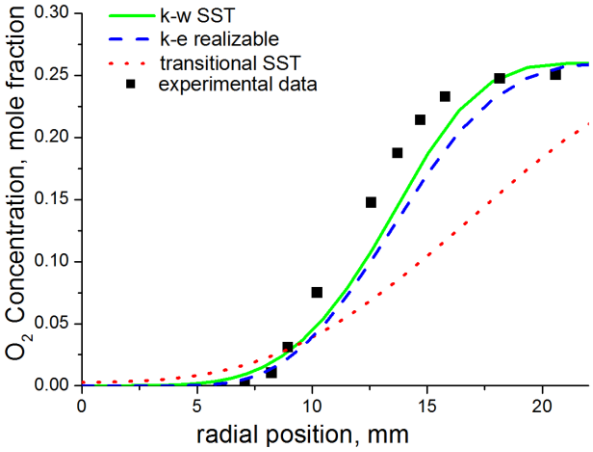

(b)

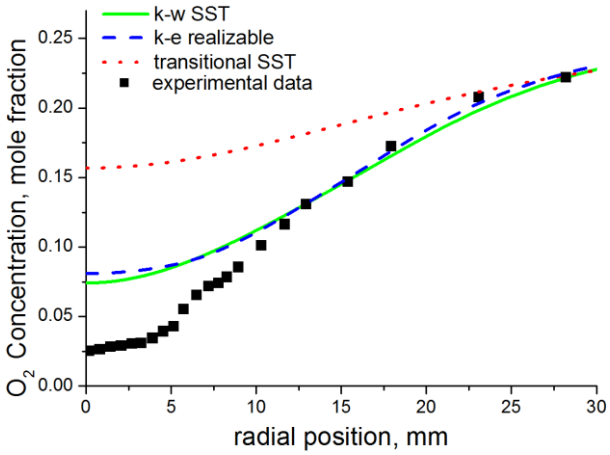

(c)

Figure 4-6 Radial predictions of the oxygen concentration at (a) x/d_i = 9, (b) x/d_i = 60, and (c) x/d_i = 170 for a methane-air jet diffusion flame at Re = 5700.

The predictions of the oxygen concentration distribution as a function of the radial position are shown in Figures 4-6 (a) – (c) for the selected axial locations. Once again, the superior performance of the $k-\omega$ SST and $k-\varepsilon$ realizable models over the transitional SST model is clearly observed. The oxygen concentration is observed to decrease from 26 % in the free stream to zero inside the flame, as expected (Figure 4-6 (a) and (b)). The oxygen concentration in the free stream is higher than the ambient value of 21 % at these axial locations because the shroud air was enriched to 26 % oxygen as described in the experimental work of Lee Howard (1999), and this has been correctly predicted by the models. Further downstream at x/d_i = 170, the value of the oxygen concentration in the free stream drops to 21 % due to the dilution with the ambient air. However, oxygen begins to appear at the flame centreline at this downstream location due to the entrainments of air into the flame further downstream of the pipe, and the value of the oxygen concentration at the flame centreline is seen to rise from zero at x/d_i = 9 to to 2.5 % at x/d_i = 170. This increase in the centreline concentration of oxygen at this downstream location has also been predicted by the models, however there was an over-prediction of this experimental value of 2.5 % by all the models, and especially the transitional SST (Figure 4-6 (c)). The $k-\omega$ SST model shows a slightly better performance than the $k-\varepsilon$ realizable model at x/d_i = 9, especially for 0 < r < 5 mm (Figure 4-6 (a)), however the predictions of the temperature were better with the $k-\varepsilon$ realizable model at this location as discussed earlier. At x/d_i = 60 (Figure 4-6 (b)), both models show a similar performance by showing a good trend with the experimental data, although there was a slight over-prediction between 10 mm < r < 15 mm. The positions of ambient oxygen concentrations at x/d_i = 9, 60 and 170 are observed to start from r = 7, 17 and 27 mm respectively, showing that the flame expands downstream of the pipe, and this behaviour has also been captured by the $k-\omega$ SST and the $k-\varepsilon$ realizable turbulence models. The transitional SST model on the hand failed to correctly predict the trend of oxygen at all the measurement locations, by showing a very large spreading rate at these locations. However the prediction of the transitional SST was a better at x/d_i = 60, compared to the predictions at the other two locations.

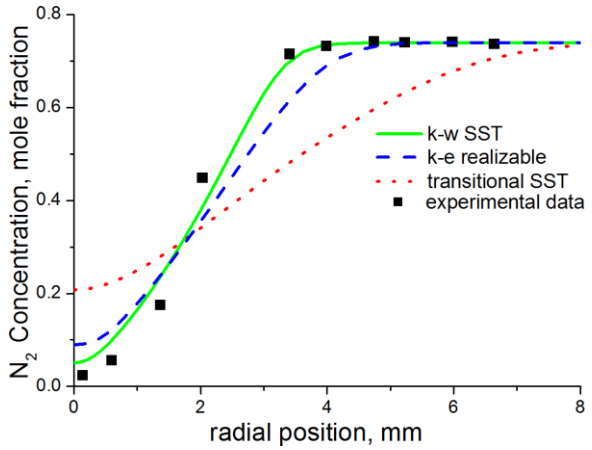

(a)

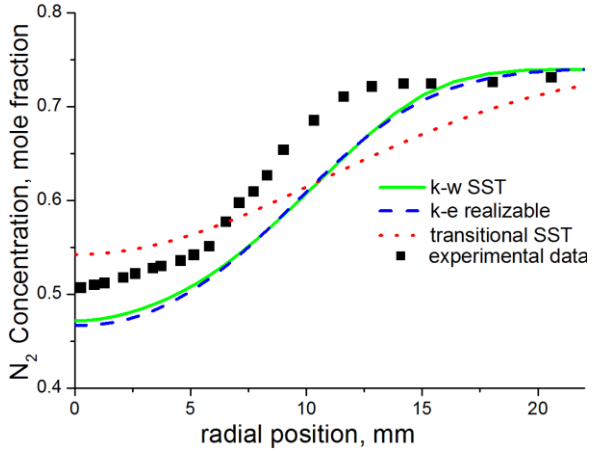

(b)

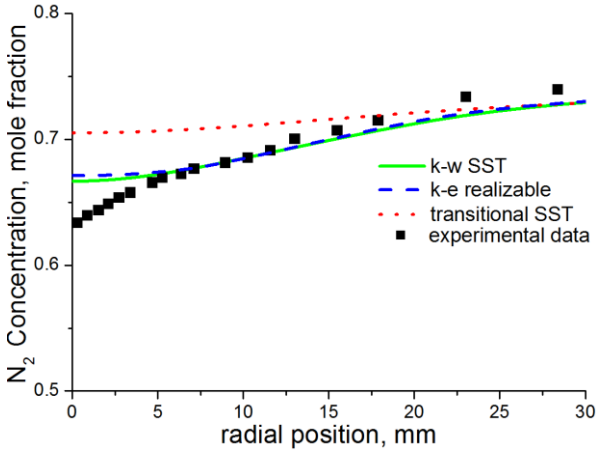

(c)

Figure 4-7 Radial predictions of the nitrogen concentration at (a) x/d_i = 9, (b) x/d_i = 60, and (c) x/d_i = 170 for a methane-air jet diffusion flame at Re = 4221.

The predictions of the nitrogen concentration distribution as a function of the radial position are shown in Figures 4-7 (a) – (c) for the selected axial locations. It can be observed that the predictions of nitrogen are much better than the predictions of oxygen at all the selected measurement locations for all the turbulence models. This can be attributed to the highly stable nature of the nitrogen molecule as a result of the presence of a triple bond. This makes the nitrogen molecule very unreactive, except at very high temperatures, which in turn makes its concentration to be relatively higher in the flame leading to more accurate predictions. Figure 4.7 (a) shows that the concentration of nitrogen increases from zero in the flame centreline to its normal value of 78 % in the free stream, and the $k-\omega$ SST model has produced an almost perfect fit to this experimental trend at this axial location in the flame. The centreline concentration of nitrogen is seen to increase very rapidly downstream of the flame (to 50 % at x/d_i = 60, and then to 65 % at x/d_i = 170) due to the entrainment of air. However, both the $k-\omega$ SST and the $k-\varepsilon$ realizable models slightly under-predicted the centreline concentration at x/d_i = 60 by 4 %, while the centreline concentration at x/d_i = 170 was over-predicted by 3 %. The ambient concentration of nitrogen is observed to be a little lower at x/d_i = 60, and 170 (about 75 %) and this may also be due to the increased reactions of nitrogen at these axial locations. Furthermore, it can be seen that the mid-flame prediction of nitrogen (Figure 4-7 (b)) is less accurate than the predictions at the near nozzle region and further downstream (Figure 4-7 (a) and (c)) and this is because more of the nitrogen is converted to nitrogen oxide at the mid-flame region since the flame temperature is higher in this region of the flame. This causes a reduction in the concentration of nitrogen in this region of the flame which leads to more difficult predictions. Although the prediction with the $k-\omega$ SST model is a little better than the prediction with the $k-\varepsilon$ realizable model at x/d_i = 9, there is no visible difference in the predictions between the two models further downstream of the flame at x/d_i = 60 and 170 (Figure 4-7(b) and (c) respectively). The predictions using the transitional SST model also showed improved results in comparison with the predictions of the oxygen concentration at all the measurement locations, especially at x/d_i = 170.

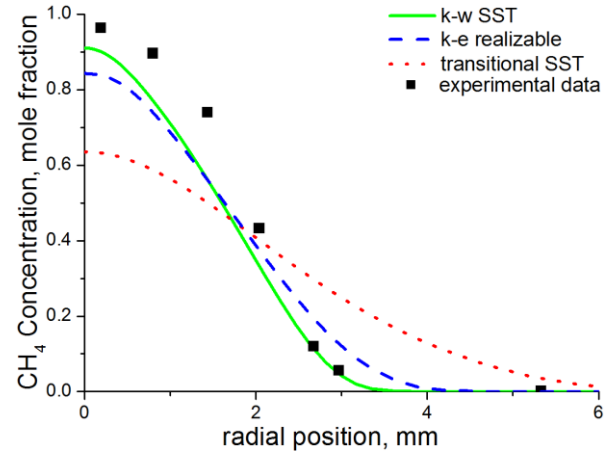

(a)

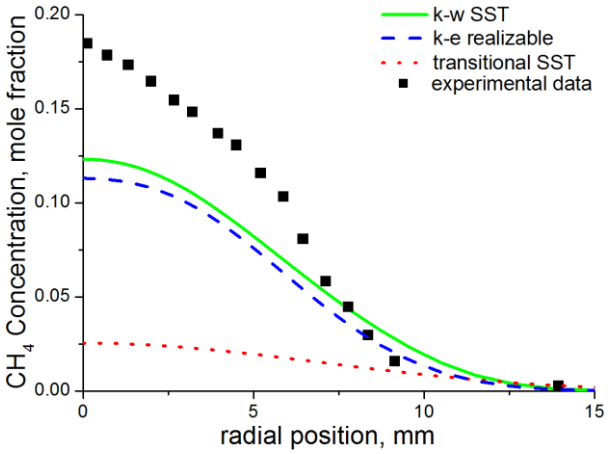

(b)

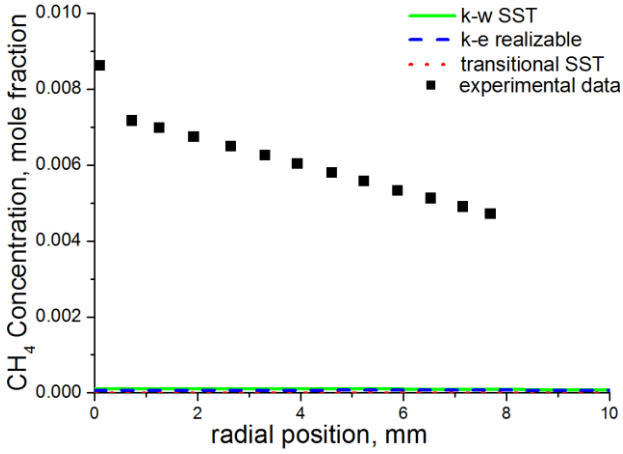

(c)

Figure 4-8 Radial predictions of the methane concentration at (a) x/d_i = 9, (b) x/d_i = 60, and (c) x/d_i = 170 for a methane-air jet diffusion flame at Re = 4221.

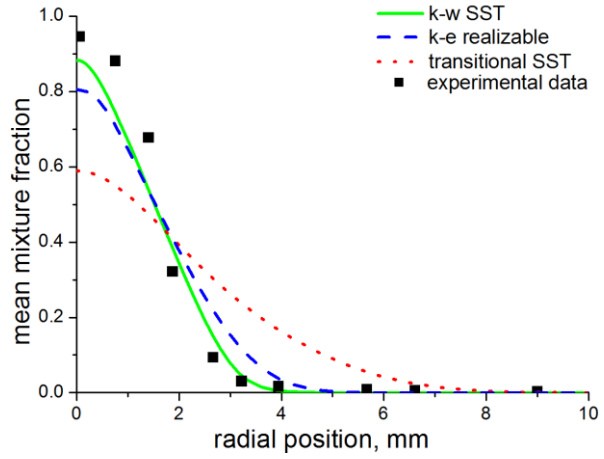

(a)

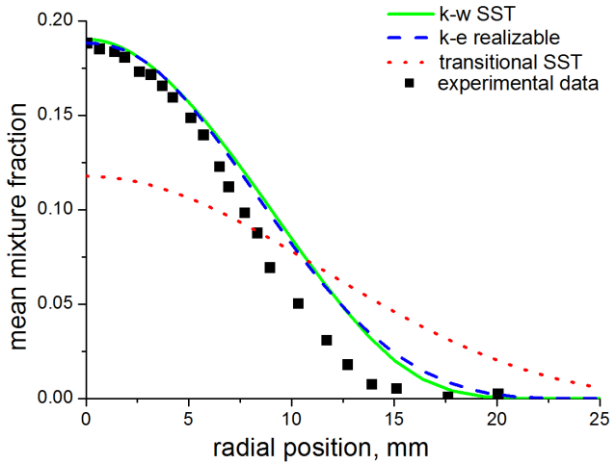

(b)

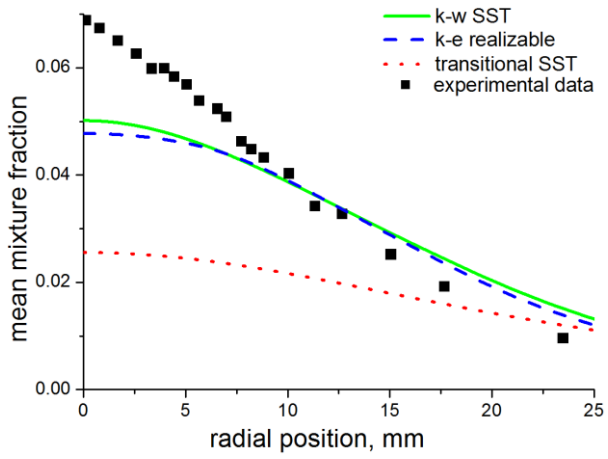

(c)

Figure 4-9 Radial predictions of the mean mixture fraction at (a) x/d_i = 9, (b) x/d_i = 60, and (c) x/d_i = 170 for a methane-air jet diffusion flame at Re = 4221.

The predictions of the methane concentration distribution as a function of the radial position are shown in Figure 4-8 (a) – (c) for the selected axial locations. The concentration of methane decreases from its peak value at the flame centreline to zero at the flame edge, and this trend has been captured by the models. The prediction at the near nozzle location (x/d_i = 9) is very good for the $k-\omega$ SST and $k-\varepsilon$ realizable models where the models under-predict the centreline concentration of methane by only 10 % and 12 %, respectively. This improved prediction at the near nozzle is due to the high concentration of methane at this location. Further downstream at x/d_i = 60 (Figure 4-8 (b)), the methane concentration decreases as the combustion intensifies and this leads to a deterioration in the predictions from the $k-\omega$ SST and $k-\varepsilon$ realizable models. Downstream of the flame at x/d_i = 170, the fuel is almost completely burnt out (mole fraction = 0.0085) which leads to a prediction of the non-existent methane concentration at this location because the models are unable to capture such low concentrations of methane in this region of the flame. Predictions with the transitional SST model are again much worse than that of the $k-\omega$ SST and the $k-\varepsilon$ realizable models and this is seen at x/d_i = 9, where the transitional SST model under-predicted the centreline concentration of methane at this location by 35 %. The predictions of the mean mixture fraction as a function of the radial position are shown in Figure 4-9 (a) – (c) for the selected axial locations. The mixture fraction is a local measure of the equivalence ratio and it was originally developed as a mathematical concept that is useful in the modelling of diffusion flames. It represents the mass fraction that originated from the fuel stream, in order words, it is the local mass fraction of burnt and unburnt fuel stream elements (C, H, etc.) in all the species (CO, H, O, etc.). Comparing the plots of methane and the mixture fraction at the corresponding axial locations shows that the mixture fraction mirrors the concentration of the fuel in the burnt and unburnt mixture. The $k-\omega$ SST and $k-\varepsilon$ realisable models give good predictions of the mixture fraction at x/d_i = 9 and 60. Plots of the temperature and the species in mixture fraction space is useful in obtaining information about the stoichiometric flame conditions as well as the fuel lean and the fuel rich regions of the flame.

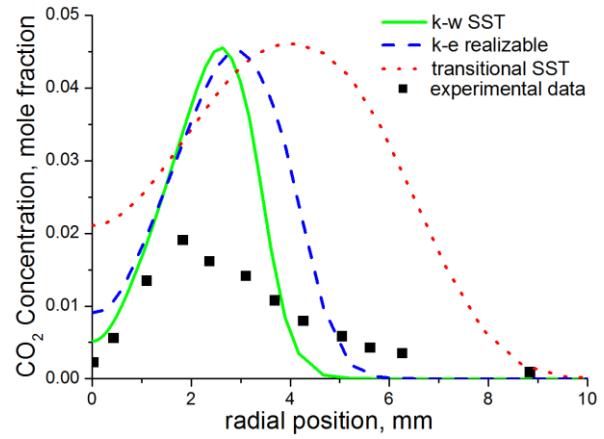

(a)

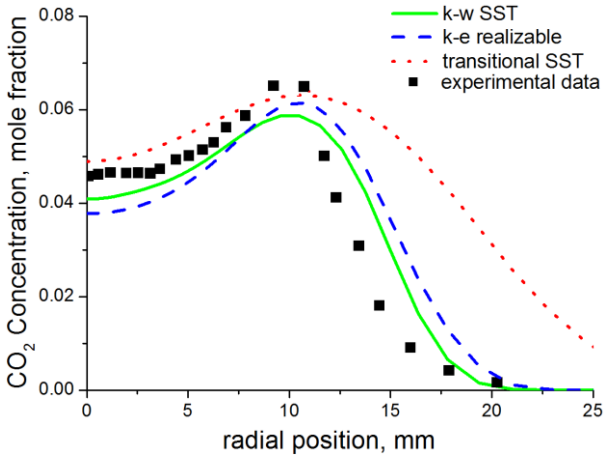

(b)

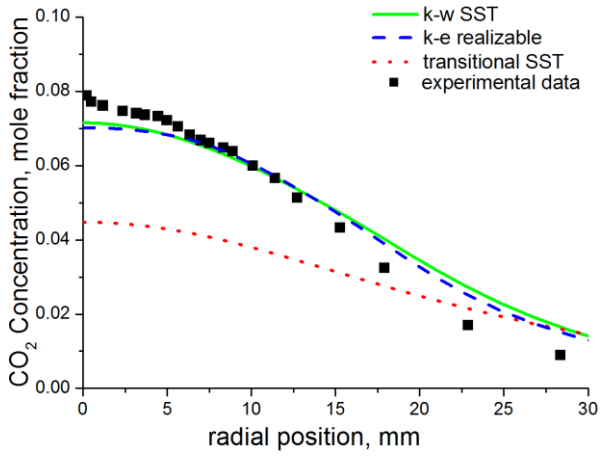

(c)

Figure 4-10 Radial predictions of the carbon dioxide concentration at (a) x/d_i = 9, (b) x/d_i = 60, and (c) x/d_i = 170 for a methane-air jet diffusion flame at Re = 4221.

The predictions of the carbon dioxide concentration distribution as a function of the radial position are shown in Figure 4-10 (a) – (c) for the selected axial locations. The trend in the experimental data has been well predicted by the $k-\omega$ SST and $k-\varepsilon$ realizable models at all the measurement locations. It can be observed that the centreline concentration of carbon dioxide is very low at the near nozzle location of $x/d_i = 9$, since the fuel concentration is still high at this location and this has been correctly predicted by the $k-\omega$ SST model. However, the $k-\varepsilon$ realizable model over-predicted the carbon dioxide centreline concentration at this location by about 20 %. Furthermore, the off- axis peak observed at r = 2 mm was correctly predicted by both models, although there was a large over-prediction. Further downstream of the flame at $x/d_i = 60$, the centreline concentration of carbon dioxide increases dramatically and all the three models made very good predictions at this location. The off-axis peak (r = 10 mm) was also well predicted by the models, however the transitional SST model produced a large spread in the data between 10 mm < r < 25 mm. The predictions were very good for the $k-\omega$ SST and the $k-\varepsilon$ realizable models at $x/d_i = 170$ (Figure 4-10 (c)), where both models produced a very good fit to the experimental data. However, the transitional SST model under-predicted the centreline concentration by over 50 % at this location. The general observation that can be made by comparing the predictions at the three axial locations is that the predictions improve downstream of the flame, i.e. the predictions at $x/d_i = 170$ are better than the predictions at $x/d_i = 9$. This is in contrast to what was observed with the oxygen, nitrogen and methane predictions (which are all reactants), which were better upstream of the flame. This reversal in the prediction accuracy in the case of carbon dioxide can be explained on the basis that carbon dioxide, being a product species will tend to increase in concentrations at the upper section of the mid-flame location where the temperatures are higher and the reactions are faster rather than in the lower section where the temperatures are lower. Furthermore, as the carbon monoxide produced in the flame rises, it becomes oxidized to carbon dioxide. This increased concentration of carbon dioxide at the downstream region will thus, tend to improve predictions at this location.

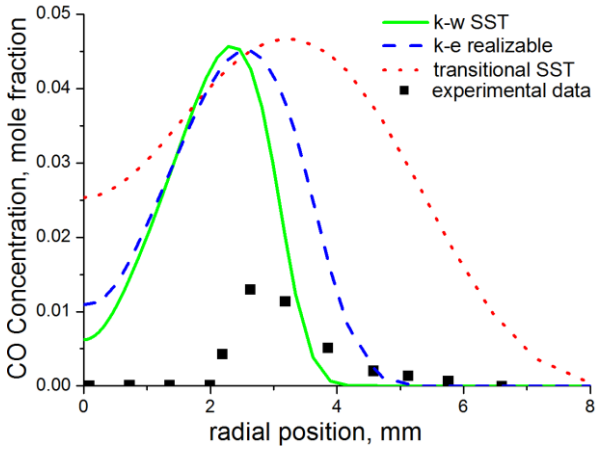

(a)

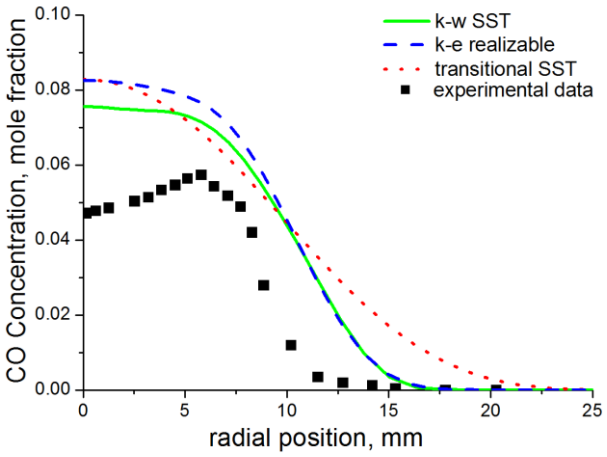

(b)

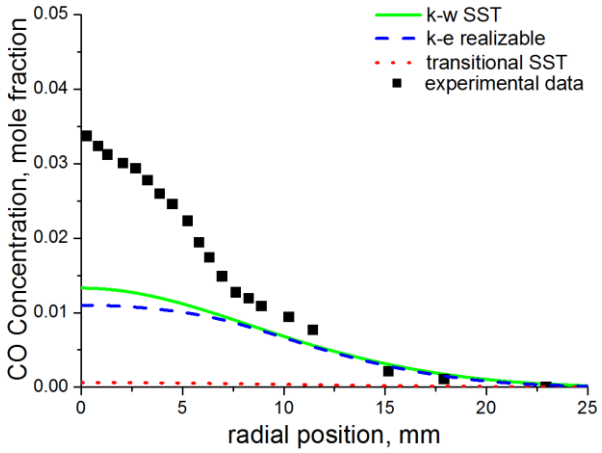

(c)

Figure 4-11 Radial predictions of the carbon monoxide concentration at (a) x/d_i = 9, (b) x/d_i = 60, and (c) x/d_i = 170 for a methane-air jet diffusion flame at Re = 4221.

The predictions of the carbon monoxide concentration distribution as a function of the radial position is shown in Figure 4-11 (a) – (c) for the selected axial locations. The results show that carbon monoxide is poorly predicted at all the measurement locations. The experimental data shows that carbon monoxide does not form at the centreline in the flame at $x/d_i = 9$, but only begins to form at about r = 2.5 mm from the flame centreline. However, the models predicted the presence of carbon monoxide at the flame centreline. Furthermore, there was a large over-prediction of the carbon monoxide concentration by all the models at this location. The predictions improved at $x/d_i = 60$, however there was still a large over-prediction of the carbon monoxide especially between $0 < r < 7$ mm (Figure 4-11 (b)). The experimental data shows that the centreline concentration of carbon monoxide decreased from 0.05 % at $x/d_i = 60$ to 0.035 % at $x/d_i = 170$, and this is expected given that carbon monoxide is readily oxidized to carbon dioxide in the flame which tends to rapidly reduce its concentration at the downstream region of the flame. This decrease in the carbon monoxide concentration downstream of the flame is also predicted by the models. The predictions of the nitrogen oxide concentration distribution as a function of the radial position are shown in Figure 4-12 (a) – (c) for the selected axial locations. The concentrations of nitrogen oxide in the flame are extremely small (in ppm), thus making the predictions of nitrogen oxide a difficult undertaking for mathematical models. These small concentrations arise from the unreactive nature of the nitrogen molecule due to its strong triple bond which requires extremely high temperatures for bond dissociation. The flamelet models are based on a transport equation for the nitrogen oxide convection, diffusion and production, as shown in equation (3.77) and implemented in the Fluent code. However the flamelet equation does not account for the kinetic effects of slow forming species such as nitrogen oxide, thus making the model inadequate for nitrogen oxide predictions. This explains the poor predictions of the nitrogen oxide concentration at all the axial locations investigated. In view of this, the pollutant model has also been investigated.

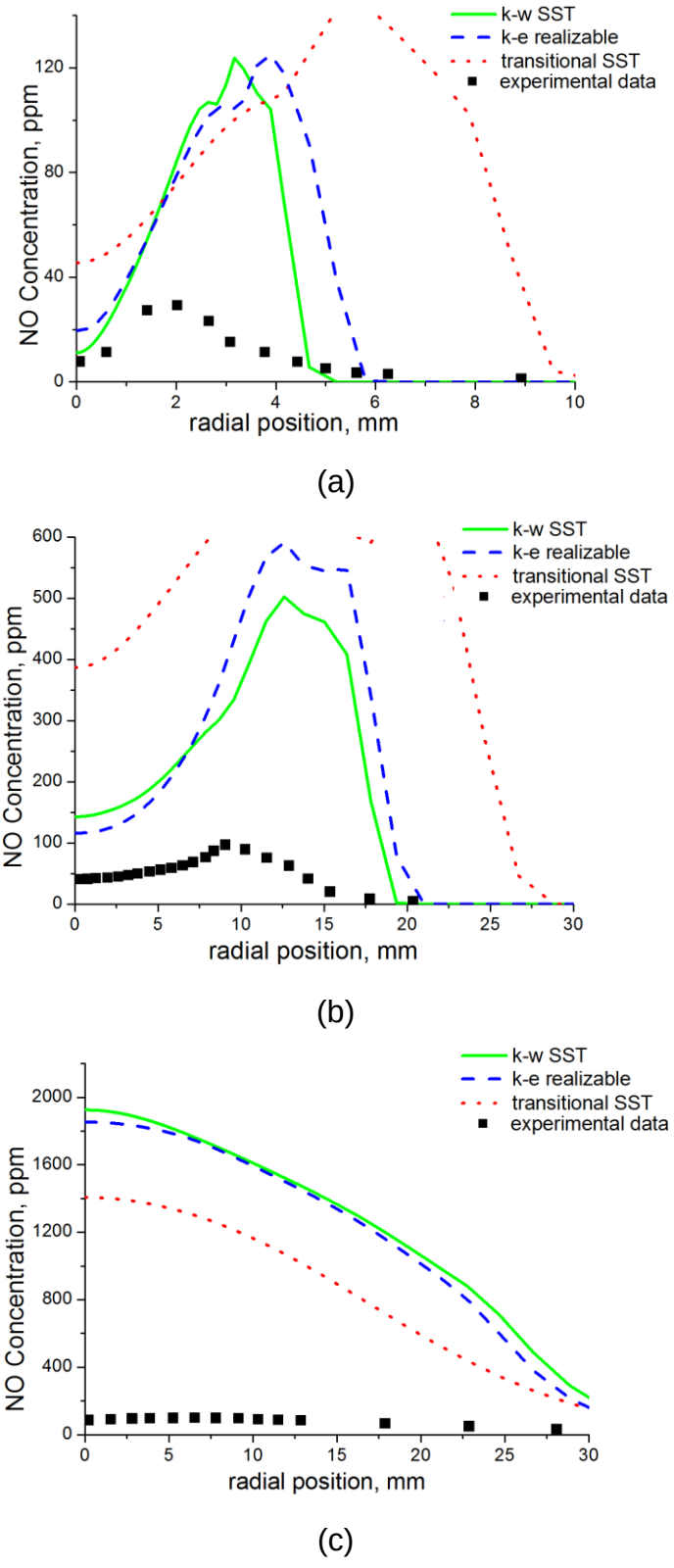

Figure 4-12 Radial predictions of the nitrogen oxide concentration at (a) x/d_i = 9, (b) x/d_i = 60, and (c) x/d_i = 170 for a methane-air jet diffusion flame at Re = 4221.

4.4.3 Comparison of the pollutant and flamelet models

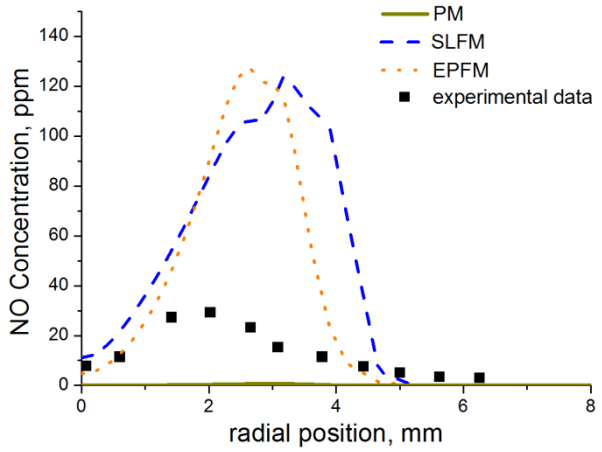

(a)

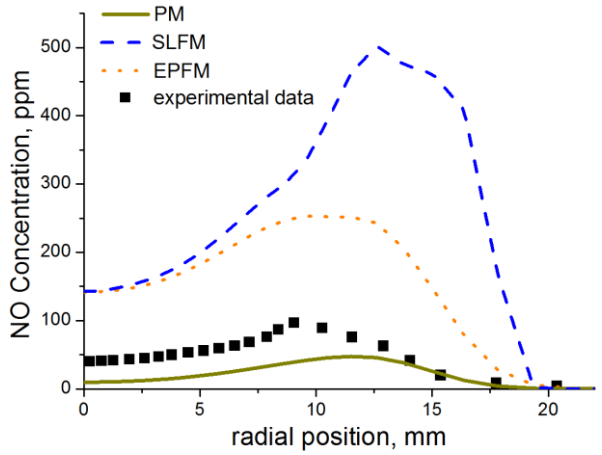

(b)

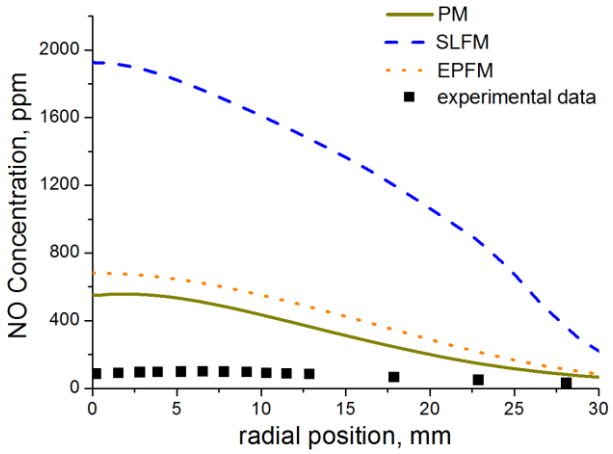

(c)

Figure 4-13 Radial predictions of the nitrogen oxide concentration at (a) x/d_i = 9, (b) x/d_i = 60, and (c) x/d_i = 170 for a methane-air jet diffusion flame at Re = 4221.

The importance of nitrogen oxide as an environmental pollutant, as well as the difficulty involved in its prediction requires more accurate mathematical models. Predictions of nitrogen oxide as a function of the radial position are shown in Figure 4-13 (a) – (c) for the selected axial locations using the stationary laminar flamelet model (Peters, 1984), the Eulerian particle flamelet model (Barths et al., 1998) and the pollutant model (Hughes et al., 2001) in an effort to compare their performances. The $k-\omega$ SST turbulence closure model has been used as a basis for the comparison, and similar results were also obtained with the $k-\varepsilon$ realisable turbulence model. The EPFM tracks sample fluid particles identified with unsteady flamelets within the flow field, thereby accounting for the spatial evolution of the flamelet profile. This requires a converged case of a SLFM calculation which retains the predicted field of the mixture fraction and its variance as well as the scalar dissipation rate. The predicted fields are then used to obtain an improved prediction of the average temperature and the average species mass fractions through the solution of the unsteady particle marker flamelet equations. The unsteady flamelet equations are solved in tandem with a transport equation for the probability of finding a fluid particle at a given location and at a given time in the flow domain. The pollutant model (PM) on the other hand uses the well-known Zeldovich (1947) and Fenimore (1971) mechanisms to model the thermal NO and the prompt NO, respectively. Partial equilibrium was assumed for the reactions involving OH while equilibrium reaction was assumed between O and O_2. Experiments have shown that at high temperatures (T > 1800 K, P = 1 atm), the reaction rates of forward and backward reactions are so fast that one obtains a partial equilibria for the reactions involving OH. However, the partial equilibrium assumption provides satisfactory results only at sufficiently high temperatures, therefore at temperatures below approximately 1600 K, partial equilibrium may not be established because the characteristic time of combustion (given as the ratio of the flame thickness and the mean gas velocity) will be faster than the reaction time. Since nitrogen oxide is a slow forming species, the pollutant model calculations for nitrogen oxide are performed after the main calculations have converged. The equations for the

flamelet, radiation and energy are deactivated in the solver and the pollutant calculation is performed until convergence is achieved. The impact of the temperature on the performance of the pollutant model can be seen from Figure 4-13 (a) where we see that the model could not detect the presence of nitrogen oxide at the near nozzle location (x/d_i = 9) due to the low temperature in this region of the flame. However, as we move downstream of the flame towards the mid-flame region (at x/d_i = 60) where the temperature is higher, the pollutant model begins to register the presence of nitrogen oxide. The prediction from the NO-Pollutant model is clearly better than the predictions from the SLFM and EPFM at this axial location. This improved performance of the pollutant model, in comparison with the flamelet models, can be attributed to the use of a rate expression which accounts for finite rate kinetics in the NO reactions whereas the flamelet models uses a transport equation to model the NO formation and combustion. Furthermore, the EPFM can be seen to perform better than the SLFM at this axial location, although the two models gave a similar performance at x/d_i = 9, where both models over-predicted the concentration of nitrogen oxide to a large extent (Figure 4-13 (c)). Pitsch et al. (1998) reported that the SLFM is incapable of responding to rapid changes in the scalar dissipation rates, consequently the solution of the SLFM inaccurately predicts slow reacting species such as CO and NO. The EPFM on the other hand is able to resolve the effect of the transient history of the scalar dissipation rate and this results in improved predictions as we progress downstream of the flame. Pitsch et al. (1998) have recommended incorporating smaller values of the scalar dissipation rate in the flamelet equation to account for slow reacting species and this approach was adopted in the present calculation. The ranges of the scalar dissipation rates adopted were from 0.0001, which is close to equilibrium condition to 25 s^{-1} with scalar dissipation steps of 2.5 s^{-1}. Figure 4-13 (c) shows that EPFM and the PM perform on an almost equal level, although both models significantly over-predict the concentration of nitrogen oxide. However, in comparison with the the SLFM, the EPFM and the PM show about 70 % improvement at this axial location. The prediction of NO_x still remain a difficult undertaking in

turbulent diffusion flames due the ongoing challenge of resolving the interaction between the turbulence and the the chemistry of nitrogen oxide formation and hence the previous investigations on NO_x formation in turbulent diffusion flames has shown that the flamelet approach still has difficulties in reproducing the experimental NO data (Mahmud et al., 2007).

4.5 Conclusions

In this chapter, the details and results obtained in the numerical investigation of a turbulent methane jet diffusion flame have been presented and discussed and the following conclusions have been reached.

- The $k-\varepsilon$ realizable and $k-\omega$ SST turbulence closure models have been found to perform well in predicting the temperature and species in a turbulent methane jet diffusion flame. The $k-\omega$ SST model performed slightly better than the $k-\varepsilon$ realizable model in predicting the reactant species (oxygen and methane) at the near nozzle region where the concentrations of these species were higher, However the $k-\varepsilon$ realizable version made better predictions for the temperatures and the product species.
- The transitional SST model, which is a four equation model did not perform as good as the $k-\varepsilon$ realizable or $k-\omega$ SST models, which are both two equation models. The model significantly over-predicted the concentration of species and also displayed a large spreading rate in all the predictions.
- A comparison of the SLFM, EPFM and the Pollutant Model was made with respect to their capabilities in predicting the nitrogen oxide in methane flames and the result showed that the Pollutant Model performed better than the flamelet models. This has been attributed to the ability of the Pollutant Model to account for finite rate kinetic effects in slow forming species, such as the oxide of nitrogen. Also, the EPFM was also found to perform better than the SLFM due to the incorporation of smaller scalar dissipation steps in the flamelet equations.

Chapter 5

Experimental and Numerical Investigation of Vertical Methane and Propane Flares

5.1 Background

This chapter is concerned with the experimental and numerical investigations of methane and propane jet diffusion flames. Many studies have been made of methane and natural gas flames but relatively few have been made of propane flames. Thus many generalizations about flare behaviour have been concerned only with methane flames. This investigation is concerned with the difference in behaviour between methane and propane flames when the two flames are compared on the basis of a similar Reynolds number. Flame lengths, lift-off heights, in-flame temperatures, in-flame and post-flame concentrations of species and soot have been predicted and compared with the experimental measurements. The burner used by Lee Howard (1998) has been used for the present work. The mesh generated to simulate the burner has been validated against the experimental data of Lee Howard (1998) in the previous chapter. Modifications were made to the mesh to simulate the propane combustion. The kinetics of the propane reactions were modelled using the CRECK mechanism of Ranzi et al. (2012). The propane combusted was supplied by BOC and classified as commercial grade. Experimental research carried out by other authors (Huang & Yang, 1996; Turns & Lovett, 1989) revealed that commercial grade propane has propane composition of about 90 – 97 %. In view of this, a sensitivity analysis was performed to test the responsiveness of the CRECK mechanism to the ranges of propane compositions in typical commercial grades. Furthermore, flame stability has been investigated by comparing the lift-off behaviour of the methane and the propane flames when the thickness of the fuel pipe nozzle is varied. Flame lift-off is important in gas flares because lifted flames are less stable and thus more susceptible to blow-outs, especially in the presence of a cross-wind.

5.2 Experimental details

- *Measurement of the flame temperature*

The burner was mounted on a three-dimensional (XYZ) traverse grid system, and the origin was centered at the exit plane of the burner tube. The fuel flow rate was measured using a calibrated rotameter, and the average jet velocity u_f was calculated from the fuel flow rate. Radial measurements of the in-flame temperature were taken at three axial flame locations using a Pt-Pt/13-%-Rh thermocouple with a bead diameter of 213 μm. The thermocouple was coated with a thin layer of silica to avoid catalytic reactions on the bead surface. The output of the thermocouple was processed by a computer controlled data acquisition system and the data were later corrected for radiation and convection heat transfer between the thermocouple bead and the surroundings using the method of Kaskan (1957). There are other factors other than the ambient temperature reading or radiation losses that contribute to errors in the temperature readings. These include probe induced perturbations from aerodynamic disturbances in the flow field and conduction losses(Heitor & Moreira, 1993). However, due to the small bead diameter used in this work, these problems have been minimised. The silica coating on the thermocouple bead also helps to minimize errors that may arise from catalytic heating due to the recombination reactions occurring on the thermocouple surface (Peterson et al., 1985).

- *Measurement of the species and soot concentration*

Gas samples were extracted at the post flame region using a quartz probe with a 1 mm tip diameter. The samples withdrawn through the probe were then passed through a heated sample line to a Horiba VS-3000 gas conditioning system and passed into a Horiba VA 3000 chemiluminescent NO_x analyzer and an infrared CO/CO_2 analyzer. The total unburnt hydrocarbons in the post-flame region were determined using a MEXA-1170 HFID flame ionization detector (FID). The gas analyzers were calibrated with certified standard mixtures of 52 ppm, 8.02 %, and 6.25 % of NO, CO and CO_2 in nitrogen, respectively. Zero and span calibrations were performed

before and after each measurement in order to minimize the influence of instrument drift on the measurements. The soot mass in the post flame region was determined gravimetrically using filter papers in a holder. The filter papers were oven-dried and then weighed before and after the soot deposition, with the difference in weight calculated to be approximately equal to the soot deposited. The fuels were combusted on a basis of a similar Reynolds number and several runs were carried out for each fuel. The methane fuel was combusted longer than the propane fuel (40 min versus 20 min) due to the low sooting nature of the methane flame.

- *Measurement of the flame lengths and lift-off heights*

Both the visible flame lengths - defined as the axial distance between the burner exit plane and the tip of the visible flame, and the lift-off heights of the flames – defined as the distance between the nozzle and the base of the lifted flame, were obtained by averaging a video record of the flames over 30 frames using a 12.1 megapixels CMOS camera (Canon PowerShot SX260HS). The burner was a simple pipe of internal diameter d_i of 3. 25 mm, external diameter d_o of 6.2 mm and length 450 mm. The average jet velocity u_f for the methane and propane flames were calculated to be about 27 m/s and 7.6 m/s respectively, while both flames were kept a fixed Reynolds number of about 5700. The flames were shielded from the surrounding disturbances by employing shroud air flowing at a velocity of about 0.3 m/s. The properties of the flames are shown in Table 5-1.

Table 5-1 Flame properties.

Parameter	Methane	Propane
Reynolds Number	5700	5700
Froude Number	21000	1800
Jet Velocity (m/s)	27	7.6
Shroud Velocity (m/s)	0.3	0.3
Visible Flame Length (cm)	51.6 ± 3.5	60.7 ± 4.8
Lift off height (cm)	8.5 ± 1.7	-

5.3 Computational details

- *Mesh independent study*

The computational simulation was achieved on a two-dimensional structured quad mesh generated using the ANSYS-ICEM meshing software. The mesh domain extended 2.3 m ($700d_i$) in the axial direction and 0.55 m ($170d_i$) in the radial direction, where d_i is the internal diameter of the pipe. 520 and 112 mesh nodes where used in the axial and radial directions, respectively, with the origin centered at the burner exit. Fine grid cells were placed near the pipe wall in the order to capture the boundary layer flow. This ensured that the numerical nodes nearest to the inlet pipe wall were at $30<y^+<60$ (Figure 5-2). Further away from wall, relatively coarser grids were used by increasing the mesh size at a growth ratio of 1:1. Furthermore, the mesh distribution option was selected so as to place a finer node distribution at the pipe exit since the combustion begins in this region. Further away at the entraiment region, much coarser grids were employed. The quality of the mesh was checked for the aspect ratio, a_r (ratio of longest to shortest edge of a cell) and the skewness, Sk (a measure of how close the cell is to its ideal shape) of the elements using the ANSYS-ICEM software. The analysis of the mesh quality revealed that 60 % of the mesh elements had an aspect ratio of $0.5 \leq a_r \leq 1$, where cells with a_r = 1 are considered ideal. Also, the skewness of the cells were between $0.95 \leq Sk \leq 1$ where for a quad. element, the skewness is normalized so that 1 is ideal and 0 is the worst possible (ANSYS, 2014). Furthermore, it was ensured that that best elements were concentrated in the pipe outlet region and in the near-burner region where combustion is initiated. Also, a mesh refinement study was conducted to ensure the independence of the solution on the mesh size and density. This entailed comparing the profiles for mesh sizes of 8 E4, 1.6 E5 and 2.2 E5 cells, as shown in Figure 5-1 (a-d). Mesh predictions for the axial and radial components of the velocity in the pipe, as well as the velocity at the pipe exit and the axial trend of the temperature were compared for the three mesh resolutions. All the mesh predictions were shown to be in good agreement.

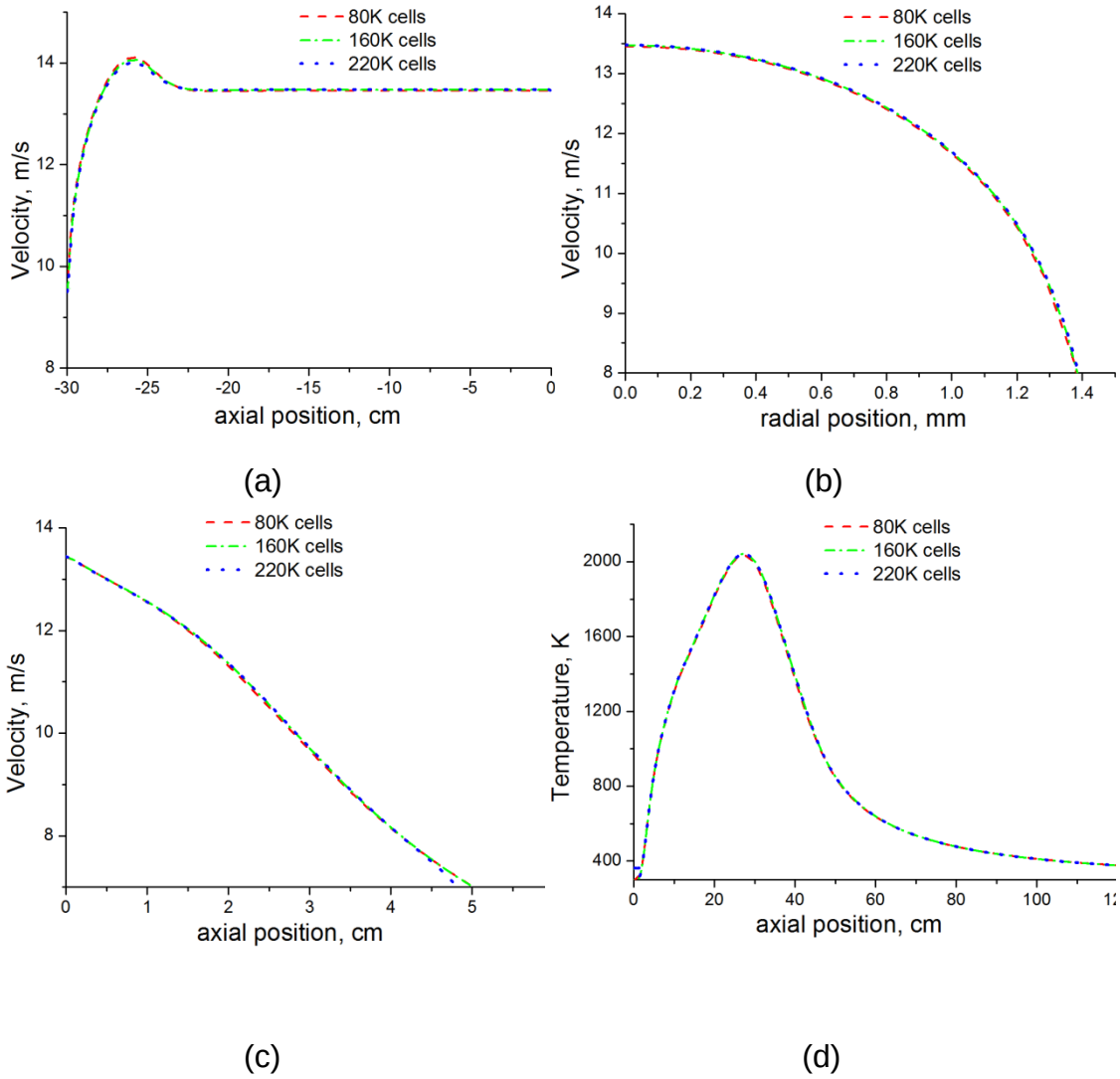

Figure 5-1 Predictions of (a) axial velocity (b) radial velocity (c) velocity at pipe exit (d) axial temperature, for 80,160 and 220K mesh sizes at Re=5700.

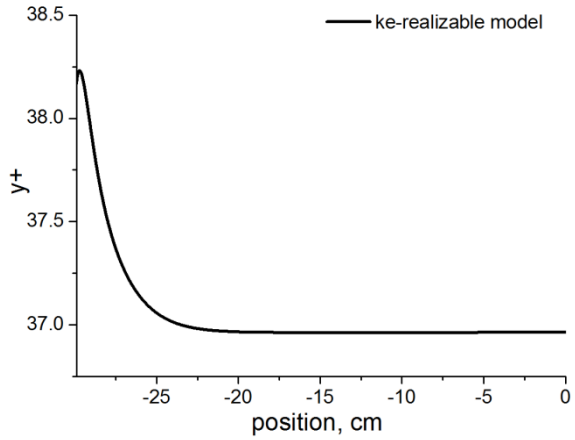

Figure 5-2 Pipe wall y^+ values for $k-\varepsilon$ realizable, at Re = 5700.

- *Boundary conditions*

Axisymmetric condition was implemented in the ANSYS-Fluent solver in view of the symmetry in the geometry. Pressure inlet boundary conditions were employed at the entrainment boundaries, located 0.4m ($120d_i$) and 0.50m ($155d_i$) from the burner exit in the axial and radial directions, respectively. A pressure outlet boundary condition was employed at the outflow, located 1.9 m ($580d_i$) from the burner outlet. 5% turbulence intensity was specified at the velocity inlet and 0.2% backflow turbulence intensity was prescribed at the pressure outlet, while the entrainment boundaries were defined by 2% turbulence intensity. Buoyancy production was activated during the calculation and the numerical solution was accomplished using a finite-volume discretization technique. No adjustments were made to the model constants and all the terms in the flow and combustion equations were discretized using the second-order upwind scheme, while the coupling between the pressure and velocity fields were handled via the SIMPLE (Pantakar, 1980) algorithm. Radiation, which appears as a sink in the energy equation was accounted for using the Discrete Ordinate Model (Fiveland, 1986). In luminous flames such as propane flames, soot is the predominant radiating specie. Gases and soot present quite distinct spectral behaviour given that the spectrum of participating gases can be formed by millions of spectral lines, while in soot the absorption coefficient varies linearly with the wave number. Hence when soot radiation is dominant, the gray gas model (Hottel, 1954) may be employed instead of the sophisticated models that are required in gas-dominant radiation. The flow field was modelled using the RANS equation incorporating the standard $k-\varepsilon$ realizable turbulence closure model. Combustion was modelled via the laminar flamelet approach. The non-premixed combustion model was employed for the propane combustion while the partially premixed combustion model was employed for the methane reaction. The chemical kinetic were modelled using the CRECK reaction mechanism and the GRI 3.0 reaction mechanism for the propane and the methane flames, respectively. Soot in the propane flame was modelled using the Moss-Brookes model (1999).

5.4 Results and discussion

5.4.1 Investigation of the CRECK reaction mechanism

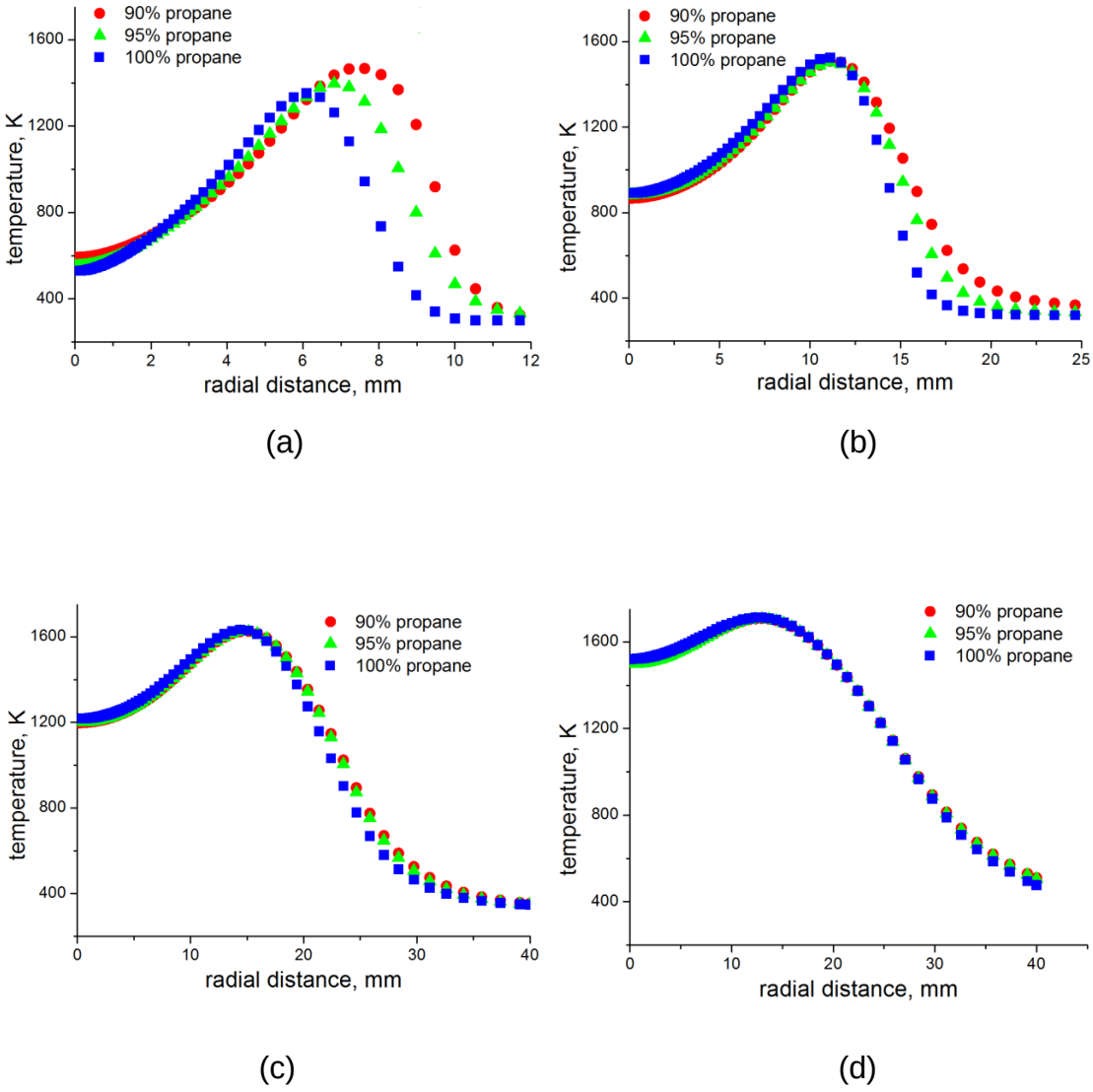

Figure 5-3 Radial predictions of the temperature at (a) x/d_i = 15 (b) x/d_i = 30, (c) x/d_i = 60, and (d) x/d_i = 90 in a propane flame for different composition of propane in the fuel.

Predictions of the temperature as a function of the radial position are shown in Figures 5-3 (a) – (d) for three selected axial locations for different propane concentrations in the fuel. The results show the sensitivity of the CRECK reaction mechanism to the different propane concentrations in commercial

Table 5-2 Composition of the fuels employed.

components	Fuel 1	Fuel 2	Fuel 3
Propane	90 %	95 %	100 %
Ethane	7.5 %	3.5 %	-
Butane	2.5 %	1.5 %	-

grade fuels with 90 % and 95 % propane concentration in comparison with pure propane. The propane fuel used for the experiments was supplied by BOC and denoted as “commercial grade”. Commercial grade propane has been used by several researchers to investigate the properties of propane and most of these researchers have reported 90–95 % propane in the fuel with little contamination with ethane and butane (Huang & Yang, 1996, Turns & Lovett, 1989). The composition of the fuels used to investigate the CRECK reaction mechanism are shown in Table 5-2, while the results of the simulations are presented in Figure 5-3 (a) – (d). From Figure 5-3 (a), it can be seen that there is clearly a difference between the predicted temperatures for the different concentration of propane in the fuels at the near-nozzle location of x/d_i = 15 (50 mm above the burner tip). The difference is most obvious between 6 mm < r < 10 mm, where it can be observed that the fuel with the lowest propane concentration displayed the highest temperature. This implies that fuel contamination with hydrocarbons of lower molecular weight may lead to an over-prediction of the experimental flame temperature measurements. This is also the case at the flame centreline at this axial location, where the fuel with the lowest propane concentration also shows the highest flame temperature. While the difference in the temperatures at the flame centreline are quite small, the off-axis peak temperature difference between the 90 and 100 % propane fuels was about 125 K at this axial location. A similar trend can also be observed at x/d_i = 30 (Figure 5-3 (b)), however the difference in the predicted flame temperatures between the fuels was less significant at this axial location, especially between the fuel with the 90 % propane and the

fuel with the 95 % propane in it. Further downstream of the flame at x/d_i = 60 and 90, the difference between the predicted flame temperatures for the different fuels becomes almost negligible. This is because the fuel concentration decrease downstream of the flame since most of the fuel gets consumed by the flame. Furthermore, the measurements conducted in the present study were for axial locations of 105, 205 and 305 mm above the burner nozzle, corresponding to x/d_i = 32, 64 and 92, respectively. Hence we can safely assume that the variations in the compositions that exists in commercial grade propane will not significantly impact on the predicted results.

The CRECK reaction mechanism is highly detailed containing 113 species and 1901 reactions, and it is designed to handle the high temperature pyrolysis, partial oxidation and combustion of hydrocarbon fuels with up to three carbon atoms (Ranzi et al., 2012). Furthermore, Ranzi et al. (2012) have reviewed several successful applications of the mechanism to the modelling of hydrocarbon and oxygenated fuels such as alkanes, alkynes and alcohols. The mechanism is implemented in the CHEMKIN format and it took about 24 hours (using an 8 GB RAM processor running on 4 cores) to generate a flamelet library consisting of 16 flamelets with 32 grid points in each flamelet. The initial scalar dissipation was set at 0.01 s^{-1} in scalar dissipation steps of 1s. Apart from the turbulence-chemistry interaction, the combustion chemistry presents the most difficult challenge in the modelling of combustion processes. Hence it is important that the mechanism employed must be as detailed as possible, but also involving a possible minimum number of species in order to make the calculations more tractable. A further advantage of the CRECK mechanism is that it is also applicable to hydrocarbon fuel mixtures making it suitable for combustion processes in which commercial grade propane is used as the fuel, as is the case in the present simulation.

5.4.2 Soot and minor species prediction in the propane and methane flames

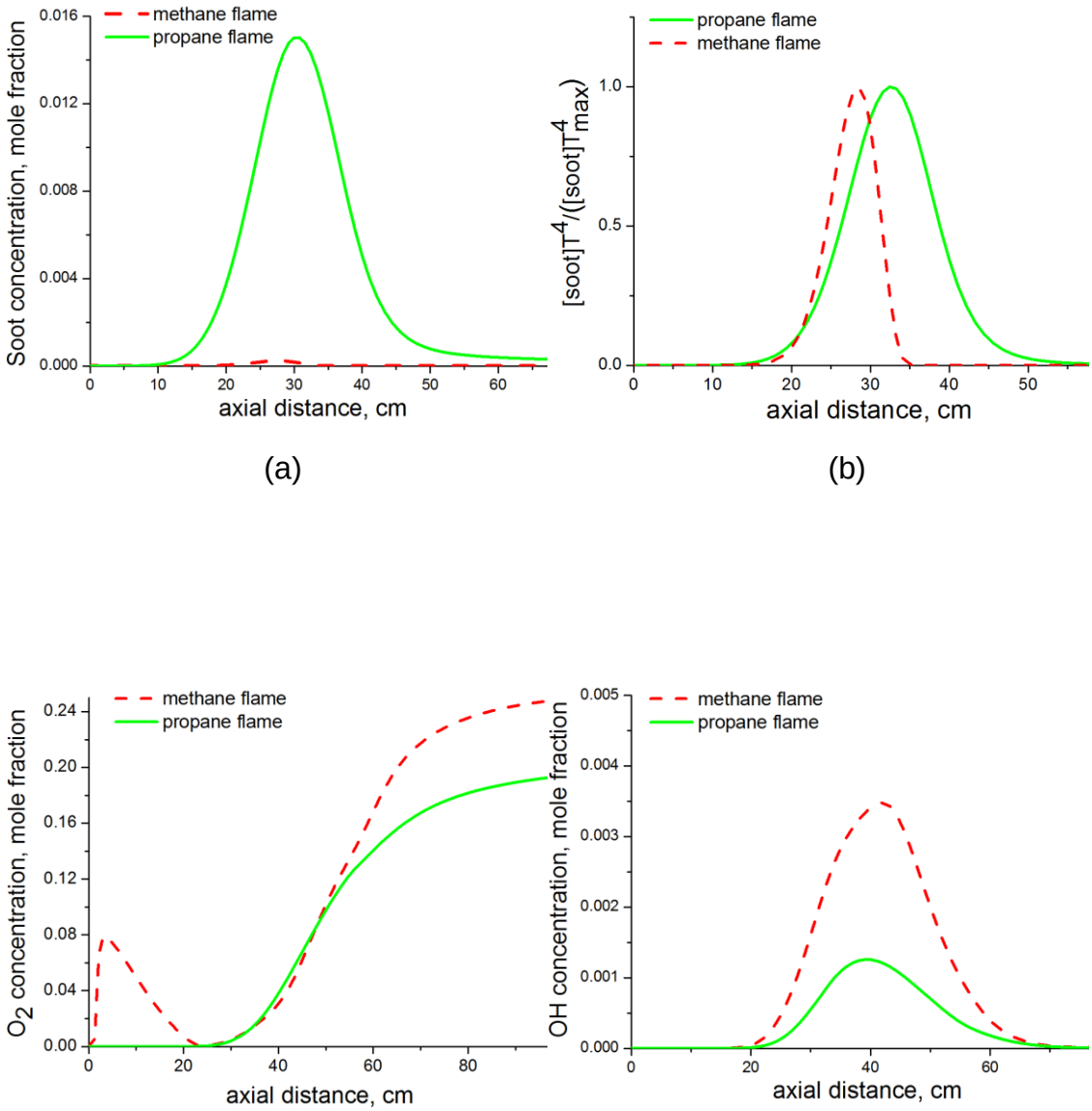

Figure 5-4 Axial predictions of (a) soot concentration, (b) luminosity, (c) oxygen concentration, and (d) hydroxyl radical concentration, for a propane-air and methane-air jet diffusion flame at Re = 5700.

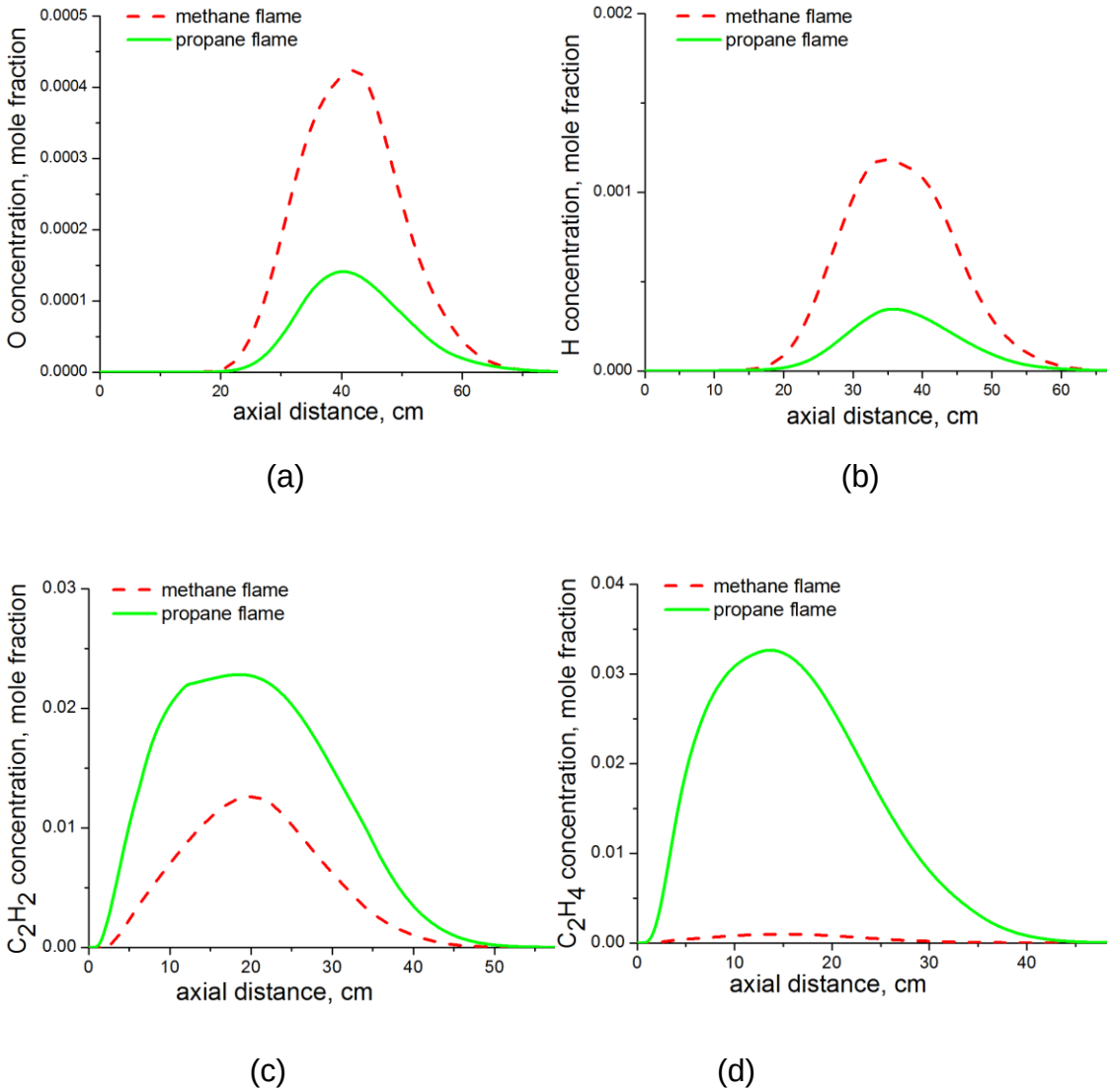

Figure 5-5 Axial predictions of (a) oxygen atom concentration (b) hydrogen atom concentration (c) acetylene concentration, and (d) ethylene concentration, for a propane-air and methane-air jet diffusion flame at Re = 5700.

The Moss-Brookes model (1999) was used to model the soot in the flames. The soot prediction as a function of the axial position is given in Figure 5-4 (a) and gives a good understanding of the difference in the soot concentration between the two buoyancy-dominated flames. It has been shown experimentally that a relatively low concentration of soot is present in lifted methane jet diffusion flames at atmospheric pressure (Brookes & Moss, 1999), and hence the non luminous appearance and higher temperature in these flames (Bandaru & Turns, 2000). Figure 5-4 (a) shows

that the maximum soot production occurs at about the mid-flame region for the propane flame (32 cm) and soot burn-out occurs around the flame tip region (60 cm), and this is in agreement with the work of Santoro et al. (1987). Figure 5-4 (b) shows an estimation of the normalised luminosity from the soot particles based on the relationship:

$$I = \frac{[S]T^4}{([S]T^4)_{max}} \tag{5.1}$$

where I is the soot luminosity, $[S]$ is the soot concentration in mole fraction and T is the flame temperature in Kelvin. The plot shows peak luminosity occurring at the mid-flame region which is at about 26 cm and 32 cm along the flame axis for the methane and propane flames, respectively, and this corresponds to the locations of the maximum soot formation along the flame axis. Figures 5-4 (d) and 5-5 (a) show the predictions of OH radical and oxygen atoms, respectively along the flame axis. According to Puri and Santoro (1994), the contribution of O_2 to the soot oxidation rate is small and the majority of soot oxidation is due to OH reactions in the flames. Fenimore and Jones (1967) also found that the oxygen atom makes an important contribution to the soot oxidation rate. Figures 5-4 (d) and 5-5 (a) show that the peak OH and the peak oxygen atom concentration occurs where the soot concentration begins to decrease steeply and this corresponds to the axial location of 40 cm for the propane flame. Furthermore, Figures 5-4 (d) and 5-5 (a) show lower concentration of OH radicals and oxygen atoms in the propane flame in comparison with the methane flame. This can be attributed to the higher concentration of soot in the propane flame, leading to a higher consumption of the OH and oxygen atoms, thus reducing their concentration in the flame. Figures 5-5 (b) show lower concentration of the hydrogen atom in the propane flame in comparison with the methane flame. This may be due to the higher air entrainment along the length of the propane flame, thus leading to a higher conversion of hydrogen atoms to H_2O or OH and this reduces the hydrogen atom concentration in the flame. In contrast, Figures 5-5 (c) and (d) show higher concentrations of the soot precursors acethylene and ethylene in the propane flame in comparison with the methane flame and this is as expected.

5.4.3 Temperature predictions in the propane and methane flames

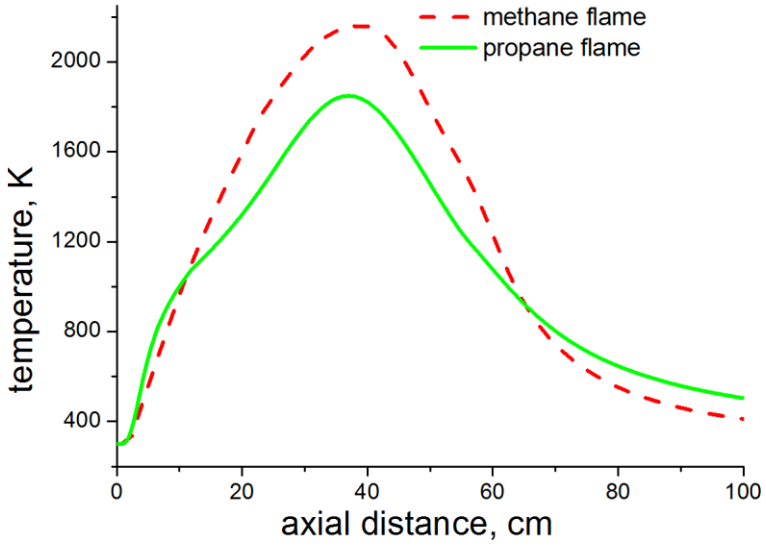

Figure 5-6 Axial predictions of the temperature for a propane-air and methane-air jet diffusion flame at Re = 5700.

The predictions of the temperature as a function of the axial position for the methane and propane flames are shown in Figures 5-6. The plots show that the predicted peak temperature along the flame axis is lower for the propane flame than for the methane flame (by about 18 %). This is due to the higher concentration of soot in the propane flame which results in increased radiation from the flame, thus lowering the flame temperature. Another probable reason for the lower temperature in the propane flame could be the greater air entrainment along the length of the flame (The propane flame is about 16 % longer) as well as the higher turbulence in the flame. The predicted peak temperature along the axis for the methane flame is about 2050 K and this is about a 150 K higher than the experimentally observed peak temperature of 1980 K, which represents an over-prediction of about 7.5 %. The propane flame simulation predicted a peak axial temperature of about 1800 K, which is 10 % higher than the experimentally observed peak temperature of about 1700 K. The methane flame showed higher temperatures all along the flame axis except between 70 cm < a < 100 cm, where the propane flame showed higher temperatures.

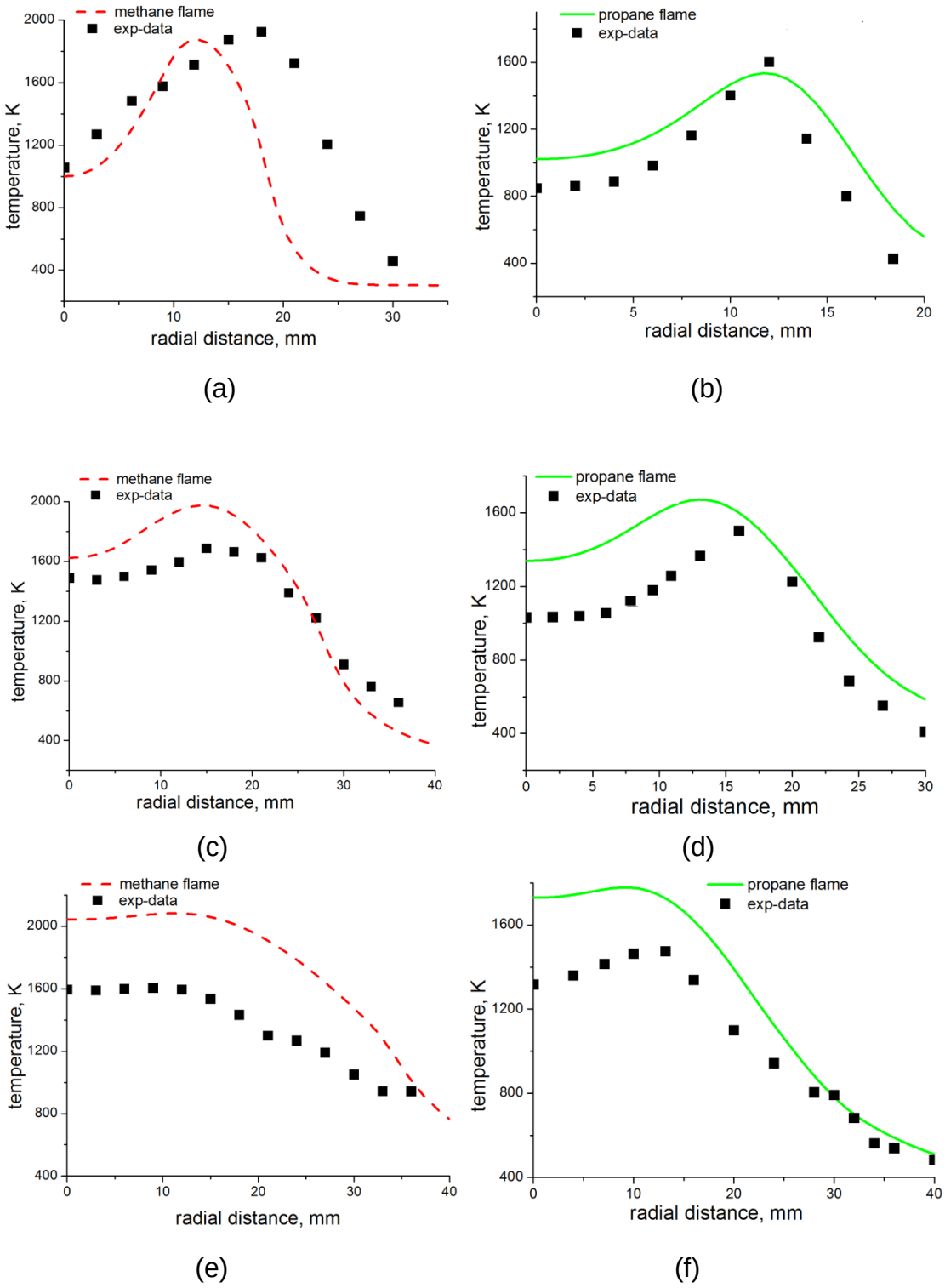

Figure 5-7 Radial predictions and measurements of the temperature at x/d_i = 32 (a,b); x/d_i = 64 (c,d); and x/d_i = 94 (e,f) for a methane-air, and propane-air jet diffusion flame at Re = 5700.

Figures 5-7 (a) – (f) show the prediction of the temperature as a function of the radial position for the methane and propane flames. The predictions are compared with the experimental data and, from the comparison, we see that the temperature predictions are better upstream of the flame, towards the burner nozzle for both flames. The numerical model has been able to predict the trend of the experimental data at all the measurement locations. The mid-flame temperature in the methane flame has been correctly predicted by the model at x/d_i = 32 and 64 (Figure 5-7 (a) and (c)). Furthermore, the off-axis peaks in the temperature that occur at x/d_i = 32 and 64 in both flames have been correctly predicted by the models. An off-axis peak temperature was observed in the propane flame at x/d_i = 94, but not in the methane flame and this has also been predicted by the model. The experimental temperature measurements at the flame axis were higher for the methane flame for all three sets of measurements carried out at 100, 205 and 305 mm above the burner nozzle, corresponding to x/d_i = 32, x/d_i = 64, and 94, respectively. The prediction for the methane flame at 105 mm above the nozzle (Figure 5-7 (a)) show good trend with the experimental measurement. However, the spreading rate in the flame has not been properly captured by the model at this location, probably due to the lifted behaviour exhibited by the flame. In the case of the propane flame, the spreading rate and the off-axis peak temperature prediction at 105 mm above the burner nozzle was better predicted (probably due to the flame being an attached flame), however, the temperature at the flame axis has been over predicted by about 12 %. Further downstream of the flame at 205 mm (at the midflame region) above the burner, there was an over-prediction in the numerical results for $0 < r < 20$ mm, but the results tend to improve for 20 mm $< r <$ 40 mm, for both the methane and the propane flames. At 305 mm above the burner, predictions for both flames begin to degrade rapidly due to the increased flame turbulence downstream of the pipe region. Further measurements were not made downstream of the pipe due to the higher turbulence and flame fluctuations and also due to safety concerns, since the propane flame intruded into the exhaust hood when the burner was adjusted for measurements at the near tip locations.

5.4.4 Major species prediction in the propane and methane flames

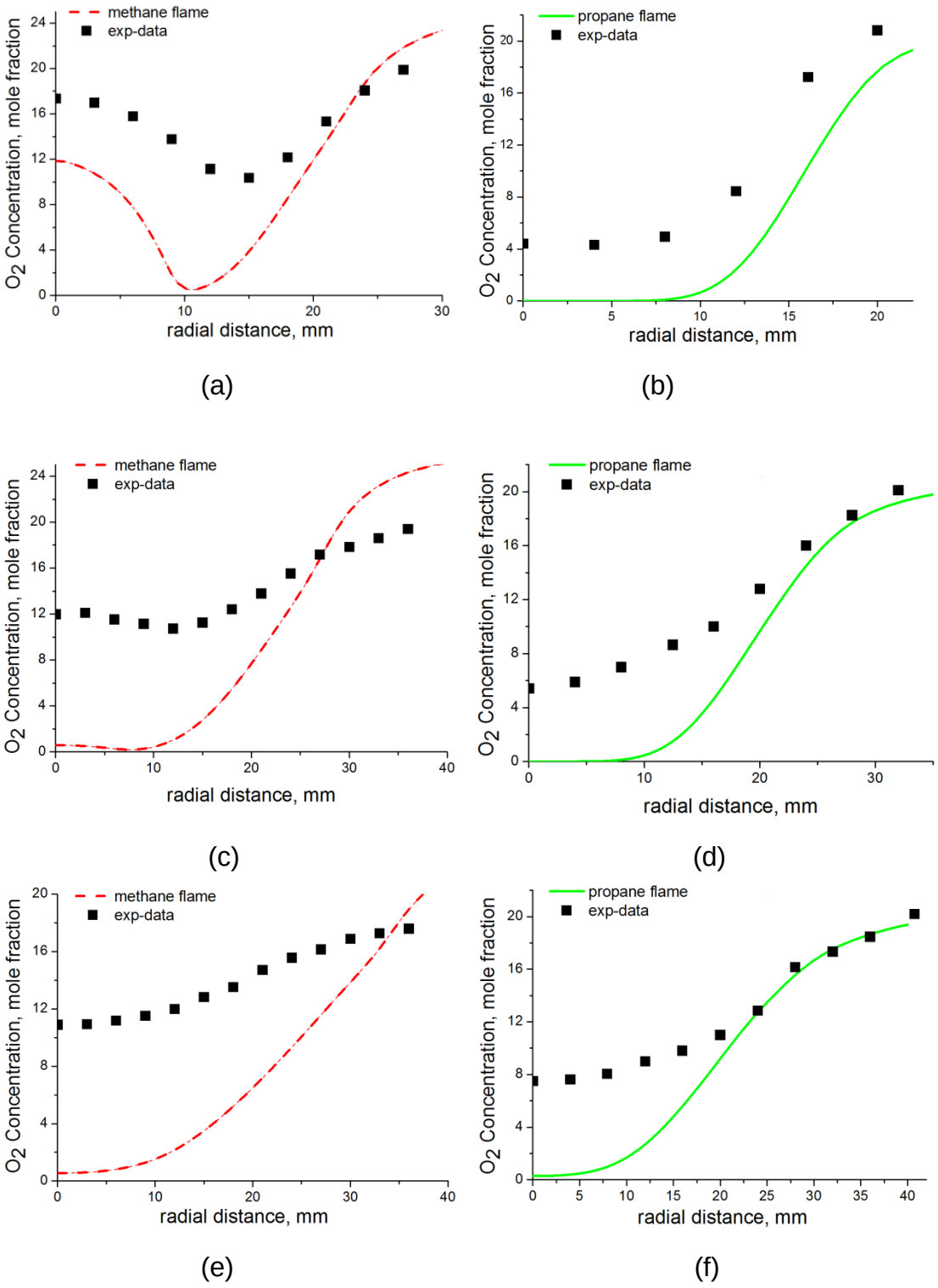

Figure 5-8 Radial predictions and measurements (dry basis) of the oxygen concentration at x/d_i = 32 (a,b); x/d_i = 64 (c, d); and x/d_i = 94 (e,f) for a methane-air, and propane-air jet diffusion flame at Re = 5700.

Figures 5-8 (a) – (f) show the predictions and measurement of the oxygen concentration distribution as a function of the radial position at the three selected axial stations for the methane and propane flames. The measurements have been carried out on a dry basis and the method employed has been described in section 3.2.4. The trend in the experimental data has been correctly predicted by the models, and especially in the case of the propane flame where there is an increase in the concentration distribution of oxygen from the flame centre to its atmospheric value of 21 %. However, the concentration of oxygen at the mid-flame has been wrongly predicted by the models for both the methane and the propane flames. The under-prediction of the oxygen concentration at the flame centreline is especially very pronounced in the case of the methane flame, and this may be due to the lifted nature of the flame as well as the under-prediction of the flame lift-off height by the model. Furthermore, the experimental data for the methane flame shows a v-shaped trend at x/d = 32 (Figure 5-8 (a)), and this is due to the increased air entrainment under the base of the lifted methane flame (see Figure 5-13). This v-shaped trend has been captured by the numerical models, however the trend was poor and this is again attributed to the inability of the numerical models to correctly predict the lift-off height in the methane flame. The propane flame being attached, gave better predictions at all the measurement locations, however there was a large under-prediction of the oxygen concentration between $0 < r < 20$ mm at $x/d_i = 64$ and 94 (Figures 5-8 (a) and (f), respectively. However, the predictions are seen to improve between $20 \text{ mm} < r < 40$ mm for the propane flame. Comparing the experimental results between the methane and propane flames in Figure 5-8 (a), we see that the concentration of oxygen at the flame centreline is about 19 % in the case of the methane flame and about 4 % in the case of the propane flame. This near-ambient concentration of oxygen at flame centreline has already been attributed to the lifted nature of the methane flame. However another contributing factor could be the low soot concentration in methane flames relative to propane flames since the absence of soot in the methane flame would mean no oxygen will be consumed due to soot oxidation.

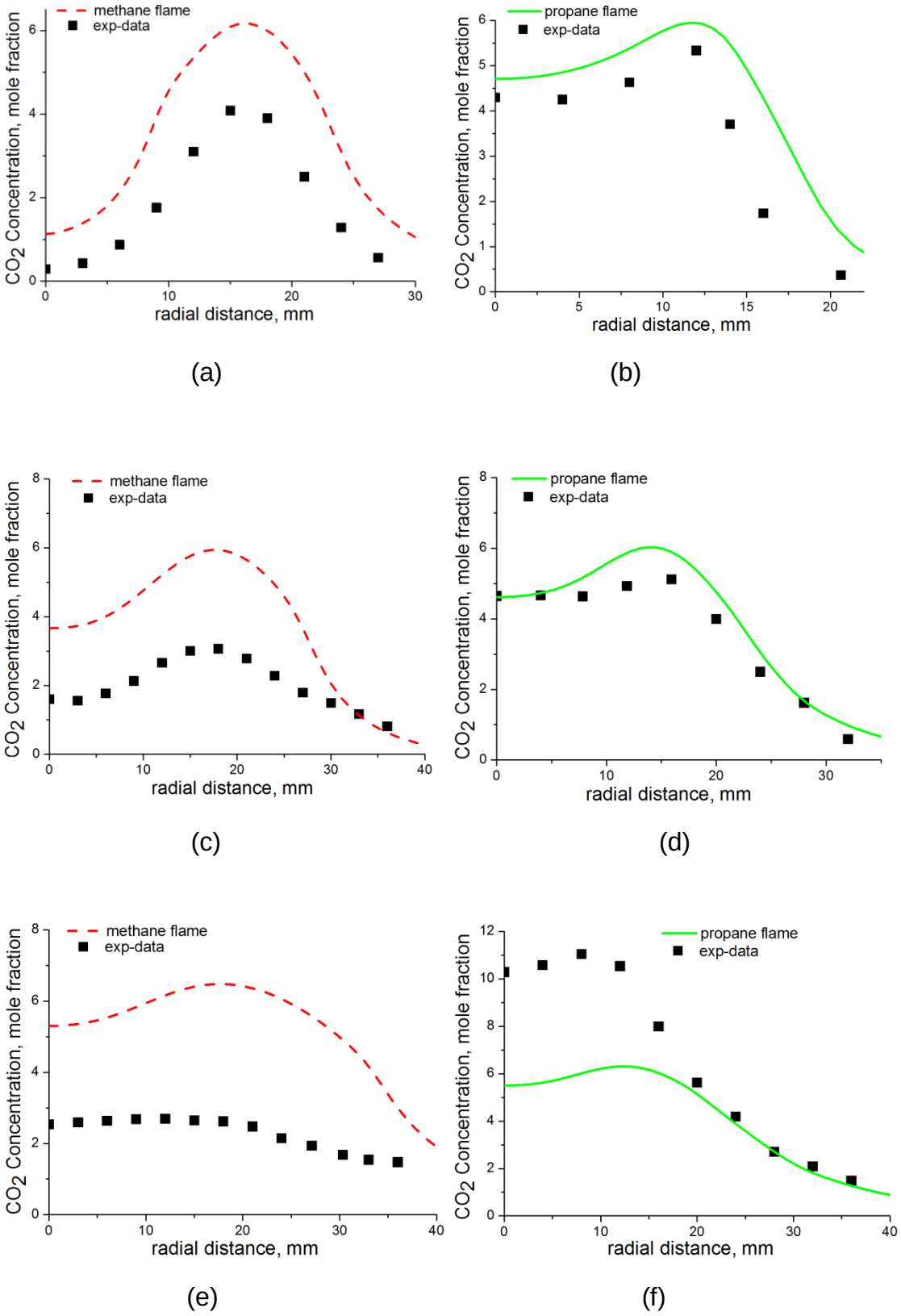

Figure 5-9 Radial predictions and measurements (dry basis) of the carbon dioxide concentration at x/d_i = 32 (a,b); x/d_i = 64 (c, d); and x/d_i = 94 (e,f) for a methane-air, and propane-air jet diffusion flame at Re = 5700.

Figures 5-9 (a) – (f) show the predictions and measurement of the carbon dioxide concentration distribution as a function of the radial position at the three selected axial stations for the methane and the propane flames. The trend of the carbon dioxide concentration has been well captured by the models for both the methane and the propane flames at all the measurement locations. This is especially true for the propane flame at x/d_i = 32 and x/d_i = 64, where the centreline concentration as well as the off-axis peak concentration have been correctly predicted by the models (Figure 5-9 (b) and (d), respectively). The results show that the centreline concentration of carbon dioxide in the methane flame was over-predicted at all the measurement locations, however the off-axis concentration was better predicted at x/d_i = 32 than at x/d_i = 64 and 94. The experimental data shows a very little centreline concentration of carbon dioxide (about 0.2 %) in the methane flame at x/d_i = 32 (Figure 5-9 (a)), and this is due to the increased entrainment of air into the base of the lifted flame. In contrast, the propane flame shows a much higher concentration of carbon dioxide at this location (about 4.5 %) and this is consistent with the predicted data. Further downstream of the flame there is a high over prediction of the carbon dioxide concentration in the flame, especially in the methane flame where the amount of carbon dioxide produced is expected to be less than that in the propane flame as shown by the experimental data. The propane flame prediction was also found to be better at x/d_i = 94, for 15 mm < r < 40 mm, but was largely under-predicted for 0 < r < 15 mm. The predictions of the carbon dioxide concentration for the methane flame at this axial location was much worse than that of the propane flame and this is in contrast to predictions made for carbon dioxide in the methane-air jet diffusion flame in chapter 4 of this thesis, where the predictions were observed to improve downstream of the flame. The difference is that the methane flame investigated in this chapter is highly lifted and hence complicated by the air entrainment at the base of the flame while the methane flame investigated in chapter 4 was attached to the burner rim. Furthermore, the under-prediction of the lift-off height in the methane flame contributes to the over-prediction of the carbon dioxide concentrations.

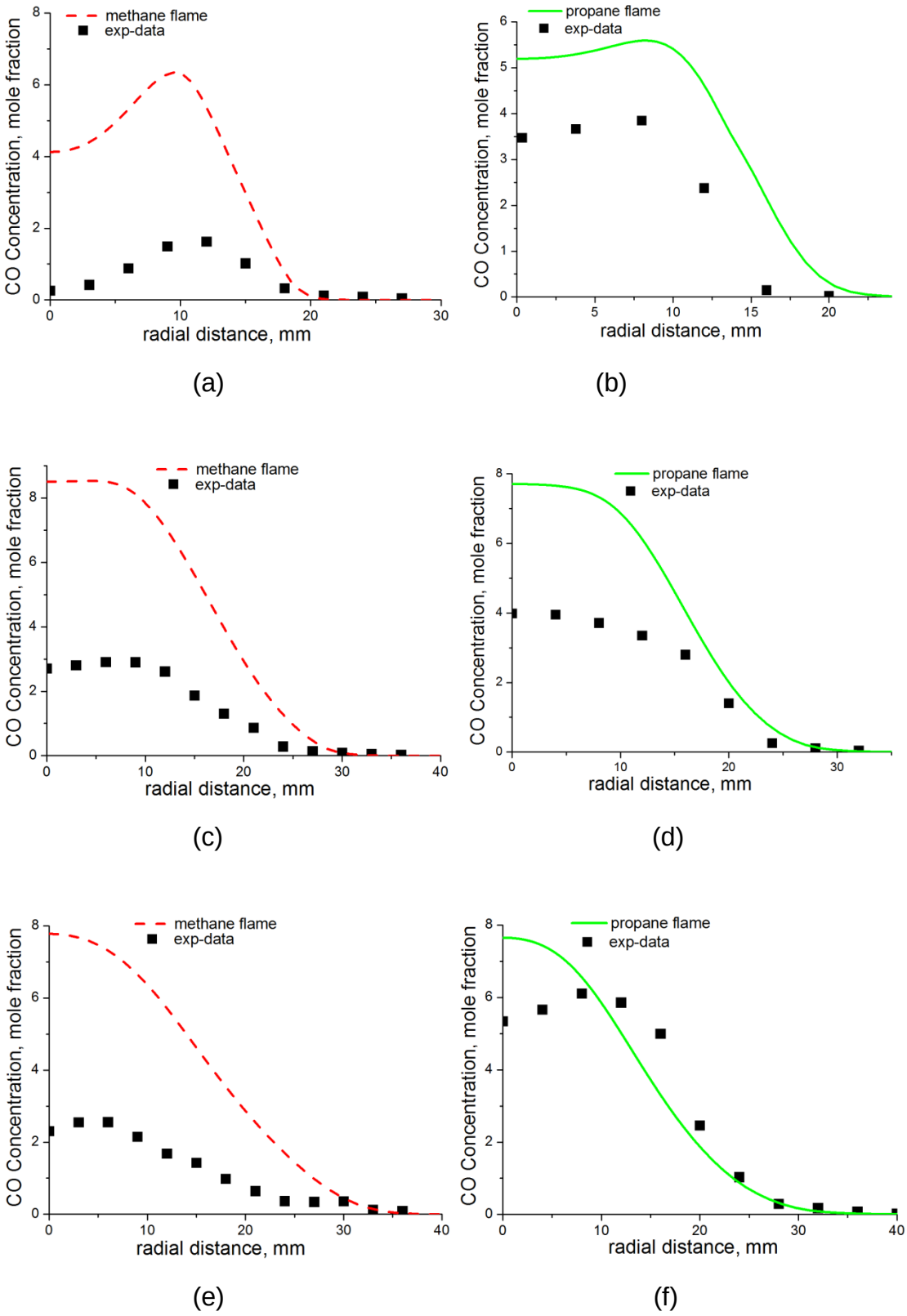

Figure 5-10 Radial predictions and measurements (dry basis) of the carbon monoxide concentrations at $x/d_i = 32$ (a,b); $x/d_i = 64$ (c, d); and $x/d_i = 94$ (e,f) for a methane-air, and propane-air jet diffusion flame at Re = 5700.

Figures 5-10 (a) – (f) show the predictions and measurement of the carbon monoxide concentration distribution as a function of the radial position at the three selected axial stations for the methane and propane flames. The trend in the predictions matches well the experimental trend for both the methane and the propane flame at all the measurement locations. However, once again there is a large over-prediction of the experimental data, especially in the case of the methane flame where there is an over-prediction of the centreline concentration of oxygen by about four fold at all the measurement locations. This is probably due to the inability of the flamelet model to account for the kinetic effects of slow forming species, such as carbon monoxide. The predictions for the methane flame were however found to be correct at the radial position where the carbon monoxide concentration goes to its ambient value (r = 20 mm for x/d_i = 32, and r = 30 mm for x/d_i = 64 and 94), thus correctly predicting the size of the flame. The carbon monoxide concentration in the propane flame is expected to be much higher than that obtained in the methane flame. The models on the other hand, have not been able to validate this expected behaviour in the flames, except at x/d_i = 32 (Figure 5-10 (a)), where the models predict higher concentrations of carbon monoxide at the flame centreline for the propane flame than for the methane flame. Further downstream of the pipe at x/d_i = 64 and 94, the carbon monoxide predictions for the methane and propane flame was about the same at the centreline. However the experimental data shows that there was almost three times as much carbon monoxide in the propane flame to that measured in the methane flame at the centreline for the axial location of x/d_i = 94 (Figure 5-10 (e) and (f)). Furthermore, it can be observed that the predictions of the carbon monoxide concentration in the propane flame were better downstream of the flame, and this can be attributed to the attached nature of the flame as well as the increase in the concentration of the carbon monoxide downstream of the flame as the products of the combustion rise due to buoyancy effects. This improved prediction at his downstream region is most apparent between 10 mm < r < 40 mm in Figure 5-10 (f), however we observe a slight under-prediction between 0 < r < 10 mm.

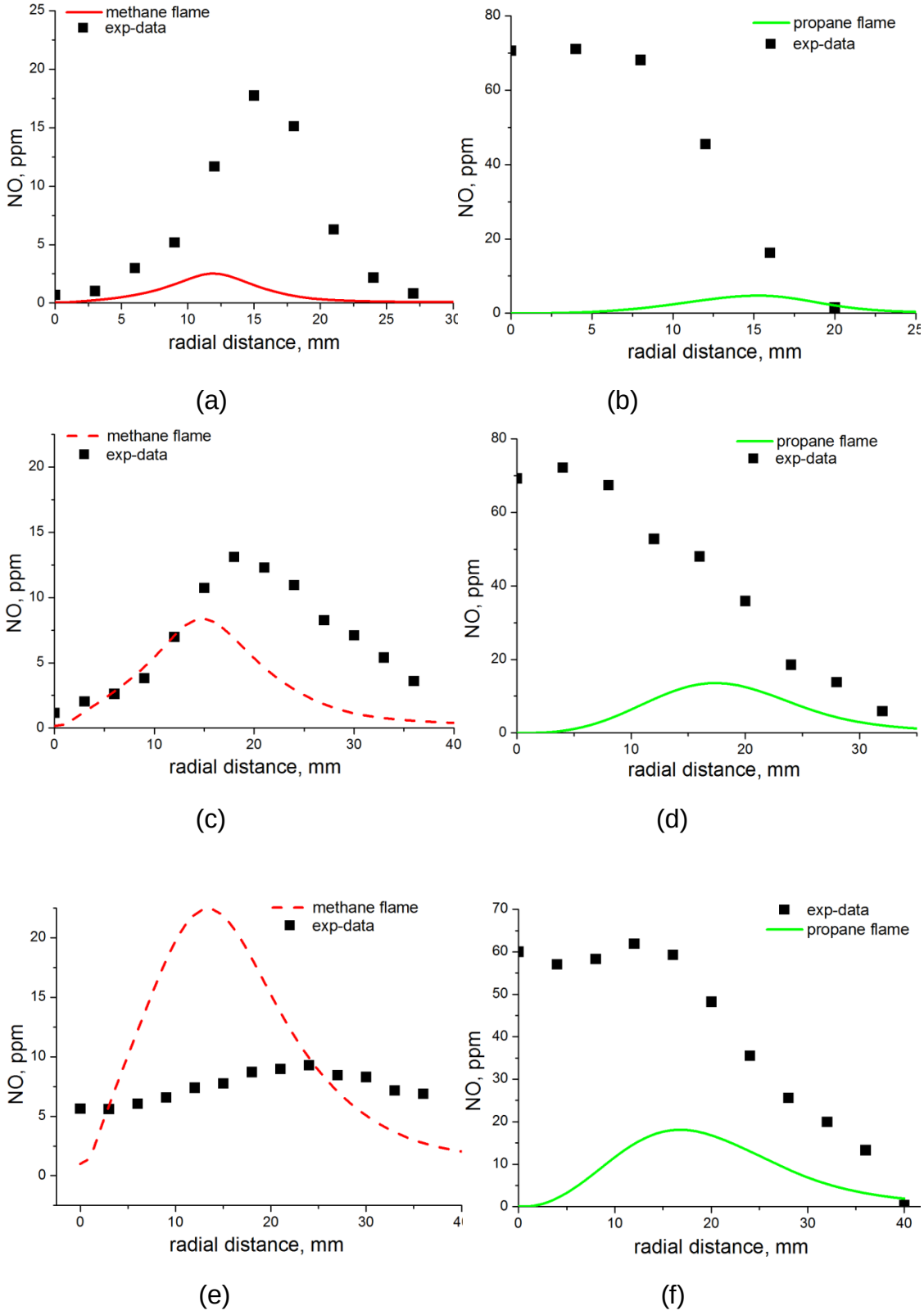

Figure 5-11 Radial predictions and measurements (dry basis) of the nitrogen oxide concentrations at x/d_i = 32 (a,b); x/d_i = 64 (c, d); and x/d_i = 94 (e,f) for a methane-air and propane-air jet diffusion flame at Re = 5700.

Figures 5-11 (a) – (f) show the predictions and measurement of the nitrogen oxide concentration as a function of the radial position at the three selected axial locations for the methane and propane flames. The NO Pollutant Model (Hughes et al., 2001) implemented in the Fluent code has been used to predict the nitrogen oxide concentration, given that the model is better able to account for the chemistry of slow forming species such as nitrogen oxide. This model has been compared with the flamelet equations in the previous chapter and has been found to have a superior performance. The results show that the model predicts the experimental trend of nitrogen oxide quite well for the methane flame at x/d_i = 32 and 64 (Figure 5-11 (a) and (c), respectively). However the trend was not captured at x/d_i = 94 (Figure 5-11 (e)), which is further downstream of the flame. The prediction was particularly good for the methane flame at x/d_i = 64, which is somewhat as expected given that more nitrogen oxide is normally produced in the mid-flame region where the flame temperature is higher. In contrast, the predictions were found to be much less accurate in terms of the trend at x/d_i = 32 and 94, corresponding to the base region and the the near tip regions of the flame. This is because less nitrogen oxide is formed at the base region due to lower temperature, and also less nitrogen oxide is available at the near tip region due to oxidation of nitrogen oxide to nitrogen dioxide. The centreline concentration of nitrogen oxide has also been correctly predicted at x/d_i = 32 and 64, which was almost zero at these locations. In the case of the propane flame, the models completely failed to capture the experimental trend, with the models predicting the absence of nitrogen oxide at the flame centreline while in contrast, the experimental data shows that maximum production of nitrogen oxide occurs at the flame centreline. This inability of the Pollutant Model to accurately predict the experimental trend in the case of the propane flame could be attributed to the inability of the model to resolve the interaction between the soot and NO_x chemistry. Furthermore, the difference in soot concentration between the methane and propane flames can be visualized by the amount of inflame soot collected on the quartz probe as shown in Figure 5-21.

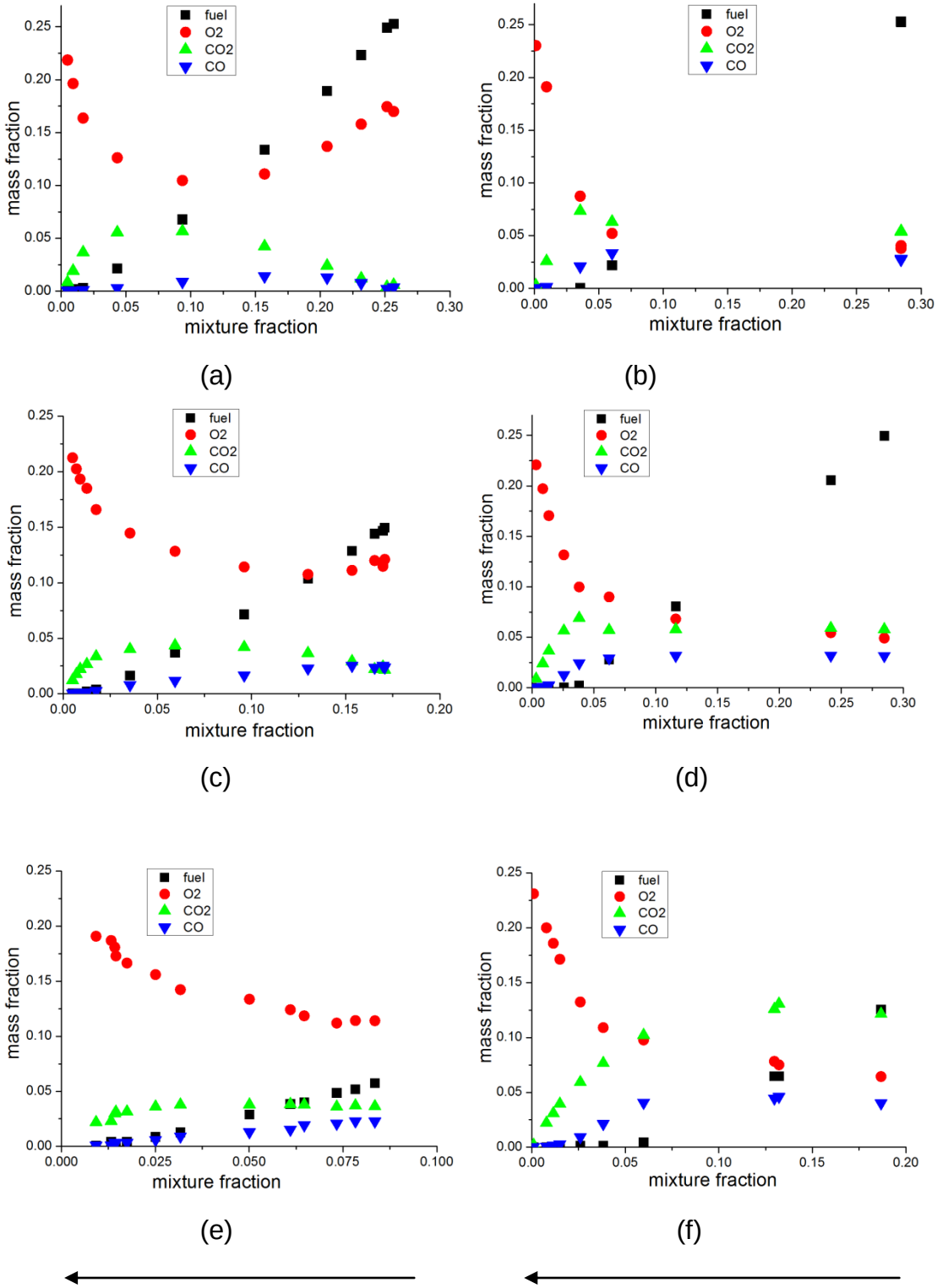

Figure 5-12 Radial plots of the species in mixture fraction space at x/d_i = 32 (a,b); x/d_i = 64 (c, d); and x/d_i = 94 (e,f) for a methane-air (left plots), and propane-air (right plots) jet diffusion flame at Re = 5700.

Figure 5-12 (a) – (f) show the radial plots of the total hydrocarbons (THC), as well as plots of the oxygen, carbon dioxide and carbon monoxide, in mixture fraction space at the three selected axial positions for the methane flame (on the left) and the propane flame (on the right), respectively. The arrows point from the flame centreline towards the flame edge (in the radial direction) and we can see from the plots that the fuel concentration is at its highest at the flame centreline and then decreases radially outwards and towards the flame edge and into the atmosphere, where the oxygen concentration is seen to be at its highest (ambient concentration). This divides the plot into the fuel rich (to the right of the plot) and the fuel lean (to the left of the plot) regions of the flame. The oxygen concentration was very high at the centreline for the methane flame at the three axial stations investigated due to the lifted behaviour exhibited by the flame. This is most visible at x/d_i = 32 (Figure 5-12 (a)), where we observe an oxygen concentration of about 18 % at the flame centreline. In contrast, the oxygen concentration in the propane flame at the same location in the flame was only about 4 % (Figure 5-12 (b)). Furthermore, a decrease in the fuel concentration can be observed as we move downstream of the flame from the near nozzle location of x/d_i = 32 towards the flame tip region at x/d_i = 94, while the concentrations of carbon dioxide and carbon monoxide are seen to increase in this direction, especially in the case of the propane flame. The mean mixture fraction, ξ was calculated according to the formula (Masri & Bilger, 1986):

$$\bar{\xi} = \frac{\frac{m}{MW}\bar{Y}_f + \frac{12}{28}\bar{Y}_{CO} + \frac{12}{44}\bar{Y}_{CO2}}{\bar{Y}_C} \tag{5.2}$$

where MW is the molecular weight of the fuel, m is the mass of the carbon atoms in a fuel molecule, $\bar{Y}_f$, $\bar{Y}_{CO}$ and $\bar{Y}_{CO2}$ are the mass fractions of the fuel, carbon monoxide and carbon dioxide, respectively, and $\bar{Y}_C$ is the mean mass fraction of the carbon atoms in the fuel ($\bar{Y}_C$ = 0.75 for methane and $\bar{Y}_C$ = 0.82 for propane).

5.4.5 Prediction of the flame lengths

The capability of the numerical models in predicting the flame lengths of the methane and propane flames was also investigated. Figure 5-13 shows the photographs of the flames and it can be see that the methane flame appears blue, while the propane flame appears yellow. This is due to the chemiluminescence in the flames, i.e. the generation of light due to a chemical reaction. The exited particles in the flame loose energy in the form of light, as they return to the ground state. The yellow colour observed in the propane flame is due to the incandescence of the very fine soot particles that are produced in the flame. A blue color is observed in less sooty flames, where reaction intermediates such as CH and C_2 radicals, dominate**,** and this is observed in the lifted methane flame. The measured flame lengths are shown in Table 5-1, with the methane and propane flames having an average flame length of 51.6 cm and 60.7 cm, respectively. The numerical work predicts the visible flame length by using the carbon monoxide burn-out height along the flame axis as an indicator of the chemical flame length. Carbon monoxide becomes oxidized to carbon dioxide towards the flame tip, hence the position along the flame axis where the carbon monoxide concentration falls to zero is a likely indication of where the flame ends. The predicted flame lengths can be oberved from the carbon monoxide contours and plots in Figure 5-14 and Figure 5-15, respectively. The temperature profile along the flame axis is also investigated as a means for predicting the flame length as shown in Figure 5-16. However, the agreement between the predicted result and the experimental data was not as good as that obtained for the carbon monoxide predictions. The carbon monoxide predictions are better appreciated when viewed from the plots and we observe from Figure 5-15 that the position along the flame axis where the carbon monoxide burns out (indicated by the vertical dash on the horizontal axis) approximates the experimentally measured visible flame length quite well, for both the methane and the propane flames. In the case of the propane flame, the prediction shows a better match with the visible flame length, falling within the experimental range of 60 ± 4 cm.

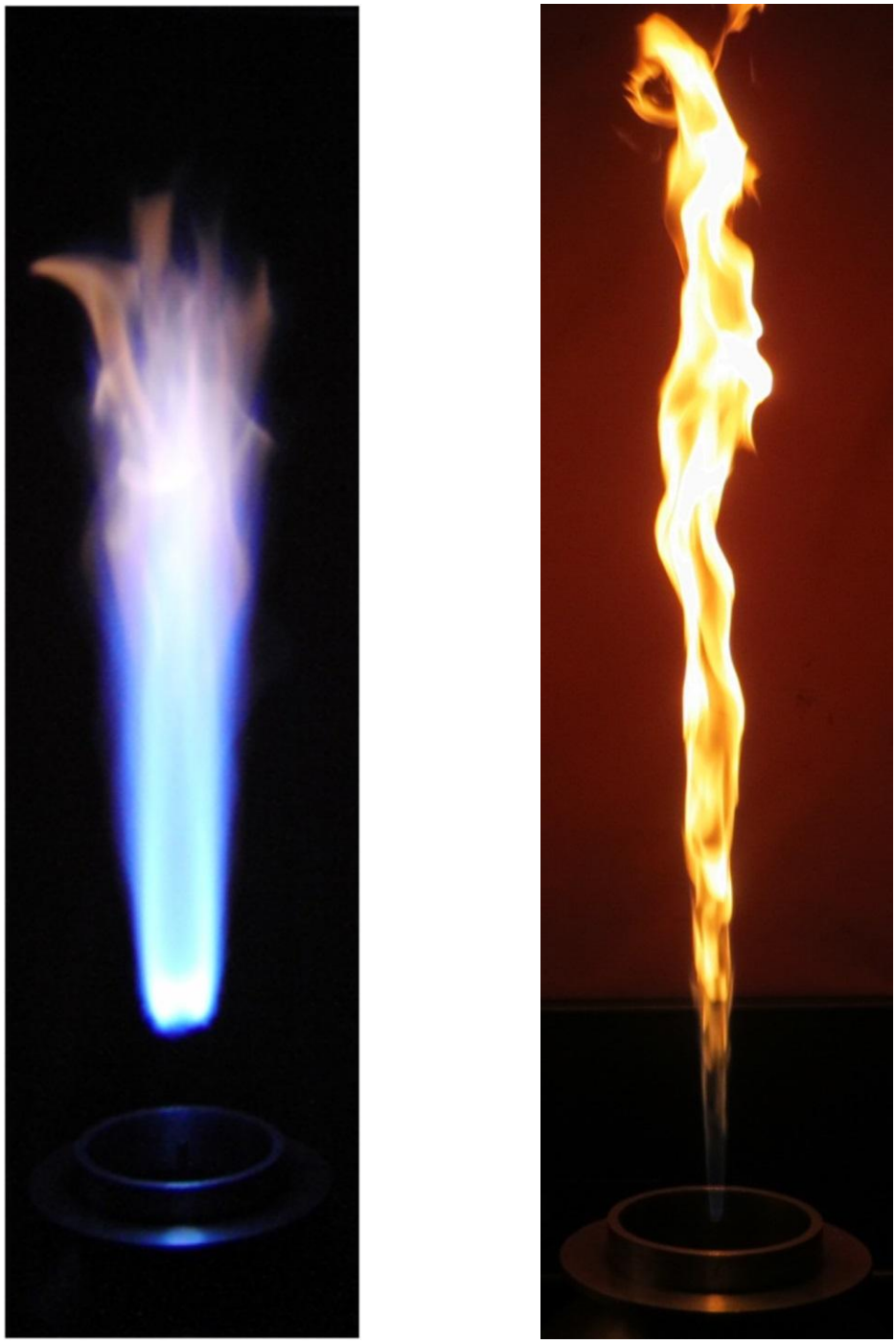

(a) (b)

Figure 5-13 Photographs of the (a) methane, and (b) propane flame at Re = 5700.

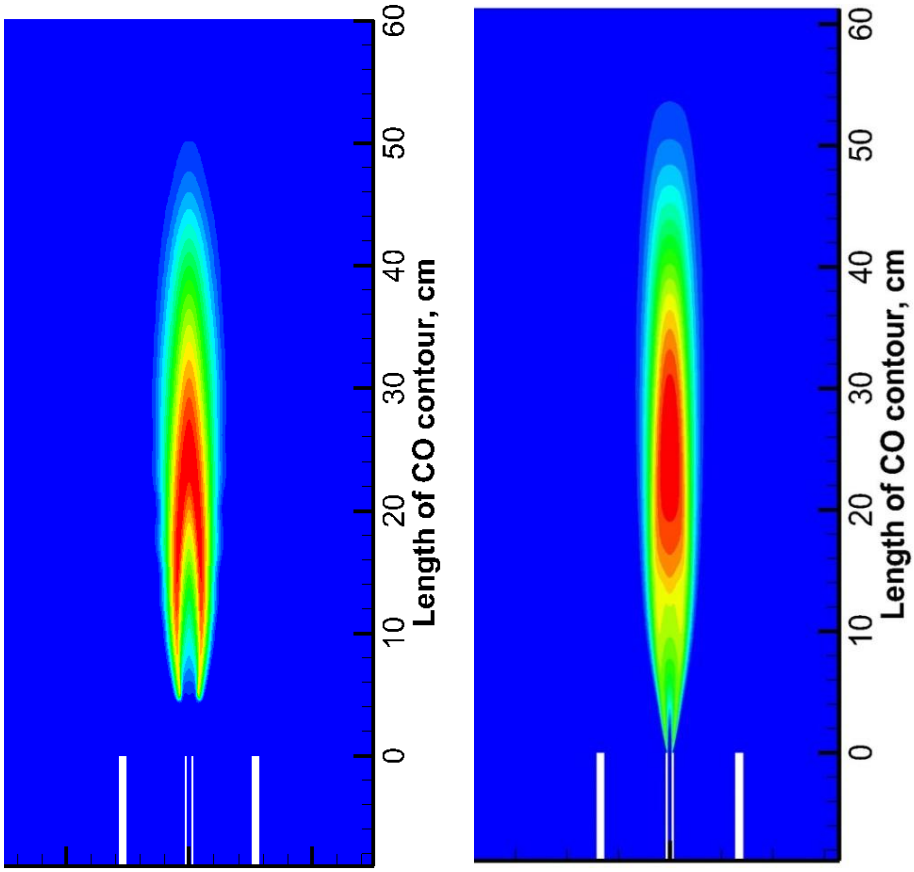

(a) (b)

Figure 5-14 RANS predictions of the flame lengths showing carbon monoxide contours in the (a) methane, and (b) propane flame at Re = 5700.

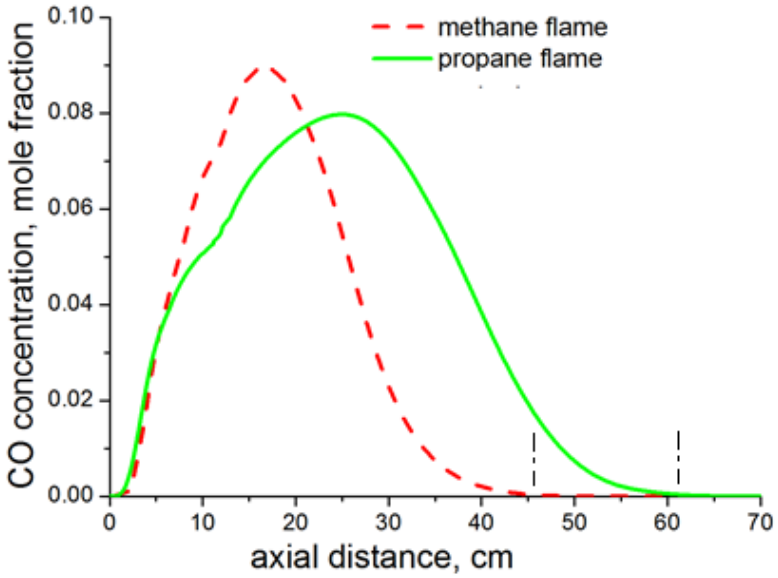

Figure 5-15 CO plots of the methane and the propane flame at Re = 5700.

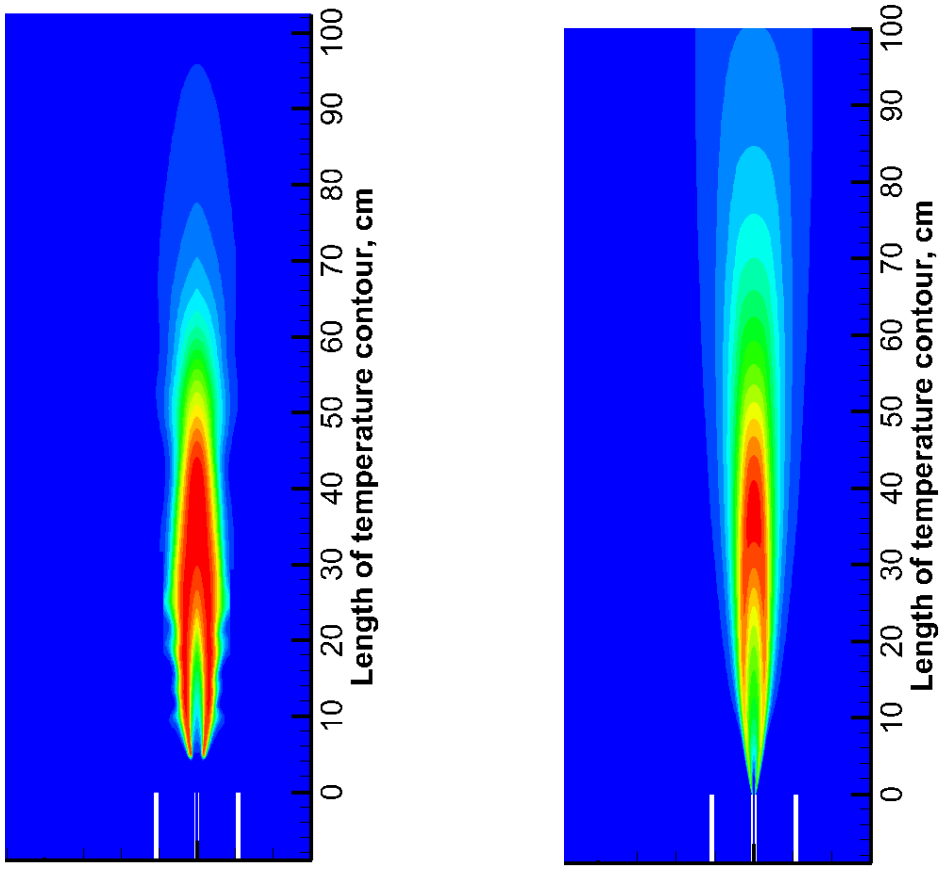

(a) (b)

Figure 5-16 RANS predictions of the flame lengths showing temperature contours in the (a) methane, and (b) propane flame at Re = 5700.

5.4.6 Measurement of the flame lift-off heights

Table 5-3 Properties of the pipe and fittings used.

Case	Pipe Internal Diameter (mm)	Pipe External Diameter (mm)	Thickness (mm)
1	4.4	6.4	1
2	4.4	8.4	2
3	4.4	10.4	3

The flame lift-off is important in gas flares because lifted flames are less stable and thus more susceptible to blow-outs, especially in the presence of a cross-wind. This section investigates the effect of the pipe nozzle-wall thickness on the flame lift-off heights. Three cases have been investigated for the methane and propane jet diffusion flames. The first case uses a 1 mm thick pipe, while the second and third cases use 2 and 3 mm thick pipes in the form of pipe fittings as shown in Figure 5-19. The pipe internal and external diameters are presented in Table 5-3, showing a consistent internal diameter for the three pipes while the thickness has been varied by varying the pipe external diameter. It was observed that a decrease in the flame lift-off height occurred when the thickness of the nozzle was increased, as illustrated in Figure 5-17 (a),(c) and (e) and Figure 5-17 (b),(d) and (f) for the methane and propane flames, respectively. Furthermore, the methane flame shows a higher lift-off height than the propane flame for all the cases investigated. Figure 5-20 shows a graph of the dependence of the flame lift off heights (to the nearest millimeter) on the pipe nozzle thickness, represented by an outer diameter of 6.4, 8.4 and 10.4 mm. From the figure, we see that the steep change in the lift-off height (from 6 mm to 3 mm) occurred in the propane flame due to a slight change in the nozzle thickness (from 1 mm to 2 mm). However, this behaviour was not observed in the methane flame. A further increase in the nozzle thickness (from 1 mm to 3 mm) was required to observe a decrease in the lift-off height in the case of the methane flame. Kalghatgi (1981a) demonstrated that the flame lift-off height is independent of the burner internal diameter. However the pipe external diameter will affect the lift-behavior of the flame due to recirculation effects at the base of the lifted flame. This recirculation can be visualized from the velocity vectors in figure 5-18 (c) where we can observe that a low pressure region has developed at the base of the flame, setting up the recirculation there. Figures 5-18 (a) and (b) show the simulation of the methane flame using the 1 and 2 mm thick pipes and it can be visualized from the temperature contours that the difference in lift-off observed experimentally was not reproduced numerically. A 3D simulation is therefore required to capture the turbulence more effectively.

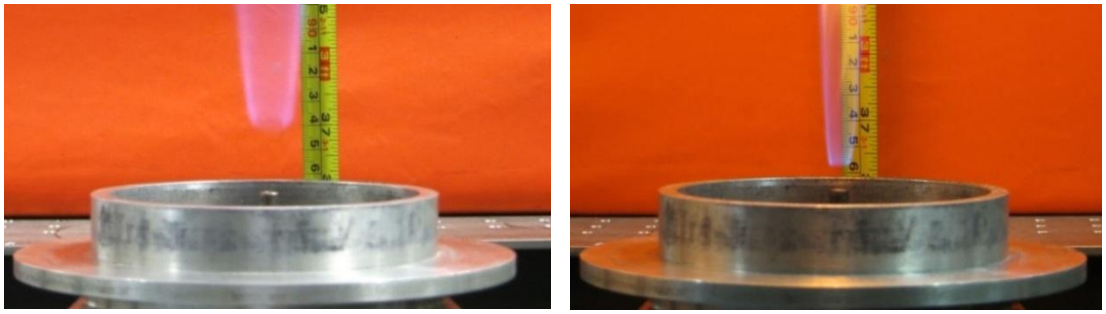

(a) (b)

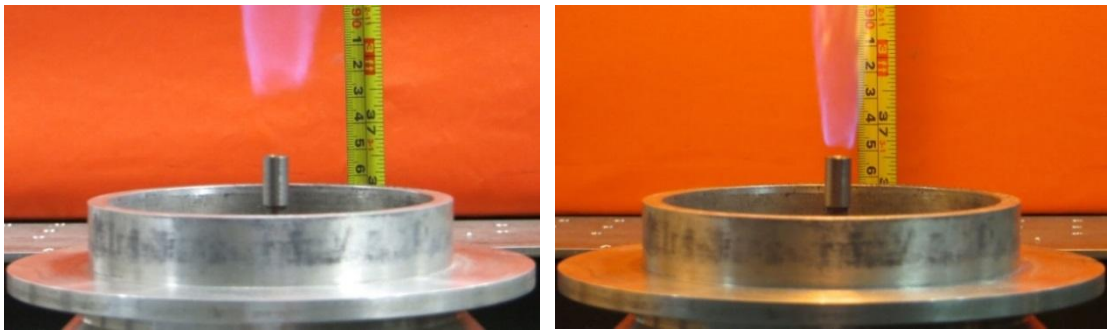

(c) (d)

(e) (f)

Figure 5-17 Mean images of the initial lift-off in the methane (left) and propane (right) flames using (a,b) 1 mm, (c,d) 2 mm, and (e,f) 3 mm thick pipes, respectively.

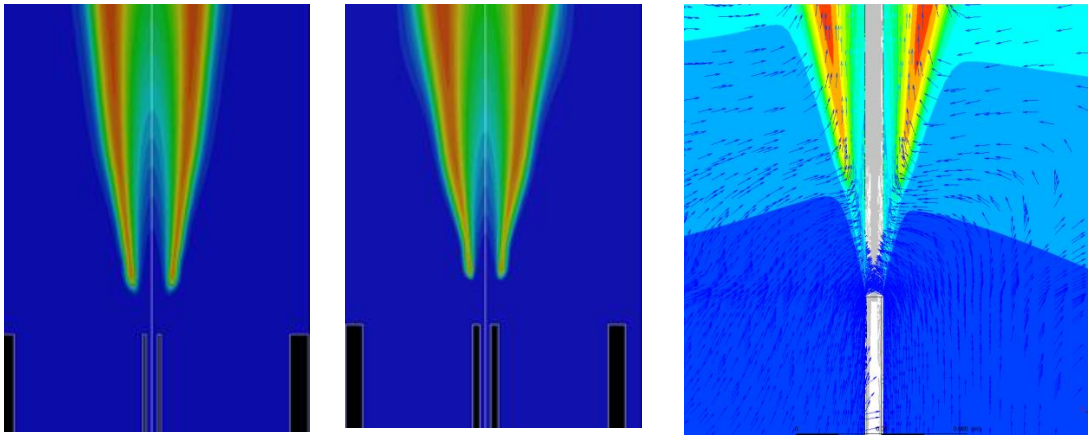

(a) (b) (c)

Figure 5-18 RANS simulation of lift-off using (a) 1 mm, (b) 2 mm thick pipes, and (c) velocity vectors showing recirculation at the flame base.

(a) (b)

Figure 5-19 Photos of the pipe fittings of thickness (a) 2 mm, and (b) 3 mm.

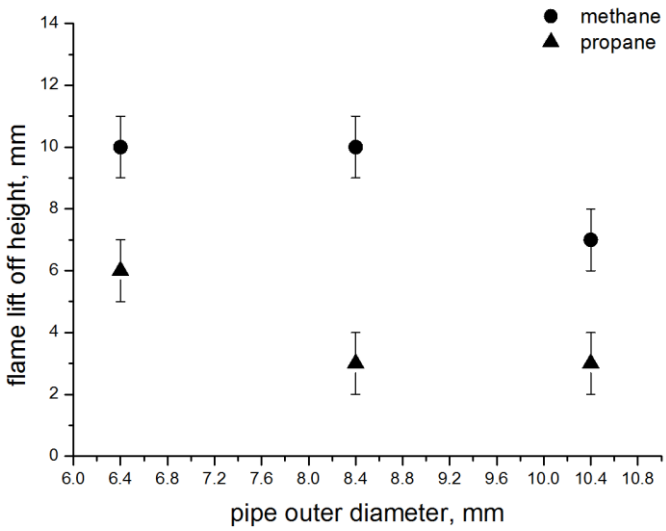

Figure 5-20 Dependence of the flame lift-off height on the nozzle thickness.

5.4.7 Measurement of the post flame emissions

Table 5-4 Results of the post flame measurement of the emissions.

Parameter	Methane	Propane
$EINO_x$ (g/Kg)	1.31	0.9
EICO (g/Kg)	320.9	230.8
Unburned HC (ppmc)	3.09 ± 0.01	3.36 ± 0.02
Soot EF (Kg/m^3)	0	0.09

The post flame emissions of soot, unburned hydrocarbons, CO and NO_x are a major source of environmental pollution in gas flares and the measurements made, given in Table 5-4, provides the relative amount of these pollutants in methane and propane flames operating under the same Reynolds number of 5700.The emission of NO_x, CO and unburned hydrocarbons was measured as described in Section 3.2.4 and the emission indices of NO_x and CO ($EINO_x$, EICO) were calculated according to the method by Turns and Lovett (1989), which has been used by other authors (Meunier et al., 1998; Yap et al., 1998) and is given as:

$$EIX_i(g/kg) = \frac{n[X_i]MW_i 1000}{[CO_2]MW_f} \tag{5.3}$$

where MW_f is the molecular weight of the fuel, MW_i is the molecular weight of the species, X_i is the mole fraction of the species and n is a factor which accounts for the number of moles of CO_2 produced for each mole of fuel burnt. The NO_x emission indices have been found to be invariant with axial and radial positions in the post flame region (Turns et al., 1993) and the uniformity of NO_x emission indices both axially and radially indicates that NO_x in the post flame region is well mixed with the products of combustion and entrained air. This was also observed in the present study to be valid for CO. Also, it is worth noting that NO is converted to NO_2 in the post flame region, therefore NO_x is reported as NO_2 equivalent, thus implying that the

molecular weight of NO_2 is used in the $EINO_x$ calculations in equation (5.2). A comparison of $EINO_x$ for the methane and propane flames is presented in Table 5-4 and shows a higher value for the methane flame. This observation has also been reported by other authors (Lyle et al., 1999; Wang et al., 2002). A possible explanation for this trend could be the higher temperature generated in lifted flames which will lead to higher NO_x production, since NO_x formation is temperature dependent (Yap et al., 1998). Furthermore, EICO was observed to be slightly higher in the methane flame and this is rather unexpected given that the Inflame measurements of carbon monoxide showed higher production in the propane flame. The amount of soot was determined according to the method described in section 3.2.5 and the soot emission factor (EF) was calculated according to the formula given as (McEwen and Johnson, 2012):

$$EF = \left(\frac{m_s}{v_g}\right) \times F_d \tag{5.4}$$

where m_s is the mass of soot collected in kilograms, v_g is the volume of gas burnt in m^3 and F_d is the dilution factor which is given by

$$F_d = \frac{v_a}{v_p} \tag{5.5}$$

where v_a is the volumetric flowrate of air through the duct, in m^3/s and v_p is the volumetric flowrate of the post flame sample passing through the sample line, in m^3/s. The soot emission factor for the methane and propane flames are given in Table 5-4 and the results show that no soot could be detected in the lifted methane flame. Lifted methane flames are known to contain little or no soot at atmospheric conditions hence the results are in agreement with other works (Brookes & Moss 1999; Bandaru and Turns, 2000). Soot is however detectable in the propane flame as expected and the amount of soot in the propane flame in comparison to the methane flame can be observed in Figure 5-19, where the soot is collected on the probe during the inflame measurement of species. The photographs were taken after a period of about 20 minutes of burning the propane fuel and 45 minutes of burning

(a) (b)

Figure 5-21 Photographs of the soot collected on probe after inflame measurements for (a) methane, and (b) propane flames after 45 and 20 min respectively, at Re = 5700.

the methane fuel and from the figures, we observe that no visible soot is seen to have collected on the probe in the case of the lifted methane flame, while the probe was completely covered in soot in the case of the propane flame.

5.5 Conclusions

In this chapter, the behavior of a methane and propane jet diffusion flame issuing from the same burner, and having the same Reynolds number, has been compared experimentally and numerically with the following conclusions:

- The Brookes & Moss (1999) soot model has been able to reproduce the relative difference that exists in the inflame soot concentration between a lifted methane and an attached propane flame. It should be noted that previous investigation by Bandaru and Turns (2000) has shown that lifted methane flames contain very little soot at atmospheric pressure.
- The flame lengths of the methane and the propane flames were reasonably predicted by the models as showed by the burn out position of th soot and the carbon monoxide along the flame axis, which approximated the experimentally measured flame length.
- Inflame measurements of carbon monoxide and nitrogen oxide showed higher levels of both pollutants in the propane flame. However the post flame measurement of the emissions showed slightly higher levels of carbon monoxide in the methane flame. This could be attributed to the higher dilution of air in the post flame region in the case of the propane flame.
- The Pollutant Model produced a better prediction of the trend in the nitrogen oxide concentration distribution in the methane flame compared to the propane flame. This inability of the Pollutant Model to accurately predict the experimental trend in the case of the propane flame may be due to the difficulty of resolving the interaction between the soot and NO_x chemistry
- Investigations of the effect of variations in the burner nozzle thickness on flame lift-off showed that the initial lift-off height decreased as the burner nozzle thickness was increased. Furthermore, the propane flame was observed to respond quicker to changes made to the thickness of the burner nozzle in comparison with the methane flame.

Chapter 6

Numerical Study of a Wake-stabilized Propane Diffusion Flame in a Cross-flow

6.1 Background

The jet diffusion flame in a cross-flow represents the closest model of a flare burning in a cross-wind and has therefore been studied by several researchers on the experimental level to extract valuable information about the nature of flares in a cross-wind. These investigations have been reviewed in chapter 2 and of note is the observation that a lot of these flames in a cross-wind eventually become stabilized in the wake of the burner. Huang & Chang (1994) observed that if a flame was lit at a cross-wind velocity above a critical value, then the flame base could never leave the burner before blow-off, i.e. the flame always attached to the wake of the burner, even at high jet exit velocities. This type of flare regime is especially common in production flares where the flare design is a simple cylindrical pipe and the cross-wind velocity is often high. Wake-stabilized flames in a cross-flow have been described by Gollahalli & Nanjundappa (1995) as consisting of three main flow structures. These are the recirculating eddy attached to the wake of the pipe, an upper shear layer consisting of fuel-air mixture that becomes partially premixed by the turbulence with combustion occurring in a stratified medium, and an axisymmetric region downstream of the flame. Johnson et al. (2001) studied the emission of unburnt hydrocarbons from a wake-stabilized propane diffusion flame in cross-flow and concluded that the path of escape of the unburnt fuel was from the under-side of the flame downstream of the junction between the planar recirculation zone and the axisymmetric main tail of the flame (see Figure 1-4). They further observed that the mean flow induced by the standing vortex that exists on the lee side of the burner pipe transported and stretched the ring vortices from the upper shear layer in the non-combusting region and ejected them on the underside of the flame, thus creating an

observed burst of hydrocarbons that are eventually stripped away from the jet without burning. They attributed the driving mechanism for the recirculation around the outside of the pipe to a pair of counter rotating vortices that usually exists when a jet is injected into a transverse stream and is bent over (Moussa et al., 1977). A form of coherent motion is associated with the counter rotating vortex pair, which appears as kidney-shaped flame structures that contributes to the overall mixing in the flow field (Gollahalli et al., 1975). The recirculation zone, which is stabilized in the wake of the burner due to the low pressure in this region, is primarily responsible for the enhanced flame stability in this regime. This has a profound influence on the residence time of the reactive gases in the vortex cores and consequently could impact on the emission of pollutants. Numerical predictions of the emissions from cross-flames require that all the controlling flow features in the flame should be properly predicted and this requires an adequate turbulence model that can capture the cross-flow interactions with the fuel jet. Lawal (2011) applied the non-premixed combustion model to a methane flame burning in a cross-flow and was able to predict the counter rotating vortex pair downstream of the flame as well as the secondary flame region trapped in the wake of the pipe. However, he was unable to predict the non-reacting mixing layer, which consists of a partially premixed non-combusting region of fuel-air mixture. He attributed this shortcoming to the drawbacks of the non-premixed combustion model. In this chapter, the non-premixed and the partially premixed combustion models are compared in their ability to predict the flow structures in a wake-stabilized propane flame burning in a cross-flow. The CRECK mechanism (Ranzi et al., 2012) was used to model the kinetics of the propane reactions while the Reynolds stress model (RSM) and the $k-\varepsilon$ realizable turbulence model (with enhanced wall functions) were compared in their ability to capture the flow field. Furthermore, in-flame predictions of the temperature and the species have been made in the near field and compared with the experimental data of Huang and Yang (1996). A Large Eddy Simulation (LES) of the flame was also carried out in order improve on the predictions from the RSM model by capturing the transient behaviour of the flame.

6.2 Experimental details

The section describes the experimental work performed by Huang and Yang (1996). The experiment was performed in a suction type, open circuit wind tunnel. The test section of the wind tunnel had dimension of 30 × 30 × 110 cm^3. The combustor was a stainless pipe of inner diameter d_i = 5.0 mm, outer diameter 6.4 mm and length 250 mm. The pipe was positioned perpendicularly to the aluminium floor of the test section and protruded 180 mm into the wind tunnel. The origin was centred at the exit plane of the burner tube and the description was in terms of a rectangular coordinate system (X, Y, and Z) as shown in Figure 6-1. Commercial grade propane of about 95.0 % C_3H_8, 3.5 % C_2H_6 and 1.5 % C_4H_{10} was used as the fuel and the average jet velocity, u_f was calculated (using the flow rate) to be 5.78 m/s while the fuel Reynolds number was calculated to be about 7000 for the case investigated. The cross-flow velocity u_{cf} was fixed at 4.86 m/s, giving a jet-to-cross-flow momentum ratio R, of about 2.16. The maximum turbulence intensity of the cross-flow in the wind tunnel section as measured by a hot-wire anemometer, was less than 0.5 % in the experimental range. The thermal structure of the flame was measured with a Pt-Pt/13 % Rh home-made L-shaped thermocouple probe with a wire diameter of 125 μm and a junction diameter of 150 μm mounted on a two-dimensional traversing mechanism. Temperature measurements were not corrected for the radiative losses from the thermocouple and according to the calculation of the energy balance, the deviation of the measured temperature from the actual value was estimated to be about 50 ºC at a temperature of 1600 ºC. The concentrations of carbon dioxide and carbon monoxide were measured with infra-red analyzers while the concentration of oxygen was measured with a paramagnetic analyzer. Gas sampling was achieved with a stainless steel probe with a tip diameter of 1 mm. The suction rate of the sample gas was adjusted using a needle valve to minimize the disturbances introduced by the probe into the flow field (i.e. iso-kinetic conditions was maintained).

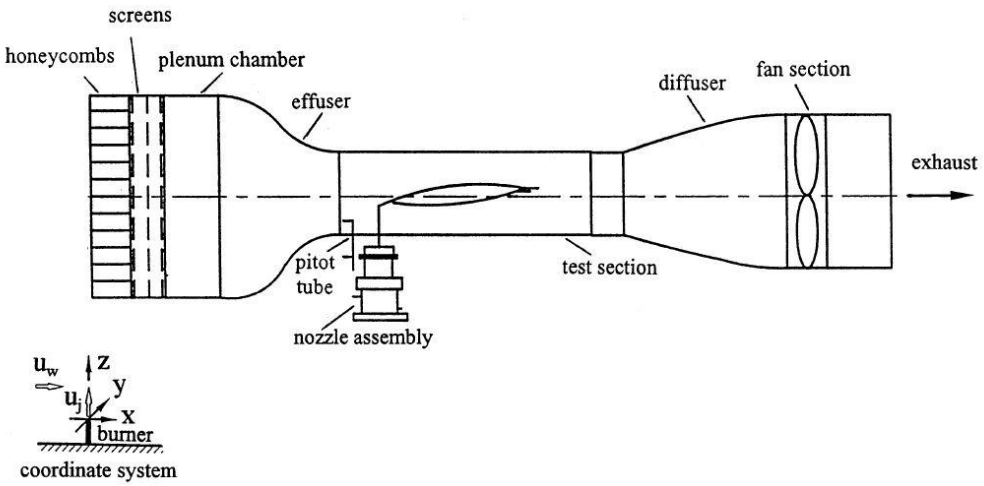

Figure 6-1 The experimental set-up of Huang and Yang (1996) for the simulation of a propane diffusion flame in cross-flow.

6.3 Computational details

- *Grid independent study and solution methods*

The computational simulation was achieved on a three-dimensional structured hex mesh generated using the ANSYS-ICEM meshing software. The size of the computational domain was based on the volume of the test section of the wind tunnel ($30 \times 30 \times 110$ cm^3), with the origin at the center of the burner outlet. The burner was represented by a cylindrical tube with dimensions consistent with that used in the experimental set up. The tube was positioned approximately 240 mm from the cross-flow inlet boundary and it extended 180 mm into the combustion zone (Figure 6-2). A mesh independent study was conducted (for the RANS calculations) to ensure the independence of the solution on the mesh size. This entailed comparing the velocity and temperature profiles for mesh sizes of 1.24 E6, 2.52 E6 and 3.48 E6 elements, as shown in Figure 6-3 (a) – (c). Mesh predictions for the axial and radial components of the velocities, as well as the axial trend of the temperature, were compared for the three mesh resolutions and the comparison shows a good agreement for all three mesh sizes, except the temperature, which showed a slight variation between the 1.24 E6 and the 2.52 E6 mesh sizes. Further refinement of the mesh to 3.48 E6 cells produced no further variations and a mesh size of 2.52 E6 cells was found to

suffice. The mesh distribution option was selected so as to place a finer node distribution in the pipe exit region and coarser nodes further away from the pipe region. The wall y^+ was checked and found to be about 1.5 (see Figure 6-3 (d)). The cells were checked for sudden changes between the cell volumes and the results were satisfactory (Appendix III (b)). The reacting flow simulation was started from a converged non-reacting case file and was calculated for a total number of 16 flamelets over a scalar dissipation rate in the range of 0.0001 to 30 s^{-1} in scalar dissipation steps of 2.5 s^{-1}.

The solution obtained from the steady state RANS calculation was used as the initial condition for the LES calculation. The LES calculation was performed in time step sizes of 1.2 -E-4 for a flow time of 0.70s in order to achieve a pseudo-steady state solution, i.e. a state of thermo-chemical equilibrium in the solution domain. The flow time is approximately three flow residence times through the solution domain and the cell Courant number had stabilized at about 1.5 at the end of the calculations with all iteration residuals below 10^{-6}. To achieve convergence, trial and error were carried out to correct the floating point errors in the solver. To this end, the under-relaxation factors where decreased midway into the calculation to avoid divergence in the AMG solver. This is because over relaxation speeds up the convergence, but at the same time will reduce the calculation stability. This also necessitated a switch of the pressure-velocity coupling discretization technique from SIMPLE to Couple in order to stabilize the LES calculation (Béghein et al., 2005). Temporal averages of the instantenous LES simulation were sampled at specific intervals in order to determine whether the LES calculation had reached a statistically steady state. To this end, profiles of the mean mixture fraction were taken after 0.42s at three successive intervals of 0.033, 0.037 and 0.041s at the wake of the burner and at the burner exit (Figure 6-6 (a) and (b)). The results obtained shows that the mixture fraction profiles obtained at the three sampling intervals are quite similar for both locations in the flame indicating that the flow field solution was statistically steady. The Smagorinsky model (1963) was used to approximate the subgrid scale turbulence in the flow domain while kinetics

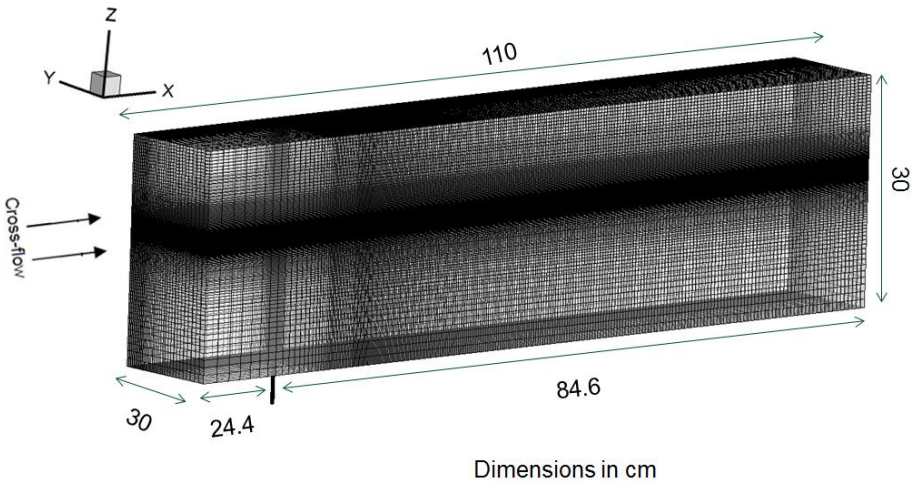

Figure 6-2 Mesh of the wind tunnel test section for the Huang and Yang (1996) experiments.

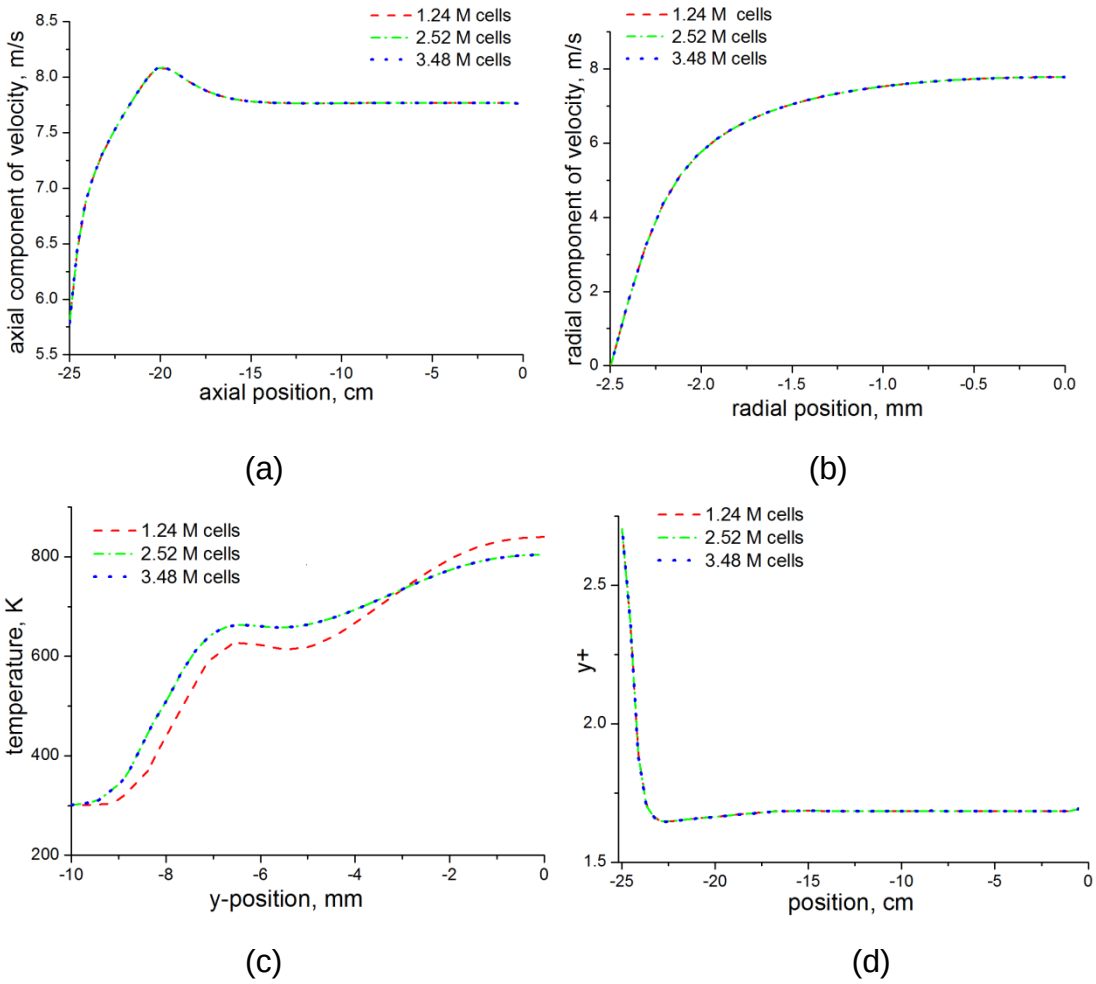

Figure 6-3 Predictions of (a) axial, (b) radial veocity,(c) temperature at, x=8.2,z=3 mm, and (d) pipe wall y^+ for 1.24, 2.52, and 3.48E6 cells for Re=7000.

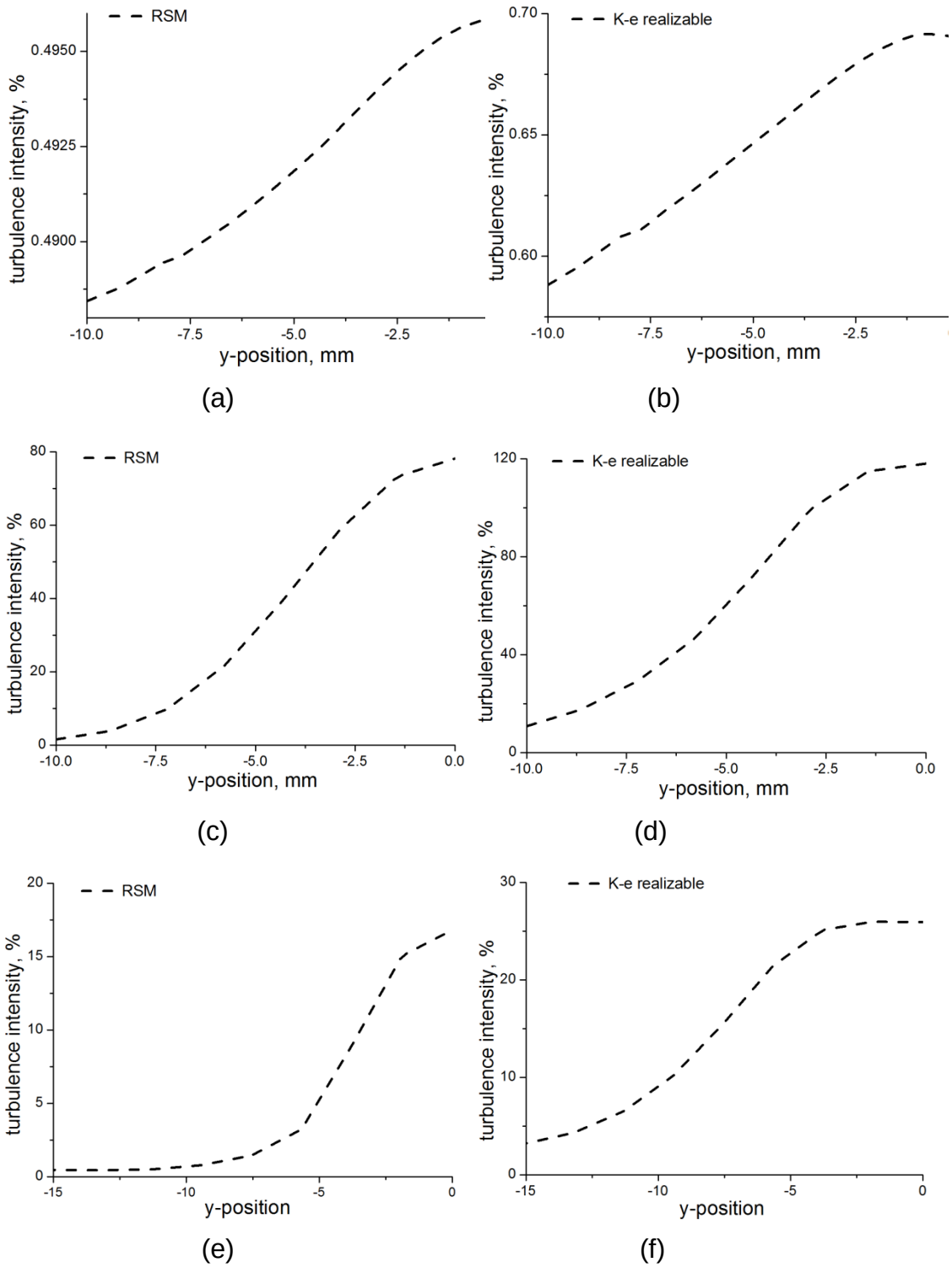

Figure 6-4 Predictions of the turbulence intensity upstream of the pipe, (a),(b); wake of the pipe, (c),(d) and; downstream of the pipe, (e),(f), using the RSM and the $k-\varepsilon$ realizable models

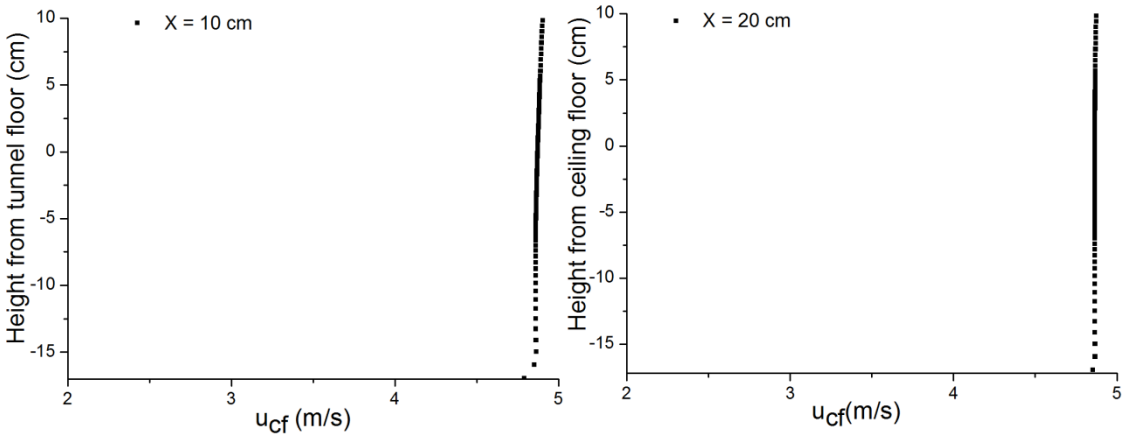

(a) (b)

Figure 6-5 Predictions of the velocities for cross sections taken at (a) 10 cm from the pipe, and (b) 20 cm from the pipe in the y=0 plane of the wind tunnel section using the RSM.

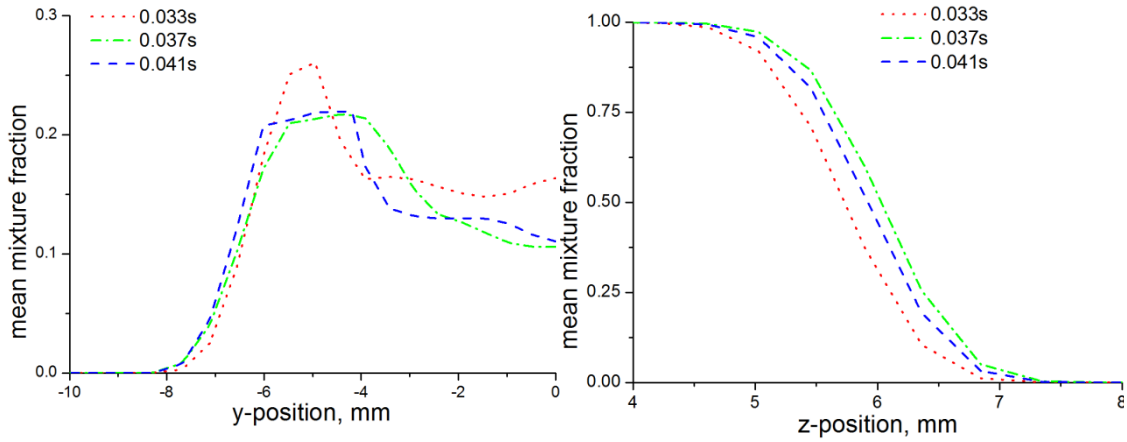

(a) (b)

Figure 6-6 Comparison of the mean mixture fraction obtained from the temporal averaging of the LES calculation over different time intervals at (a) x=8.2, z=-3 mm, and (b) x=0, y=0 (pipe exit)

of the propane reactions was accounted for using the CRECK reaction mechanism (Ranzi et al., 2012). Combustion was modelled using the partially premixed and the non-premixed models and the two models have been compared. Soot in the flame was modelled with the Moss-Brookes-Hall model (1997). Soot oxidation was accounted for using the model of Lee et. al (1962). Reactions by the OH radical were assumed to proceed under partial equilibrium conditions. Radiation, which appears as a sink in the energy equation was modelled with the Discrete Ordinate Model (Fiveland, 1984). As a reasonable compromise between the efficiency and the accuracy of the DOM calculations, the S_2 quadrature is used for the angular discretization and hence the computational domain was discretized into eight angular directions and the RTE is then solved for these directions, within which the radiation intensity is assumed constant. The pipe was made from stainless steel hence an emissivity value of 0.6 was assigned. The pipe thickness was about 0.5 mm and the temperature of the gas in the pipe was assumed to be ambient. The effect of the heat transfer in the pipe is shown in Appendix III (d). No adjustments were made to the model constants and all governing equations were discretized using the second-order upwind scheme while the pressure-velocity coupling was resolved by the SIMPLE algorithm (Pantakar, 1980). Figures 6-4 (a) – (f) show the prediction of the turbulence intensity as a function of the y-position upstream of the pipe (x= -25 mm, z=0), at the wake of the pipe (x= 30 mm, z=0) and downstream of the pipe (x = 185 mm, z=0) using the $k-\varepsilon$ realizable turbulence model (with enhanced wall functions) and the RSM. The turbulence intensity is observed to be at its peak value at the centre of the wind tunnel and then decreases from the centre towards the wall of the wind tunnel. Furthermore, the turbulence intensity is observed to be very low upstream of the pipe for both the RSM and the $k-\varepsilon$ realizable turbulence model (Figure 6-4 (a) and (b)). However, the RSM produced a slightly lower turbulence intensity in comparison with the $k-\varepsilon$ realizable model (0.45 and 0.75, % respectively) and this is agreement with the experimentally measured turbulence intensity in the wind tunnel section. This very low turbulence intensity upstream of the

fuel pipe can also be observed from Figure 6.5 (a) and (b) which shows the prediction of a uniform velocity profile in this section of the wind tunnel at two upsteam locations of the pipe using the RSM. The turbulence intensity is observed to increase dramatically at wake of the pipe due to the interaction of the cross-flow with the fuel jet (Figure 6-4 (c) and (d)). However, it is observed that the RSM predicted about 30 % lower turbulence intensity than the $k-\varepsilon$ realizable model at this location. It is worth noting that the RSM is able to account for the anisotropy of turbulence which is often associated with the large eddies, while the $k-\varepsilon$ realizable model on the other hand is unable to achieve this (Pfeiler & Raupenstrauch, 2010). Further downstream of the flame, it is observed that the turbulence intensity begins to fall due to the dissipation of the turbulent kinetic energy at the downstream region of the pipe.

- *Boundary conditions*

Boundary conditions have been prescribed as follows: on the *z-x* plane, a no slip wall boundary condition was specified at the front and back of the box. On the *z-y* plane, corresponding to the cross-flow inlet, a uniform velocity profile and 0.3% turbulence intensity was defined (Huang and Yang, 1996). Downstream of this plane, outflow conditions were implemented where a zero value of the normal gradient for all flow variables, except the pressure, were specified. At the pipe inlet, a uniform fuel velocity was specified with a 5 % turbulence intensity, which is representative of the fully developed flow in the pipe. Stationary and no-slip wall boundary conditions were also specified at the top and bottom of the box. Free stream constant pressure boundary conditions were also investigated. However, the sensitivity of the results obtained from the converged results using either the wall or pressure boundary conditions was found to be negligible. This is partly because of the positioning of these boundaries, being sufficiently far from the jet flow and the reaction zone. The calculation was performed on the Advanced Reasearch Computer (ARC) at the University of Leeds and required a computing time of approximately 1500 hrs when 16GB RAM and 16-processor computing nodes was requested.

6.4 Results and discussion

6.4.1 Comparison of the results obtained from the turbulence models

Predictions of the pressure and velocity fields are shown in the form of pressure contours and velocity vectors in Figures 6-7 and 6-8 for the $k-\varepsilon$ realizable turbulence model and the Reynolds stress model, respectively. A comparison of the pressure contours show that the RSM is better able to resolve the pressure field, as seen from the pressure drop across the pipe (see appendix III (b)) as well as in the flow domain. Also, we observe that the low pressure region in the wake of the pipe is better resolved by the RSM. In Figure 6-8, the recirculation that occurs in the wake of the pipe due to the low pressure in this region has been captured by both the realizable $k-\varepsilon$ and the Reynolds stress models. However, we can observe that the Reynolds stress model was better able to resolve this flow pattern. This is because the resolution of the Reynolds stress components enables the RSM to resolve the complex turbulence interaction that occurs between the jet and the cross-flow. The magnitude and direction of the velocity vectors in Figure 6-8 shows the strength and the direction of the cross-flow, respectively. The complex interactions that occur between the jet, the cross-flow and the burner at the recirculation region can be observed form the vectors. The recirculation zone increases with an increase in the cross-flow velocity relative to the jet velocity (i.e. a decrease in the jet-to-cross-flow momentum ratio) since more flow is drawn into the low pressure region and this produces the so called “down-wash phenomena”, as observed by Castiñeira and Edgar (2008). The $k-\varepsilon$ realizable model was applied to model this interaction between the cross-flow and the jet for a methane/air cross-flow flame with good success (Lawal et. al., 2010). The present work applies the Reynolds stress model to a propane flame in cross-flow in order to show that the model can be applied to higher molecular weight hydrocarbon fuels with equally good results. A comparison of the combustion models that have been employed for the simulation is presented in the next section.

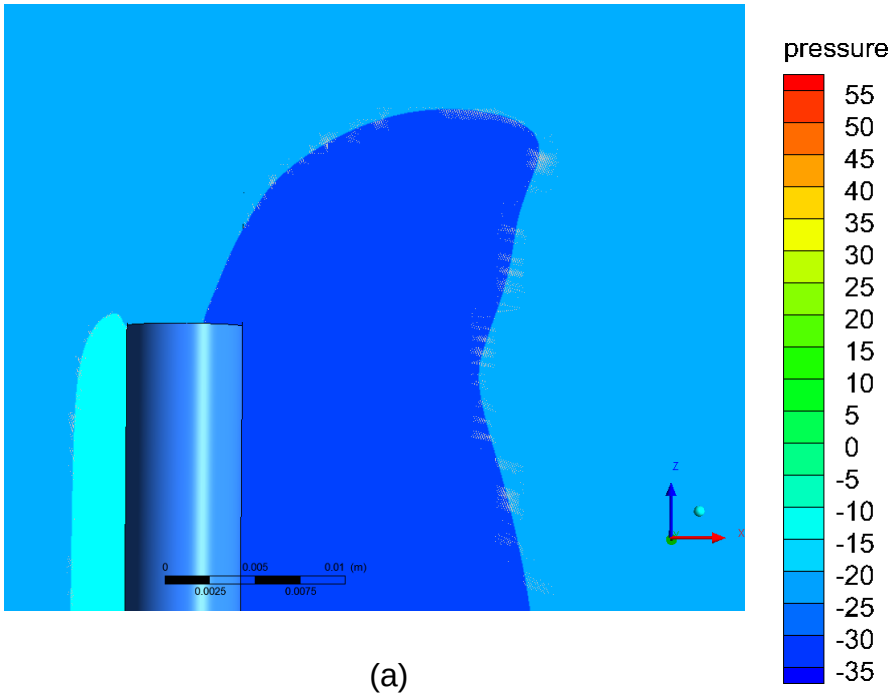

(a)

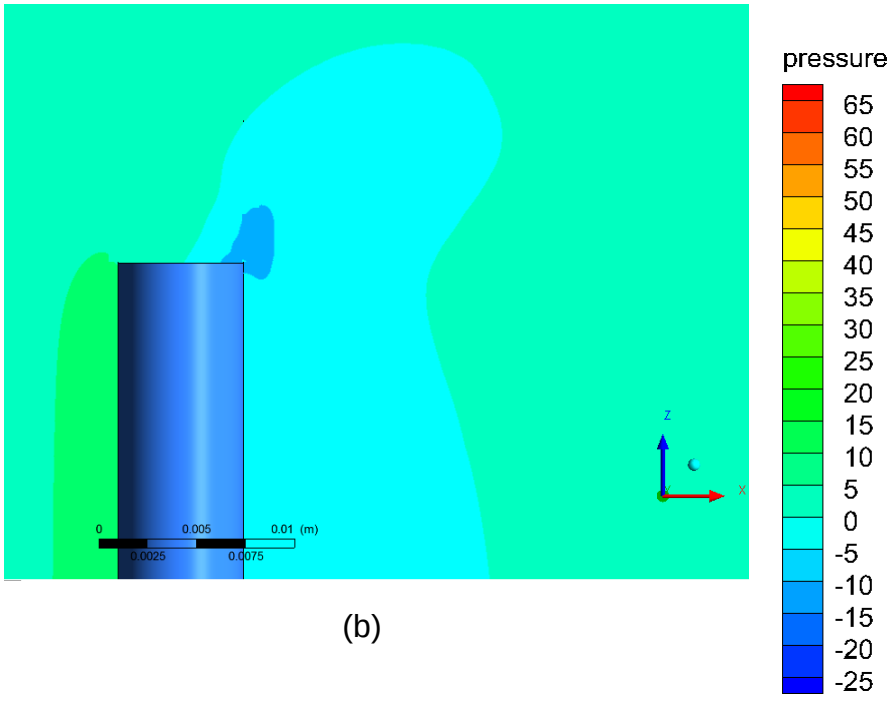

(b)

Figure 6-7 Pressure contours (Pa) showing the low pressure region at the wake of the pipe for (a) RSM, and (b) $k-\varepsilon$ realizable models, respectively. Pressure is highest at the pipe inlet (not shown).

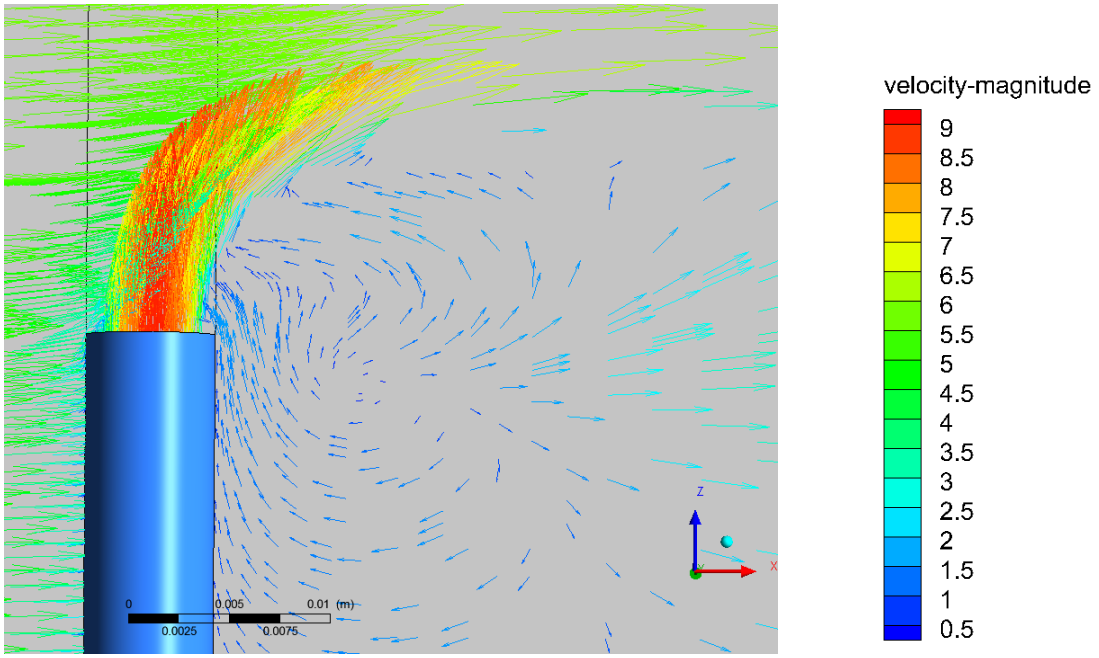

(a)

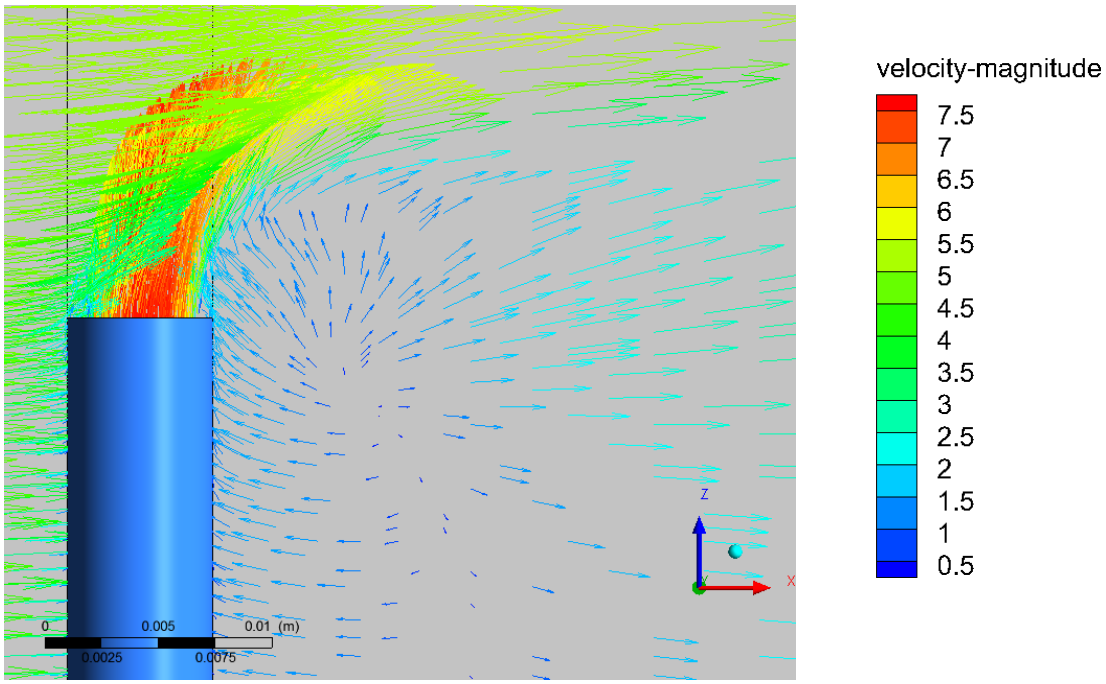

(b)

Figure 6-8 Velocity vectors (m/s) showing the recirculation zone at the wake of the pipe for (a) RSM, and (b) $k-\varepsilon$ realizable models, respectively.

6.4.2 Comparison of the results obtained from the combustion models

This section presents and discusses the results of the predictions made using the non-premixed and the partially premixed combustion models in conjunction with the Reynolds stress model (RSM). The predictions are validated against the experimental work of Huang and Yang (1996), where the authors reported the flame structure and the in-flame temperature and species concentrations measurements for a propane diffusion flame in cross-flow. The cases selected for simulation featured a wake-stabilized flame with a jet velocity, $u_f = 5.78$ m/s (R = 2.16) and a pre-blowoff case with a jet velocity $u_f = 14.0$ m/s (R = 12.82). Predictions of flame structures were performed for both cases and predictions of the inflame temperature and species concentrations were carried out for first case, and the results of the CFD predictions are presented in form of temperature contours as well as plots of temperature and species and these are discussed next.

6.4.2.1. Prediction of the flame structure of the cross-flow flames

Studies of wake-stabilized propane flames in a cross-flow of air have revealed a three-zone flame structure made up of a recirculating eddy attached to the lee-side of the pipe, a mixing layer of non-reacting fuel from the pipe carried over the eddy, and an axisymmetric main tail of the flame (Gollahalli & Nanjundappa, 1995). In this flow regime, the momentum of the cross-wind dominates the entrainment and mixing because of the low values of the jet momentum in comparison with the value of the cross-flow momentum. This produces a wake-stabilized flame, with a jet to cross-flow momentum ratio of 2.16 on the lee-side of the burner, as observed in the hand sketches of the top and side view of the flame made by Huang and Yang (1996) and shown in Figures 6-9 (a) and 6-10 (a), respectively. Lawal et al. (2010) performed a RANS simulation of a methane flame in cross-flow using the non-premixed combustion model in conjunction with the k-ε realisable model but was unable to predict the visible mixing layer of non-reacting fuel in the fuel-air shear layer. This was attributed to the draw-

backs of the non-premixed combustion model, one of which is that the model is unable to account for regions of the flame that are partially-premixed. Observation of the wake-stabilized flames reveal that they are loosely attached to the lee-side of the fuel pipe and this suggests that they are subject to lifting and reattachment on an intermittent basis, thus creating regions of partial premixing at the base of the flame. In view of this observation, the partially premixed model has been applied to model the wake-stabilized flame reported by Huang and Yang (1996). The predictions of the flame structure using the two combustion models namely the non-premixed and the partially premixed models, have been compared to the observations made by Huang and Yang (1996). A comparison of the predicted temperature contour (using steady state RSM simulation) is made with hand sketches of the visible flame in Figures 6-9 and 6-10 for the wake-stabilized flame ($u_f = 5.78$ m/s, and R = 2.16). It is clear from these figures that the partially premixed model has been able to reproduce the physical structure of the wake-stabilized flame, while the non-premixed model was unable to achieve this. Interestingly, the curve formed by the flame at the wake of the pipe as it intermittently detaches and reattaches itself to the wake of the burner has also been captured by the partially premixed model, as seen in Figure 6-9 (a). This is akin to a lift-off and reattachment behaviour in a straight jet flame, which occurs primarily due to the effect of the premixing of the fuel and air at the base of the flame. This could explain the capability of the partially premixed model in capturing the shape of the flame at this location. Huang and Yang have described the shape of the flame in this near burner region as being in a “dual mode” due to the split that occurs in the flame in this region. Furthermore, the necking of the flame and the further expansion of the combustion region downstream of the flame has also been resolved by the partially premixed model. This can be better visualized from an aerial view of the pipe, as shown in Figure 6-10 (b). From this view, we can observe the necking of the flame more clearly at about 5 mm < x < 10 mm, with the flame expanding further downstream of the pipe. Huang and Yang calculated that the neck has a width of about $0.75d_i$ and they also observed that the combustion around

the neck of the flame was very violent. In addition, Huang and Yang (1996) have depicted a slight detachment of the flame from the burner in the aerial sketch and the partially premixed model has also captured this behaviour rather well, especially in the core of the flame where the flame attains a temperature of about 1800 K and higher, thus making the flame more luminous and visible in this region due to the combustion of the soot particles. The non-premixed combustion model on the other hand severely over predicts the spreading rate in the flame, as seen from the side view. This is also visible from an aerial view of the burner where we observe that the flame expands significantly in the near burner region and continues to expand further downstream. The non-premixed model on the other hand was not able to capture the necking of the flame as depicted in the hand sketch. Furthermore, we see that the down-washed region was much larger for the non-premixed model. Such a large down wash region is usually associated with flames of lower jet to cross-flow momentum ratios in the range of about 0.04 to 1.6 (Huang and Wang, 1999). In such cases, the jet momentum is not strong enough to sustain the impingement and shear effects of the cross-flow, hence the jet is deflected through a large angle from the vertical axis of the tube. Also, the slight detachment of the flame from the burner-wake which was observed by Huang and Yang was not captured by the non-premixed model ((Figure 6-9 (c)). In contrast, we observe that the flame is firmly attached to the wake of the pipe, up to a distance of about 30 mm below the pipe exit. The peak average temperature attained in the flame can be seen from the temperature scale to be about the same value for both models (2000 K or 1750 ^{0}C), which is consistent with the experimentally observed peak temperatures in a propane/air diffusion flame. Both the partially premixed and the non-premixed combustion models employ the mixture fraction approach in the mathematical formulation of the combustion equation. However, the partially premixed model also incorporates the reaction progress variable approach which is used in modelling premixed flames. The partially premixed model solves a transport equation for the mean reaction progress variable $\bar{c}$, as well as the mean mixture fraction $\bar{z}$, and the mean mixture fraction variance $\bar{z}'^2$.

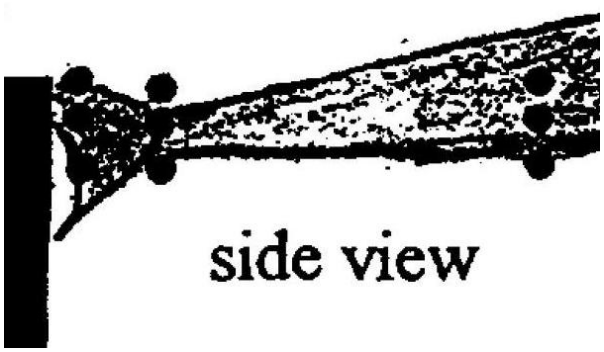

(a)

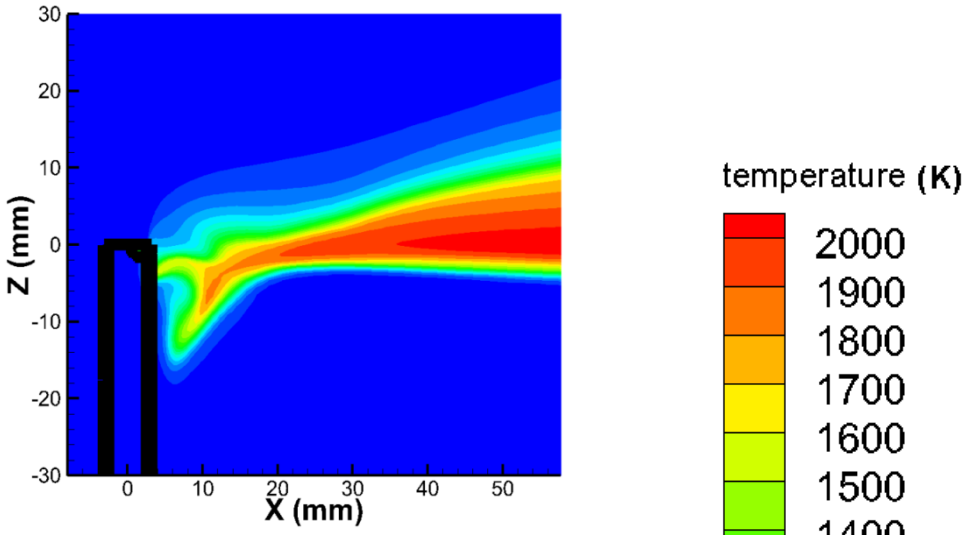

(b)

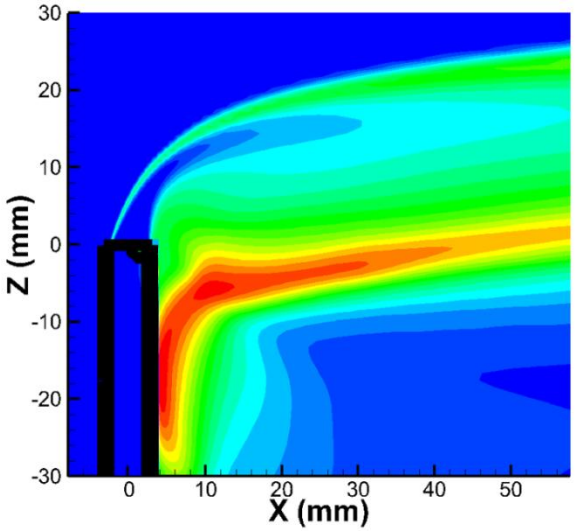

(c)

Figure 6-9 (a) Side view of the wake-stabilized flame (Huang & Yang, 1996), (b) Temperature contour, partially premixed model, and (c) Temperature contour, non-premixed model at u_f = 5.78 m/s, u_{cf} = 4.86 m/s, and R = 2.16.

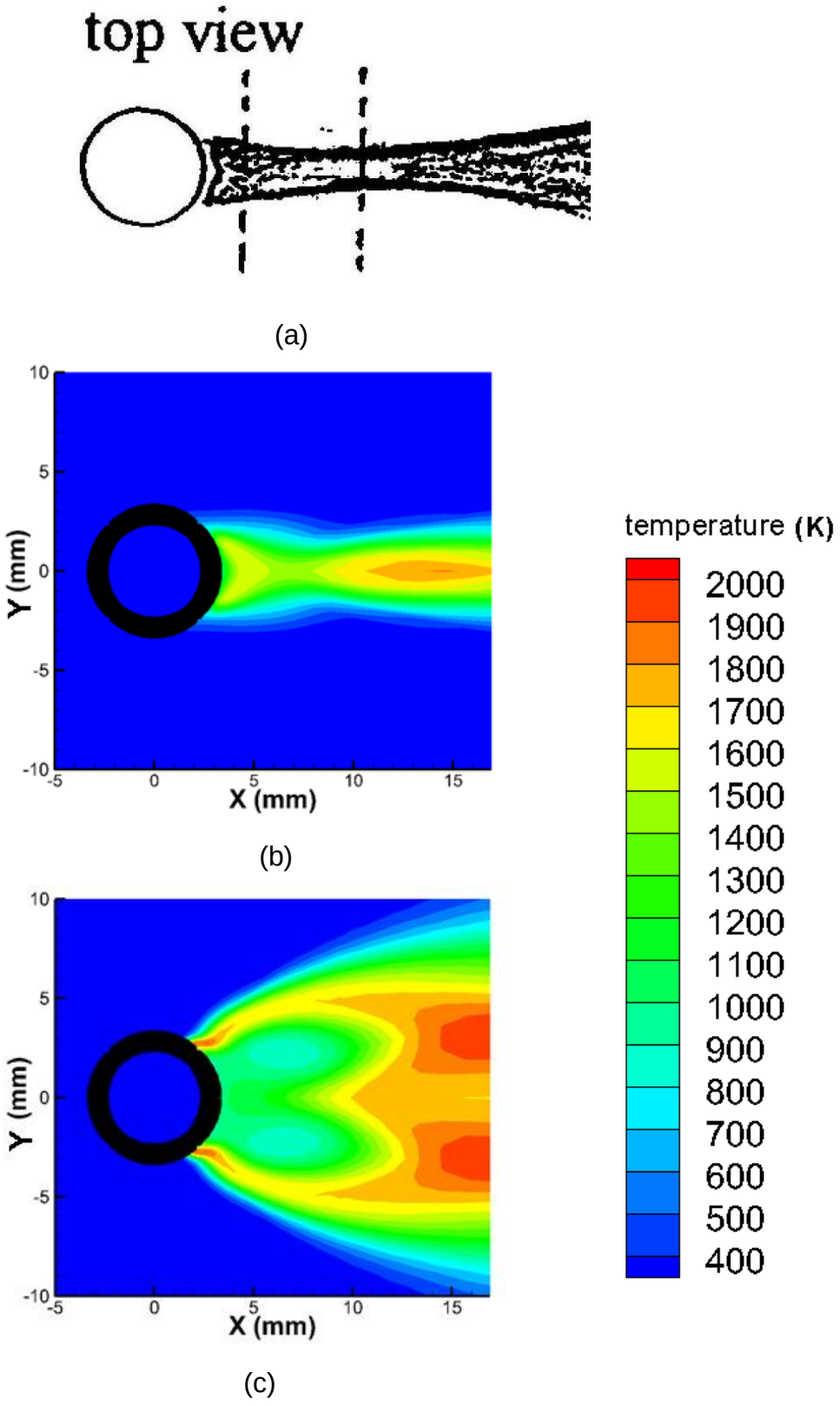

Figure 6-10 (a) Top view of the wake-stabilized flame (Huang & Yang, 1996), (b) Temperature contour, partially premixed model, (c) Temperature contour, non-premixed model at u_f = 5.78 m/s, u_{cf} = 4.86 m/s, and R = 2.16.

Figures 6-11 and and 6-12 show the contour of the temperature for the pre-blowoff case ($u_f = 14$ m/s, and R = 12.82), which Huang and Yang (1996) also investigated. At such high values of the jet-to-cross-flow momentum ratios, the momentum of the jet dominates over the momentum of the cross-flow. The downwash region completely disappears and the flame becomes completely detached from the burner as seen in the hand sketches of Huang and Yang (1996) (Figures 6-11 (a) and 6-12 (a)). This behaviour has been captured by the partially premixed model to some extent, where we observe the initial detachment of the flame from the burner (Figure 6-11 (b)). This is similar to the aerodynamic induced lift-off observed in straight jet flames. Furthermore, Figure 6-12 (b) shows the prediction for the partially premixed model from the top of the pipe, where we can observe that the large spreading rate in the hand sketch (Figure 6-12 (a)) has also been captured by the model. Furthermore, the separation that occurs in the flame, downstream of the pipe has also been captured by the partially premixed model. However, the spread of the flame has a “concave” shape while the model produced a “convex-shaped” spread. Also, Huang and Yang (1996) observed a rapid lowering of the flame temperature with an increase in the fuel jet velocity prior to blowoff. They observed that the maximum flame temperature at a velocity of 14 m/s was about 1700 K and this value decreased to about 1100 K at a velocity of 16 m/s, at which point the flame blows off. This has also been observed with the partially premixed model, where the temperature was observed to decrease with increasing jet velocity. The non-premixed model also showed this decrease in the flame temperature with an increase in the jet velocity, however the shape of the flame was poorly predicted by the model as seen from Figure 6-12 (c). Predictions of the thermo-chemical structure of the flame was also made and compared with the experimental measurements of Huang and Yang (1996). The predictions of the temperature were made at four locations in the flame namely x = 8.2 mm, z = 0; x = 8.2, z = 7 mm; x = 23.2, z = 3 mm and x = 183.2 mm, z = 0, while measurement of species were made at the first three locations. The results of the comparison made are presented in the next section.

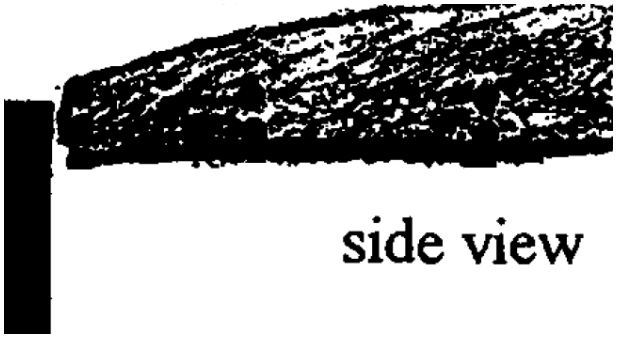

(a)

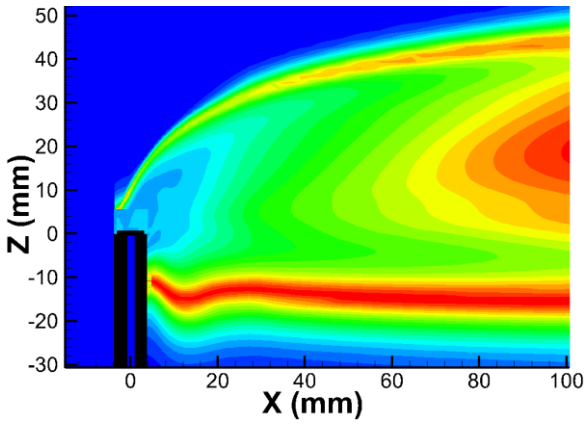

(b)

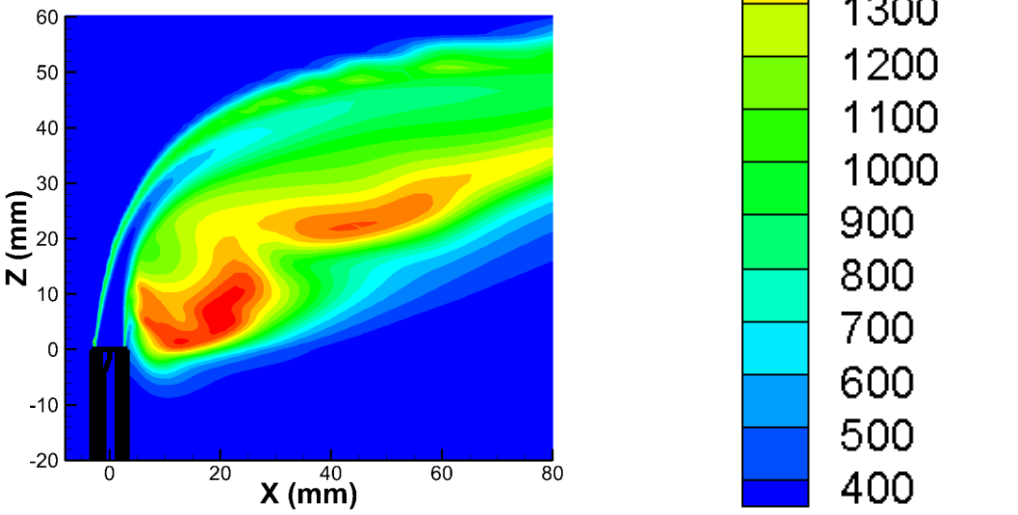

(c)

Figure 6-11 (a) Side view of the pre-blowoff flame (Huang & Yang, 1996), (b) Temperature contour, partially premixed model, and (c) Temperature contour, non-premixed model at $u_f = 14.0$ m/s, $u_{cf} = 4.86$ m/s, and $R = 12.82$.

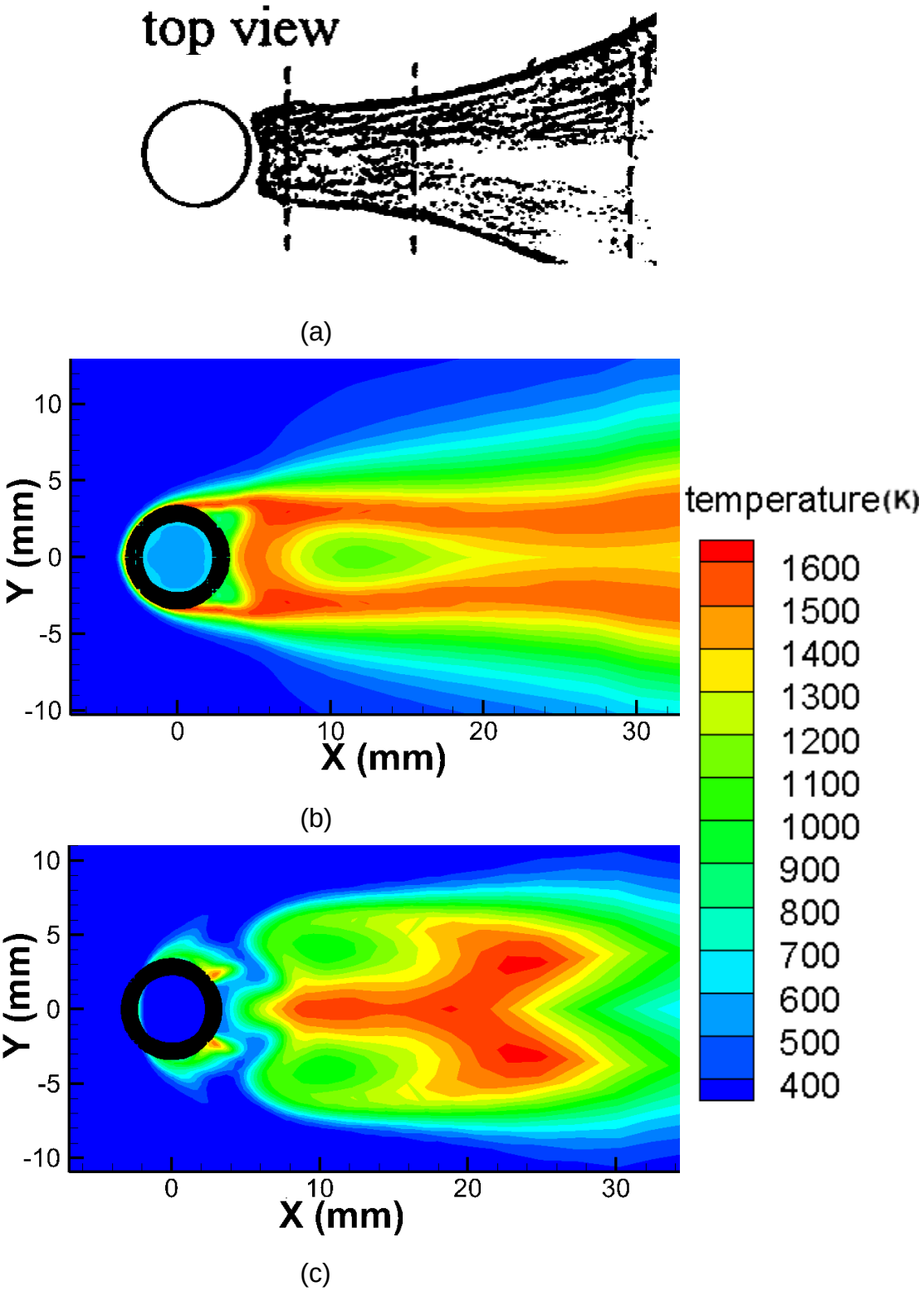

Figure 6-12 (a) Top view of the pre-blowoff flame (Huang & Yang, 1996), (b) Temperature contour, partially premixed model, and (c) Temperature contour, non-premixed model at $u_f = 14.0$ m/s, $u_{cf} = 4.86$ m/s, and $R = 12.82$.

6.4.2.2. Prediction of the temperature in the wake-stabilized flame

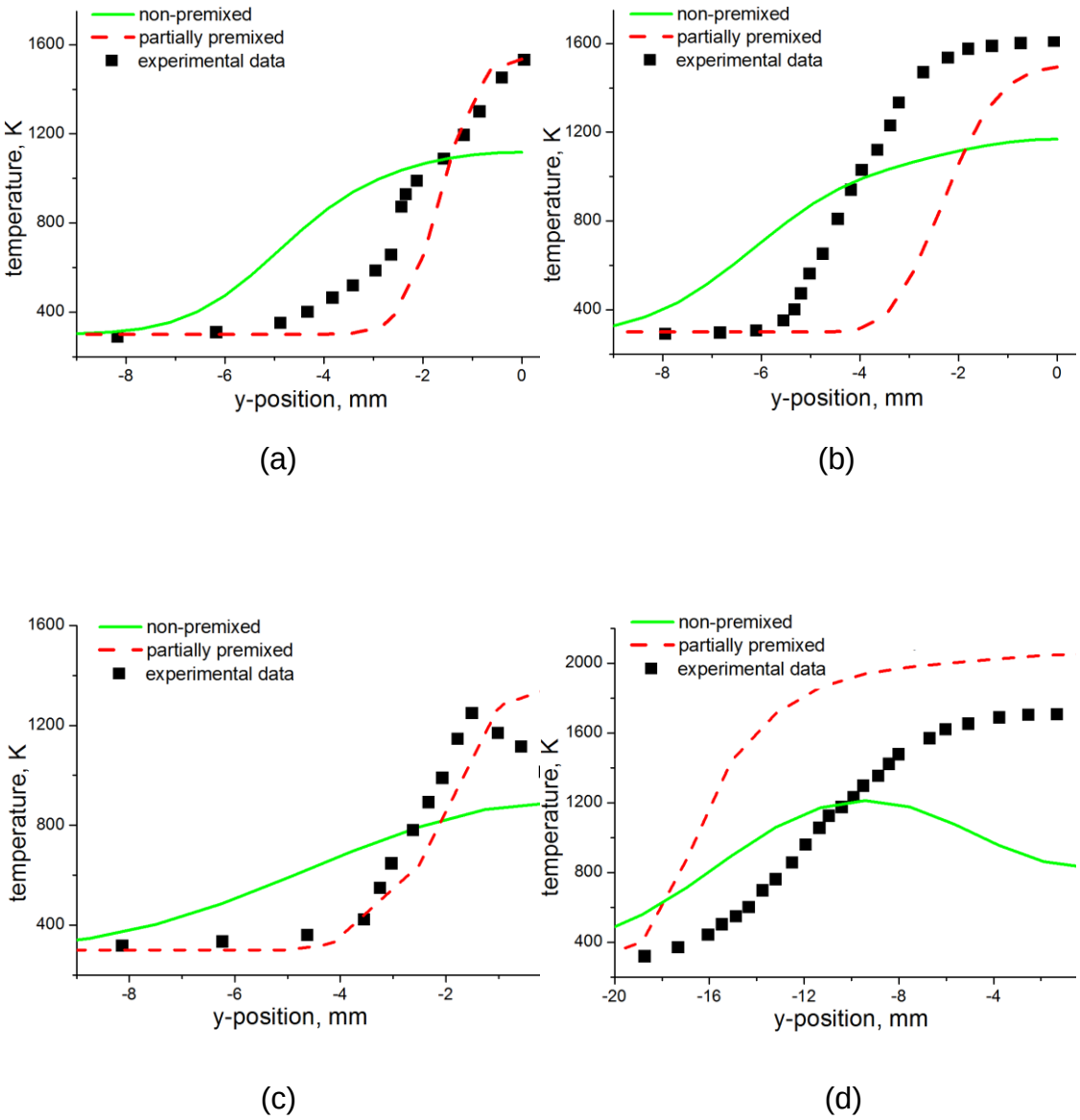

Figure 6-13 RSM predictions of the temperature for a wake-stabilized propane flame using the non-premixed and the partially premixed combustion models at (a) x=8.2 mm, z=0 (b) x=8.2, z=7 mm, (c) x=23.2, z=3 mm, and (d) x= 183.2 mm, z=0.

Figures 6-13 (a) – (d) show the predictions of the temperature as a function of position in the y-direction at four selected locations in the flame using the non-premixed and the partially premixed combustion models for the wake-stabilized case (u_f = 5.78 m/s, and R = 2.16). The predictions made

with the partially premixed model show a good agreement with the experimental data of Huang and Yang (1996) at the near burner region of x = 8.2 mm, z = 0, and further downstream at x = 23.2, z= 3 mm (Figures 6-13 (a) and (c)). The experimental data shows that the peak temperature is almost the same at all the measurement locations (about 1600 K), except at x = 23.2, z = 3 mm, where the temperature decreases to about 1200 K at y = -2 mm. A further decrease was observed in the temperature to about 1100 K at y = 0. This trend was not captured by the partially premixed model at this position, where the the temperature continued to increase at y = -2 mm, instead of reducing. The trend of the temperature predictions at x= 8.2, z = 7 mm and at x = 183.2, z = 0 (Figures 6-13 (b) and (d)) match the experimental data for the partially premixed mode. However the partially premixed model produced a large spreading rate in the predictions at this location as well as an over-prediction of the centreline temperature at x = 183.2, z = 0. This could be attributed to the increased turbulence in the far field (i.e. at x = 183.2, z = 0) due to the increased air entrainment, as well as the strong mixing in the shear layer downstream of the pipe at x= 8.2, z = 7 mm, which the partially premixed model could not capture. However the observation that the flame becomes wider as one progresses from the base of the flame towards the flame tip has been captured by the partially premixed model, and this can also be interpreted from the temperature plots, where the temperature is about 1600 K at y = -4 mm, for x = 183.2, z = 0 (Figure 6-13 (d)), while the temperature at the same position for x= 8.2, z = 7 mm (which is closer to the base of the flame) was about 400 K. The non-premixed model on the other hand has failed to reproduce the experimental trend at any of the selected locations in the flame. The temperatures at the flame axis (y = 0) has been under-predicted by the model, however the predictions of the non-premixed model were slightly better at the near field than at the far field just as obtained with the partially premixed model. The poor performance of the models at the far field could also be due to the higher turbulence from the effect of the cross-wind.

6.4.2.3. Prediction of the species in the wake-stabilized flame

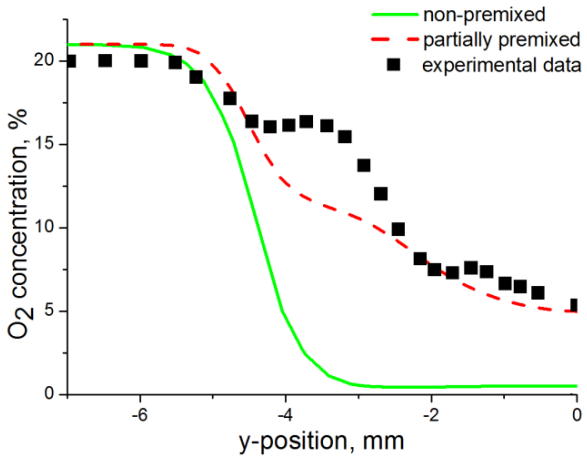

(a)

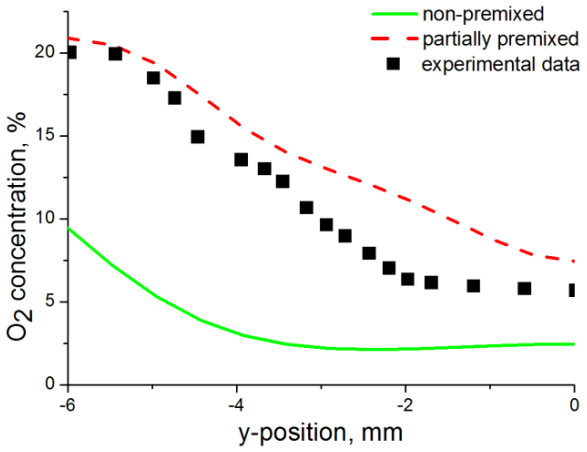

(b)

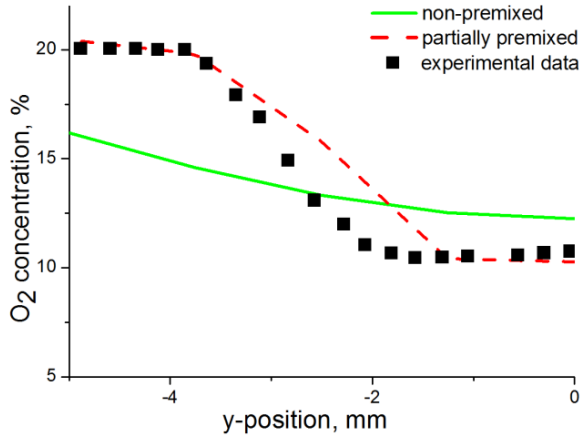

(c)

Figure 6-14 RSM predictions of the oxygen in a wake-stabilized propane flame using the non-premixed and the partially premixed combustion models at (a) x=8.2 mm, z=0 (b) x=8.2, z=7 mm, and (c) x=23.2, z=3 mm.

Figures 6-14 (a) – (c) show the predictions of the concentration distribution of the oxygen as a function of the position in the y-direction at three selected locations in the flame using the non-premixed and the partially premixed combustion models for the wake-stabilized case ($u_f = 5.78$ m/s, and R = 2.16). The trend in the concentration distribution of oxygen, as shown in the experimental data has been matched by the partially premixed model at the three locations in the flame, especially at x= 8.2, z = 0 and at x= 8.2, z = 7 mm, where there is a good fit to the experimental data, except at -4 mm < y < -2 mm and at -3 mm < y < -1.5 mm, for the former and the latter case, respectively (Figures 6-14 (a and (d)). The experimental data shows that the peak concentration of oxygen occurred at -6 mm for the locations at (a) and (b), which are both at x = 8.2 mm, while the peak occurred at -4 mm for the location at (c), which is at x = 23.2 mm. This observation can also be made from the predictions made with the partially premixed model, and this is expected, given that the flame becomes wider away from its base and towards the tip. Therefore the concentration of oxygen downstream of the flame will be higher than that in the near burner region. Furthermore, it can also be oberved in the predictions with the partially premixed model that the oxygen concentration at the flame centreline (y = 0) is higher at x = 23.2 mm (about 10 %) than it is for the locations at x = 8.2 mm (about 5 %). This again is expected given that the entrainment of air into the flame increases downstream of the pipe due to the increased turbulence. It should also be noted that the relatively lower temperature at this location (Figure 6-14 (c)) indicates that less soot is generated there, and hence less oxygen is consumed due to soot oxidation, which contributes to the increased oxygen concentration at this location. The decrease in the oxygen concentration from its normal value of 21 % in the free stream to a value of 5 % and 10 % (at x = 8.2 and 23.2 mm, respectively) inside the flame is consistent with other works that have been performed on cross-flow propane diffusion flames (Gollahalli et al., 1982; Turns and Lovett, 1989). The non-premixed model on the other hand was not able to correctly predict the oxygen trend in the flame at x= 8.2, z = 7 mm, and at x= 23.2, z = 3 mm, except at x= 8.2, z = 0 between -7 mm < y < -4 mm.

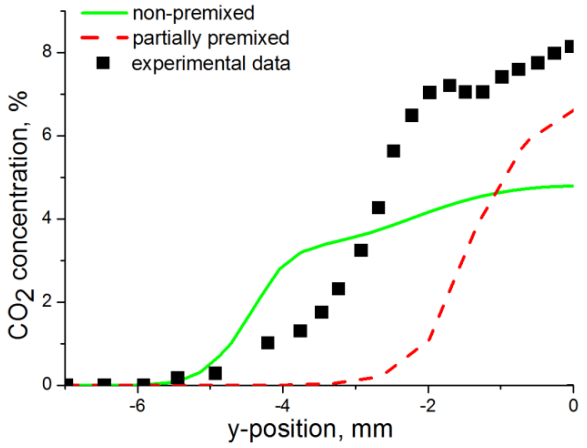

(a)

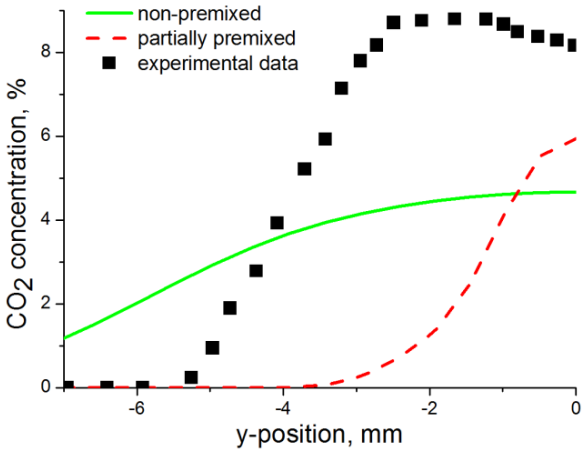

(b)

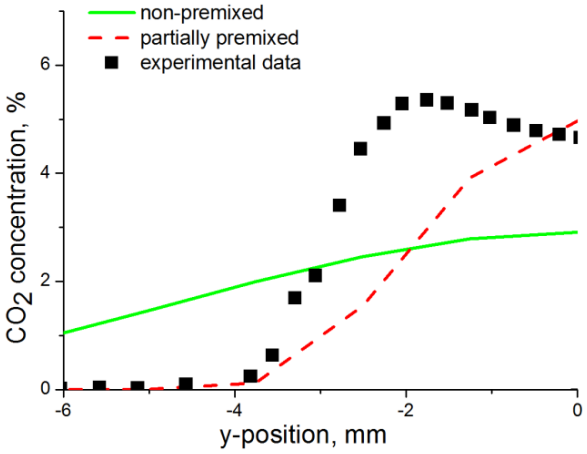

(c)

Figure 6-15 RSM predictions of the carbon dioxide in a wake-stabilized propane flame using the non-premixed and partially premixed combustion models at (a) x=8.2 mm, z=0 (b) x=8.2, z=7 mm, and (c) x=23.2, z = 3 mm.

Figures 6-15 (a) – (c) show the predictions of the concentration distributions of the carbon dioxide as a function of the position in the y-direction at three selected locations in the flame using the non-premixed and the partially premixed combustion models for the wake-stabilized case ($u_f = 5.78$ m/s, and R = 2.16). The trend of the experimental data is correctly predicted by the partially premixed model at the selected locations, where we observe an increase in the concentration of the carbon dioxide from almost zero in the free stream to its peak value at the flame centreline (near burner location). The experimental data shows that the peak value of carbon dioxide in the flame does not occur at the flame centreline (y = 0) for the locations at x = 8.2, z = 7 mm and at x = 23.2, z = 3 mm, but had higher values at the off-axis position of 2 mm (Figure 6-15 (b) and (c)). This trend was not captured by the partially premixed model and furthermore the partially premixed model produced a large spreading rate at the selected locations, especially at x = 8.2, z = 7 mm. The experimental data shows that the centreline concentration of carbon dioxide in the downstream region x = 23.2, z = 3 mm is lower than the centreline concentration in the near burner region x = 8.2, z = 0 (5 % and 8 % respectively). This is in contrast to the observation made in the trend of the oxygen concentration, where we see a higher centreline concentration of oxygen in the downstream region x = 23.2, z = 3 mm. This trend has been captured by the partially premixed model where we observe that the centreline concentration of carbon dioxide is about 7 % in the near burner region (an under prediction of about 12 %) and the centreline concentration further downstream at x = 23.2, z = 3 mm was about 5 % (which is in agreement with the experimental data). The predictions of the non-premixed model on the other failed to match the experimental trend, except at the near burner region (Figure 6-15 (a)) where there is a good trend between - 7 mm < y < -4 mm. There is a similar trend in the predictions of the non-premixed model at = 8.2, z = 7 mm and at x = 23.2, z = 3 mm, where there is large over-prediction of the ambient concentration of carbon dioxide (about 1 % as against an ambient value of 0.05 %).Further, the centreline concentration of carbon dioxide was poorly predicted by the non-premixed model at all the measurement locations.

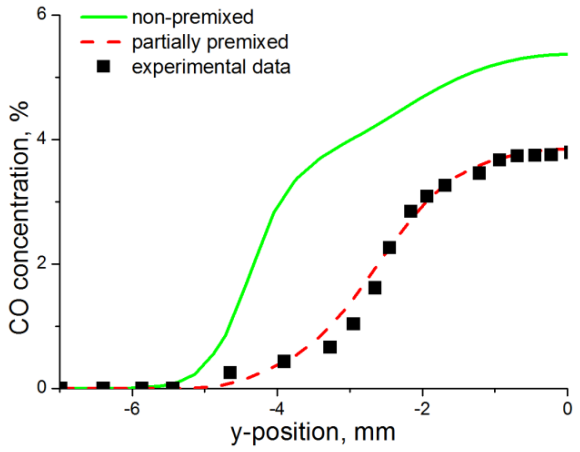

(a)

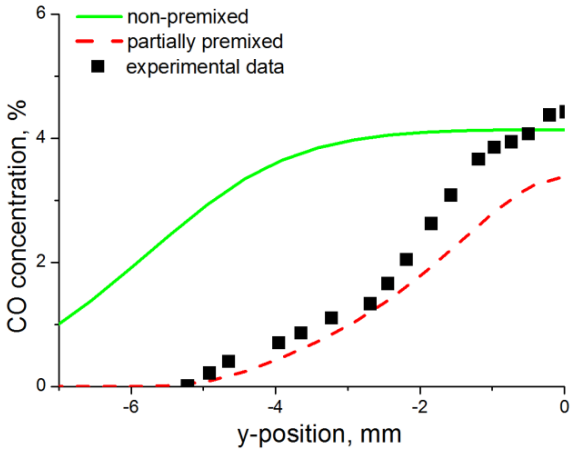

(b)

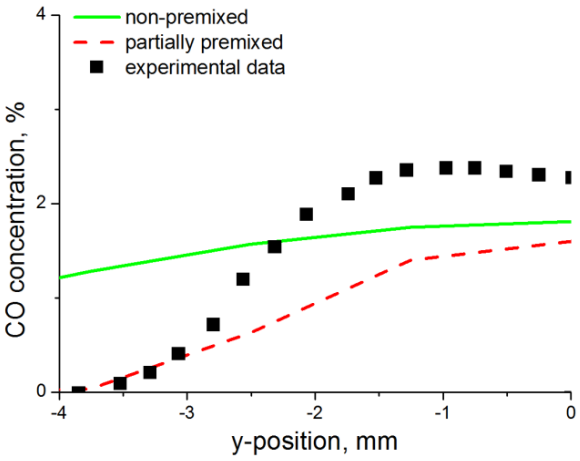

(c)

Figure 6-16 RSM predictions of the carbon monoxide in a wake-stabilized propane flame using the non-premixed and partially premixed combustion models at (a) x=8.2 mm, z=0 (b) x=8.2, z=7 mm, and (c) x=23.2, z=3 mm.

Figures 6-16 (a) – (c) show the predictions of the concentration distributions of the carbon monoxide as a function of the position in the y-direction at three selected locations in the flame using the non-premixed and the partially premixed combustion models for the wake-stabilized case (u_f = 5.78 m/s, and R = 2.16). Again, as for the carbon dioxide, the trend of the experimental data is correctly predicted by the partially premixed model at the selected locations, where we observe an increase in the concentration of the carbon monoxide from almost zero in the free stream to its peak value at the flame centreline for all the measurement locations. However, in contrast to the carbon dioxide, the fit of the predicted data to the experimental data is much better for the carbon monoxide predictions, especially at the near burner location x = 8.2, z = 0. The centreline concentrations of carbon monoxide is also observed to be higher at the near burner location of x = 8.2 mm, z = 0, than at the downstream location of x = 23.2, z = 3 mm, (4 % and 2 %, respectively) which the partially premixed model has correctly predicted. However, there was an under-prediction of the carbon monoxide concentration by 25 % at x = 23.2, z = 3 mm. The ambient value of the carbon monoxide was also accurately predicted by the partially premixed model at all the measurement locations. Carbon monoxide is usually oxidized to carbon dioxide in the flame, hence it is expected that the concentration of carbon monoxide will be lower than that of carbon dioxide, especially downstream of the flame where there is increased oxygen concentration due to air entrainment. Carbon monoxide, unlike carbon dioxide is a poisonous gas and hence its oxidation to carbon dioxide is of vital importance. Predictions with the non-premixed model showed a good trend with the experimental data at the near burner location x = 8.2 mm, z = 0 (Figure 6-16 (a)), with the model correctly predicting the ambient concentration of carbon monoxide between - 7 mm < y < - 5 mm. However, there is a large over prediction between - 5 mm < y < 0. Further downstream of the pipe, at x = 8.2, z = 7 mm, and at x = 23.2, z = 3 mm (Figures 6-16 (b) and (c) respectively), the predictions of the non-premixed model completely deviates from the experimental trend, with a large over-prediction of the carbon monoxide concentration.

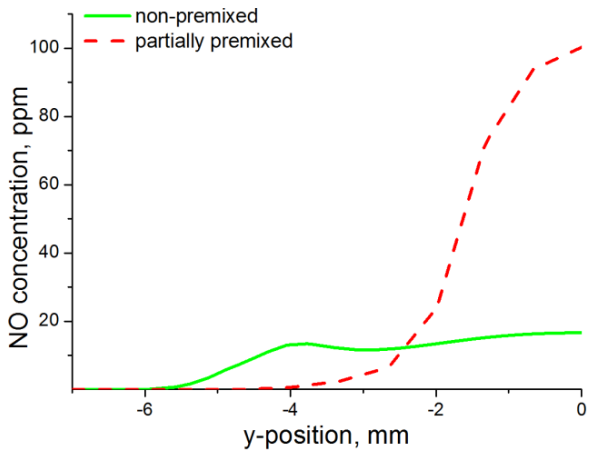

(a)

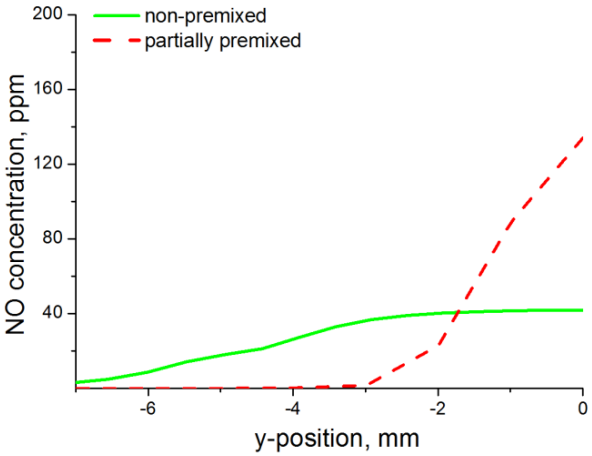

(b)

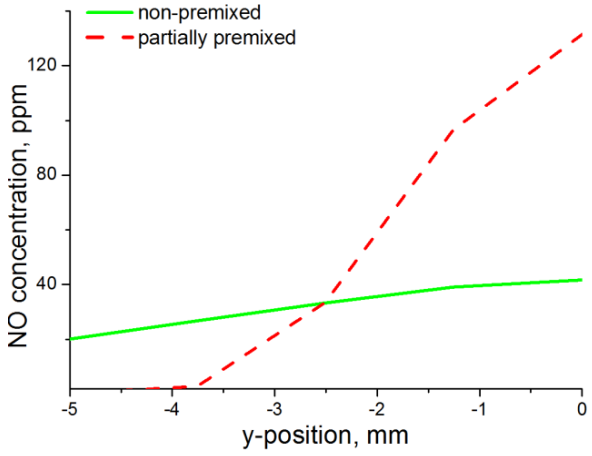

(c)

Figure 6-17 RSM predictions of the nitrogen oxide in a wake-stabilized propane flame using the non-premixed and partially premixed combustion models at (a) x=8.2 mm, z = 0 (b) x=8.2, z=7 mm, and (c) x=23.2, z=3 mm.

Figures 6-17 (a) – (c) show the predictions of the concentration distributions of the nitrogen oxide as a function of the position in the y-direction at three selected locations in the flame using the non-premixed and the partially premixed combustion models for the wake-stabilized case ($u_f = 5.78$ m/s, and R = 2.16). Huang and Wang (1996) did not provide experimental measurements for the nitrogen oxide, however the predicted results will be presented here. The predictions of nitrogen oxide concentration obtained from the partially premixed combustion model gives a more reasonable trend than the predictions obtained from the non-premixed combustion model. The predictions from the partially premixed model show that the centreline concentration of the nitrogen oxide is about 40 % higher at x = 23.2, z = 3 mm than at x = 8.2, z = 0, and this is expected given that the concentration of nitrogen oxide in the flame is usually lower upstream of the flame (near nozzle region) where the temperature is lower. The experimental work performed in chapter 5 shows that the concentration of nitrogen oxide is about 70 – 80 ppm for the vertical propane jet diffusion flame investigated. The value obtained for the present cross-flow simulation (with a burner of a similar dimension and a fuel jet velocity comparable to that used in chapter 5) show that the effect of the cross-flow can almost double the nitrogen oxide concentration in the flame. A similar observation has been made by Bandaru and Turns (2000), where they studied the NO_x emissions from the vertical and cross-flow propane diffusion flames and reported that the flames subjected to a cross-flow produced higher NO_x emissions with levels that are typically two or three times greater than those produced by similar straight jet flames. They postulated that substantially less soot is formed in the flames due to the cross-flow (i.e. there is increased soot oxidation due to increased air entrainment), and this in turn makes the flame less radiative and thus hotter, which in turn, leads to the higher NOx emissions.

The LES is a flow model that is capable of producing improved predictions in both the thermo-chemical and the physical structure of the flame and this method has also been investigated in this thesis. The results and discussion on the LES investigation is presented in the next section.

6.4.3 The LES results for the wake-stabilized cross-flow propane flame

The LES resolves the large scale eddies in the flow and hence the Navier-Stokes equation is solved in real time, unlike the RSM model which is time-averaged. Further, LES resort to the modelling of the smaller scale eddies and this makes the LES method more tractable in comparison with the DNS approach which resolves all the time scales. Nevertheless, LES is still a costly approach in terms of the computer resources and simulation time required. Several models are available for modelling the sub-grid scale eddies and the Smagorinsky model (1963) has been adopted in this work. The results of the LES simulation for the wake-stabilized flame in conjunction with the partially premixed combustion model are presented in Figures 6-18 to 6-22 and they are compared with the results of the predictions from the RSM model. It is observed that all the LES predictions are better than the RSM predictions at the upstream locations of x = 8.2 mm, z = 0, and x = 8.2, z= 7 mm. This is most apparent for the temperature prediction at x = 8.2 mm, z= 7 mm (Figure 6-18 (b)) where the large spreading rate produced by the RSM between -6 mm $\leq$ y $\leq$ 0 mm was well resolved by the LES. The peak temperature predicted by the LES was also in the same range as that obtained with the RSM. Predictions of temperature at the downstream location x = 23.2 mm, z = 3 mm show a good trend with the experimental data for the RSM predictions, except for $-1 \leq y \leq 0$ where the predicted temperature profile began to increase instead of decreasing. However, the trend of the LES was not so good at this position, especially at $-3 \leq y \leq 0$, where we observe a deviation from the experimental trend. The predictions of the oxygen concentration was also very good for the LES at all the measurement locations, especially at x = 8.2 , z = 7 mm (Figure 6-19 (b)) and at x = 23.2, z= 3 mm (Figure 6-19 (c)), where we observe a very good fit to the experimental data. However, at x = 8.2 mm, z= 0 (Figure 6-19 (a)), we observe a high fluctuation in the flame (as shown by the experimental data) which the RSM could not resolve at $-4 \leq y \leq 2$. However, The LES resolved this trend at this position, but was unable to resolve this further upstream of the flame.

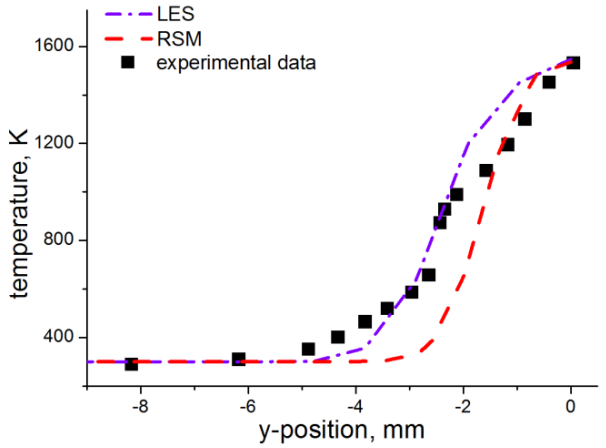

(a)

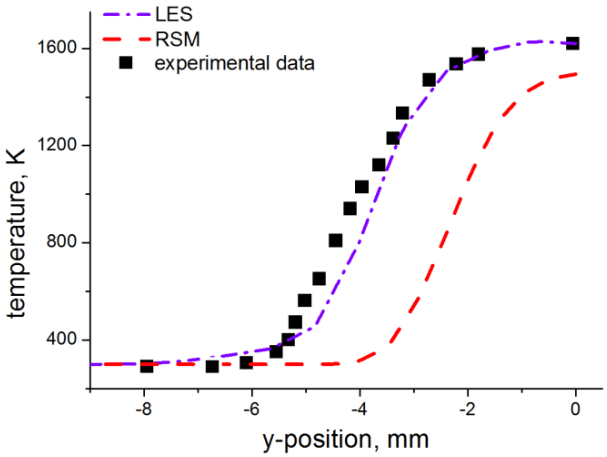

(b)

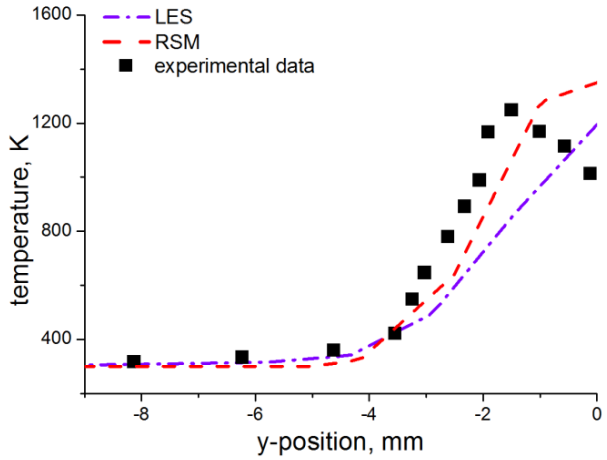

(c)

Figure 6-18 LES and RSM predictions of the temperature in a wake-stabilized propane flame using the partially premixed combustion model at (a) x = 8.2 mm, z = 0 (b) x = 8.2, z = 7 mm, and (c) x= 23.2, z = 3 mm.

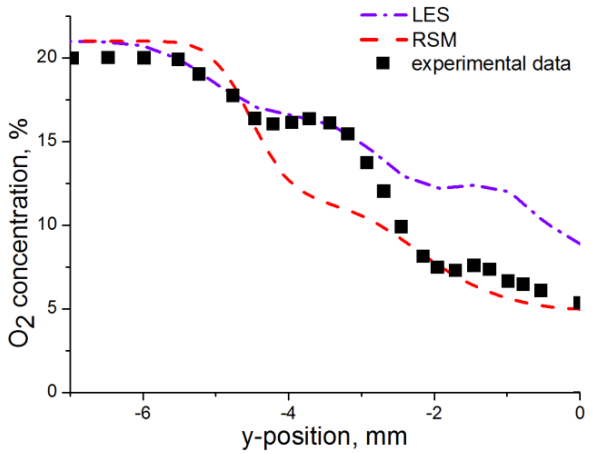

(a)

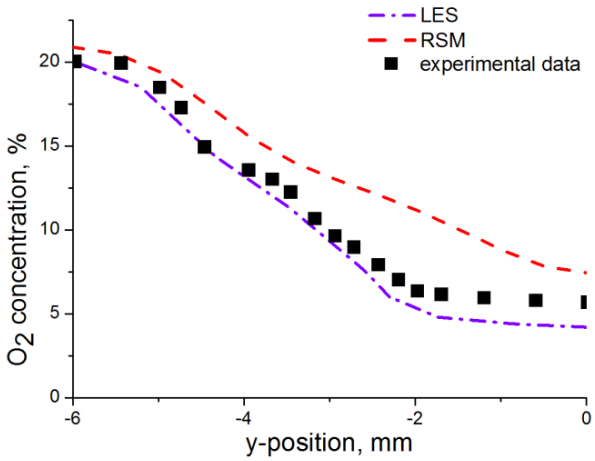

(b)

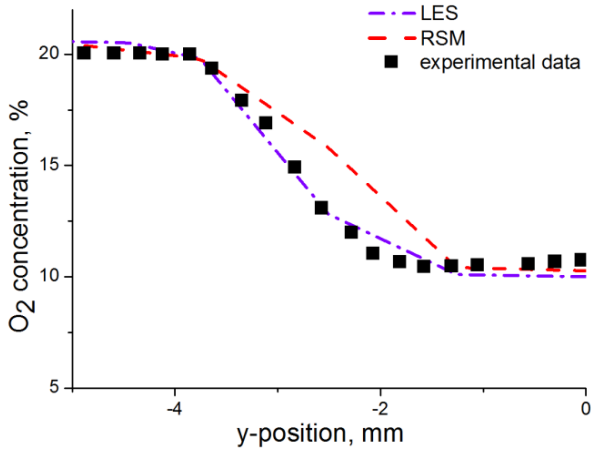

(c)

Figure 6-19 LES and RSM predictions of the oxygen in a wake-stabilized propane flame using the partially premixed combustion model at (a) x = 8.2 mm, z = 0 (b) x = 8.2, z = 7 mm, and (c) x= 23.2, z = 3 mm.

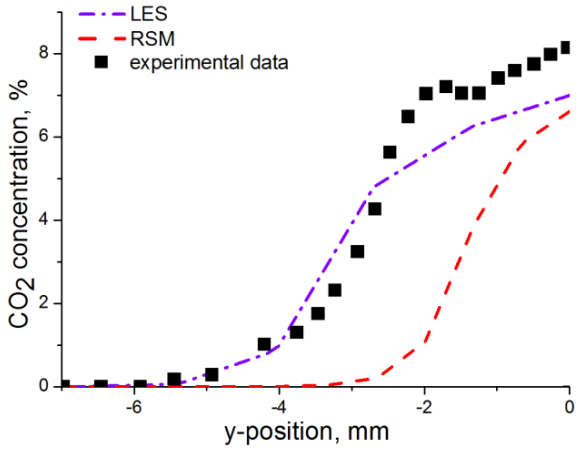

(a)

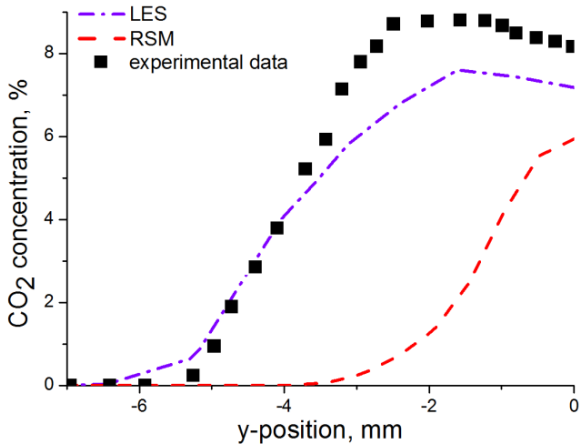

(b)

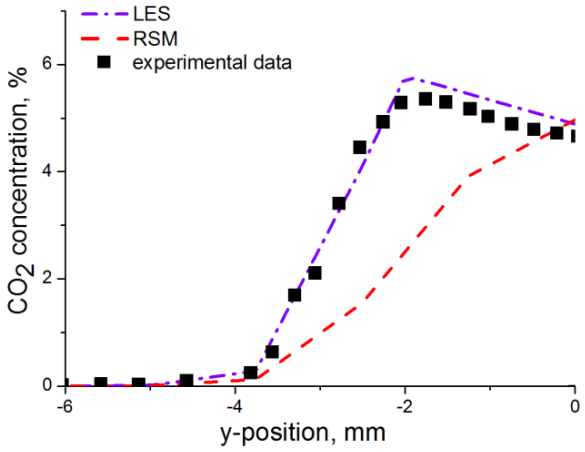

(c)

Figure 6-20 LES and RSM predictions of the carbon dioxide in a wake-stabilized propane flame using the partially premixed combustion model at (a) x = 8.2 mm, z = 0 (b) x = 8.2, z = 7 mm, and (c) x= 23.2, z = 3 mm.

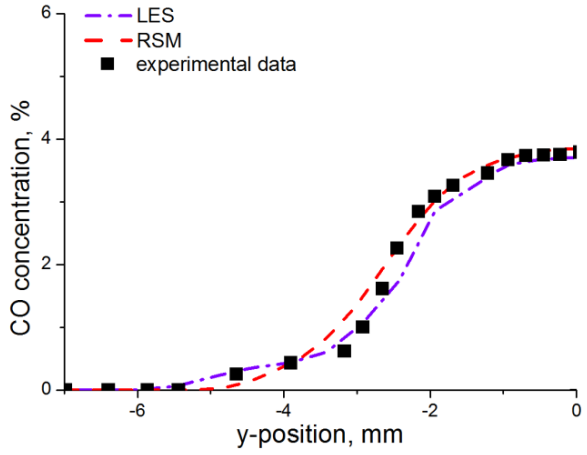

(a)

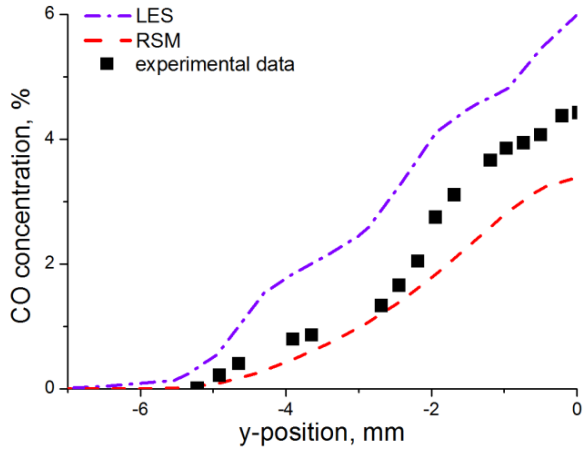

(b)

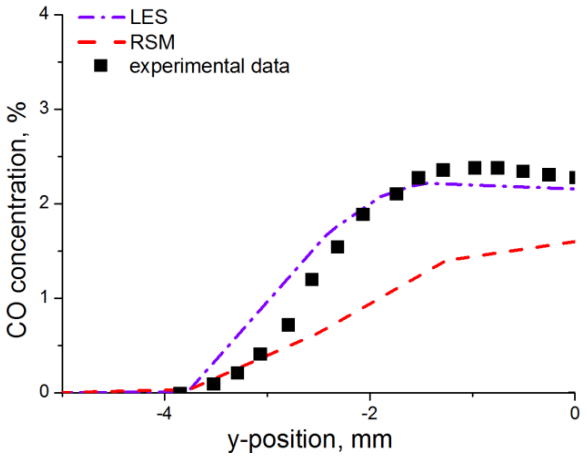

(c)

Figure 6-21 LES and RSM predictions of the carbon monoxide in a wake-stabilized propane flame using the partially premixed combustion model at (a) x = 8.2 mm, z = 0 (b) x = 8.2, z = 7 mm, and (c) x= 23.2, z = 3 mm.

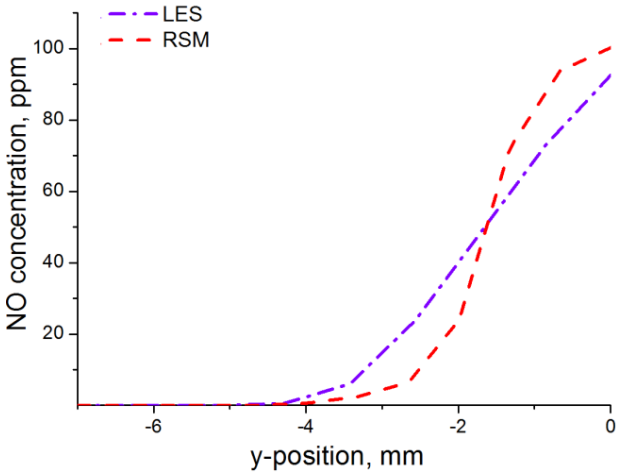

(a)

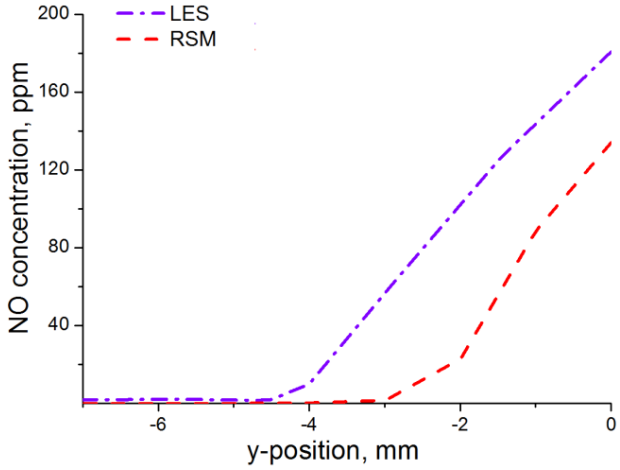

(b)

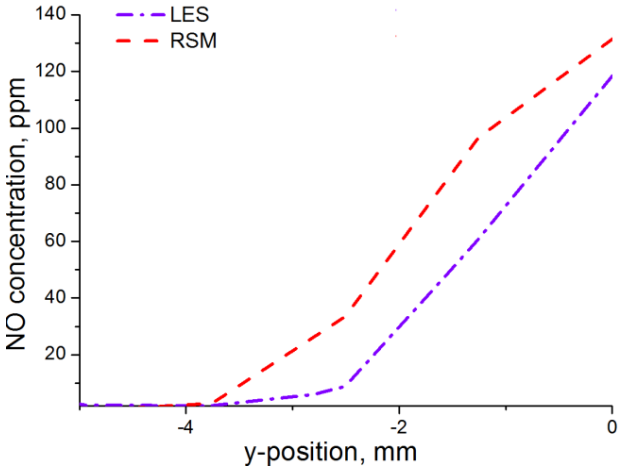

(c)

Figure 6-22 LES and RSM predictions of the nitrogen oxide in a wake-stabilized propane flame using the partially premixed combustion model at (a) x = 8.2 mm, z = 0 (b) x = 8.2, z = 7 mm, and (c) x= 23.2, z = 3 mm.

The predictions of the oxygen concentration using the RSM was also satisfactory at the locations investigated and also the trend of the experimental results was properly captured by the model. The oxygen concentration tends to increase downstream of the flame because the entrainment of the air into the flame increases along the length of the flame and this increased concentration of oxygen will contribute to the improved predictions of the oxygen at the downstream locations x = 8.2 mm, z= 7 and x= 23.2 mm, z= 3 mm, as compared to the upstream location x = 8.2 mm, z= 0. The predictions of the carbon dioxide concentrations were also better with the LES than with the RSM for all the locations investigated, especially at the downstream region of x = 23.2 mm, z = 3 mm (Figure 6-20 (c)) where we observe an almost perfect fit to the experimental data. The inability of the RSM to predict the carbon dioxide concentration can be observed especially at x = 8.2, z = 7 mm where the RSM produces a large spreading rate in the measurements. The trend in the carbon dioxide concentration is expected to be proportional to the trend in the temperature, i.e. the carbon dioxide concentration is expected to reduce with a reduction in temperature and it is expected to increase with an increase in the temperature and this is what has been obtained in both the experimental and the predicted values of both the LES and the RSM at the locations investigated. The RSM and LES predictions of the carbon monoxide concentrations were both very good at x = 8.2, z = 0 (Figure 6-21 (a)), with both models producing an almost perfect fit to the experimental data at this location. The fit to the experimental data was also very good with the LES at x = 23.2 mm, z = 3 mm (Figure 6-21 (c)), and this is interesting given that carbon monoxide is usually difficult to predict since it forms very slowly in the flame and reaches partial equilibrium much later in the flame. The improved predictions of the carbon monoxide concentrations could be attributed to the fine mesh employed as well as the range of scalar dissipation rate and the scalar dissipation step employed (0.0001 to 30 s^{-1} in scalar dissipation steps of 2.5 s^{-1}). This range of scalar dissipation steps have been found to be sufficient in accounting for the relaxation effects on the pollutant species as well as on the radiation effects associated with lower values of the scalar dissipation rates (Lawal et

al., 2010). The predictions of the nitrogen oxide concentration is shown in Figures 6-22 (a) – (c) for the locations investigated, and although Huang and Yang (1996) did not report nitrogen oxide concentrations in their paper, the predicted trend of nitrogen oxide is satisfactory for both the RSM and the LES predictions at the locations investigated. Nitrogen oxide, like carbon monoxide, is a slow forming species and its prediction is very difficult given that it forms at very low concentrations in the flame. Furthermore, the interaction between NO chemistry and flame turbulence is a difficult undertaking for combustion modellers (Mahmud et al., 2007). The concentration of nitrogen oxide is observed to be lower at the upstream region of x = 8.2, z = 0, and higher at the downstream of the flame at x = 8.2, z = 7 mm and x = 23.2, z =3 mm, with peak values of about 100, 180 and 120 ppm for the LES at these respective locations. The peak concentration of nitrogen oxide does not differ much between the RSM and the LES predictions at these locations, with a difference of only about 15 %, 20 % and 10 % for the respective locations. Furthermore, it is observed that the peak concentration of nitrogen oxide occurs at the flame centerline which is expected given that the flame temperature will be highest at the centerline and decrease outwards from the flame centerline, and since the formation of nitrogen oxide is direct function of the temperature, we can conclude the predicted trend is accurate. Wang & Pitsch (2007) have also used the partially premixed model in combination with the LES approach to model an industrial furnace featuring a heated cross-flowing jet of fuel and they reported satisfactory agreement between the experimental data and the predictions for the major species, such as carbon dioxide and oxygen. However, the predictions of the minor species, such as nitrogen oxide and carbon monoxide were less accurate in comparison with the major species. It may be, in general suggested that the resolution of the large scale turbulence motion in the LES approach produces improved predictions of the thermo-chemical properties of the flame. Figure 6-23 show the temperature contour of the LES simulation of the wake-stabilized propane diffusion flame and the large fragmentations in the flame due to the cross-flow has been captured as seen from the contour.

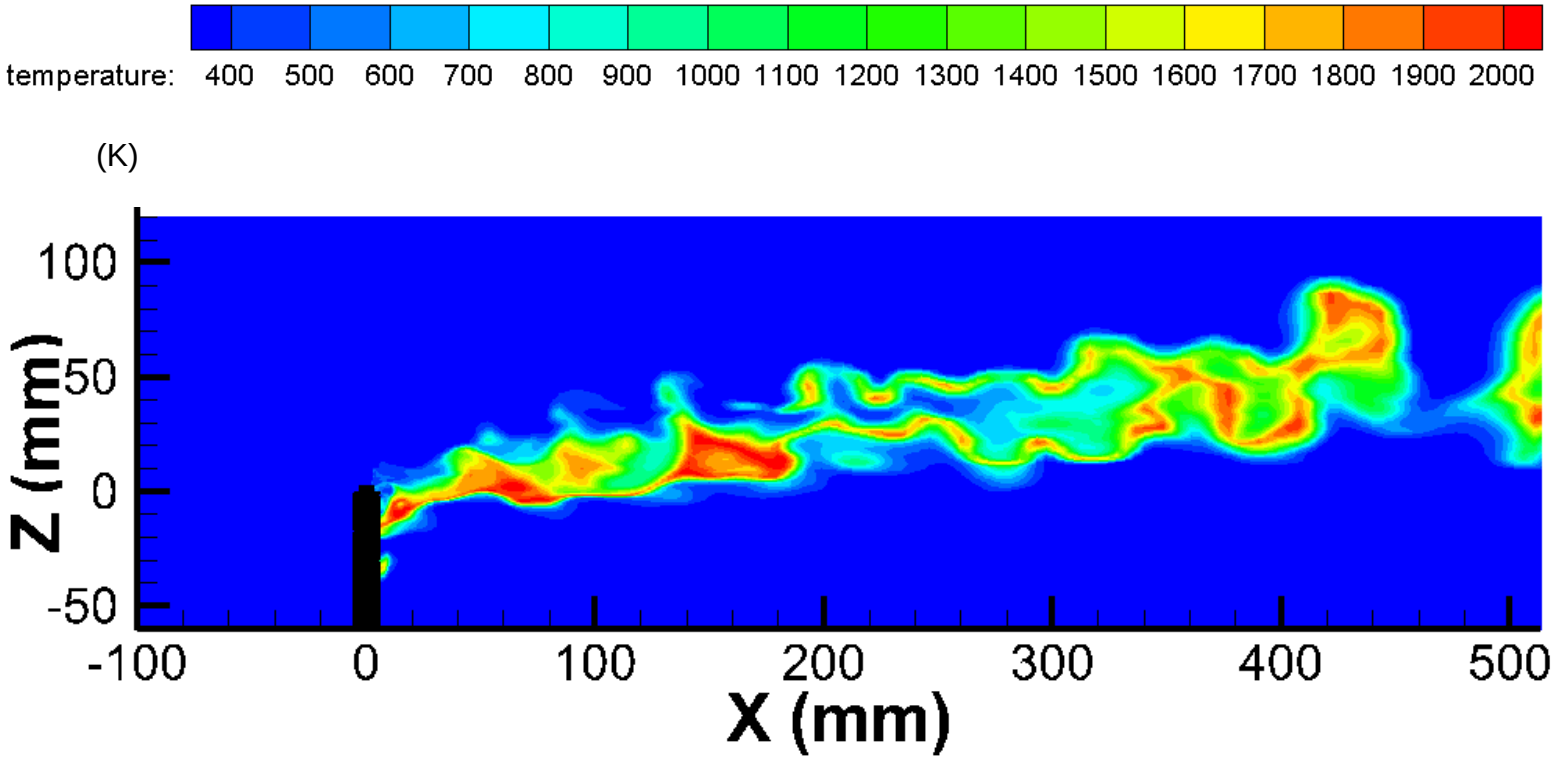

Figure 6-23 Instantaneous LES prediction of the wake-stabilized propane flame at u_f = 5.78 m/s, u_{cf} = 4.86 m/s, and R = 2.17.

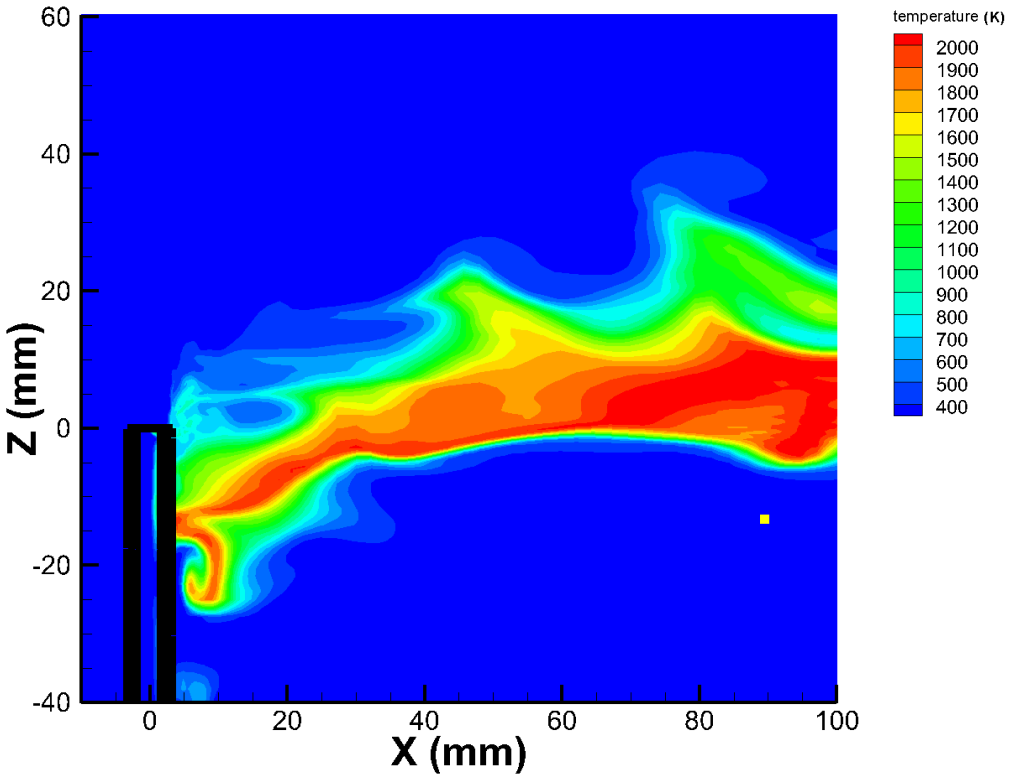
temperature (K)
2000
1900
1800
1700
1600
1500
1400
1300
1200
1100
1000
900
800
700
600
500
400
60
40
20
0
-20
-40
Z (mm)
0
20
40
60
80
100
X (mm)

(a)

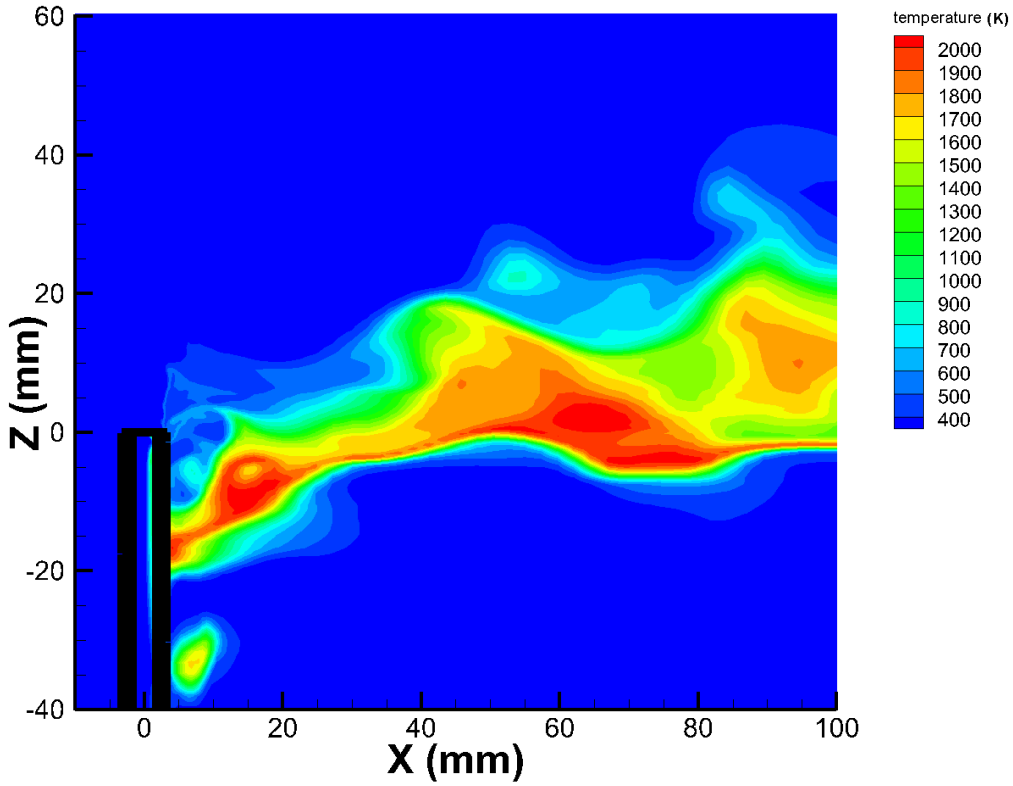
temperature (K)
2000
1900
1800
1700
1600
1500
1400
1300
1200
1100
1000
900
800
700
600
500
400
60
40
20
0
-20
-40
Z (mm)
0
20
40
60
80
100
X (mm)

(b)

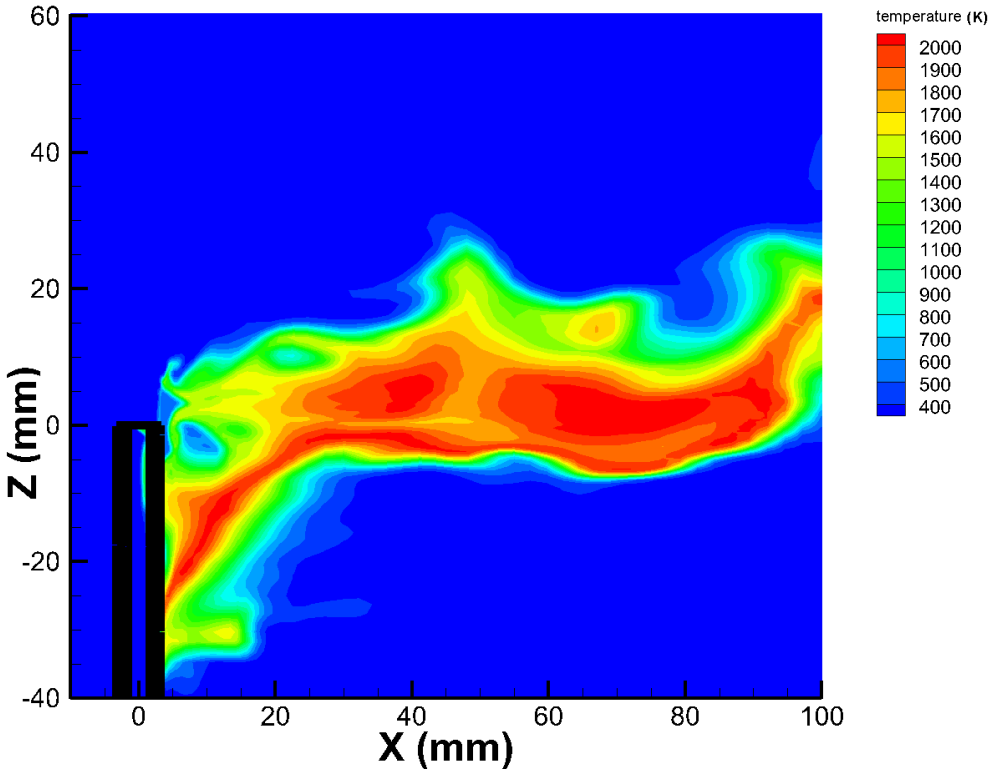

(c)

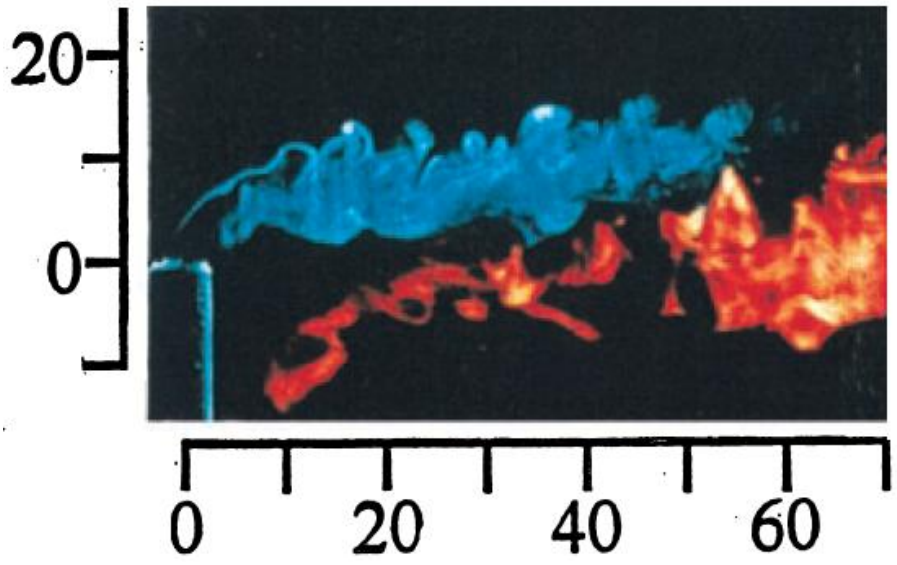

(d)

Figure 6-24 Instantaneous LES predictions of the wake-stabilized propane flame at u_f = 5.78 m/s, u_{cf} = 4.86 m/s, and R = 2.16 for time (a) 0.42s (b) 0.64s, and (c) 0.78s (d) Titanium tetrachloride flow visualization of a similar propane flame at u_f = 6.20 m/s, u_{cf} = 4.86 m/s, and R = 2.47 (Huang and Wang, 1999).

Figure 6-24 (d) shows a titanium tetrachloride flow visualization of a similar cross-flow propane diffusion flame investigated by Huang and Wang (1999), which is similar to that investigated by Huang and Yang (1996). The cross-flow diffusion flame can be observed to be in two layers namely an upper layer of fuel-air mixture (blue layer) and a combusting layer beneath the pipe exit level. This is compared against the instantaneous temperature contour from the LES simulation of the wake-stabilized flame taken at three different time intervals in the calculation (Figure 6-24 (a) - (c)). It can be observed from the contours that the LES was able to reproduce the combusting layer beneath the pipe exit level but was unable to satisfactorily reproduce the non-combusting layer of the fuel-air mixture above the pipe exit level, although the two flames vary slightly in the values of their jet-to-cross-flow momentum ratios (2.16 and 2.47, respectively). This difficulty in resolving the shear layer – the region of the fuel-air interaction that becomes partially premixed by the turbulence, has been highlighted in the review of the literature, where Lawal (2010) was also unable to capture this region of the flame. However, the fragmentation in the flame, as the well as the lower temperatures obtained at this layer, was reproduced by the LES simulation, especially in the region near the pipe exit. The turbulence-chemistry and soot-radiation interaction in LES calculations are more complicated than what obtains in RANS, making predictions much more difficult for the LES. Figure 6-25 shows the contours of the soot produced in the cross-flow propane diffusion flame (Figure 6-25 (b)) and in the straight jet propane diffusion flame (Figure 6-25 (a)) investigated in chapter 5 of this thesis. Comparison of the soot contours from the two flames reveal that significantly less soot is produced in the cross-flow propane diffusion flame due to more entrainment of air from the cross-flow, as confirmed by the experimental data of Bandaru and Turns (2000). Also, several investigations have shown that soot is usually formed in the mid-flame region of the flame and becomes consumed further downstream of the flame (Nishida et al.,1982; Santoro et al.,1987). This is because at the mid-flame region in the flame, the soot nucleation and growth will have proceeded to a stage that will allow the coagulation and the agglomeration of the soot particles to begin.

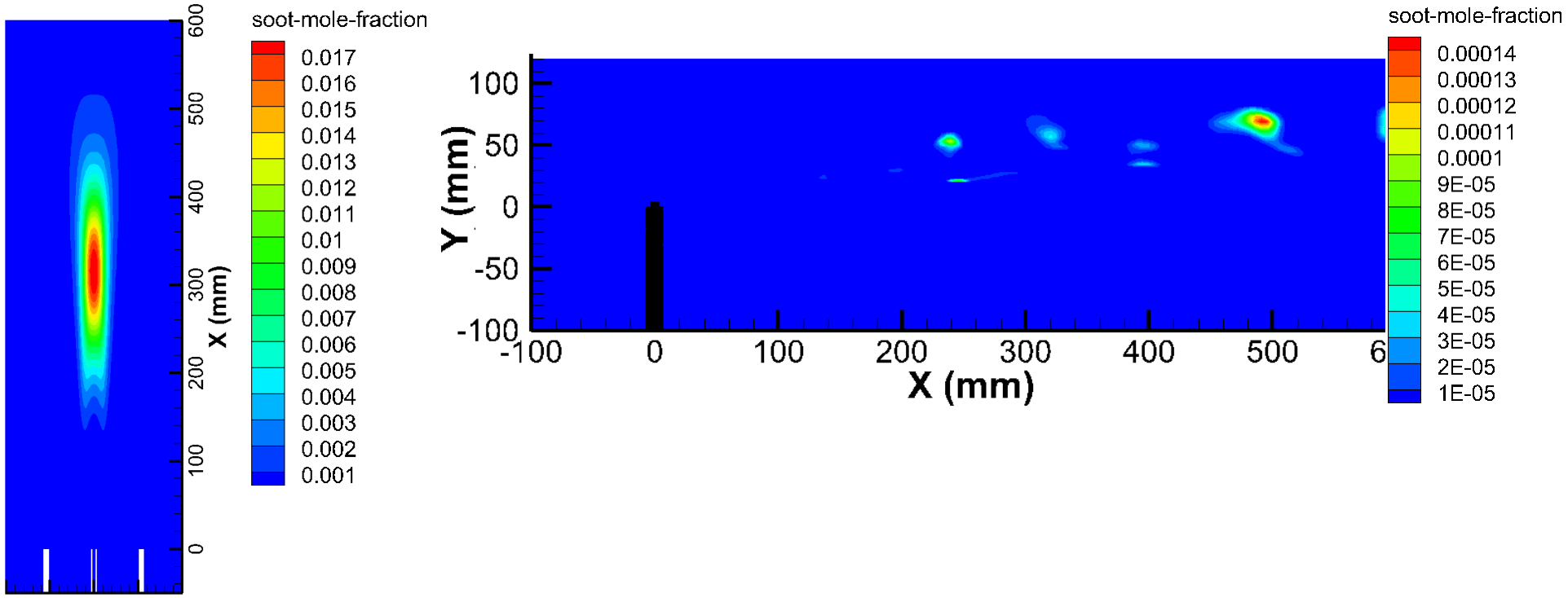

(a) (b)

Figure 6-25 Contours of the soot in (a) straight jet propane diffusion flame at u_f = 7.60 m/s, Re = 5700, and (b) wake-stabilized propane diffusion flame at u_f = 5.78 m/s, u_{cf} = 4.86 m/s, Re = 7000, and R = 2.16.

6.5 Conclusion

In this chapter of the thesis, a three-dimensional numerical simulation of the experimental work of Huang and Yang (1996) for a propane diffusion flame in cross-flow has been performed with the following conclusions.

- The partially premixed combustion model (which uses the mixture fraction/progress variable approach) performed much better than the non-premixed combustion model (which uses the mixture fraction approach only) in predicting the flame appearance as well as the thermo-chemical properties of the wake-stabilized cross-flow propane flame.
- The LES approach performed better than the RSM in predicting the trend of temperature. However both models correctly predicted the peak temperatures at the measurement locations investigated. Predictions of the species were also better with the LES, except for the carbon monoxide at the near nozzle region where the RSM performed just as well as the LES. In general, the RSM gives a reasonable prediction of the thermo-chemical properties of the flame which should serve as an attractive alternative to the much more expensive LES.

- The CRECK reaction mechanism of Ranzi et al. (2012) and the Moss-Brookes-Hall soot model (1997) have been shown to work well in conjunction with the partially premixed combustion model for predicting cross-flow propane diffusion flames.

- Predictions of the inflame soot concentration in the cross-flow flame have been compared with predictions of inflame soot in a similar straight jet flame and the results show that less inflame soot is produced in cross-flow flames than in straight jet flames which is in agreement with the experimental data by Bandaru and Turns (2000).

Chapter 7

General Conclusions and Suggestions for Future Investigations

This study has looked into the behaviour of gas flares by studying vertical jet diffusion flames and cross-flow diffusion flames on the laboratory scale and also by using numerical methods. The experimental work was performed on a simple jet diffusion flame burner featuring shroud air to shield the flame from external disturbances, while the numerical aspect was achieved using the governing equations that describe the phenomena of turbulence, combustion and radiation as implemented in the ANSYS Fluent solver. The regimes of gas flares can be broadly categorized as flares operating in quiescent atmospheres and flares operating in a strong cross-wind and these two broad categories of flares can be modelled in the laboratory as a vertical jet diffusion flame and as a jet diffusion flame in a cross-flow of air, respectively. This approximation is necessary in order to facilitate their study in the laboratory since the study of full scale flares is technically very challenging. The jet diffusion flame in a cross-flow is further categorized into high momentum flares and low momentum flares depending on the value of the jet-to-cross-flow momentum ratio – a dimensionless parameter used to characterize the strength of the cross-flow relative to the fuel jet. Flares that operate under high cross-flows eventually become stabilized on the lee side of the pipe and thus giving rise to the so called “wake-stabilized flares”. These types of flares are ubiquitous in oil and gas production fields where much of the gas is flared and hence their combustion characteristics present an interesting topic of study. Natural gas is often flared on production fields and given that natural gas is predominantly methane, much research work has been performed on methane in an effort to study the behaviour of natural gas flares. However, the composition of natural gas varies from one field to another and some fields also have propane as a major constituent of the flared gases. Furthermore, the waste gases flared in oil and gas refineries also contain a significant quantity of propane. In view of this,

propane has been selected as the major fuel of investigation in this thesis, in addition to the work performed on methane. The scope of the project has been limited by funding as well the facilities available for research and in view of this the achievements from the research were as follows:

- Comparison of the $k-\varepsilon$, $k-\omega$ and transitional SST models in their ability to predict a vertical jet diffusion methane flame burning in enriched air (26 % oxygen).
- Comparison of the flamelet models and the NO-Pollutant model (implemented in the ANSYS-Fluent-solver) in their ability to predict the in-flame concentration of nitrogen oxide in the methane flame.
- Comparison of the behaviour of methane and propane jet diffusion flames burning under similar Reynolds numbers. This includes comparing their flame lengths, lift-off heights, and temperature and in-flame species distributions. The post flame concentration of species and soot was also investigated. The measurements obtained from the laboratory are then validated against numerical data obtained using the mathematical codes implemented in the ANSYS-Fluent solver.
- Investigation of the effect of the pipe nozzle thickness on the flame stability.
- Comparison of the non-premixed and the partially-premixed combustion models (implemented in the ANSYS-Fluent-solver) in predicting the structure of a wake-stabilized propane diffusion flame in a cross-flow of air.
- Comparison of the Reynolds stress model and large eddy simulation technique (implemented in the ANSYS-Fluent-solver) in predicting the thermo-chemical properties of a wake-stabilized propane diffusion flame in a cross-flow of air.

The experimental study was performed with an aim to determine the effect of variations in the burner geometry on the flame stability. To this effect, the burner nozzle thickness was investigated and the effect on the flame lift-off behaviour was observed. The results showed that an increase in the burner nozzle thickness produced a decrease in the flame lift-off height for both the

propane and the methane flames. Furthermore, the propane flame was observed to be more sensitive to variations made to the burner thickness by showing a decrease in the lift-off height faster than for the methane flame. The lift-off height is important in flares because lifted flames are generally less stable than their burner-attached counterparts and the higher the flame is lifted, the more likely it is to blow-off, especially in the presence of a strong cross-wind. Furthermore, the thermo-chemical properties of the methane and a propane flames were investigated both experimentally and numerically and the results were compared for a Reynolds number of 5700. The methane flame was lifted while the propane flame was still attached under the Reynolds number investigated. This difference in lift-off behaviour between the two flames under this value of the Reynolds number (5700) is due to the difference in the physical properties of these two fuels (such as the density and viscosity). Comparison of the radial trends of temperature and species at various axial locations above the burner showed good agreements with the predicted data except at the downstream location where the predictions were less accurate due to flame turbulence. The CRECK reaction mechanism (Ranzi et al., 2012) was employed to model the kinetics of the propane reactions while the GRI mech. 3.0 was employed to model the kinetics of the methane reactions. Furthermore, the simulation of methane was performed without including a soot model since soot production in laboratory-scale methane/air jet diffusion flames has been shown to be negligible at atmospheric pressure (Brookes & Moss, 1999). The Moss-Brookes model was used to model soot in the propane flame and soot inception was based on acetylene as the gas phase as well as the nucleation species. Radiation, which appears as a sink in the energy equation was modelled with the discrete ordinate model, which accounts for both the absorption and emission of radiation. Soot-radiation interaction was taken into account by including the effect of the soot concentration on the radiation-absorption coefficient. NO_x was modelled using the flamelet approach and the Pollutant model, implemented in the Fluent solver, and the two models have been compared. The flamelet approach to predicting NO_x uses the transport equation for the nitrogen oxide convection, diffusion and

production. However the source term in the flamelet equation does not account for kinetic effects of slow forming species, such as nitrogen oxide, thus making the model less accurate. The pollutants model (PM) on the other hand uses the well-known Zeldovich and Fenimore mechanisms to model thermal NO and prompt NO, respectively, which includes a rate expression to model the chemical kinetics of slow forming species. The results showed that the pollutant model performed better than the flamelet model for modelling NO in methane flames, especially in the mid-flame region where temperatures were highest. However, application of the pollutant model to the propane flame did not produce the experimental observed trend as was the case with the methane flame. This could be due to the inability of the model to adequately resolve the interaction between soot and chemistry of nitrogen oxide formation. Experimental measurements of the post flame emissions of soot, carbon monoxide, nitrogen oxide and unburnt hydrocarbons were also carried out in this thesis and following observations were made:

- Inflame measurements of carbon monoxide and nitrogen oxide showed higher levels of both pollutants in the propane flame and lower levels in the methane flame. However the post flame measurement of emissions showed slightly higher levels of the pollutants in the methane flame. This could be attributed to higher dilution of air in the post flame region in the case of the propane flame.
- The post flame measurement of soot showed that there was no detectable soot present in the lifted methane jet diffusion flame. This is attributed to the relatively higher temperature in the lifted methane flame as well as the high entrainment of air into the base of the lifted flame which ensures that all the inflame soot are consumed before escaping into the atmosphere. Other similar works have also shown that relatively little soot is present in lifted methane diffusion flames at atmospheric pressure (Bandaru and Turns, 2000). However, the propane flame showed high inflame soot production. This higher soot

production in the propane flame is due to the higher carbon content of propane fuel as well as the fact that the propane flame was attached to the burner rim at the Reynolds chosen for the investigation. This cause less air entrainment at the base of the flame, which results in less inflame soot combustion and more soot escaping into the atmosphere.

- The Pollutant Model produced a better prediction of the trend in the nitrogen oxide concentration distribution in the methane flame compared to the propane flame. This inability of the Pollutant Model to accurately predict the experimental trend in the case of the propane flame could be due to the difficulty of resolving the interaction between the soot and NO_x chemistry.

Furthermore, the capability of the models to predict the flame lengths was investigated by comparing the predicted flame length with the experimentally measured flame lengths. The numerical flame length was based on the burnt out position of the carbon monoxide along the flame axis and the results showed that the values of the predicted flame lengths obtained was a good approximation to the experimentally measured flame lengths for both the methane and the propane flames.

A three-dimensional simulation of a propane diffusion flame in a cross-flow of air was also performed to study the capability of the numerical models available in the Fluent code to predict the experimental work performed by Huang and Yang (1996). The non-premixed and the partially premixed combustion models were investigated and compared with respect to their ability to predict the flame structure, as well as the thermo-chemical properties of the flame. Two different regimes were selected from the experimental work of Huang and Yang for the investigation namely a wake-stabilized regime (u_j = 5.78 m/s, R = 2.16) where the cross-flow momentum dominated over the momentum of the jet and a pre-blowoff regime (u_j = 5.78 m/s, R = 2.16), where the jet momentum was higher than the cross-flow momentum. Comparison of the predicted flame structures (in the form of temperature contours) with hand sketches of the visible flame as

observed and drawn by Huang and Yang (1996) showed the partially premixed model was better able to predict the flame structure, especially for the wake-stabilized regime. Furthermore, predictions of the inflame temperature and species distribution for the wake-stabilized flame showed that the partially premixed model correctly resolved the trend of the temperature and all the species at the selected measurement locations in the flame. On the other hand, the non-premixed model could not correctly predict the experimental trend. Both the partially premixed and the non-premixed models use the mixture fraction approach in the mathematical formulation of the combustion equation, however, the partially premixed model also incorporates the reaction progress variable approach which enables it to account for the regions of partial premixing in the flame. This explains the superior performance of the partially premixed model over the non-premixed model in the modelling of wake-stabilized cross-flow flames. The Reynolds Stress Model (RSM) was also compared with the Large Eddy Simulation (LES) technique in attempt to improve the fit to the experimental data and the results illustrated that the flow field was better resolved using the LES technique. Furthermore, a comparison of the NO_x and soot predictions from the straight jet and the cross-flow flames showed that the cross-flow effect can almost double the amount of NO_x produced in the flame, but will substantially reduce the amount of soot produced. This is in agreement with experimental work performed by Bandaru and Turns (2000). The strong interaction between the cross-flow and jet produces very high turbulence intensities in the flow field which was better resolved using the more complex LES technique leading to improved predictions of the temperature and species distributions. However, the RSM is still a more practical alternative to the LES given the large amount of computer resources and time required for an LES simulation. Wake-stabilized propane flames are common in the oil and gas production fields where the momentum of the cross-flow overrides the momentum of the fuel jet. These flames are usually stabilized at the lee side of the pipe because of the recirculation which arises due to the low pressure in this zone. This zone is known to have a profound influence on the residence time of the reactive

gases in the vortex cores and consequently could impact the emission of pollutants. This work has validated the experimental data in straight jet and cross-flow diffusion flames against numerical predictions with a good level of success. However, more work can be done to test these codes and improve on the results obtained. Some suggestions regarding future investigations are as follows:

- the lift-off height prediction of the lifted methane diffusion flame could be improved by investigating more detailed combustion models, such as the PDF transport model which accounts for finite rate kinetic effects in the species transport equation.
- The CRECK reaction mechanism has been shown to work well for predicting the chemistry of propane reactions in cross-flow diffusion flames. However the mechanism is highly detailed and therefore requires high computing resources, especially when used in conjunction with a soot model and the LES technique. In view of this, a reduced mechanism may be developed from the CRECK mechanism in order to facilitate the computing process.
- Huang and Yang performed several other experiments for cross-flow propane diffusion flames operating under different values of the jet-to-cross-flow momentum ratios and these experiments can be employed to further test the validity of the models that are available in ANSYS Fluent codes.
- The absence of a wind tunnel in the present project has made it difficult to conduct a similar experiment to that performed by Huang and Yang (1996). However, if such a wind tunnel could be procured, then it could help in the further investigation of the cross-wind effects on flare efficiencies such as the effect of the wind direction and humidity on flame emissions.

Appendices

Appendix I

(a) A hex mesh of the flow domain for the Lee Howards case.

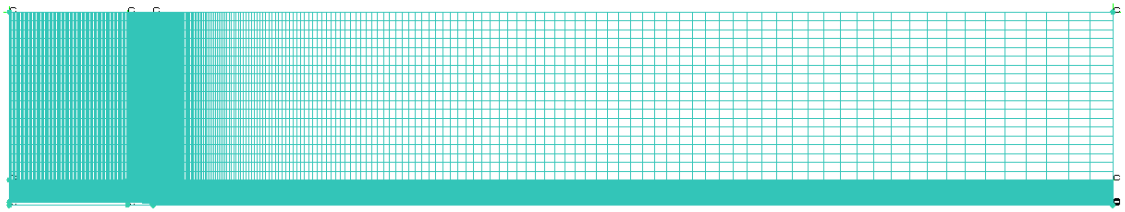

(b) Mesh of the pipe region using the ANSYS-ICEM software.

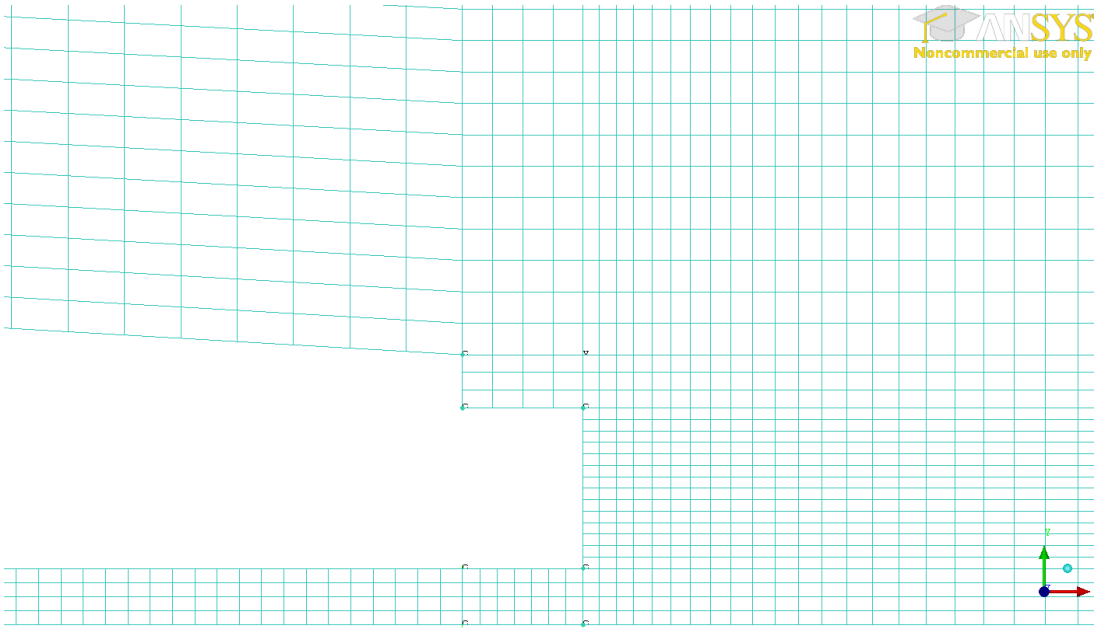

(c) Aspect ratio of the elements.

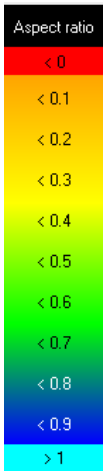

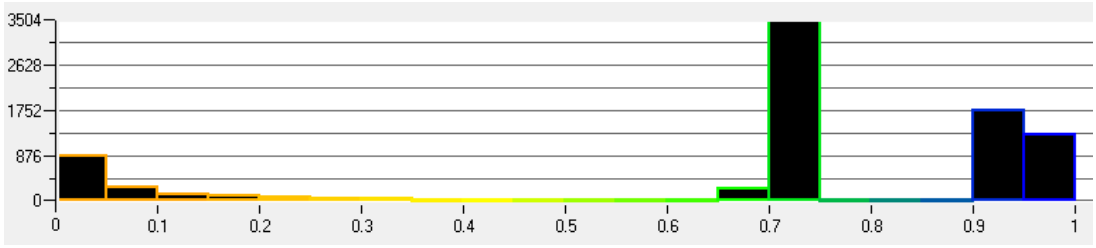

(d) Appendix IV: Orthogonal quality.

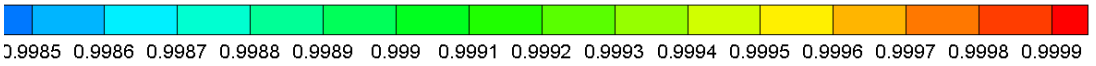

Appendix II

(a) Rotameter calibration chart using the Excel spreadsheet.

FLOW METER CALIBERATION TABLE AND CHART

FLOW METER_JE2

diameter of bubble tub	D	5.53	cm	density of propane	p	1.87	kg/m3
length of bubble tube	h	50	cm	viscosity of propane	w	0.000008	N-s/m2
radius of bubble tube	r	2.765	cm	diameter of fuel pipe		0.00325	m
volume of bubble tube	$\pi r^2 h$	1201.065	cm^3				
room temperature		295.15	K				
atmospheric pressure		1013	mbar				
radius of fuel pipe	R	0.001625	m				
cross sec area of fuel p	pir2	8.3E-06	m2				

PROPANE FLOW CALIBERATION

Ref	No of experimental runs (sec)				Avg (sec	Flow rates					Velocity	Re
	1	2	3	4		cm^3/s	m^3/s	L/min	L/min(corrected)	m^3/s (corrected)	m/s	
2	21	23	22	23	22.25	53.98044258	5.39804E-05	3.233428511	2.991675698	4.9961E-05	6.021686	4574.6
4	13	13	13	13	13	92.38960365	9.23896E-05	5.534137259	5.120368022	8.55101E-05	10.30635	7829.6
6	10	10	10	10	10	120.1064848	0.000120106	7.194378437	6.656478429	0.000111163	13.39825	10178
8	8	8	8	8	8	150.1331059	0.000150133	8.992973046	8.320598036	0.000138954	16.74781	12723
10	7	7	7	7	7	171.5806925	0.000171581	10.27768348	9.509254898	0.000158805	19.14036	14541

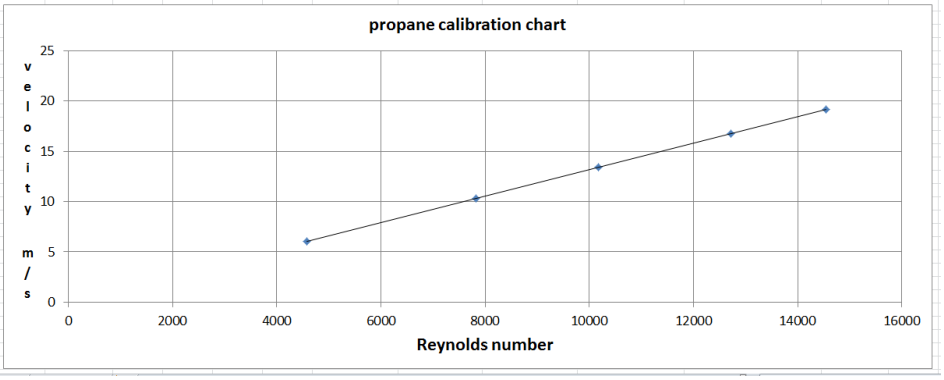

(b) Dependence of the thermal conductivity and viscosity of methane and propane on the temperature.

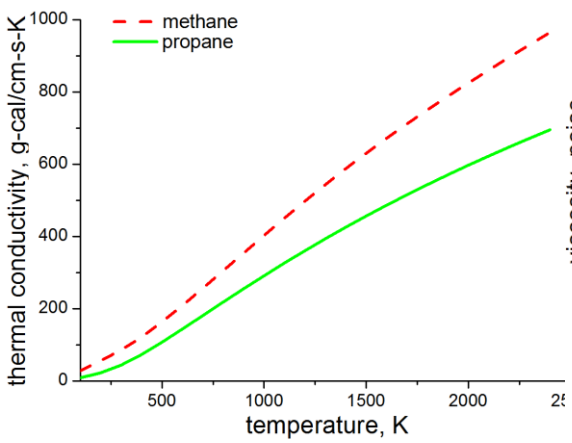

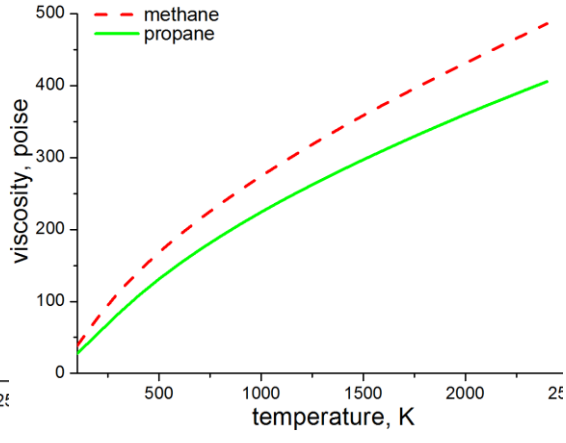

Appendix III

(a) Mesh of the fuel pipe inlet.

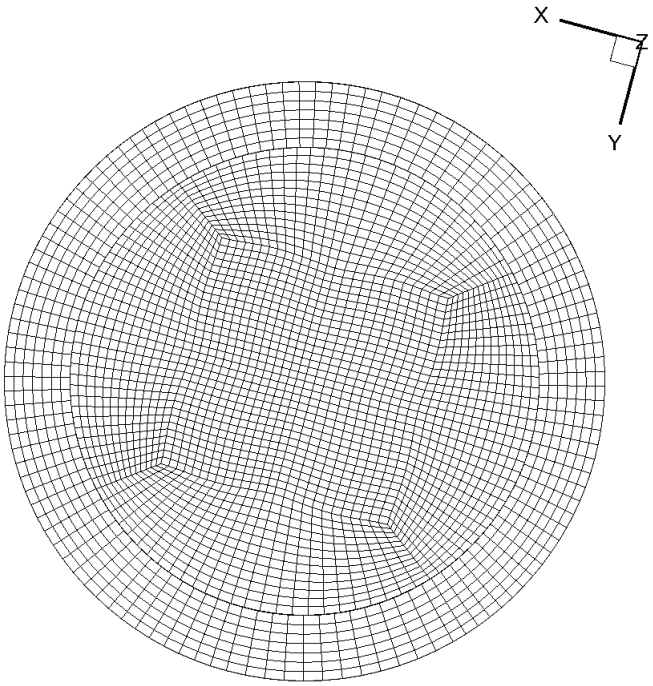

(b) Cell volume change in the near pipe region

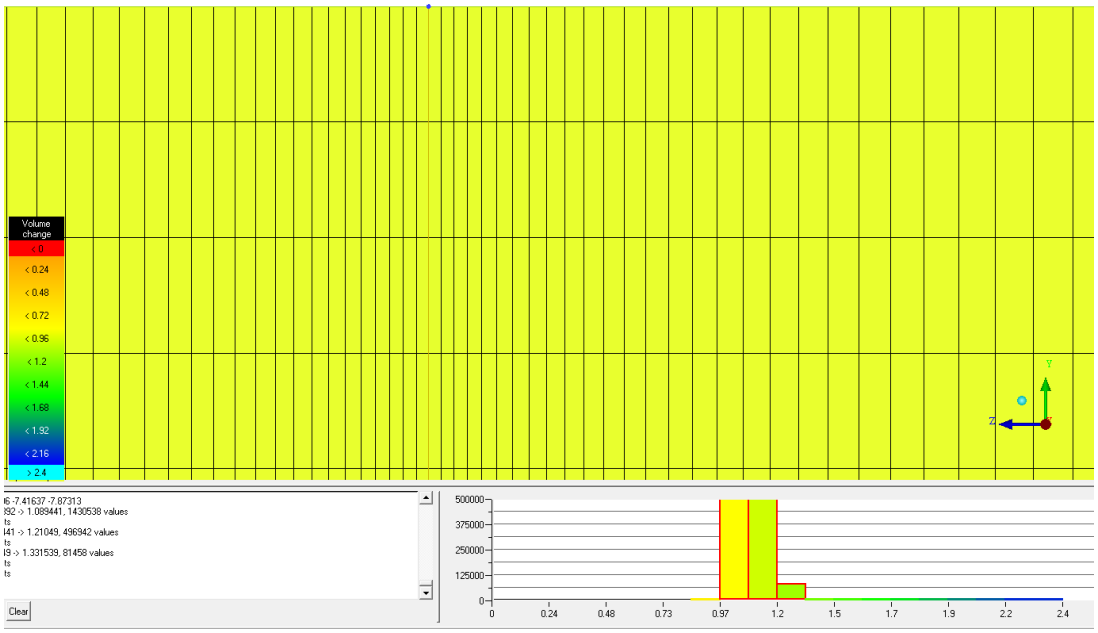

(c) Variations in pressure at the pipe inlet and outlet

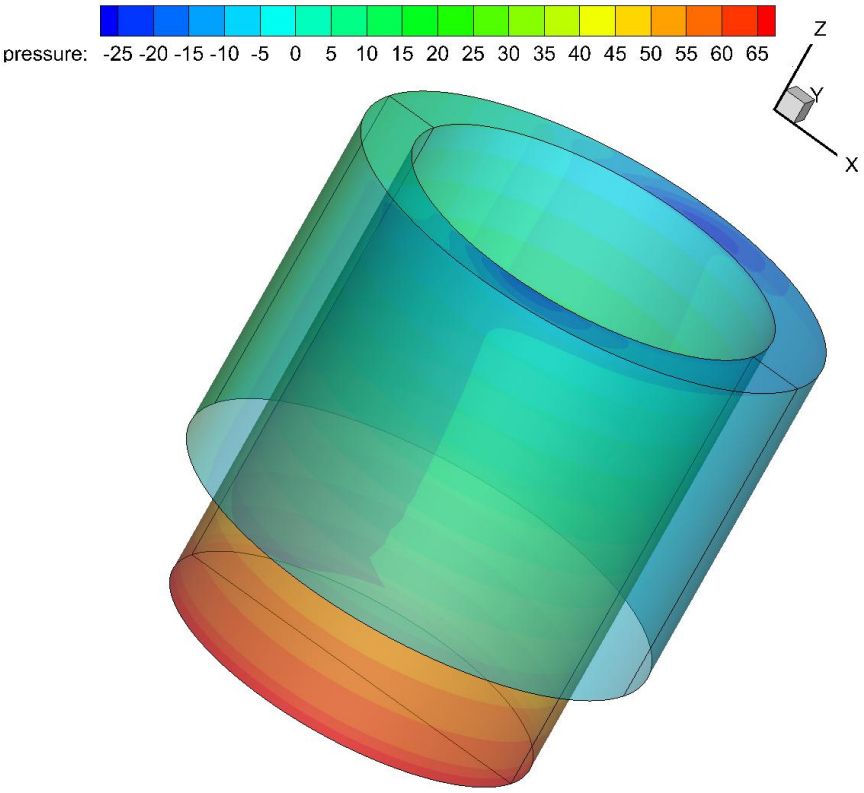

(d) Effect of the flame impingement on the side of the pipe due to the cross-flow.

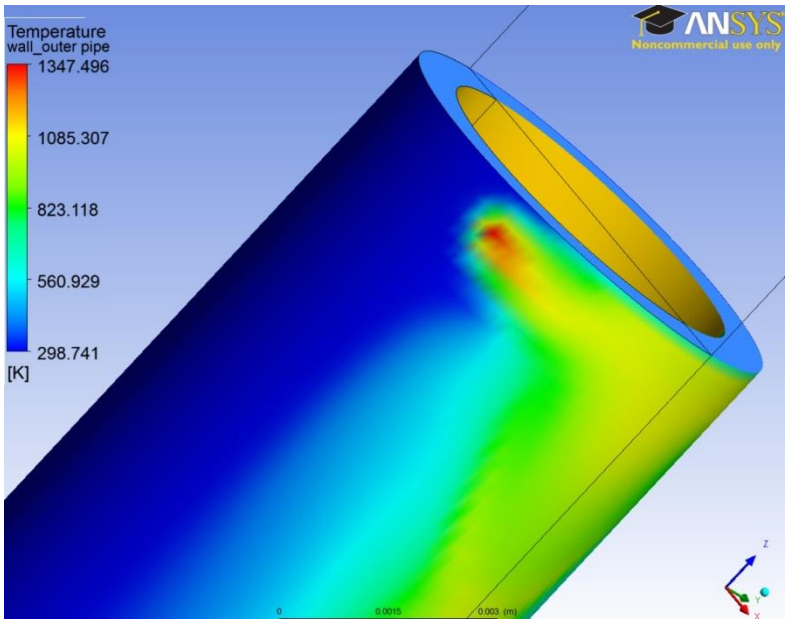

Bibliography

Ansys-Fluent. (2014). Theory Guide. Version 14.5 Sheffield, U.K., ANSYS-Fluent Europe, Limited.

Andrew, C. M., & Ralph, F. K. (1999). Precise atmospheric oxygen measurment with a paramagnetic oxygen analyzer. *Global Biochemical Cycles*, *13*, 1107–1115.

API Recommended Practice, 521 (1982). Guide for pressure-relieving and depressurizing systems. *American Petroleum Institute*, *Second Edition.*

Aziz, T. N., Raiford, J. P. & Khan, A. A. (2008). Numerical simulation of turbulent jets. *Engineeering Applications of Computational Fluid Mechanics*, *2*, 234–243.

Bandaru, R. V, & Turns, S. R. (2000). Turbulent jet flames in a crossflow: effects of some jet, crossflow, and pilot-flame parameters on emissions. *Combustion and Flame*, *121*, 137–151.

Barths, H., Peters, N., Brehm, N., & Mack, A. (1998). Simulation of pollutant formation in a gasturbine combustor using unsteady flamelets. *Proccedings of the Combustion institute Institute*, *27*, 1841–1847.

Becker, H. A., Liang, D. (1978). Visible lengths of vertical free turbulent diffusion flames. *Combustion and Flame*, *32*, 115–137.

Béghein, C., Jiang, Y., & Chen, Q. (2005). Using Large Eddy Simulation to study particle motions in a room. *Indoor Air*, 281–290.

Bilger, R. W. (1976). The structure of diffusion flames. *Combustion Science and Technology*, *13*, 155–170.

Bilger, R. W., Pope, S. B., Bray, K. N. C. & Driscoll, J. F. (2005). Paradigms in turbulent combustion research. *Proceedings of the Combustion Institute*, *30*, 21–42.

Birch, A. D., Brown, D. R., Fairweather, M. & Hargrave, G. K. (1989). An experimental study of a turbulent natural gas jet in a cross-flow. *Combustion Science and Technology*, *66*, 217–232.

Botros, P. E., & Brzustowski, T. A. (1979). An experimental and theoretical study of the turbulent diffusion flame in cross-flow. *Proceedings of the Combustion Institute*, *17*, 389–398.

Boudier, G., Gicquel, L. Y. M., Poinsot, T., Bissières, D., & Bérat, C. (2007). Comparison of LES, RANS and experiments in an aeronautical gas

turbine combustion chamber. *Proceedings of the Combustion Institute*, *31*, 3075–3082.

Bray, K. N. C. & Peters, N. (1994). Laminar flamelets in turbulent flames. *Turbulent reacting flows*. 2nd ed. California, Academic Press.

Brookes, S. J. & Moss, J. B. (1999). Prediction of soot and thermal radiation in confined turbulent jet diffusion flames. *Combustion and Flame*, *116*, 486–503.

Brzustowski, T. A. (1976). Flaring in the energy industry. *Progress in Energy and Combustion Science*, *2*, 129–141.

Burke , S. P. , and Schumann, T. E. W. (1928). Diffusion flames. *Industrial & Engineering Chemistry*, *29*, 998-1008.

Castiñeira, D., & Edgar, T. F. (2008). Computational fluid dynamics for simulation of wind-tunnel experiments on flare combustion systems. *Energy & Fuels*, *22*, 1698–1706.

Clough, P. N., & Thrush, B. A. (1967). Mechanism of chemiluminescent reaction between nitric oxide and ozone. *Transactions of the Faraday Society*, *925*, 915–925.

Colket, M. B., Chiappetta, L., Guile, R. N., Zabielski, M. F., & Seery, D. J. (1982). Internal aerodynamics of gas sampling probes. *Combustion and flame*, *44*, 3–14.

Cyberhawk Innovations. (2012). Retrieved February 15, 2014, from http://www.thecyberhawk.com/inspections/onshore-oil-gas/

Dally, B.B., Masri, A. R., Barlow, R. W. and Fiechtner, D. F. (1996). Measurements of NO in turbulent non premixed flames stabilized on a bluff body. *Proccedings of the Combustion Institute*, *26*, 2191–2197.

Dapazo, C. & O'Brien, E. E. (1974). An approach to the description of turbulent mixture. *Acta Astronaut*, *1*, 1239–1266.

DECC. (2009). UK low carbon transition plan (Ed. London, DECC). *National strategy for climate and energy*.

Delichatsios, M. A. (1993). Transition from momentum to buoyancy-controlled turbulent jet diffusion flames and flame height relationships. *Combustion and Flame*, *2180*, 349–364.

Dewar, R. A. (1960). The flame ionization detector a theoretical approach. *Journal of Chromatography*, *6*, 312–323.

Drake, M. C. & Blint, Richard. J. (1991). Relative Importance of nitric oxide formation mechanisms in laminar opposed-flow diffusion flames, *203*, 185–203.

Dreamstime Images. (2011). Retrieved November 12, 1BC, from http://www.dreamstime.com/

Elvidge, C. D., Ziskin, D., Baugh, K. E., & Tuttle, B. T. (2009). A fifteen year record of global natural gas flaring derived from satellite data. *Energies*, *2*, 595–622.

Fairweather, M., Jones, W. P., Lindstedt, R. P., & Marquis, A. J. (1991). Predictions of a turbulent reacting jet in a cross-flow. *Combustion and Flame*, *84*, 361–375

Fairweather, M., Jones, W. P., & Lindstedt, R. P. (1992). Predictions of radiative transfer from a turbulent reacting jet in a cross-wind. *Combustion and Flame*, *89*, 45–63.

Fairweather, M., Jones, W. P., & Lindstedt, R. P. (1992). Predictions of radiative transfer from a turbulent reacting jet in a cross-wind. *Combustion and Flame*, *89*, 45–63.

Farina, M. F. (2011). Flare Gas Reduction: Recent global trends and policy considerations. *GE Energy, Global Strategy and Planning*, 10–15.

Favre, A. (1969). Statistical equations of turbulent gases, in problems of hydrodynamics and continuum mechanics. *SIAM, Philadelphia*, 231–266.

Fenimore, C. P., & Jones, G. W. (1967). Oxidation of soot by hydroxyl radicals. *Journal of physics and chemistry*, 593–597.

Fenimore, C. P. (1971). Formation of nitric oxide in premixed hydrocarbon flames. *Proccedings of the Combustion Institute*, *13*, 373 –379.

Ferziger, J. H. (1976). Large eddy simulations of turbulent flows. *American Institute of Aeronautics and Astronautics*, *14*, 75–76.

Fiveland, W. A. (1984). Discrete-ordinates solution of the radiative heat transport-equation for rectangular enclosures. *ASME Journal of Heat Transfer*, *106*, 699–706.

Frenklach, M., Smith, G. P., Golden, D. M., Moriarty, N. W., & Eiteneer, B. (2012). GRI MECH 3.0. Retrieved November 10, 2012, from http://www.me.berkeley.edu/gri-mech/version30/text30.html

Galant, S., Grouset, D., Martinez, G., & Micheau, P. (1985). Three-dimensional steady parabolic calculations of large scale methane

turbulent diffusion flames to predict flare radiation under cross-wind conditions. *Proceedings of the Combustion Institute*, *20*, 531–540.

Giordano, P., & Lentini, D. (2001). Combustion, radiation and turbulence interaction modelling in absorbing/emitting non-premixed flames. *Combustion Science and Technology*, *172*, 1–22.

Gogolek, P., Caverly, A., Schwartz, R., Seebold, J. & Pohl, J. (2010). Emission from elevated Flares - A Survey of the Literature. *AFRC 2010 Pacific Rim Combustion Symposium. Maui, USA, IFRF*.

Gollahalli, S. R., & Nanjundappa, B. (1995). Burner wake stabilized gas jet flames in cross-flow. *Combustion Science and Technology*, *109*, 327–346.

Gollahalli, S. R., & Zadeh, G. K. (1985). Flame structure of attached and lifted jet flames of low-calorific-value gases. *Energy Sources*, *8*, 43–66.

Hall, R. J., Smooke, M. D., & Colket, M. B. (1997). In Physical and Chemical Aspects of Combustion. Gordon and Breach.

Hartel, C. (2004). Turbulent flows: Direct Numerical Simulation and Large Eddy Simulation. hand book of Computational Fluid Dynamics. San Diego, Academic Press.

Heitor, M. V. & Moreira, L. N. (1993). Thermocouples and sample probes for combustion studies. *Progress in energy and combustion science*, *19*, 259–278.

Hinze, J. O. (1975). Turbulence. *New York, McGraw-Hill.*

Hottel , H. C., & Hawthorne, W. R. (1949). Diffusion in laminar flame jets. *Proceedings of the Combustion Institute*, *3*, 254–266.

Hottel , H. C. (1954). Radiation-heat transmission. New York, Mc-Graw Hill.

Hottel , H. C., and Sarofim, A. F. (1967). Radiative transer. New York, Mc-Graw Hill.

Howard, L., Yap, L., Pourkashanian, M., Williams, L., & Yetters, R. (1998). Nitric-oxide emission scaling of buoyancy-dominated oxygen-enriched and preheated methane turbulent-jet diffusion flames. *Proccedings of the Combustion institute Institute*, *27*, 1451–1460.

Howard, L. M. (1998). An experimental investigation of oxygen-enriched methane turbulent diffusion flames. *Ph.D. Thesis, The University of Leeds, UK*.

Huang, R. F., & Chang, J. M. (1994). The stability and visualized flame and flow structures of a combusting jet in cross flow. *Combustion and Flame*, *98*, 267–278.

Huang, R. F., & Yang, M. J. (1996). Thermal and concentration fields of burner-attached jet flames in cross flow. *Combustion and Flame*, *105*, 211–244.

Huang, R. F., & Wang, S. M. (1999). Characteristic flow modes of wake-stabilized jet flames in a transverse air stream. *Combustion and Flame*, *117*, 59–77.

Hughes, K. J., Tomlin, A. S., Dupont, V. A., Pourkashanian, M. (2001). Experimental and modelling study of sulfur and nitrogen doped premixed methane flames at low pressure. *Faraday Discuss., 119, 337-352*.

Jones, W. P. & Launder, B. E. (1972). The Prediction of laminarization with a two-equation model of turbulence. *International Journal of Heat and Mass Transfer*, *15*, 301–314.

Jones, W. P. and Whitelaw, J. H. (1982). Calculation methods for reacting turbulent flows: A review. *Combustion and Flame*, *48*, 1–26.

Kalcevic, V. (1980). Control device evaluation flares and the use of emissions as fuels. *Organic Chemical Manufacturing; Combustion Control Devices*, *4*, 4–5.

Kalghatgi, G. T. (1981a). Blow-out stability of gaseous jet diffusion flames in still air: Part I. *Combustion Science and Technology*, *26*, 233–239.

Kalghatgi, G. T. (1981b). Blow-out stability of gaseous jet diffusion flames Part II : effect of cross-wind. *Combustion Science and Technology*, *26*, 241–244.

Kaskan, W. E. (1957). The dependence of flame temperature on mass burning velocity. *Proceedings of the Combustion Institute*, *6*, 134–143.

KLM Technology group. (2012). Retrieved January 15, 2012, from http://www.klmtechgroup.com

Kostiuk, L. W., Johnson, M. R. & Thomas, G. (2001). University of Alberta Flare Research Project. *Effects of a fuel diluent on the efficiencies of jet diffusion flames in crossflow*, *1*, 1–6.

Launder, B. E., Gibson, M. M., & Gatski, T. B. (1978). Ground effects on pressure fluctuations in the atmospheric boundary layer. *Journal of Fluid Mechanics*, 86, 491–511.

Launder, B. E. & Sharma, B. I. (1974). Application of the energy-dissipation models of turbulence to the calculation of flow near a spinning disc. *Letter Heat and mass Transfer,*, *1*, 131–138.

Launder, B. E., Reece, G. J. & Rodi, W. (1975). Progress in the development of a Reynolds-stress turbulence closure. *J.Fluid Mech*, *68*, 537–566.

Launder, B.E. & Spalding, D. B. (1972). Mathematical models of turbulence. *Academic Press, London.*

Launder, B.E. & Spalding, D. B. (1974). The numerical computation of turbulent flows. *Computational Methods in Applied Mechanics and Engineering, 3, 269-289.*

Lawal, M., Pourkashanian, M., Williams, A., Ingham, D., & Ma, L. (2010). Numerical studies of emission characteristics of a jet flame in a crossflow. *Combustion Science and Technology*, *182*, 1491–1510.

Lawal, M. S. (2011). Numerical modelling of jet flames in a cross-flow : Application to flares. *Ph.D. Thesis, The University of Leeds, UK*.

Leonard, A. (1974). On the energy cascade in large-eddy simulations of turbulent flows. *Advanvces in Geophysics*, *18*, 237-249.

Lee, K. B., Thring, M. W., & Beer, J., M. (1962). On the rate of combustion of soot in a laminar soot flame. *International Flame Research Foundation, The Netherlands & The University of Sheffield England*.

Leung, K. M., Lindstedt, R. P., & Jones, W. P. (1991). A simplified reaction mechanism for soot formation in nonpremixed flames. *Combustion and Flame*, *87*, 289–305.

Libby, P. A. & Williams, F. A. (1994). Turbulent reacting flows. *California, USA, Academic Press*.

Lockwood, F. C. (1977). The modelling of turbulent premixed and diffusion combustion in the computation of engineering flows. *Combustion and Flame*, *29*, 111–122.

Lockwood, F. C., & Shah, N. G. (1981). A new radiation solution method for incorporation in general combustion prediction procedures. *Proccedings of the Combustion Institute*, *18*, 405–1413.

Ludwig, C. B., Malkmus, W., Reardon, J. E., Thomson, J. A. (1973). Handbook of infra-red radiation from combustion gases, NASA SP-3080, scientific and technical information office, Washington D.C.

Lyle, K. H., Tseng, L. K., Gore, J. P., & Laurendeau, N. M. (1999). A study of pollutant emission characteristics of partially premixed turbulent jet flames. *Combustion Science and Technology*, *116*, 627–639.

Magnussen, B. F. (1981). On the structure of turbulence and a generalized eddy dissipation concept for chemical reaction in turbulent flow. *American Institute of Aeronautics and Astronautics, 19, 1456-1465.*

Mahesh, K., Constantinescus, G., Apte, S., Iaccarino, G., Ham, F., & Moin, P. (2006). Large-Eddy Simulation of reacting turbulent flows in complex geometries. *Journal of Applied Mechanics*, *73*, 374-386.

Mahmud, T., Sangha, S. K., Costa, M., & Santos, A. (2007). Experimental and computational study of a lifted, non-premixed turbulent free jet flame. *Fuel*, *86*, 793–806.

Majeski, A., Chui, H. & Kostiuk, L. (2003). Reynolds-averaged modelling of low momentum propane jet diffusion flames in cross-flow. *Combustion Canada, 1, 15-25.*

Masri, A. R., & Bilger, R. W. (1986). Turbulent non-premixed flames of hydrocarbon fuels near extinction: mean structure from probe measurements. *Proccedings of the Combustion institute Institute*, *21*, 1511–1519.

Mcdaniel, M. (1983). Flare efficiency study. *Washington DC, USA Environmental Protection Agency (EPA), EPA-600/2-83-052*.

Menguc, M. P., & Viskanta, R. (1986). Radiative transfer in axisymmetric, finite cylindrical enclosures. *Journal of Heat Transfer*, *108*, 271–277.

Menter, F.R., Langtry, R. B. & Volker, S. (1994). Two-equation eddy-viscosity turbulence model for engineering applications. *American Institute of Aeronautics and Astronautics*, *32*, 1598–1605.

Menter, F. (2005). Transition modelling for general purpose CFD codes. ERCOFTAC Int. Symp. Engineering Turbulence Modelling and Measurements.

Meunier, P., Costa, M., & Carvalho, M. G. (1998). On NOx emissions from turbulent propane diffusion flames. *Combustion and Flame*, *112*, 221–230.

Modest, M. F. (2003). *Radiative Heat Transfer, London, Academic Press.*

Morvan, D., Porterie, B., Larini, M., & Loraud, J. C. (1998). Numerical simulation of turbulent diffusion flame in cross flow. *Combustion Science and Technology*, *140*, 93–122.

Moss J.B., S.L., P., Stewart, C. D., & Makida, M. (2003). Radiation heat transfer in gas turbine combustors. *Proccedings of the Combustion Institute*, *16*, 691–692.

Moussa, Z. M., Trischka, J. W., & Eskinazi, S. (1977). The near field in the mixing of a round jet with a cross-stream. *Journal of Fluid Mechanics*, *80*, 49–80.

Mulkey, S., Smith, M., & Louis, S. (2008). *Measurement of Photosynthesis by Infra-red Gas Analysis,* pp. 1–4.

Nishida, O., & Mukohara, S. (1982). Characteristics of soot formation and decomposition in turbulent diffusion flames, *47*, 269–279.

Norton, T. S., Smyth, K. C., Miller, J. H., & Smooke, M. D. (1993). comparison of experimental and computed species concentration and temperature profiles in laminar, two dimensional methane-air diffusion flames. *Combustion Science and Technology*, *90*, 1–34.

Pantakar, S. V. (1980). *Numerical Heat Transfer and Fluid Flow*. New York, McGraw Hill.

Pardiwalla, D. (1996). Elliptic gas jet flames in a cross-flow. MSc thesis, the University of Oklahoma, USA.

Peters, N. (1984). Laminar diffusion flamelet models in non-premixed turbulent combustion. *Progress in Energy and Combustion Science, 10, 319-339.*

Peterson, R. C. & Laurendeau, N. M. (1985). The emittance of yttrium-beryllium oxide thermocouple coating. *Combustion and Flame*, *60*, 279–284.

Pierce, C., & Moin, P. (2004). Progress-Variable approach for Large-Eddy Simulation of non-premixed turbulent combustion. *Journal of Fluid Mechanics*, 70, 502–504.

Pfeiler, C., & Raupenstrauch, H. (2010). Application of different turbulence models to study the effect of local anisotropy for a non-premixed piloted methane flame. *European Symposium on Computer Aided Process Engineering.*, *20*, 14–28.

Piomelli, U., Yu, Y., & Adrian, R. J. (1996). Subgrid-scale energy transfer and near-wall turbulence structure. *Physics of Fluids*, *12*, 8215–8224.

Pitsch, H., Chen, M., & Peters, N. (1998). Unsteady flamelet modeling of turbulent hydrogen-air diffusion flames. *Proccedings of the Combustion Institute*, *27*, 1057–1064.

Pohl, J. H., Tichenor, B. A., Lee, J., & Payne, R. (1986). Combustion Efficiency of Flares. *Combustion Science and Technology*, *50*, 217–231.

Pope, S. B. (1985). Probability density function methods for turbulent reacting flows. *Progress in Energy and Combustion Science*, *11*, 119–192.

Pope, S. B. (2000). Turbulent flows. *Cambridge, Cambridge University Press.*

Puri, R., & Santoro, R. J. (1994). The Oxidation of Soot and Carbon Monoxide in Hydrocarbon Diffusion Flames, *Combustion and Flame*, *97*, 125–144.

Ranade, V. V. (1988). Computational flow modelling for chemical reactor engineering. *London, Academic Press.*

Ranzi, E., Frassoldati, A., Grana, R., Cuoci, A., Faravelli, T., Kelly, A. P., & Law, C. K. (2012). Hierarchical and comparative kinetic modelling of laminar flame speeds of hydrocarbon and oxygenated fuels. *Progress in Energy and Combustion Science*, *38*, 468–501.

Ranzi, E., Faravelli, T., Kelly, A., & Law, C. (2012). CRECK mechanism. Retrieved from http://creckmodeling.chem.polimi.it/index.php/current-version-december-2012/c1c3-high-temperature-mechanism

Rodi, W. (1984).Turbulence models and their application in hydraulics. *IAHR Monograph series.*Revise ed., Netherlands, Taylor and Francis.

Rogallo, R.S. and Moin, P. (1984). Numerical simulation of turbulent flows. *Ann. Rev. Fluid. Mech*, *16*, 93–137.

Roger, A. S. (1962). Estimated viscosities and thermal conductivities of gases at high temperatures.*Technical Report, NASA,* 22 – 30.

Rothman, L. S. (1992). *Quant. spectroc. rad. transfer*, *48*, 469-507.

Salim, M., & Cheah, S. C. (2009). Wall y^+ Strategy for Dealing with Wall-bounded Turbulent Flows. *Proccedings of the International Multiconference of Engineers and Computer Scientists.*, *2*, 18–25

Santoro, R. J., Yeh, T. T., Horvath, J. J., & Semerjian, H. G. (1987). The Transport and Growth of Soot Particles in Laminar Diffusion Flames. *Combustion Science and Technology*, *53*, 89–115.

Shih, T. H., Liou, W. W., Shabbir, A., Yang, Z. & Zhu, J. (1995). A new $k-\varepsilon$ eddy viscosity model for high Reynolds number turbulent flows: model development and validation. *Computers & Fluids*, *24*, 227–238

Smagorinsky, J. (1963). General circulation experiments with the primitive equations: I. The basic equations. *Monthly Weather Review*, 91,99–164.

Smith, T. F., Shen, Z. F. & Friedman, J. N. (1982). Evaluation of coefficient for the Weighted-Sum-of-Gray-Gas-Models. *Journal of Heat Transfer*, 104, 602–608.

Spalding, D. B. (1971). Mixing and chemical reaction in steady confined turbulent flames. *Proceedings of the Combustion Institute*, 13, 649–657.

Speziale, C. G., Abid, R. & Anderson, E. C. (1992). Evaluation of two-eqation models for near-wall turbulence. *American Institute of Aeronautics and Astronautics*, 30, 324–331.

Stone, D. K., Lynch, S. K., & Pandullo, R. F. (1995). Flares. *U.S. Environmental Protection Agency*, 1–44.

Strosher, M. (1996). Investigations of Flare Gas Emissions in Alberta. *Final Report to: Environmental Canada Conservation and Protection, Alberta Research Council Calgary, Alberta*, 39–50.

Strosher, M. T. (2011). Characterization of Emissions from Diffusion Flare Systems, (October 2012), 37–41.

Syed, K. J., Stewart, C. D., & Moss, J. B. (1990). Modelling soot formation and thermal radiation in buoyant turbulent diffusion flames. *Proceedings of the Combustion Institute*, 23, 1533–1541.

Thermal Solutions Asia Pte Ltd. (2012). Retrieved February 14, 2012, from http://www.thermalsolutionsasia.com

Tidona, R. J., Nizami, A. A., & Cemansky, N. P. (1988). Reducing interference effects in the chemiluminescent measurement of nitric oxides from combustion systems. *Journal of Air Pollution and Control Association*, *38*, 806–811.

Tsuji, H. & Yamaoka, I. (1969). The structure of counterflow diffusion flames in the forward stagnation region of a porous cylinder. *Proccedings of the Combustion Institute*, *12*, 997–1005.

Turns, S R, & Lovett, J. A. (1989). Measurements of oxides of nitrogen emissions from turbulent propane jet diffusion flames. *Combustion Science and Technology*, *66*, 37–41.

Turns, S.R., Myhr, F. H., Bandaru, R. V., & Maund, E. R. (1993). Oxides of nitrogen emissions from turbulent jet flames: Part II – Fuel dilution and partial premixing effects. *Combustion and Flame*, *93*, 255–269.

Versteeg, H. K., & Malalasekera, W. (2007). An introduction to computational fluid dynamics: The finite volume method. 2nd edition. Pearson prentice Hall.

Wang, B. L., & Pitsch, H. (2007). Large-eddy simulation of an industrial furnace with a cross-flow-jet combustion system. *Combustion Science and Technology*, 23, 231–240.

Wang, L., Endrud, N. E., Turns, S. R., D'Agostini, & Slavejkov, A. G. (2002). A study of the influence of oxygen index on soot, radiation, and emission characteristics of turbulent jet flames. *Combustion Science and Technology*, *174*, 45–72.

Wen, Z., Yun, S., Thomson, M. J., & Lightstone, M. F. (2003). Modeling soot formation in turbulent kerosene/air jet diffusion flames. *Combustion and Flame*, *135*, 323–340.

Westoreland, P. R., Howard, J. B., & Longwell, J. P. (1986). Tests of published mechanisms by comparison with measured laminar flame structure in fuel-rich acetylene combustion. *Proccedings of the Combustion Institute*, *18*, 773-780.

Wilcox, D. C. (1988). Reassesment of the scale-determining equation for advanced turbulence models. *American Institute of Aeronautics and Astronautics*, *26*, 1299–1310.

Wilcox, D. C. (1993). Turbulence modeling for CFD. *DCW Industries Inc., La Canada, California.*

Williams, F. A. (1985). Combustion theory, 2nd edn. *Addison-Wesley, Redwood City, CA.*

Zeldovich, Y. B., Sadovnikov, Y. P., & Frank-Kamenetskii, D. . A. (1947). Oxidation of nitrogen in combustion. *Academy of sciences of the USSR, Moscow*.